FY25
LABORATORY DIRECTED RESEARCH & DEVELOPMENT
ANNUAL REPORT

Savannah River National Laboratory®

SRNL-STI-2026-00180

Disclaimer

Message from the Deputy Lab Director for Science and Technology

At Savannah River National Laboratory (SRNL), we put science to work to provide solutions to the Department of Energy (DOE) and other federal government partners. SRNL remains committed to advancing its mission through strategic investments that align with laboratory and national priorities, ensuring our science and technologies continue to address the nation's most pressing challenges.

The Laboratory Directed Research and Development (LDRD) Program represents one of SRNL's most valuable tools for cultivating innovation and aligning with the laboratory's forward-looking strategy. Investments through the LDRD Program drive research and technological advancements that support SRNL's mission areas: National Security, Environmental Stewardship, and Energy Resilience. FY25 marked a renewed focus on partnerships, targeted investments, and collaboration, fostering scientific and technical excellence.

Strengthening partnerships, including those with our BSRA university partners, remains a strategic priority for the laboratory. The Laboratory Director's Postdoctoral Fellowship exemplifies this commitment by supporting postdoctoral researchers who work alongside SRNL experts and joint appointees. This collaborative framework accelerates the development of technical talent and ensures alignment with emerging sponsor priorities.

SRNL continued substantial investments in its Strategic Initiatives portfolio in FY25, which allows the laboratory to address critical needs identified by senior leadership. This year has seen significant advancements in areas such as artificial intelligence for national security applications and nuclear fuel cycle optimization for energy resilience. These initiatives not only enhance SRNL's research capabilities but also support inter-laboratory collaborations, such as SRNL's participation in the Interlaboratory LDRD Call for Proposals, aimed at advancing research in fusion systems and energy infrastructure resilience.

This Annual Report celebrates the remarkable achievements made possible by SRNL's LDRD Program in FY25. It shows how our strategic investments, innovative research, and collaborative efforts continue to deliver value to DOE, other stakeholders, and the broader scientific community.

Tammy Taylor, Ph.D., P.E.

Deputy Laboratory Director for Science and Technology, Chief Research Officer

Contents

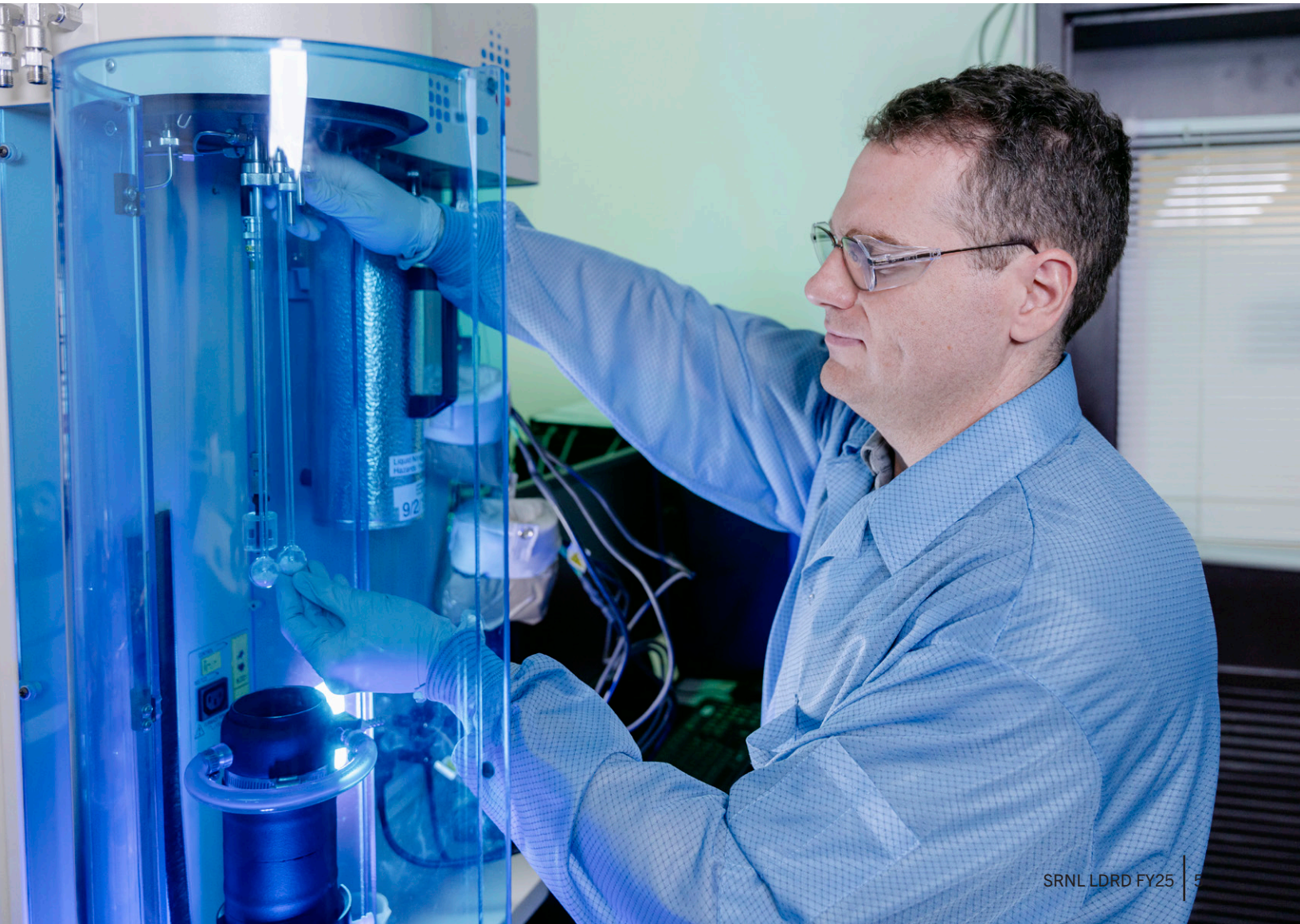

SRNL Team Wins R&D 100 Award for Advanced Engineered Cellular Magmatics Project

The Savannah River National Laboratory Advanced Engineered Cellular Magmatics (AECM) technology team has been named as a winner for the 2025 R&D 100 Awards.

SRNL Researcher Cory Trivelpiece and his team developed the technology in partnership with Silica-X, Inc. Often called the "Oscars of Innovation," the R&D 100 Awards recognize the most significant scientific and technological breakthroughs worldwide since 1963. The foundation for this successful partnership was initiated and cultivated through the LDRD-funded project called *Functionalized Cellular Magmatics* in 2020. The success of the LDRD project garnered critical DOE-EM follow-on funding, which enabled additional innovations and advancements in the field. With encouragement and support from lab leadership, SRNL's Technology Partnership Office identified the AECM project as a strong candidate for the award. The communication department at SRNL, in partnership with Savannah River Nuclear Solutions, created supporting content and marketing materials to support the application process. This collaborative effort across SRS resulted in the first R&D award in several years.

"I'm incredibly proud of our SRNL team, led by Dr. Cory Trivelpiece, for earning this R&D 100 Award in partnership with Silica-X," said Dr. Johney Green, SRNL director. "This recognition highlights the power of innovation and reflects not only our world-class science but also the commitment of SRNL and our collaborators to deliver solutions that advance national priorities and create lasting impacts."

The AECMs were originally synthesized from post-consumer waste glass – tricolored "recycled" glass that constitutes most common consumer product containers. As much as 85% of curbside "recycled" glass is sent to landfills in the U.S., because it is cheaper to throw away a glass bottle than to recycle it into a new glass bottle. This is where AECMs have their greatest strength: many of the issues that prevent glass manufacturers from incorporating more recycled products into their feedstocks don't apply to AECM production. SRNL has expanded those feedstocks to include commercial waste glass and waste-to-energy-ash.

The flexibility of AECMs stems from their ability to be tailored chemically, mineralogically, and physically to meet the needs of multiple use cases. Born out of a need to mimic the properties of volcanic tephra thought to play a role in the extreme durability of ancient Roman concrete, SRNL researchers unlocked fundamental aspects of AECM processing that enable targeting of seemingly unrelated applications with minor modification to formulation and processing.

If implemented, this would enable a containerized waste form that requires no mixing equipment and minimal onsite operations – simply add the liquid waste to any container full of AECMs and chemistry takes care of the rest. Watch a video showcasing this technology.

"It's an honor for me and this team to get recognition from the awards committee – to be selected for the award along with other national labs and some of the largest R&D companies in the world is truly humbling and amazing," said Trivelpiece.

The Secretary of Energy visited SRNL on August 6. Trivelpiece briefed the secretary on AECMs during his visit. The secretary posted on his Facebook page next day, stating "The Savannah River Site showcases the U.S. Department of Energy's commitment to accelerating remediation and minimizing waste. The future of next gen nuclear material processing is being forged now, and I applaud Savannah River Site for setting the standard for responsible disposition of nuclear materials."

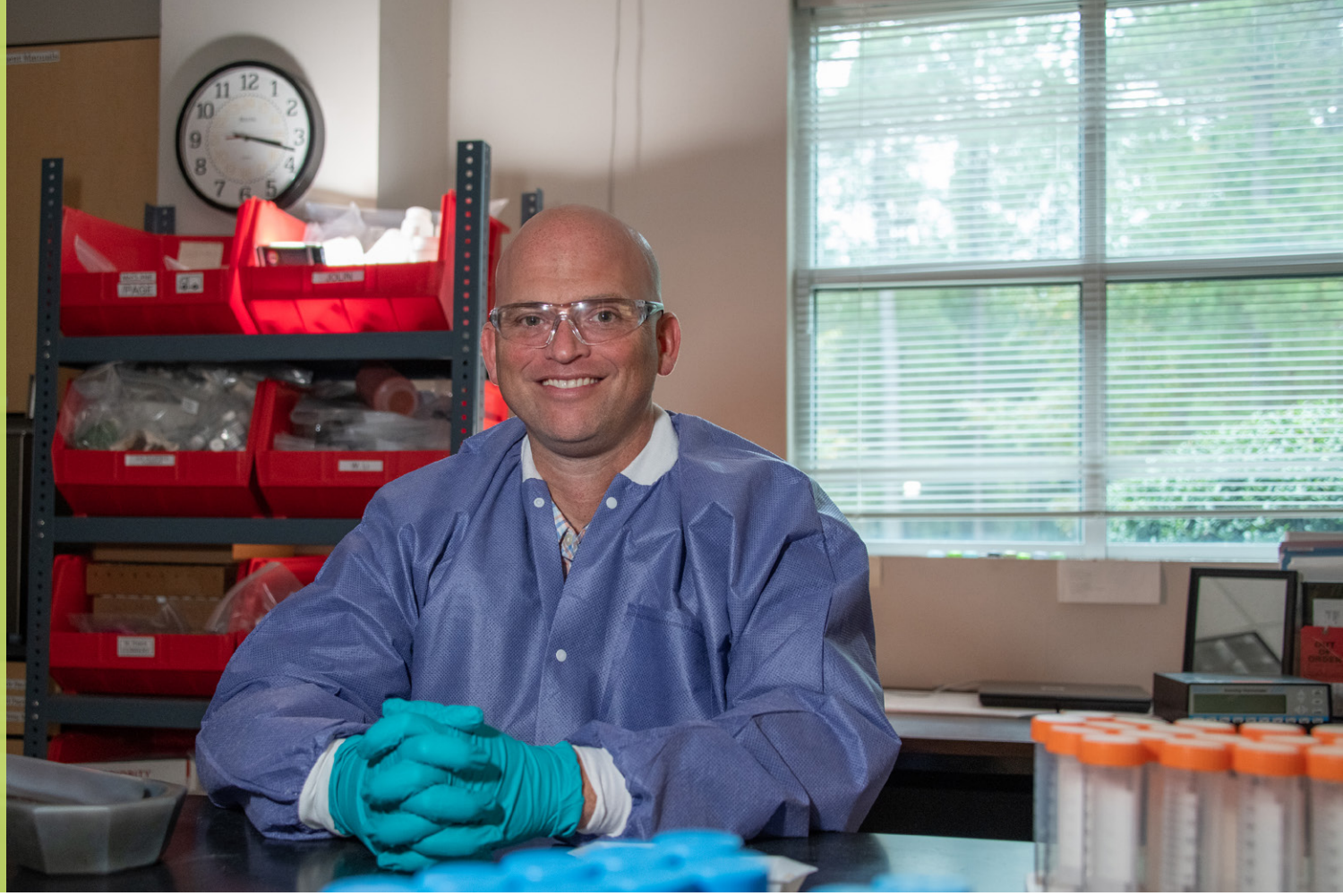

Trivelpiece's team is moving their laboratory into the Advanced Manufacturing Collaborative (AMC) facility to continue advancing the technology. SRNL recently constructed the facility on the University of South Carolina, Aiken campus. "This is an example why the recently completed AMC Facility is so critical to SRNL's future. And we can't wait to see what the laboratory will do next," said Roger Jarrell, principal deputy assistant secretary for EM.

The AECM technology is currently funded by the DOE Office of Environmental Management's Laboratory Policy Office through the Hanford tank waste research and development program. According to Dr. Ming Zhu, EM's senior advisor for laboratory policy, SRNL has been expanding its research portfolio through public-private partnership to position the laboratory for an enduring mission as EM works towards the completion of nuclear legacy cleanup since EM awarded the laboratory's management and operating contract to Battelle Savannah River Alliance, LLC in 2021.

"SRNL's partnership with Silica-X, Inc. enables real-time tech-to-market analysis of laboratory-scale results and the ability to translate these results to industrial scale solutions," noted Trivelpiece. "This system of parallel scientific exploration and technoeconomic analysis rapidly intensifies commercialization and shaves years off the national laboratory's product development cycle. This synergy enables SRNL researchers to develop solutions that are designed to end the cycle of take-make-waste all while accelerating EM's cleanup mission at sites like Hanford."

Philip Galland, CEO of Silica-X, Inc., SRNL's industry partner, first presented the idea for collaboration in developing the AECM technology in a panel session at the DOE Waste Management 2022 Conference. After winning the Hanford tank waste research and development project in 2024 and the 2025 R&D 100 Award with Trivelpiece, Galland added:

"Being named an R&D 100 Winner with SRNL is a testament to what's possible when national labs and industry collaborate to innovate — taking breakthrough science to market faster. Our partnership model not only accelerates solutions for urgent challenges like EM's cleanup mission at sites like Hanford but also proves that collaboration is the winning formula for rapid impact at an industrial scale."

Philip Galland, CEO of Silica-X, Inc.

Overview

The Laboratory Directed Research and Development (LDRD) program represents a cornerstone of foundational scientific research and development (R&D) at SRNL. It is central to advancing SRNL's mission areas—National Security, Environmental Stewardship, and Energy Resilience—while aligning with the laboratory's Strategic Plan to deliver long-term benefits to the Department of Energy (DOE) and other key stakeholders.

To achieve SRNL's mission, the laboratory is guided by six strategic directions:

1) Expanding nuclear deterrence and nonproliferation missions while accelerating environmental cleanup efforts
2) Fostering a culture of scientific innovation, collaboration, and empowerment integrated with safety, security, and operational principles
3) Maximizing the impact of the Advanced Manufacturing Collaborative
4) Driving innovation in energy technologies
5) Advancing emerging technologies for defense mission priorities
6) Strengthening partnerships with national labs, academia, industry, and community stakeholders

Underpinning these strategic directions are SRNL's 10 R&D priorities, which serve as the foundation for achieving the laboratory's goals:

- Tritium & Hydrogen Isotopes Science
- Applied Actinide Science & Technology
- Nuclear Materials Science and Sensing
- Nuclear Fuel Cycle Optimization and Processing
- Environmental Remediation
- Fusion Fuel Cycle Science
- Critical Infrastructure and Grid Resilience Test & Evaluation
- Cyber Assurance Test & Evaluation
- Applied Advanced Manufacturing & Automation
- Decision Science & Artificial Intelligenceta

SRNL has focused LDRD Program investments to expand and strengthen the SRNL core competencies. Each project aligns with one or more of the technical core competencies. In addition to supporting SRNL's core competencies, each LDRD investment aligns with one or more of three overall program objectives:

The Three Main Objectives of the LDRD Program

LDRD FY25 by the Numbers

46
Total Projects

$10.54M
Total Program Cost
Fully Burdened

Universities Engaged

- Augusta University Research Institute
- Bowling Green State University
- Clemson University
- Georgia Institute of Technology
- North Carolina State University
- The Ohio State University
- Univeristy of South Carolina, Columbia
- University of Flordia
- University of Georgia
- University of North Carolina, Chapel Hill
- University of South Carolina, Aiken
- University of Tennessee - Knoxville

26
Peer-Reviewed Publications
Manuscripts are evaluated in an independent review where experts assess the research for quality and accuracy prior to publication acceptance.

6
Patents Issued

3
Patent Applications

2
Invention Disclosures

31
Postdocs Funded
over 10% of total hours

5
Postdocs Converted to Staff Hires

39
Projects Involving Postdocs

26
Projects Led by Early Career Staff
Early career: within 5 years of terminal degree

6
Projects Involving Interns

Applied Actinide Science and Technology

Chemical Vapor Transport for the Preparation of Single Crystals of Actinide Complexes

Shawna Tazik

Actinide-containing materials have shown promise for applications in electronics and quantum computing applications due to many being strongly correlated materials. Furthermore, fine-tuned synthesis of two-dimensional materials is of interest due to potential for unique dimension-related properties. In this study, uranium-based single crystals were synthesized and analyzed for key physical properties.

Introduction

Ferromagnetic materials are pivotal for the development of logic and optoelectronic devices. Memory devices employ ferromagnetic spintronics which capitalize on the spin and charge of electrons to achieve faster, non-volatile memory. Recently, f-block elements have attracted significant attention owing to their strong spin-orbit coupling, which have enhanced magnetic properties in low-dimensional materials.[1,2] Crystalline transition metal chalcogenides, in particular, are noteworthy because they form van der Waals layers, resulting in ease of exfoliation to two-dimensions. Among these, uranium ditelluride (UTe_2) has garnered immense interest following its identification as an unconventional superconductor.[3] While UTe_2 has been significantly studied, the uranium tritelluride (UTe_3) analog has been comparatively overlooked.

Initially, UTe_3 was structurally determined to be in the monoclinic $P2_1/m$ space group.[4] Later, a new polymorph was characterized in the orthorhombic *Cmcm* space group.[5] Several studies have reported on the magnetism of monoclinic α-UTe_3 but the results have been seemingly contradictory, possibly due to inclusion of the β-UTe_3 in the crystals.[4,6,7] Meanwhile, the orthorhombic β-UTe_3 has been reported only once and is posited to have ferromagnetic behavior.[5] In an effort to optimize the synthesis of UTe_3 for polymorph control to obtain the target posited ferromagnetic β-UTe_3, we have collaborated with the University of Georgia. The synthesized β-UTe_3 was thoroughly characterized to understand its physical properties. Additionally, the team has set-up a radioactive material capable chemical vapor transport crystal growth system on-site, enabling future work in the field of single crystal growth with applications in detectors, quantum science, and electronics.

Approach

Crystal quality and purity are essential for obtaining accurate measurements of physical properties. To achieve this, precise control of the synthesis parameters was employed to deconvolve the growth of the α-UTe_3 and β-UTe_3 polymorphs and to prevent cross-inclusion in the targeted β-UTe_3 material. Both polymorphs were synthesized using the chemical vapor transport (CVT) method (**Figure 1**) with $TeBr_4$ as the transport agent, yielding gold-colored β-UTe_3 crystals with silver-colored α-UTe_3 crystals (**Figure 2**).

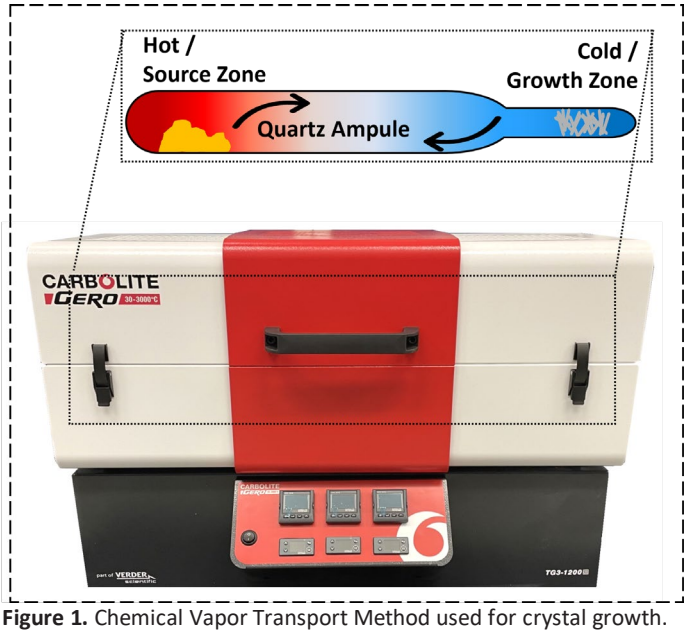

Figure 1. Chemical Vapor Transport Method used for crystal growth.

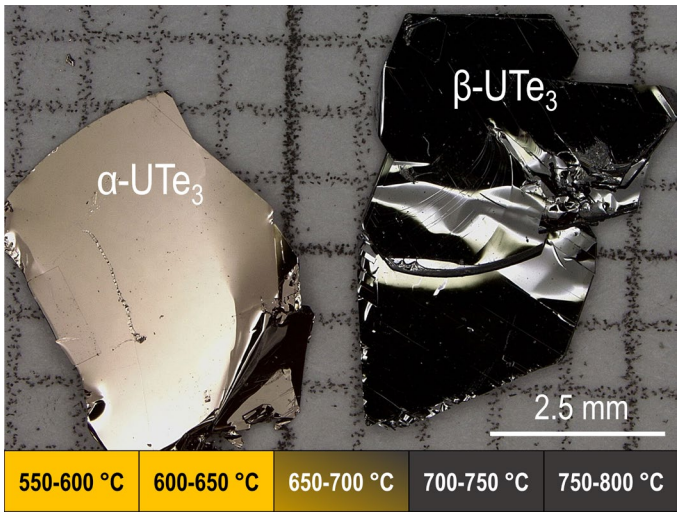

Figure 2. Single crystals of α-UTe_3 (left) and β-UTe_3 (right) optimized at different synthetic temperature profiles.

Structural characterization of optimized polymorphs was done using Single-Crystal X-Ray Diffraction (SC-XRD), with purity confirmed by powder X-Ray Diffraction (pXRD) and Energy Dispersive Spectroscopy (EDS). The magnetic properties of β-UTe_3 were investigated via temperature-dependent magnetization, specific heat measurements, and neutron diffraction. Despite no magnetic Bragg peaks in neutron diffraction, Density Functional Theory (DFT) calculations provided insight into the magnetic ground state. Project efforts were further expanded into synthesizing and investigating other actinide-bearing, chalcogenide-containing materials. This work aims to deepen our understanding in the field and support discovery of novel materials and properties.

Accomplishments

- Successfully deconvolved the synthesis of the α-UTe_3 and β-UTe_3 polymorphs using precise temperature control with the CVT method; this is unlike previous literature that used a broad temperature range.[5] This approach prevents inclusion of the other polymorph in the single crystals for optimized physical property measurements. Each polymorph was structurally confirmed via SCXRD and their purity confirmed via pXRD (**Figure 3**).

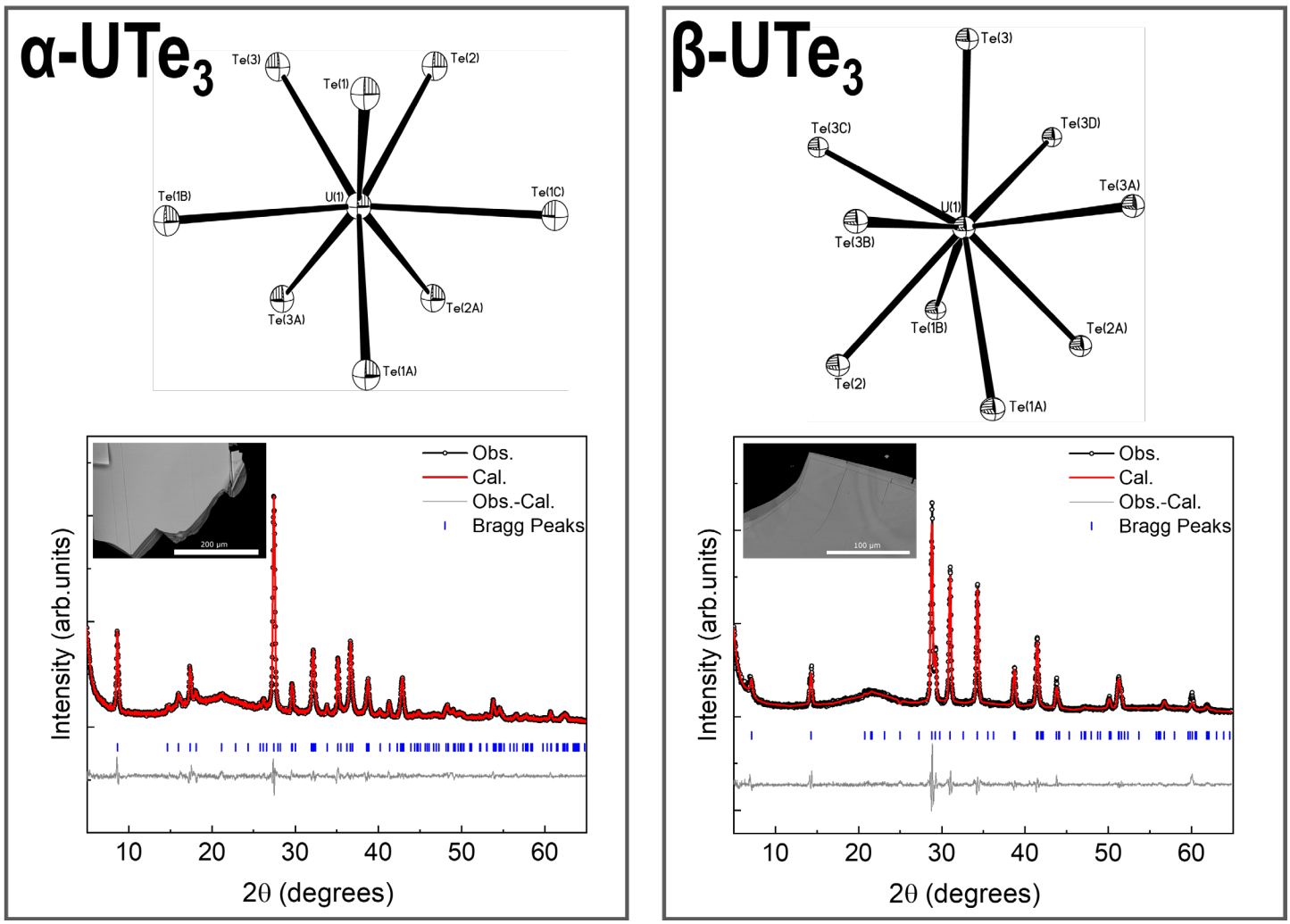

Figure 3. SCXRD of α-UTe_3 (left) and β-UTe_3 (right) single crystals grown, demonstrating the eight-fold and nine-fold coordination of the crystals, respectfully. Purity of the crystals were demonstrated with pXRD of pulverized crystals together with the LeBail fitting (red line) and Bragg positions (vertical lines).

- Performed temperature-dependent magnetization measurements on the targeted β-UTe_3, which showed an upturn in magnetization around 20 K under a magnetic field of μ_0H = 0.02 T. This behavior is similar to that which was reported for α-UTe_3,[6] possibly explaining some of the contradictory results observed for that polymorph.
- The magnetization revealed a magnetic anomaly around 12 K, which is consistent with the ferromagnetic phase transition reported.[5]
- Specific heat measurements were obtained on β-UTe_3 crystals, which confirm an anomaly at 12 K.
- DFT calculations were performed for β-UTe_3 to determine the lowest energy state. This revealed the ferromagnetic configuration has an energy several meV lower than the antiferromagnetic configuration. Furthermore, the DFT calculations support the conclusion that the magnetic moments are aligned along the *b* direction.
- This work has expanded into the synthesis of other uranium chalcogenides and thorium chalcogenide materials. Structural and magnetic properties of these materials will be processed and presented in time.
- With this project's efforts, there is now a CVT set-up available for radioactive materials at SRNL.

Team Members

Shawna Tazik, Binod Rai, Lorianne Shultz-Johnson*, Matthew Simmers, Rosalie Greer, Nicholas Sesing[a], Tina Salguero[a], Shuxiang Zou[b], Krysztof Gofryk[b], Volodymyr Buturlim[b]*, Matthias Frontzek[c], Sabin Regmi[b], Si Athena Chen[c].

[a]*University of Georgia*
[b]*Idaho National Laboratory*
[c]*Oak Ridge National Laboratory*
**Postdoctoral Researcher*

References

1. Liu, J.; Wang, H.; Fang, C; Qian, X. Van der Waals Stacking-Induced Topological Phase Transition in Layered Ternary Transition Metal Chalcogenides. *Nano Lett.* **2017**, *17* (1), 467-475.
2. Vila, M.; Hsu, C. H.; Garcia, J. H.; Benitez, L. A.; Waintal, X.; Valenzuela, S. O.; Pereira, V. M.; Roche, S. Low-Symmetry Topological Materials for Large Charge-to-Spin Interconversion: The Case of Transition Metal Dichalcogenide Monolayers. *Phys. Rev. Res.* **2021**, *3* (4), 043230.
3. Ran, S.; Eckberg, C.; Ding, Q. P.; Furukawa, Y.; Metz, T.; Saha, S. R.l Liu, I. L.; Zic, M.; Kim, H.; Paglione, J.; Butch, N. P. Nearly Ferromagnetic Spin-Triplet Superconductivity. *Science* **2019**, *365* (6454), 684-687.
4. Noel, H. Magnetic Susceptibility of the Uranium Trichalcogenides US_3, USe_3 and UTe_3. *J. Less-Common Met.* **1986**, *121*, 265-270.
5. Noel, H.; Levet, J. Characterisation d'un Tritellurure d'Uranium: β-UTe_3 de Structure Type $NdTe_3$. *J. Solid State Chem.* **1989**, *79* (1), 28-33
6. Suski, W. Magnetic and Structural Properties of Actinide Compounds. *Phys. B+C* **1977**, *86*, 11-15.
7. Janus, B.; Suski, W.; Blaise, A. Magnetic Properties of the Uranium Trichalcogenides. *Crystalline Electronic Field Effects in f-Electron Magnetism*; Springer Nature, 1982; pp 539-544.

Surface Modifications to Reduce Tantalum Attack by Chlorine Gas in Molten Salt

Tatiana Ayers

Plutonium purification demands inert materials capable of withstanding harsh conditions, such as molten salt and chlorine/oxygen gas mixtures at high temperatures. A surface treatment with corrosion resistance materials superior to that of carburization of tantalum would benefit plutonium manufacturing by reducing process downtime associated with replacing corroded components, thus helping to limit operator exposure by reducing manual steps required for the processes and enhance product quality by reducing the contaminants from corroded materials.

Introduction

The project's objective is to explore surface modifications to reduce tantalum corrosion in chlorine/oxygen gas mixtures. Tantalum chloride gases form when tantalum is exposed to chlorine gas, causing significant material loss. Untreated tantalum parts fail prematurely under these conditions. In the 1990s, chemical surface modifications of tantalum showed modest performance improvements in molten salt and chlorine gas.[1-3] Carburizing treatments were adopted despite their limited effectiveness in chlorine/oxygen gas mixtures. Since then, various novel surface treatments have been invented, but their performance in chlorine/oxygen gas has been minimally studied.[4] Alternative treatments may offer a more substantial barrier to protect tantalum parts from the gas phase.

Based on a literature review, various surface modifications were selected that had shown promise in corrosion testing with chlorine gas. Working with vendors, procedures to produce tantalum coupons with surface treatments (gas carburization, nitriding, oxynitriding, and ion nitriding) and coatings (rhenium, alumina, and silicon nitride) were developed. The as-received coupons were characterized to evaluate these treatments and coatings. Initial evaluation revealed poor adhesion, surface coverage, and cracking with the rhenium, alumina, and silicon nitride coatings, respectively. After reapplying the rhenium and alumina coatings, improved adhesion and surface coverage was observed. Working with the vendors, novel surface treatments and coatings were applied to Ta coupons that had not been performed previously. A new collaboration with researchers at Lawrence Livermore National Laboratory was initiated to evaluate different carburization treatments of tantalum coupons for their resistance to Cl_2 gas. The glovebox and the associated system needed for corrosion testing are now completed (See **Figure 1**), and Cl_2 gas lecture bottles have been received. Exposure testing will commence in the upcoming fiscal year once final preparations are finished.

Figure 1. Inert glovebox with furnace well and gas delivery system for corrosion testing with Cl_2 gas in molten salts at high temperatures.

Approach

The characterization of the treated, as-received coupons was accomplished using optical microscopy, SEM-EDS, and microhardness testing.

Figure 2 shows the improvement in the adhesion for the rhenium and surface coverage for the alumina coated coupons. The adhesion of the rhenium coating to the tantalum substrate was enhanced by using a tungsten interlayer, which protected the tantalum from the rhenium chloride used in the coating process. The surface coverage of the alumina coating was improved by extending the treatment duration. These improvements in adhesion and surface coverage are expected to enhance performance during exposure testing.

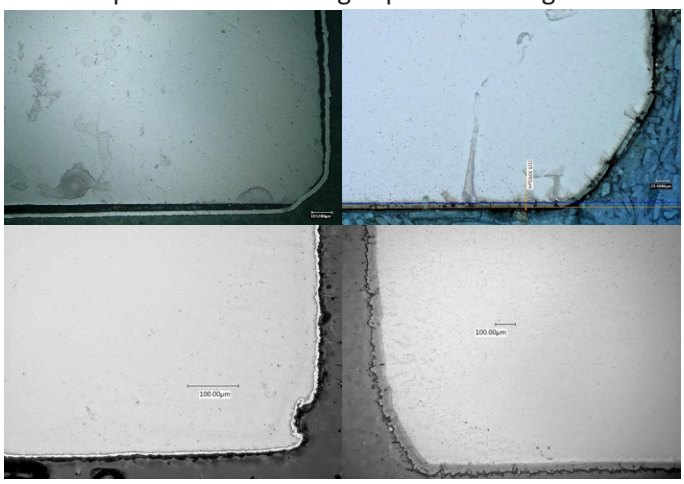

Figure 2. Inert glovebox with furnace well and gas delivery system for corrosion testing with Cl_2 gas in molten salts at high temperatures.

Figure 3 presents the microhardness test results of the surface-treated coupons, with quantitative data in **Table 1**. The case depth and maximum hardness are indicators to the effectiveness of the surface treatment in changing the microstructure of the treated coupons. The ion-nitrided coupons exhibited a larger case depth but lower maximum hardness near the surface compared to gas-nitrided coupons. The higher temperature (2100 °F) oxynitrided coupons showed a thicker case depth and higher maximum hardness than the gas-nitrided coupons. Conversely, the lower temperature (1800 °F) oxynitrided coupons had a shallower case depth and lower maximum hardness near the surface. The higher temperature oxynitride treatment was selected for exposure testing due to its superior maximum hardness and thicker case depth. SEM-EDS data supported the higher base hardness of the ion-nitrided coupons, revealing a bulk nitrogen content of approximately 4 atomic percent, compared to about 1 atomic percent in gas-nitrided and oxynitrided coupons.

Coupon	Base VH	Case Depth (um)	Max VH
Bare Tantalum	92.6	---	102
Gas Carburized	107	~10[a]	374
Gas Nitrided	84.4	358	633
Ion Nitrided	123	462	375
2100 Oxynitride	94.7	415	715
1800 Oxynitride	92.1	222	625

Table 1. Microhardness testing results for surface treated tantalum coupons.

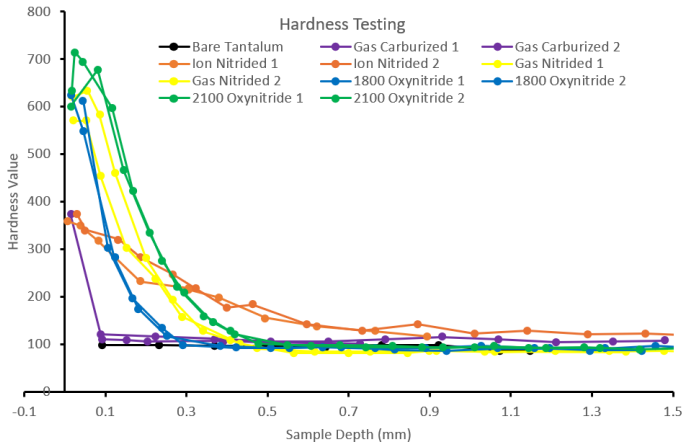

Figure 3. Microhardness testing results for surface treated tantalum coupons.

Accomplishments and Results

- A cleaning procedure was developed using Nitradd to remove the carbon and oxygen surface layers from the Ta coupons to ensure a bare surface for surface treatments and coating applications. The cleaning procedure was evaluated using SEM-EDS to validate the successful removal of the carbon and oxygen from the surface of the Ta coupons.
- ~100 coupons have been received after successfully being surface treated (gas carburized, gas nitrided, gas oxynitride, and ion nitrided) or coated (rhenium, alumina, and silicon nitride). Initial analysis was completed for a sample of each type of surface modification to characterize the as-received coupons.
- Inert glovebox with furnace well and gas delivery system was installed and transitioned to R&D personnel for Cl_2 corrosion testing of modified coupons.
- Optical microscopy was used to evaluate quality of rhenium, alumina, and silicon nitride coatings. After deficiencies were identified, SRNL worked with the vendor for reapplication of the rhenium and alumina coatings, which showed improved adhesion and surface coverage.
- SEM-EDS investigation on the treated coupons showed differences in nitrogen content among the gas nitrided, oxynitrided, and ion nitrided coupons with the ion nitrided coupons having a greater bulk nitrogen concentration. This higher bulk concentration could lead to improved corrosion resistance of the coupon below the surface. Though the lower maxiumum hardness at the surface could lead to less corrosion resistance at the surface than for the gas nitrided and oxynitrided coupons.

- Surface treatment procedures were evaluated with microhardness testing, aiding in the selection of a high-temperature oxynitride treatment over the low-temperature oxynitride treatment for corrosion testing due to its superior results. The ion-nitride, gas-nitride, and gas-carburized coupons will also undergo corrosion testing.
- Presentation given at TMS 2025 titled “Corrosion Testing of Tantalum Coupons with Modified Surfaces in a Molten Salt Environment with Chlorine and Oxygen Gases”.
- Chlorine gas was safely received at Savannah River National Lab, with final preparations underway to begin corrosion testing in the upcoming fiscal year.

Team Members

Colleen Hilla, Greg Chipman*

*Laboratory Director’s Postdoctoral Fellow

References

1. Axler, K.M., *Engineered Materials for Application in Severe Metallurgical Environments: Tantalum-Carbon Alloy Development LA-12876-T*. 1995, Colorado School of Mines: Los Alamos National Lab
2. Rense, C.E.C., et al., *Materials Compatibility During the Chlorination of Molten $CaCl_2$ CaO Salts*. 1987, Los Alamos National Laboratory
3. McLaughlin, D.F., C.E. Sessions, and J.E. Marra, *Corrosion Behavior of Silicon Nitride, Magnesium Oxide, and Several Metals in Molten Calcium Chloride with Chlorine.* Nuclear Technology, 1992. **99**: p. 242-251
4. Takeuchi, M., et al., *Corrosion resistance of ceramic materials in pyrochemical reprocessing condition by using molten salt for spent nuclear oxide fuel.* Journal of Physics and Chemistry of Solids, 2005. **66**(2-4): p. 521-525

Crystal Growth of Lanthanide and Actinide Pyrochlore Oxides

Binod K. Rai

Extensive research has focused on ceramic hosts for immobilizing and disposing of highly radioactive waste due to their chemical durability, radiation resistance, and low-temperature processing. These ceramics, also contenders for quantum materials, were synthesized as lanthanide-based solid-solutions and characterized for quantum magnetism. Two magnetic ions were introduced into the A site of the cubic pyrochlore structure (A2B2O7). with potential to replace a lanthanide ion with an actinide, offering promising advancements in nuclear waste management.

Introduction

Pyrochlore-structured compounds exhibit desirable properties for quantum- and nuclear-waste-immobilization materials. Pyrochlores can form exotic electron configurations due to triangular lattices and thus are contenders to be spin liquid quantum materials. Their quantum entanglement could be leveraged to advance fundamental understanding of quantum magnetism. $Tb_2Ti_2O_7$ and $Er_2Ti_2O_7$ both form as cubic pyrochlore structures with the *Fd-3mZ* space group, but they have different electron ground states and thus different properties. While $Tb_2Ti_2O_7$ has antiferromagnetic (AFM) near-neighbor interactions, no long-range magnetic order is present at low temperatures down to 50 mK. Instead, the material exhibits paramagnetic behavior despite the local AFM interactions [3-6]. It is not fully understood why the magnetic Tb atoms in $Tb_2Ti_2O_7$ readily couple with the nearest neighbors and yet does not exhibit long-range order. On the other hand, $Er_2Ti_2O_7$ is another cubic pyrochlore with the same space group *Fd-3mZ,* but it has long-range AFM order[6,8]. We aim to investigate the magnetic properties of solid solutions of Er-Tb titanate pyrochlores and contrast them to the parent pyrochlores of $Tb_2Ti_2O_7$ and $Er_2Ti_2O_7$.

Approach

We synthesized the pure single-phase solid solutions with the chemical compositions $Tb_{2-x}Er_xTi_2O_7$,where X= 0, 0.2, 0.6, 1.0, 1.4, 1.8, and 2 via solid-state synthesis. Phase purity of polycrystalline materials is essential for physical property measurements, but achieving single phase is nontrivial. Stoichiometric amounts of Tb_2O_3, Er_2O_3, and TiO_2 were mixed in a mortar and pestle until a homogeneous mixture was formed. The homogenized mixture was then pelleted with a hydraulic press and placed in an alumina boat. The samples were heated at elevated temperatures for 24h, then were characterized thoroughly to understand their structural and physical properties. Phase purity was confirmed using Powder X-Ray Diffraction (PXRD). The magnetic and thermodynamic properties were investigated via temperature-dependent magnetization and specific heat measurements. Project efforts were further expanded into synthesizing and investigating other pyrochlores, including actinide-containing ternary oxides. In collaboration with the University of South Carolina: Columbia and Idaho National Laboratory, this work aims to deepen our understanding of the pyrochlore system and support discovery of novel materials and properties. Additionally, the team has secured neutron diffraction beamline time to investigate the local magnetic interactions of the solid solution series.

Accomplishments

- Synthesized phase-pure samples of the solid solution series of $Tb_{2-x}Er_xTi_2O_7$,where x= 0, 0.2, 0.6, 1.0, 1.4, 1.8, and 2 via solid-state synthesis.
- Performed temperature-dependent magnetization measurements on the solid solution series, which showed fluctuating magnetization that is not proportional to either magnetic cation's concentration in the structure.
- Obtained specific heat measurements on the solid solution series, which demonstrate slight shifts in the transition temperatures and nuclear Schottky effects at lower temperatures.
- Expanded work into efforts for single crystal growth and the synthesis of actinide pyrochlores. Structural and magnetic properties of these materials will be processed and presented in time.
- Developed the controls and procedures to bring a programmable high-temperature muffle furnace intended for radioactive materials at SRNL.

Team Members

Binod Rai[a], Gia Thinh Tran[a]*, Hans-Conrad zur Loye[b], Krysztof Gofryk[c], Volodymyr Buturlim[c]*.
[a]*Savannah River National Laboratory*
[b]*University of South Carolina Columbia*
[c]*Idaho National Laboratory*
**Postdoctoral Researcher*

References

1. I. W. Donald, , B. L. Metcalfe, R. N. J. Taylor, The immobilization of high level radioactive wastes using ceramics and glasses. Journal of materials science, *32*, 5851-5887 (1997).
2. W. J. Weber, R. C. Ewing, C. R. A. Catlow, T. D. De La Rubia, L. W. Hobbs, C. Kinoshita, S. J. Zinkle, Radiation effects in crystalline ceramics for the immobilization of high-level nuclear waste and plutonium. Journal of Materials Research, *13*(6), 1434-1484 (1998).
3. E. Vance, C. Ball, R. Day, K. Smith, M. Blackford, B. Begg, and P. Angel, Actinide and rare earth incorporation into zirconolite, Journal of alloys and compounds 213, 406 (1994).
4. P. Raison, R. Haire, T. Sato, and T. Ogawa, Fundamental and technological aspects of actinide oxide pyrochlores: relevance for immobilization matrices, MRS Online Proceedings Library (OPL) 556, 3 (1999).
5. L. E. Chern and Y. B. Kim, Magnetic order with fractionalized excitations in pyrochlore magnets with strong spin-orbit coupling, Scientific reports 9, 10974 (2019).
6. M. J. Gingras and P. A. McClarty, Quantum spin ice: a search for gapless quantum spin liquids in pyrochlore magnets, Reports on Progress in Physics 77, 056501 (2014).
7. Y. Alexanian, E. Lhotel, R. Ballou, C. V. Colin, H. Klein, A. Le Priol, F. Museur, J. Robert, E. Pachoud, P. Lejay, et al., Collective magnetic state induced by charge disorder in the non-kramers rare-earth pyrochlore tb 2 scnbo 7, Physical Review Materials 7, 094403 (2023)
8. L. Bellier-Castella, M. J. Gingras, P. C. Holdsworth, and R. Moessner, Frustrated order by disorder: The pyrochlore anti-ferromagnet with bond disorder, Canadian journal of physics 79, 1365 (2001).

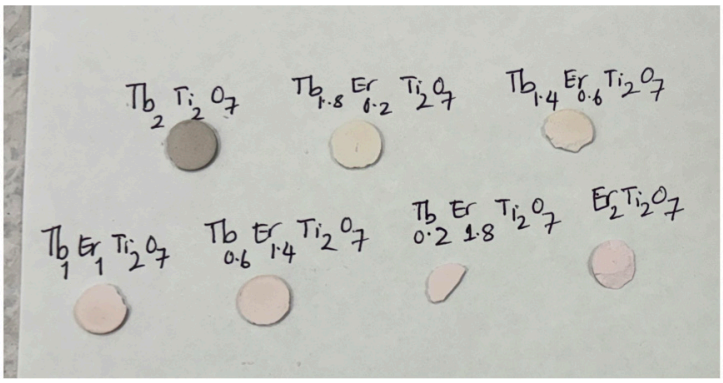

Figure 1 Pellets of $Tb_{2-x}Er_xTi_2O_7$ after annealing. The color gradient indicates a slightly different electronic structure.

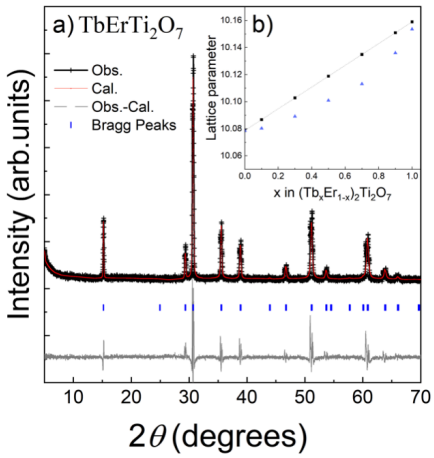

Figure 3 Waterfall plot of all tested chemical compositions of $Tb_{2-x}Er_xTi_2O_7$.

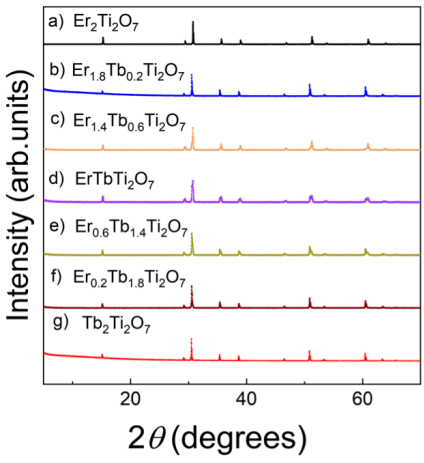

Figure 2 a) Powder X-ray diffraction of $TbErTi_2O_7$. All pyrochlore phases form the cubic structure with space group Fd-3mZ . B) Lattice parameter as a function of chemical composition where the theoretical values are shown in black squares and the experimentally determined site parameters are in blue triangles.

Determination of Actinide Ion Concentrations and Mobility by Chemical Modeling and Spectroscopy

Louis McNamara

This project's goal is to better understand the solvation and dissolution of actinide compounds. An improved understanding of the chemistry and decay dynamics of these species will improve waste disposition and advance nonproliferation efforts to monitor next generation reactor technology.

Introduction

The dissolution of actinides in aqueous environments plays a critical role in nuclear waste disposition, nuclear fuel separations, and some enrichment processes. Next generation nuclear reactors also take advantage of the actinide salts as fuel and a strong understanding of the complex interactions formed will be important for understanding the effluent released by these generation IV reactors. The extreme radiative environment found in waste processing and in nuclear reactors results in electronic excitations that have significant effects on local chemistry. These chemically reactive species are known to lead to accelerated material corrosion and nanoparticle formation but are poorly understood in the environment of nuclear waste and fuel.

Approach

This work will leverage existing SRNL resources in cryogenics, IR spectroscopy, and ultrafast transient absorption spectroscopy. We aim to build on previous results to generate and study ions generated from the dissolution and reactions of actinide species. The work will expand on previous studies by (1) studying the generation of ions in different acid-base networks (2) studying the networks of different actinide ions (3) expanding upon the applied spectroscopic techniques, (4) improving control over ion environment, and (5) applying novel chemometric models to make quantitative assertions about the species generated in these solutions.

Accomplishments and results

- Post doc has completed training and now has clearance.
- Received equipment for experiment.

Team Members

Louis McNamara, Leigh Anna Hunt[*], Martha Grover[a]

[a]*Georgia Institute of Technology*
[*]*Postdoctoral Researcher*

Applied Advanced Manufacturing and Automation

Synthesizing, Compounding, and Characterizing a Heat Labile Foam (SRNL-STI-2025-00653)

Mark Kranjc

Degradable polyurethane foams can be an attractive material to use for packaging, transporting, and dispositioning of nuclear materials. This LDRD project explored the possibility of finding a suitable polyol component that would achieve the intended results. Significant improvements were made on the initial findings of a three-month Visiting Faculty Program.

Introduction

The DOE ships low level radioactive waste items throughout its facilities for temporary and permanent waste dispositioning. This can be done using standard cargo containers. [1], [2], [3], [4] Workers currently secure the load by strapping, precise placement, and scaffolding within the cargo container. With the goal of As Low As Reasonably Achievable (ALARA, DOE Policy [5]) levels of radioactivity exposure for workers, a 2021 Visiting Faculty Program (VFP) identified novel polyol components for use in a polyurethane foam. [6] When these polyols are mixed in the right stoichiometric ratios with a diisocyanate it can be pumped, mixed, and injected into the closed cargo container using foam in place techniques for securement of the load during transport. These novel polyols contain heat labile functional groups along the backbone of the polymer such that when the cargo reaches the destination the container could be heated to elevated temperatures, and the solid foam would be converted to mostly gaseous reaction products, and the load could be removed.

In general, there is a great deal of research in the literature that discusses prevention of polyurethane foam degradation but very little to promote it. [7], [8], [9], [10] In this work we have made significant improvements in reducing degradation temperatures of polyurethane foam using off the shelf polypropylene carbonate polyols and by custom synthesizing several polycarbonates. Other applications for this technology could be as temporary labile printing inks in microelectronics. [11]

Approach

The general approach to this research is outlined in general chronological order.

Year 1

- Review and resynthesis of work covered by the 3-month VFP program.
- Test method development, safety documentation, and determine if additional equipment is needed.
- Determine various baseline components of the part A diisocyanate and part B polyol (see **Figure 1**).
- Finding, selecting, and procuring off the shelf components and samples.
- Determination of the minimum impact strength requirement and foam densities needed for load securement by the foam using Finite Element Analysis.
- Round 1 of synthesis work completed in the 4th Quarter (summer semester) by USCA.
- Preparation of the first paper and presentation for 2024 Polyurethane Conference in Atlanta.

Key isocyanate components in part A	Key alcohol components in part B
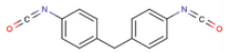 Methylene diphenyl diisocyante (MDI	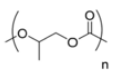 Polypropylene carbonate (PPC)
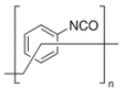 Polymeric methylene diphenyl diisocyante (PMDI)	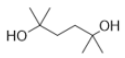 2,3-dimethyl, 2,3-hexanediol (DMDH)
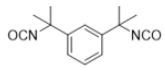 Polymeric methylene diphenyl diisocyante (PMDI)	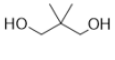 Neopentyl glycol (NPG)
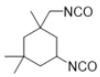 Isopherone diisocyanate (IDI)	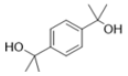 1,4 benzenediisopropanol (BDI)
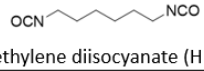 xamethylene diisocyanate (HMDI)	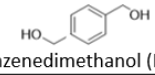 Benzenedimethanol (BDM)

Figure 1. Key primary components of part A (isocyanates) and Part B (alcohols) accumulated throughout Year 1 and 2. Synthesized components are DMDH, NPG, BDI, and BDM. All others purchased off the shelf.

Year 2

- Presentation given at the 2024 Polyurethanes Conference in Atlanta, September 30 to October 2, project outline, details, and summary of Year 1 results. [2]
- SRNL TGA results and project team analysis of Round 1, Year 1, 4th Quarter samples.
- Completion of last test to be developed (Impact Testing) at SRNL.
- Synthesis, TGA testing, and analysis of Round 2 samples.
- Synthesis, TGA testing, and analysis of Round 3 samples.
- Synthesis, TGA testing, and analysis of Round 4 samples.
- Final analysis of project.

Accomplishments and Results

Impact Testing Results:

- Instron Model 9450 Impact Drop Tower System used
- Typical commercial rigid polyurethane foam (Foam iT 3) prepared between 48 to 80 kg/m^3 (3 to 5 lbs./ft^3) density results in dynamic crush strength between 0.54 and 0.68 MPa (80 and 100 psi), within the required range calculated by FEA for this density (requirement: 0.30 to 0.75 MPa or 44 to 109 psi)

Round 1 Primary Conclusions from TGA testing (12 samples submitted)

- Decreasing the amount of water **increases** the decline in % weight loss vs Temperature in the TGA curves.
- Polyurea formed in the foaming reaction of water with isocyanate is suspected to be more difficult to decompose than the polyurethane formed from alcohol and isocyanates (see **Figures 2 and 3**)

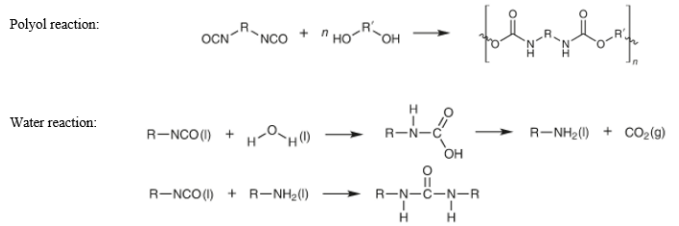

Figure 2. General reaction schemesfor polyurethane foams showing reaction of diisocyanate with dialcohol and reaction of water with isocyanate to create CO_2 foaming along with polyurea.

Round 2 Primary Conclusions from TGA testing (10 samples submitted)

- Begin use of dichloromethane (DCM), a nonreactive foaming agent (bp=40^O C) that produces no polyurea
- 50% weight loss decreased from 400^O C (commercial foam) to 235^O C using PPC 112/DCM + PMDI/MDI

Round 3 Primary Conclusions from TGA Testing (8 samples submitted)

DMDH-co-NPG aliphatic polyol (alternating copolymer) is used to create labile polycarbonate linkages and results in improved TGA curves for the polyol component; onset of significant degradation improved from 144 to 88^O C, point of 50% mass loss improved from 230 to 157^O C (see **Figure 3**)

- The tertiary carbon on DMDH provides a stable carbocation during carbon bond scission along the polymer backbone

Round 4 Primary Conclusions from TGA testing (9 samples submitted)

- The use of TMXDI with DMDH-co-NPG does not result in desired outcome (see **Figure 4**)
- Use of HMDI is the next step, however, there is concern about obtaining the desired impact strength due to creation of a nonrigid foam

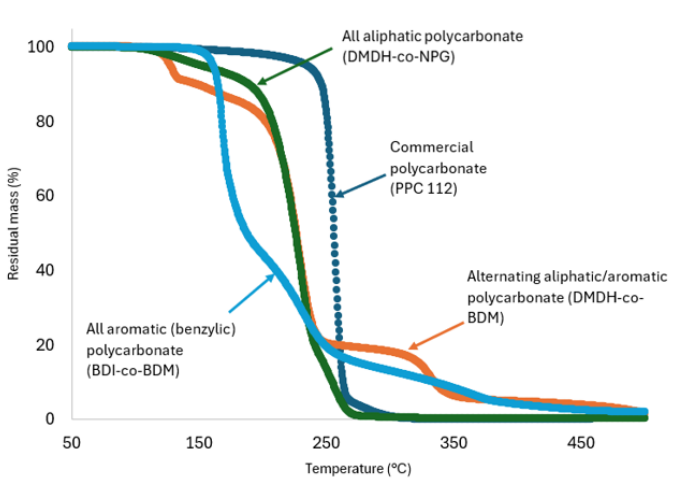

Polyol only, no degradation catalyst

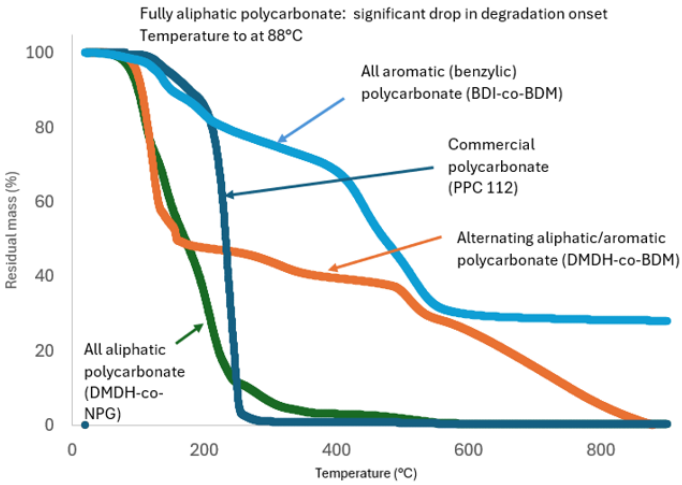

Polyol only with degradation catalyst (TsOH)

Figure 3. *Decrease in degradation onset temperature of polyol and amount of residual weight/char. Graphs show degradation of polyols purchased (PPC 112) and synthesized (all others). The fully aliphatic polycarbonate polyol of DMDH-co-NPG shows greatest promise. No isocyanate added to these.*

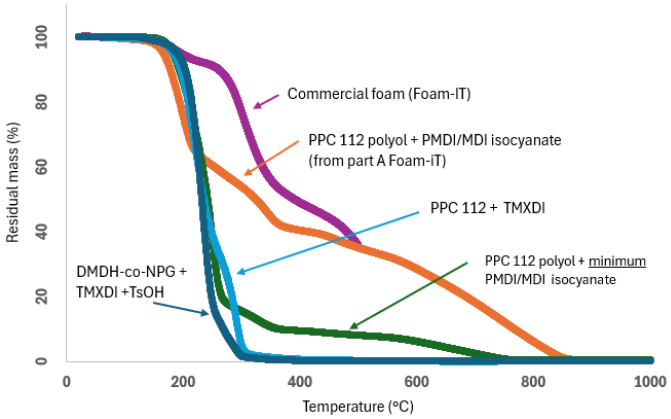

Figure 4. Progression to the use of TMXDI isocyanate did not result in as hoped results with DMDH-co-NPG polyol. Use of HMDI is the next step, however, there is concern about obtaining the desired impact strength.

Intellectual Property

Invention Disclosures

- Development of a Tailored Low Temperature Decomposed "Foam-in-Place" Load Securement Packaging Foam, SRS-22-006, August 16, 2021.

Copyright Disclosures

- For "Synthesizing, Compounding, and Characterizing a Heat Labile Foam", *Conference Proceedings of 2024 Polyurethanes Technical Conference, Center for the Polyurethane Industry of the American Chemistry Council, Atlanta*, GA, Sep. 30 to Oct. 2, 2024.

Patent Applications

- Heat Labile Foam-In-Place Polyurethane Foam, Application No. 17965297, October 13, 2022.
- Heat Labile Foam-In-Place Polyurethane Foam, Patent Application Publication, US 2024/0141127, May 2, 2024.

Team Members

Nicholas Marshall[a], Connor Murrell, Charles McKeel, Matthew Osborne, Cade Willis

[a] *University of South Carolina*

References

1. Kranjc, M.K., "Synthesizing, Compounding, and Characterizing a Heat Labile Foam", *FY24 Laboratory Directed Research and Development Annual Report*, SRNL-STI-2025-00030, p.85, January 2025.
2. Kranjc, M.K.; Marshall N.M.;.McKneel, C.A.; Morrell, C.P.; Osborne, M.L. "Synthesizing, Compounding, and Characterizing a Heat Labile Foam", *Conference Proceedings of 2024 Polyurethanes Technical Conference, Center for the Polyurethane Industry of the American Chemistry Council, Atlanta*, GA, Sep. 30 to Oct. 2, 2024.
3. 49 CFR 173.433, 2024.
4. 49 CFR 173.435, 2024.
5. DOE-HDBK-1215-2014, *Optimizing Radiation Protection of the Public and the Environment*, for use with DOE O 458.1, ALARA Requirements, 2022.
6. Marshall, N.M.; Ketusky, E.T. "Project Report: Heat Labile Foams 2021", SRNL-TR-2021-00478, August 2021.
7. Frechet, J.M.; et al, "Thermally Depolymerizable Polycarbonates. 2. Synthesis of Novel Linear Tertiary Copolycarbonates by Phase-Transfer Catalysis", *Macromolecules*, https://doi.org/10.1021/ma00155a003, 1986.
8. Vojtova, L.; Jancar, J. Method of Preparation of Thermodegradable Polyurethane Foams. WO2010066211A1, June 17, 2010.
9. Mortimer, G. A. A New High-Temperature Free-Radical Source. *J. Org. Chem.* **1965**, *30* (5), 1632–1634. https://doi.org/10.1021/jo01016a074.
10. Dol, C.; Vibert, F.; Bertrand, M. P.; Lalevée, J.; Gastaldi, S.; Besson, E. Diazene-Functionalized Lamellar Materials as Nanobuilding Blocks: Application as Light-Sensitive Fillers to Initiate Radical Photopolymerizations. *ACS Macro Lett.* **2017**, *6* (2), 117–120. https://doi.org/10.1021/acsmacrolett.6b00949.
11. Kohl, P.K.; et al "Thermal Decomposition of Poly(propylene carbonate): End-capping, Additives, and Solvent Effects", Polymer Degradation and Stability, v 125, pp 129-139, 2016.
12. Smooth-On Part A and Part B, Foam-iT!, see SDS sheet for Composition, 2022
13. C.A. McKeel, Structural Performance of Container Securements Using Foam-In-Place Methods, M-CLC-A-00768, 2024.
14. 49 CFR 393.102, 2024

High Temperature Flex Fuel Materials for Energy Resilient Systems

Junhua Jiang

The proposed novel reversible solid oxide cell technology offers a promising solution to improving energy resilience and reliability. By leveraging BSRA's expertise in high temperature materials and advanced manufacturing, SRNL can disrupt this technology to develop core competence. The goal is to prove the technology feasibility and pursue strategic collaboration.

Introduction

Reversible solid oxide cells (rSOCs) which generally operate in the range of 500-1000°C offer a promising technology for improving energy resilience and reliability compared to conventional solid oxide fuel cells [1]. Benefiting from this temperature advantage, rSOCs can directly utilize and earth-abundant non-precious materials for fabricating its cell components, such as the electrolyte and electrodes. rSOCs can produce power and heat from fuel in fuel cell mode, and store electrical energy by splitting water to produce hydrogen, CO_2 to produce CO, or their combination to produce syngas in an electrolysis mode. This dual functionality in combination with their high efficiency and fuel flexibility makes rSOCs unique for combined heat and power, and energy storage for managing intermittent renewable energy sources. Very recently, they have been studied as an energy solution for the building sector, to help stabilize grids, and to decentralize energy generation. In addition to the conventional "H_2-H_2O" cycle, rSOCs are also possible with the "hydrocarbon fuel-CO_2" cycle benefiting from its high temperature operation, which is commonly known as the syngas operation [2]. rSOC systems exploiting the beneficial effects of methane formation, either inside the rSOC or in external reactors, can reach round-trip efficiencies in the order of 70% and beyond. The inclusion of an additional energy source, the Natural Gas network, is helpful to improve resilience. The main challenges with the high operating temperature of rSOCs include longer start-up times, potential mechanical and chemical compatibility issues, and materials degradation.

Approach

This project proposes to develop a novel rSOC technology. The key innovation is that the technology operates with all oxidation reactions at the same anode and all reduction oxidations at the common cathode, as shown in **Figure 1**. This concept is substantially different from the conventional rSOCs in which the corresponding redox reactions (e.g., H_2 evolution from water and H_2 reduction to produce water) occur on the same electrode. Different couplings of the oxidation and reduction reactions shown in the table will expand the capabilities of rSOCs. The proposed rSOC technology offers a unique opportunity to address the challenges with state-of-the-art technologies through developing multi-functional high temperature materials, particularly the electrolyte and electrode materials, to meet specific requirements for both fuel cell and electrolysis modes, such as high ionic conductivity, low electronic conductivity, high chemical stability, structural stability, and facile kinetics of oxidation and reactions involved in the rSOC operation. In addition, this project also provides a unique approach to study efficient use of a range of fuels (such as methane, hydrogen and ethanol) and thermal energy (such as waste heat and nuclear thermal energy) to meet increasing power demand.

Accomplishments

- A fully assembled system with the controls of gas flow, temperature, and voltage/current for the testing of high temperature electrode materials and planar rSOC cells in a temperature range of 500 to 800°C (**Figure 2**).
- Several high-temperature multi-functional electrode electrocatalysts, oxygen-ion conducting electrolyte membrane, and the button-type membrane-electrode assemblies have been in place for evaluation using a ceramic tubular testing rig (**Figure 3**).
- SRNL has initialized the collaboration with Georgia Tech's Dr. Comas Haynes, funded via internal Ga Tech funding to understand and prioritize the opportunities for future success and build upon this seedling funding. Dr. Haynes will lead technical and economic modeling of the rSOC systems integrating thermal and electrical conversions at multiple size scales.

Collaborating Institutions/Universities

- Georgia Institute of Technology that supports this project with in-kind cost share.

Team Members

Bryce Brechin, Bronson Lynn, Charles James[a], Comas Haynes[ba] *Savannah River National Laboratory*
[b]*Georgia Institute of Technology*

References

1. Wolf, S.E., Winterhalder, F. E., Vibhu. V., de Haart. L.G., Guillon, O., Eichel. R., Menzler. N. Solid Oxide Electrolysis Cells – Current Material Development and Industrial Application. *J. Mater. Chem. A* **2023**, 11, 17977-18028.
2. Addo, P. K., Molero-Sanchez, B., Chen, M., Paulson, S., Birss, V. CO/CO_2 Study of High Performance $La0.3Sr0.7Fe0.7Cr0.3O_{3-\delta}$ Reversible SOFC Electrodes. *Fuel cells* **2015,** 15 (5), 689-696.

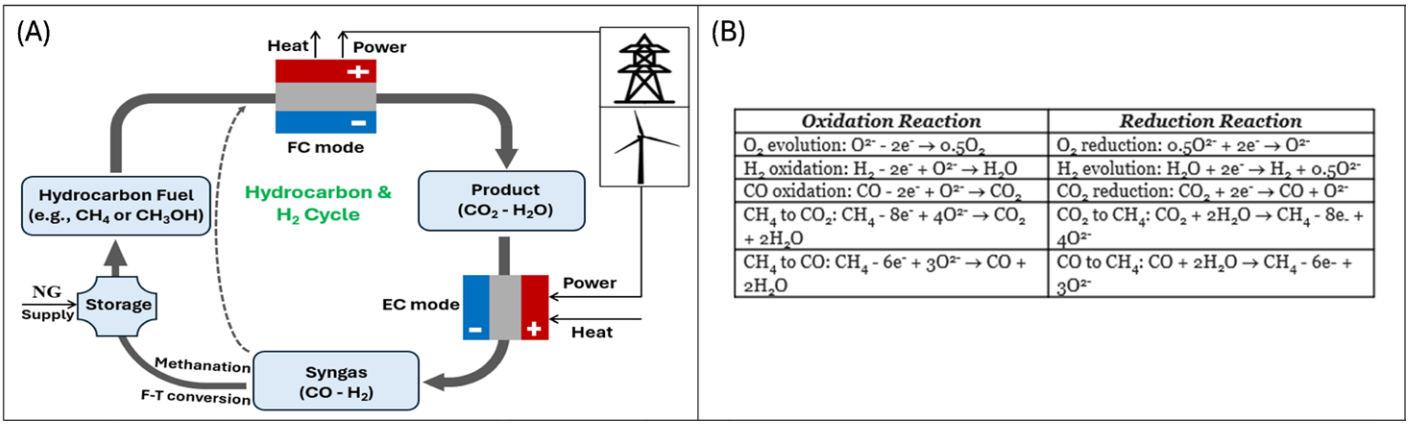

Oxidation Reaction	*Reduction Reaction*
O_2 evolution: O^{2-} - $2e^-$ → $0.5O_2$	O_2 reduction: $0.5O^{2-}$ + $2e^-$ → O^{2-}
H_2 oxidation: H_2 - $2e^-$ + O^{2-} → H_2O	H_2 evolution: H_2O + $2e^-$ → H_2 + $0.5O^{2-}$
CO oxidation: CO - $2e^-$ + O^{2-} → CO_2	CO_2 reduction: CO_2 + $2e^-$ → CO + O^{2-}
CH_4 to CO_2: CH_4 - $8e^-$ + $4O^{2-}$ → CO_2 + $2H_2O$	CO_2 to CH_4: CO_2 + $2H_2O$ → CH_4 - 8e- + $4O^{2-}$
CH_4 to CO: CH_4 - $6e^-$ + $3O^{2-}$ → CO + $2H_2O$	CO to CH_4: CO + $2H_2O$ → CH_4 - 6e- + $3O^{2-}$

Figure 1. (A) Schematic diagram of RSOFCs with syngas and H2 operation; (B) A table of exemplary oxidation and reduction reactions which could be employed in the rSOCs.

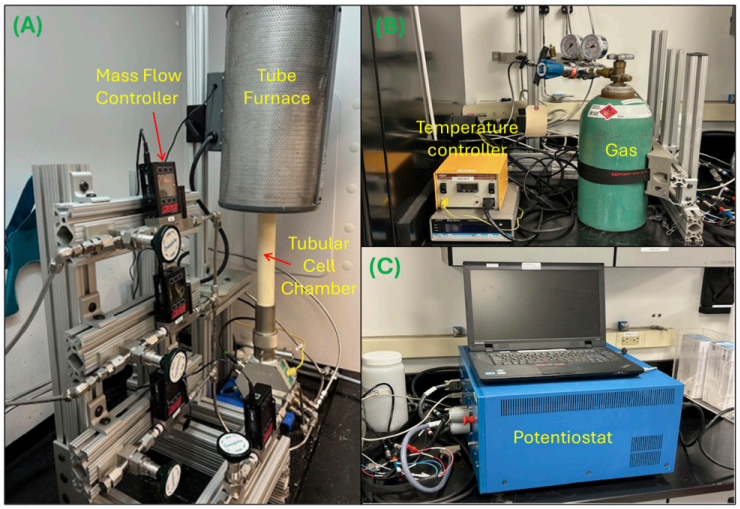

Figure 2. Completed testing system for the rSOC. (A) Tubular cell chamber, tube furnace, and mass flow controllers; (B) Temperature controller and gas cycliners; and (C) Potentiostat for electrochemical measurements.

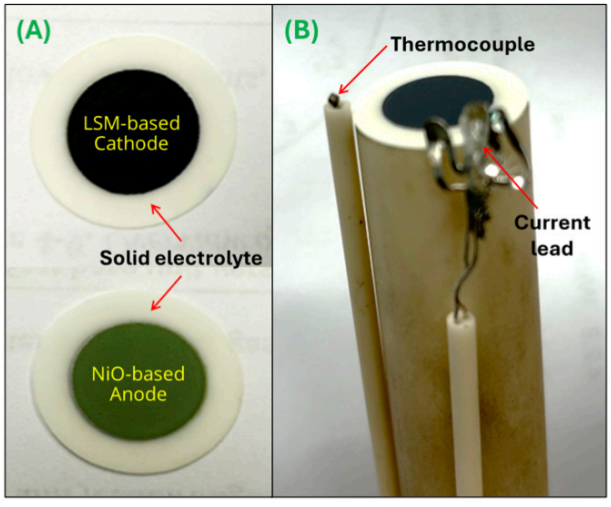

Figure 3. (A) An image of a button cell comprising of solid oxygen-ion conducting electrolyte, LSM-based cathode, and NiO-based anode; and (B) A testing rig showing the button cell, a thermocouple, and current lead.

Additive Manufacturing of Deuterated Polymers for Rheological Model Verification

Camden A. Chatham

In polymer 3D printing, the extent to which neighboring layers fuse together dictates the strength of printed objects. This work experimentally validates modelled predictions of layer fusion through deuterium labelling and spatially-resolved isotopic contrast, which directly captures molecular movement from one layer into another resulting from various manufacturing conditions.

Introduction

The additive manufacturing (AM) (aka "3D printing") layerwise paradigm enables geometric flexibility during fabrication, but results in performance properties governed by layer interfaces. Therefore, interlayer penetration (i.e., molecular diffusion) is critical for adequate part performance. Understanding and predicting part performance from printing conditions is highly desired by those intending to use AM for end-use part fabrication. Rheological models, including the Upper-convected Maxwell[1,2] and Rolie-poly models,[3,4] have been reported to estimate molecular diffusion across layer interfaces for given printing conditions and correlate with interfacial strength. However, direct measurement of interlayer diffusion is challenging since both layers are chemically identical (i.e., "self-same interface"), affording no means of distinguishing between layers on the molecular scale.

The present work introduces isotopic contrast between layers, enabling direct measurement of molecular diffusion resulting from manufacturing conditions (see **Figure 1**). Deuterium labelling provides contrast without significantly altering chemical compatibility at the layer interface, thus minimizing material differences from end-use conditions while enabling measurements enhancing understanding of polymer behavior during end-use conditions. Direct measurements are compared with traditional indirect measurements and computationally determined extent of coalescence through previously published models.

Deuterium labelling for polymer research is underutilized due to the high cost of commercial product. The team successfully deuterated high-density polyethylene (HDPE) leveraging existing SRNL capabilities. Deuterations of additional polymers were attempted but the polymers degraded during the isotope exchange reaction.

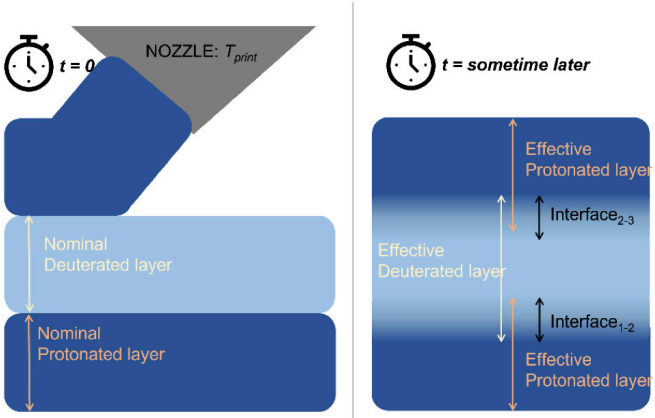

Figure 1. Graphical depiction of alternating layer deposition immediately after deposition (left) and after some elapsed time (right). Interlayer penetration is directly determined from the ratio of measured effective layer height (right) to the nominally deposited layer height (left).

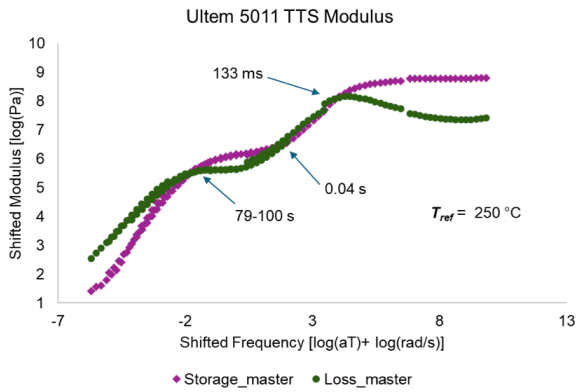

Figure 2. Modulus master curve for Ultem 5011 shifted relative to 250 °C reference temperature. The indicated key relaxation times are calculated based on points of intersection in Storage and Loss Modulus datasets. Calculated C1 and C2 WLF equation fit constants are reported in the figure. R-squared fit metric for linearized shift factors was determined to be 0.995 – a very good fit.

Generating model predictions requires measuring several temperature-dependent polymer properties governing coalescence behavior; such datasets are prerequisite for informing any computational materials engineering effort (see **Figure 2**).

Approach

The project's primary objectives are (I) coding predictive models enhancing the study of structure-process-property relationships in the chosen AM modalities of Fused Filament Fabrication (FFF) and Powder Bed Fusion (PBF) and (II) evaluating molecular diffusion across layer interfaces through deuterium labelling and isotope contrast measurements.

The chosen predictive models (Upper-convected Maxwell for PBF and Rolie-poly for FFF) require temperature-dependent measurements of several key thermal, rheological, and mechanical polymer properties in addition to the thermal environment characteristic of the corresponding AM modality. In addition to temperature profiles experimentally collected via high-speed infrared camera, simulated temperature profiles were constructed to determine the influence of specific features (e.g., peak temperature, baseline temperature, and decay time). These simulated profiles enable the team to exacerbate and isolate key features beyond what can be physically manifested in current SRNL hardware. Such simulated extremes highlight the relative impact of different temperature profile features and the sensitivity of coalescence to each feature. The investigated simulation matrix is shown in **Figure 3**.

The target models predict (i) extent of coalescence and correlate this to (ii) mechanical properties, which are often used as an indirect measurement of coalescence. Experimental isotope contrast-mapping directly identifies locations of deuterium-labelled polymer chains resulting from manufacturing conditions. In-house deuterium labelling was attempted for several polymers; however, the process was deemed viable for only HDPE and atactic polypropylene (aPP), as other polymers degraded at reaction conditions. Due to higher mechanical performance, HDPE was made into 3D printable filament and powder feedstock.

(a) $y = (a/((x+b)^c)))+d$

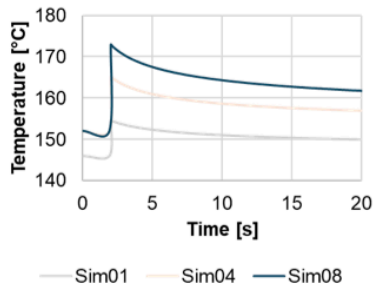

L9 Array ID	a [°C-s]		b [s]		c [-]		d [°C]	
	Relative	*Absolute*	*Relative*	*Absolute*	*Relative*	*Absolute*	*Relative*	*Absolute*
1	Low	11	Low	0.09	Low	0.34	Low	146.00
2	Low	11	Default	0.12	Default	0.43	Default	149.03
3	Low	11	High	0.17	High	0.60	High	152.00
4	Default	18	Low	0.09	Default	0.43	High	152.00
5	Default	18	Default	0.12	High	0.60	Low	146.00
6	Default	18	High	0.17	Low	0.34	Default	149.03
7	High	27	Low	0.09	High	0.60	Default	149.03
8	High	27	Default	0.12	Low	0.34	High	152.00
9	High	27	High	0.17	Default	0.43	Low	146.00

(b) $y=a*\exp(b*x)+c*\exp(d*x)+m*x+bint$

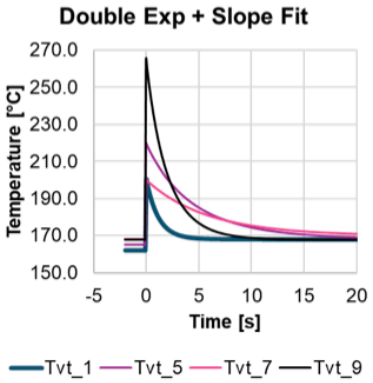

L9 Array ID	***Descriptors*** Tbed (°C)		Tmax (°C)		Peak Width (s)		Tbaseline (°C)	
	Relative	*Absolute*	*Relative*	*Absolute*	*Relative*	*Absolute*	*Relative*	*Absolute*
1	Low	162	Low	200	Low	2	Low	168
2	Low	162	Default	220	Default	5	Default	170
3	Low	162	High	265	High	10	High	172
4	Default	165	Low	200	Default	5	High	172
5	Default	165	Default	220	High	10	Low	168
6	Default	165	High	265	Low	2	Default	170
7	High	168	Low	200	High	10	Default	170
8	High	168	Default	220	Low	2	High	172
9	High	168	High	265	Default	5	Low	168

	Parameters a	b	bint	a2	b2	c	d	m
1	32	-1.73287	441.15	1	-1.73287	31	-0.8585	-0.008
2	50	-0.7824	443.15	15	-0.7824	35	-0.35553	-0.008
3	93	-0.45326	445.15	20	-0.45326	73	-0.21452	-0.008
4	28	-0.66644	445.15	1	-0.66644	27	-0.32958	-0.008
5	52	-0.39512	441.15	15	-0.39512	37	-0.18055	-0.008
6	95	-2.27694	443.15	20	-2.27694	75	-1.07937	-0.008
7	30	-0.34012	443.15	1	-0.34012	29	-0.16836	-0.008
8	48	-1.9356	445.15	15	-1.9356	33	-0.87413	-0.008
9	97	-0.91494	441.15	20	-0.91494	77	-0.43438	-0.008

Figure 3. (a) Selected Krauss Fit simulated temperature profiles with associated L9 Array parameters. (b) Selected Double Exponential + Slope Fit simulated temperature profiles with associated L9 Array parameters.

Accomplishments and results

- The fracture dataset from FY24 was completed and analyzed. Unfortunately, variability resulting from uncontrolled factors, like filament preparation and diameter, dominated results yielding no clear trends between print parameters and fracture.
- D-PMMA purchased in FY24 as an alternative to in-house deuteration was found to be crosslinked and unusable for thermoplastic printing.
- Polymer coalescence prediction code was overhauled to ensure Python compatibility.
- Work on predicting polymer coalescence from manufacturing temperature environments has been leveraged for an AI4NS (NA114) FY26 proposal (*status: submitted and pending decision*).
- Material Libraries for coalescence related properties (e.g., thermomechanical and rheological focus) composed for the following polymers: protonated HDPE (h-HDPE), deuterated HDPE (d-HDPE), Ultem 5011, poly(methyl pentene) (PMP) (see representative data in **Figure 2**).
- FY25 Deuteration efforts included the following polymers: aPP, HDPE, and PMP. aPP and HDPE were successfully deuterated in such a way to (qualitatively) preserve molecular weight.

- PMP appeared to crosslink as a byproduct of deuteration conditions thereby rendering the material unusable for thermoplastic processing.
- aPP is an amorphous polymer and thereby possess little-to-no mechanical integrity on its own proving unusable for 3D printing.
- HDPE was suitably deuterated and purified while preserving molecular weight and architecture. 3D printing filament was successfully made from this d-HDPE.

- Alternating layers of h- and d-HDPE printed via FFF (see **Figure 4**). Fabrication of such a specimen is highly novel and the resulting analysis and increased quantitative understanding of coalescence during 3D printing is expected to be correspondingly highly novel. This specimen is with UTK collaborators for quantitative coalescence analysis via secondary ion mass spectrometry (SIMS).
- The thermal and rheological properties of h- and d-HDPE were measured and compared (see **Figure 5**). The simple isotope exchange affects significant differences in polymer properties governing behavior during manufacturing. However, the isotope exchange does not impact chemical properties, which are often the driving force behind phase separation. The impacted properties are readily accounted for in the coalescence models; therefore, the quantitative approach of printing the mix of h- and d-versions of the same polymer should be preserved. This will be confirmed following SIMS.
- The following polymer powders synthesized by UTK collaborators were printed at SRNL: polypropylene (PP), polycarbonate (PC), PP:PC 50:50 blend, and PP:PC 75:25 blend (see printed mechanical test objects in **Figure 6**).
- UTK has additionally made powder from SRNL-deuterated HDPE (see **Figure 7**). SRNL will print a blend of h- and d-HDPE to generate a test artifact suitable for quantitative determination of coalescence resulting from PBF AM by SIMS as part of FY26 closeout activities. Deuterium labelling is likewise novel for probing coalescence in PBF-AM and will be of similar high impact.

Peer-reviewed Publications

- H. W. Jones, T. Guin, M. Rowland, E. C. Willis, C. A. Chatham, Effect of Deuteration on the Thermomechanical Properties of High-Density Polyethylene. Macromolecular Chemistry and Physics (submitted)*

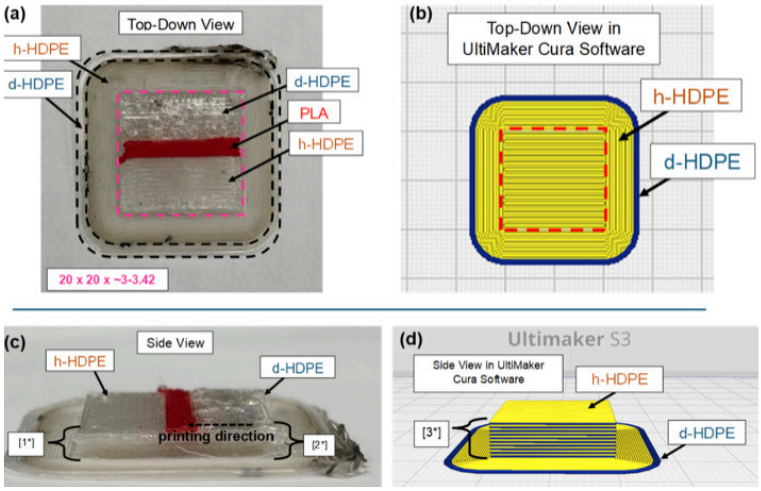

Figure 4. Top view (a-b) and side view (c-d) of fused filament fabrication (FFF) print alternating layers of h-HDPE and d-HDPE. Subfigures (a,c) depict photographs of the printed part. Subfigures (b,d) depict the corresponding multi-nozzle print instructions generated by the Cura open-source slicing software. The isotopic contrast introduced enables direct measurement of interlayer diffusion via secondary ion mass spectroscopy (SIMS) measurement. Red PLA was included as an indicating/purge material to visually identify when all d-HDPE had exited the print nozzle. **[1*]** ~3 mm thickness estimated 11 layers of alternating h/d-HDPE (top is h-HDPE). **[2*]** ~3.42 mm thickness estimated 12 layers of alternating h/d-HDPE (top is d-HDPE). **[3*]** attempted to print 21 layers of alternating h/d-HDPE. Measured height is 6.3 mm (top is h-HDPE).

Team Members

E. Cade Willis, Haley W. Jones*, Andrew P. Rhodes, Micah Rowland[a**], Mrinalini Kolaprath[b**]

[a]*Georgia Institute of Technology, Material Science & Engineering*

[b]*University of Tennessee-Knoxville, Chemistry*

**Postdoctoral Researcher*

***Student Researcher*

References

1. Chatham, C. A.; Bortner, M. J.; Johnson, B. N.; Long, T. E.; Williams, C. B. Predicting mechanical property plateau in laser polymer powder bed fusion additive manufacturing via the critical coalescence ratio *Materials & Design* **2021** *201*, 109474.
2. Bellehumeur, C. T.; Kontopoulou, M.; Vlachopoulos, J. The role of viscoelasticity in polymer sintering. *Rheologica acta* **1998** *37* (3) 270-278.
3. McIlroy, C.; Olmsted, P. D. Disentanglement effects on welding behaviour of polymer melts during the fused-filament-fabrication method for additive manufacturing. *Polymer* **2017** *123,* 376-391.
4. McIlroy, C.; Olmsted, P. D. Deformation of an amorphous polymer during the fused-filament-fabrication method for additive manufacturing. *Journal of Rheology* **2017** *61* (2), 379-397.

Figure 6. Mechanical test specimens printed from 50/50 PP/PC powder made by collaborators at UTK. SnowWhite2 PBF print parameters: Laser power - 4.9 W (39%); Scan speed- 3025 mm/s; Layer height - 0.1 mm; Hatch spacing - 0.3mm; T_{bed} -140 °C; Scan count - 2.

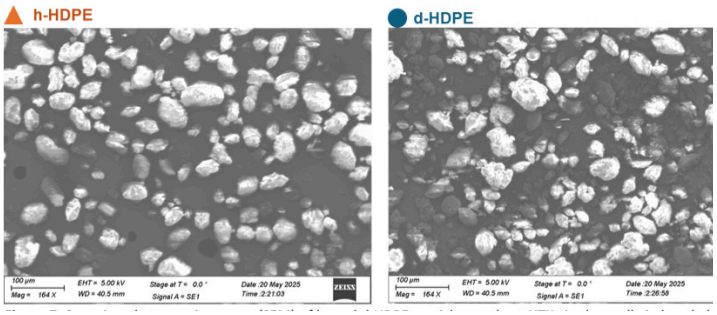

Figure 7. Scanning electron microscopy (SEM) of h- and d-HDPE particles made at UTK via thermally induced phase separation (TIPS). Particles were precipitated from a 9 % (w/w) solution of h- or d-HDPE dissolved in xylene quenched to 40 °C. Particles are appropriately sized for PBF (D50: h-HDPE = 39 µm; d-HDPE = 43 µm), but "potato shaped" instead of the desired spherical.

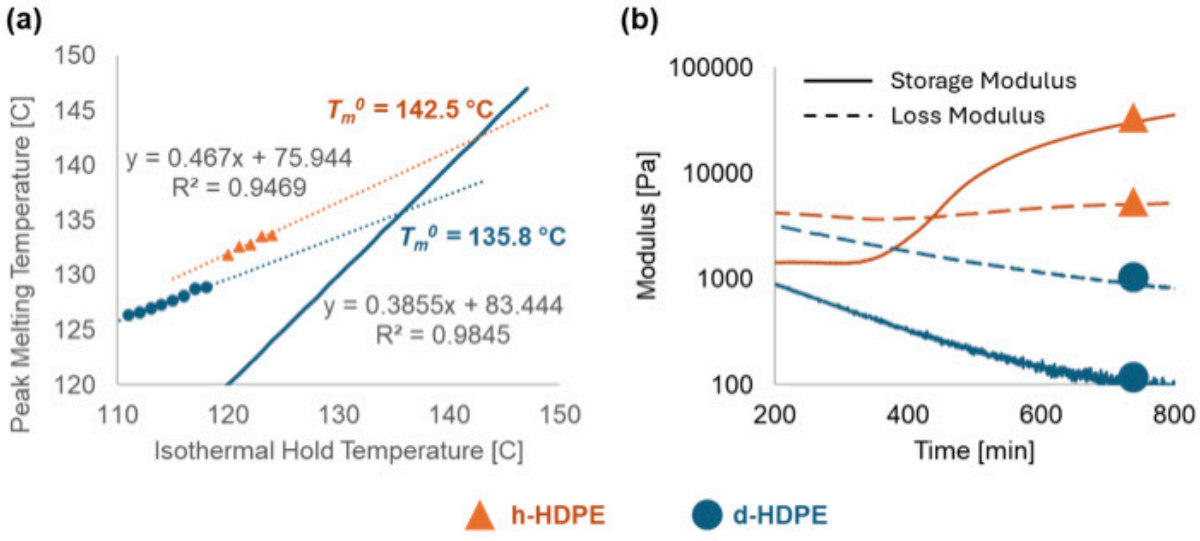

Figure 5. Differences in (a) crystallization and (b) rheological behavior resulting from isotope exchange. Orange triangles indicate h-HDPE while blue circles indicate d-HDPE. The rheology in subfigure (b) is particularly intriguing as it shows a change in oxygen stability; h-HDPE crosslinks around 450 min (i.e., crossover modulus) whereas d-HDPE remains similarly liquid over the entire 1200 min experiment.

Electrochemical Production of Calcium Hydroxide from Calcium Carbonate

Prabhu Ganesan

Calcium hydroxide is electrochemically synthesized to address SRNL core competency of Creating Manufacturing & Energy Solutions. This process is energy efficient compared to high temperature calcium carbonate decomposition to produce calcium oxide for the cement industry. Ultrasonic dehydration coupled with induction heating can further reduce the energy need for cement production.

Introduction

Electrochemical reactors are gaining traction for process intensification of existing manufacturing systems. However, economies of scale have not historically favored electrochemical processes due to material and electricity costs. With advances in technology, the transition to electrified chemical processing methods has become attractive to produce $Ca(OH)_2$ [1]. The proposed project targets the electrification of cement manufacturing. Portland cement is the most widely produced man-made material in the world. The production of cement has many steps, however as shown in **Figure 1**, most of the energy is consumed during the calcium carbonate decomposition (steps 5/6) [2-4]. If this step is carried out in some other way (e.g., electrochemical), a significant reduction of energy costs can be achieved when renewable electricity is used. The proposed project targets the electrification of cement manufacturing. Our electrochemical-based approach has the potential to produce the most widely accepted product used in cements, thereby minimizing adoption risk. However, for the electrification of $CaCO_3$ decomposition process to become an attractive alternative, we carried out the following tasks in year 1: (i) performed proof of concept of electrochemical reactions in two- and three-compartment cells, (ii) optimized applied current for the conversion of $CaCO_3$ into $Ca(OH)_2$, (iii) carried out cathode selection studies using PiperION and filter paper as separators and Pt anode in 1M $NaNO_3$ electrolyte, (iv) developed technoeconomic analysis based on the experimental results, and (v) designed a five-compartment cell and tested two- and three-compartment cells using anion (PiperION), cation (Nafion®), and filter paper (Fisher Q5) as separators.

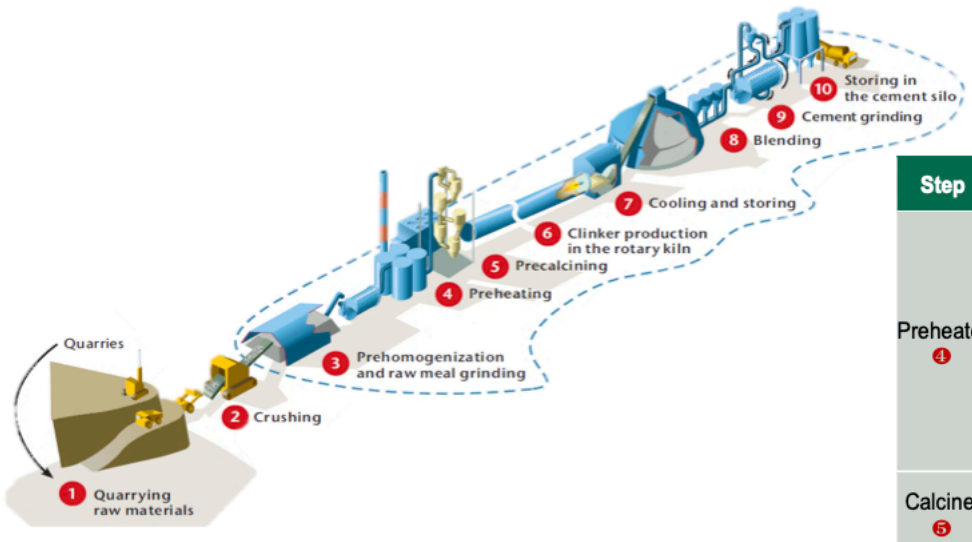

Step	Description	Energy ($kJ/kg_{clinker}$)
Preheater ❹	65-125 °C evaporation of free water	Varies on feedstock
	400-650 °C clay decomposition	42.2 kJ/kg
	500-650 °C dolomite decomposition	19.7 kJ/kg
	700-900 °C alumina and iron oxide reaction	207.2 kJ/kg
Calciner ❺	**650-900 °C calcium carbonate decomposition**	**722.5 kJ/kg**
Kiln ❻	**900-1,050 °C calcite decomposition**	**601.9 kJ/kg**
	1,300-1425 °C sintering	69.3 kJ/kg

Figure 1. Conventional cement manufacturing [3]

Approach

SRNL utilized its expertise in experimental electrochemistry and fuel cells to design and fabricate five-compartment electrolysis cell to facilitate product (calcium hydroxide) and byproduct gas (H_2, O_2, and CO_2) separation **Figure 2**. Membrane selection studies showed PiperION membrane and Fisher Q5 filter paper are good candidate materials without any structural degradation. The scanning electron microscopy (SEM) images shown in **Figure 3** indicated $Ca(OH)_2$ formation inside the Nafion® 117 and Fumasep bipolar membranes resulting in cell failure. Chronopotentiometry experiments. The inset in **Figure 4** showed that low currents (5 and 10 mA) are preferred for the $CaCO_3$ decomposition and at high currents (15 and 25 mA), recombination of H^+ and OH^- is a preferred reaction resulting in low $CaCO_3$ decomposition. X-ray diffraction results of the product $Ca(OH)_2$ showed trace amounts of $CaCO_3$, $NaClO_4$, and $Na_2CO_3.H_2O$ (**Figure 5**). Cathode screening studies were performed in H-cells using chronopotentiometry technique (10 mA) employing Pt mesh as the anode and 1M $NaNO_3$ as the electrolyte. Ni PTL, NiFeOx, NiFeReOx, and $CoFeO_4$ were used as cathodes in 50 mL two-compartment glass cell using PiperION membrane and Fisher Q5 filter paper as separators (**Figure 6** a&b). Table 1 compares the conversion of $CaCO_3$ in cells employing different cathode materials and Ni PTL and NiFeOx electrodes showed 99 and 85% conversion when PiperION membrane was used as the separator. Chronopotentiometry (at 10 mA) coupled with MicroGC experiment showed maximum CO_2 evolved from the anode after 3.5h from the start of the experiment and continued until 10.5h (**Figure 7**).

Accomplishments

- PiperION anion exchange membrane performed better compared to Nafion 117 cation exchange membrane and Fumasep bipolar membrane in two-compartment H-cells.
- X-ray diffraction of the product $Ca(OH)_2$ showed the presence of traces amounts of $CaCO_3$ and $Na_2CO_3.H_2O$.
- Chronopotentiometry studies at different applied current showed that low currents (5 and 10 mA) favor $Ca(OH)_2$ formation compared to high currents (>10 mA) which preferred recombination of H^+ and OH^- ions to produce water.
- Electrode selection studies in H-cells showed the possibility of replacing Pt with inexpensive Ni or NiFeOx cathodes. Ni and NiFeOx showed 98 and 85% conversions, respectively.
- Chronopotentiometry coupled with microGC experiment showed maximum $CaCO_3$ decomposition occurring from 3.5 to 10.5 h from the start of the experiment due to favorable pH conditions at the anode. More pH monitoring experiments are planned in year 2 to verify this observation.
- Converted literature Techno-Economic Analysis (TEA) template [5] into flexible and accurate spreadsheet for the current project TEA.
- Resultant TEA includes CAPEX (capital expenditure) and OPEX (operating expenditure) costs as well as customizable fuel energy profiles for both the conventional heating and electrochemical processes. The TEA task progresses well in advance of Milestone 2.3's proposed deadline (May 2026).

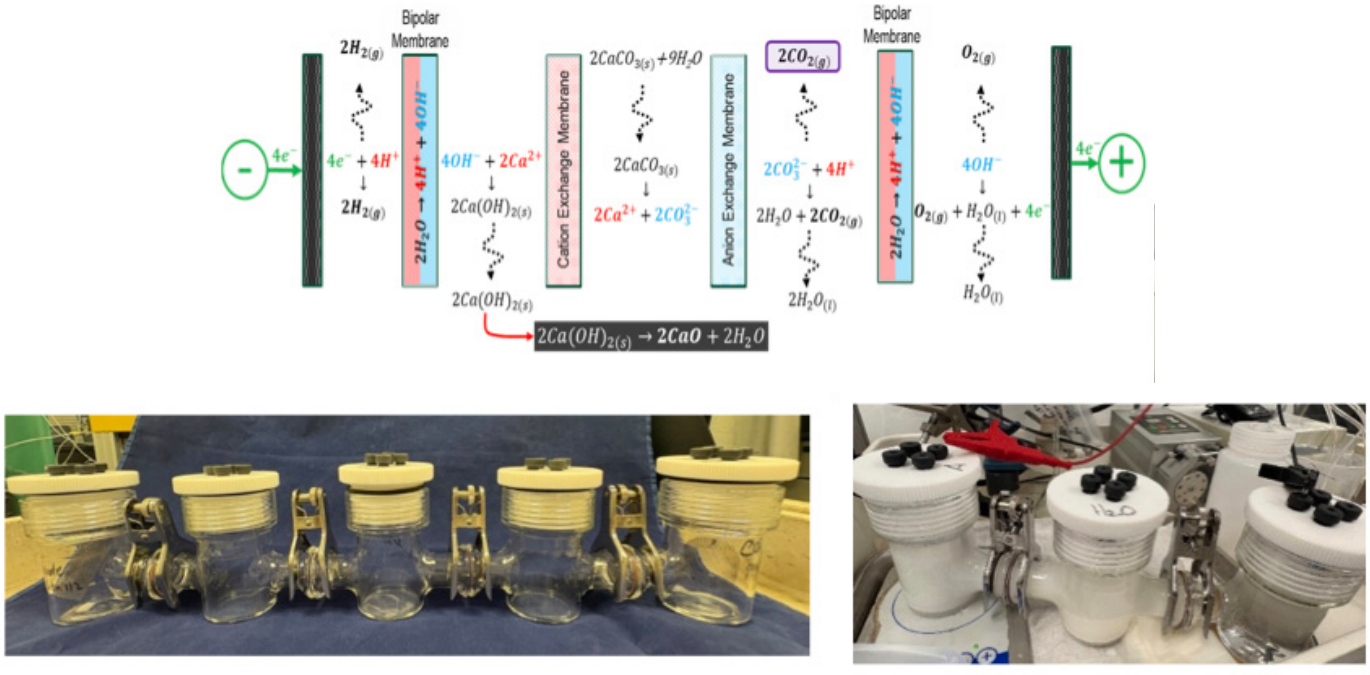

Figure 2. Schematic and photograph of five-compartment electrolysis cell to facilitate product and byproduct gas separation (left). Photograph of three-compartment electrolysis cell that is currently under testing (right).

Team Members

Zachary Tener[a], Steven Garner[a], Bryce Brechin[a], Matthew Craps[a], Hector Colon-Mercado[a], Matthew Gordon[*], William Mustain[b]

[a]*Savannah River National Laboratory*
[b]*University of South Carolina*
[*]*Postdoctoral Researcher*

References

1. Ellis L.D, Badel A.F, Chiang M.L, Park R.J, Chiang Y, Toward electrochemical synthesis of cement—An electrolyzer-based process for decarbonating, $CaCO_3$ while producing useful gas streams *Proc. Natl. Acad. Sci*., **117** (23) 12584-12591.
2. Kohobhange S.P. Karunadasa, C.H. Manoratne, H.M.T.G.A. Pitawala, and R.M.G. Rajapakse, Thermal decomposition of calcium carbonate (calcite polymorph) as examined by in-situ high-temperature X-ray powder diffraction, *J. Phys.Chem. Solids*, **134**, 21-28.
3. "Technology Roadmap - Low-Carbon Transition in the Cement Industry", *IAEA report* (2019)
4. "Concentrating Solar-Thermal Power Fiscal Year 2022 Research, *Development, and Demonstration Program*", DE-FOA-0002630.
5. Zhang, Z, Mowbray B. A. W, Parkyn C. T. E, Waizenegger C, Williams A. S. R, Lees E. W, Ren S, Kim Y, Jansonius R. P, Berlinguette C. P, Cement clinker precursor production in an electrolyzer, *Energy & Environ. Sci.* **2022**, *15* (12), 5129-5136.27, no. 5, pp. 657-677, 2014.

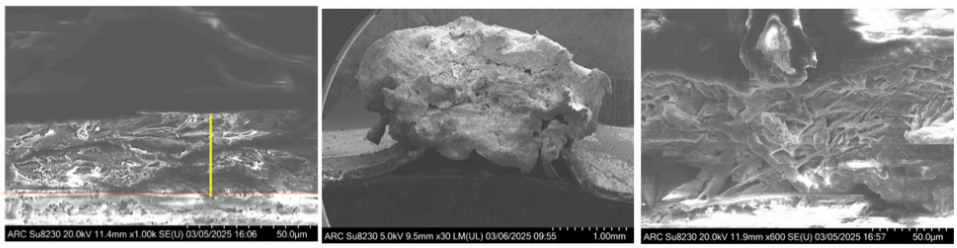

Figure 3. Cross-sectional SEM images of PiperION anion exchange membrane (left), Nafion® 117 cation exchange membrane (center), and Fumasep bipolar membrane (right). Ca(OH)2 formation within the membrane is noticed in Nafion® 117 and Fumasep membranes while PiperION membrane showed Ca(OH)2 layer on the membrane.

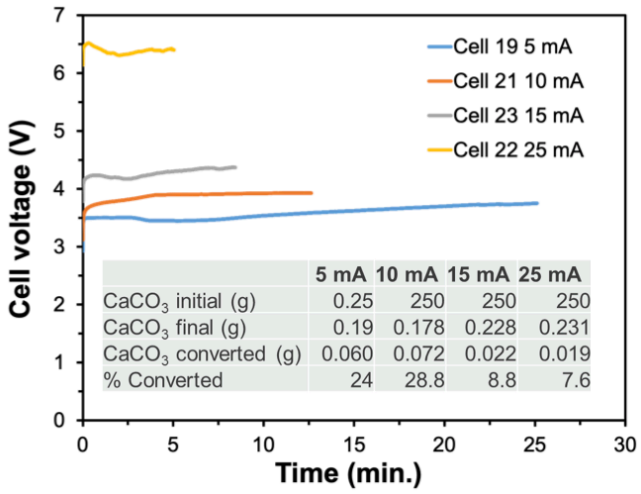

	5 mA	10 mA	15 mA	25 mA
$CaCO_3$ initial (g)	0.25	250	250	250
$CaCO_3$ final (g)	0.19	0.178	0.228	0.231
$CaCO_3$ converted (g)	0.060	0.072	0.022	0.019
% Converted	24	28.8	8.8	7.6

Figure 4. Chronopotentiometry curves at different applied current during electrochemical CaCO3 decomposition in H-cells. Anode: Pt mesh, cathode: Pt wire, electrolyte: 1M NaNO3 (room temperature). CaCO3 % conversion is shown in the inset.

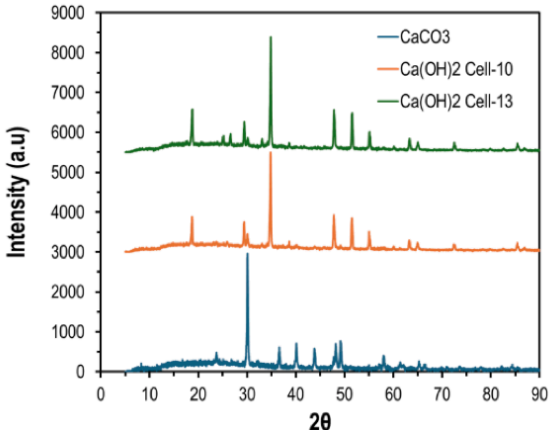

Figure 5. X-ray diffraction of Ca(OH)2 obtained from the electrochemical decomposition of CaCO3 in H-cells. Anode: Pt mesh, cathode: Pt wire, electrolyte 1M NaClO4 (room temperature).

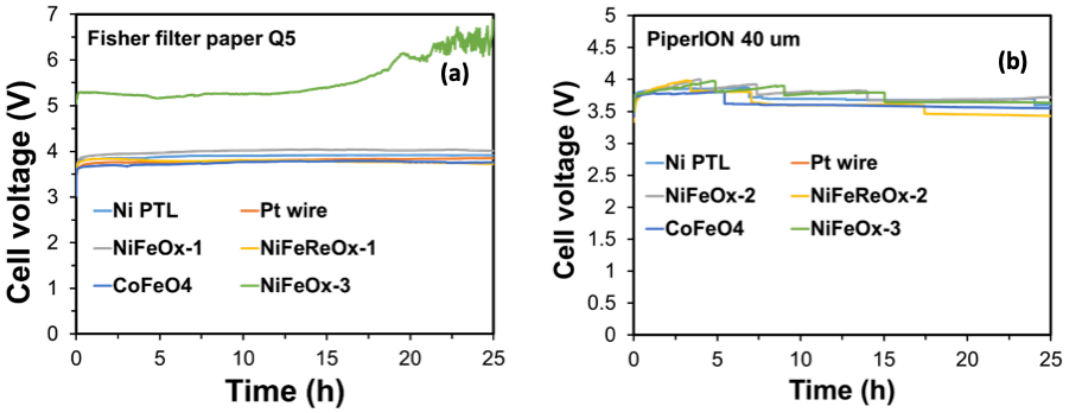

Figure 6. Chronopotentiometry curves of electrochemical CaCO3 decomposition using (a) Fisher Q5 filter paper and (b) PiperION 40µm membrane as separators. Anode: Pt mesh, electrolyte 1M NaNO3 (room temperature).

Fisher brand filter paper (Q5)						
	Ni PTL	Pt coil	NiFeOx-2	NiFeReOx-2	$CoFeO_4$	NiFeOx-3
$CaCO_3$ initial (g)	0.25	0.25	0.25	0.25	0.25	0.25
$CaCO_3$ final (g)	0.167	0.129	0.138	0.107	0.065	0.054
$CaCO_3$ converted (g)	0.083	0.121	0.112	0.143	0.185	0.196
% converted	33.2	48.4	44.8	57.2	74	78.4
PiperION 40µm anion exchange membrane						
	Ni PTL	Pt coil	NiFeOx-2	NiFeReOx-2	$CoFeO_4$	NiFeOx-3
$CaCO_3$ initial (g)	0.25	0.25	0.25	0.25	0.25	0.25
$CaCO_3$ final (g)	0.004	0.056	0.036	0.09	0.055	0.037
$CaCO_3$ converted (g)	0.246	0.194	0.214	0.16	0.195	0.213
% converted	98.4	77.6	85.6	64	78	85.2

Table 1. Comparison of different cathode materials in the CaCO3 electrolysis cell utilizing fisher Q5 filter paper and PiperION 40µm anion exchange membrane as separators in two-compartment H-cells.

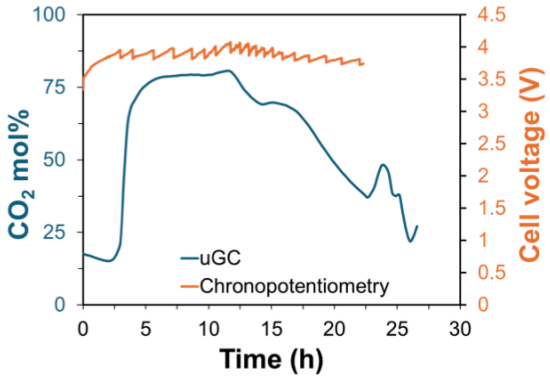

Figure 7. Chronopotentiometry and microGC results for the electrochemical CaCO3 decomposition. Anode: Pt mesh, cathode: Pt wire, separator: PiperION 40µm membrane, electrolyte: 1M NaNO3 (room temperature), and applied current: 10 mA for 25h (250 mAh total charge).

Development of Machine Learning and Additive Manufacturing Techniques for Rapid Alloy Development for Plutonium Containment and Tooling

Colleen Hilla

This work developed a platform to rapidly screen refractory metal alloys for various applications. Traditional alloy development is costly and time consuming. This framework has decreased the time and expense in analyzing alloys and allowed for the testing of exponentially more materials. Greater improvement in performance has been seen.

Introduction

Refractory metals and their alloys boast a variety of interesting properties such as a high melting point and good mechanical behavior. This makes them good candidate materials for harsh environment applications. However, many of these materials are difficult to manufacture and exhibit poor ductility. These are the primary driving forces for creating new refractory metal alloys aimed at improving these properties. The experimental data available for refractory alloy development is extremely limited. This is due to the high material cost and low manufacturability of many of these materials. The traditional alloy development process relies on an Edisonian method where compositions are produced and tested for properties. This is both time consuming and expensive, as generally large quantities of material are needed for traditional testing. This drives the need for the development of a low-cost high-throughput material development method. Due to the limited manufacturability of refractory materials, coupled with the benefits of additive manufacturing, such as design flexibility and process agility, there is also a strong interest in additive manufacturing of the designed alloys. Therefore, printability is one of the key design requirements. Additional design requirements driven by the application of plutonium containment and tooling are high melting temperature, plutonium compatibility, and corrosion resistance. This work will identify novel alloys that will improve the lifetime of tooling for plutonium processing, therefore reducing total radiological waste. Additionally, a framework that can be used for expanded alloying development work has also been produced.

Approach

This work looked at accelerating the entire material development process. This includes selection of test alloys, alloy production, and material testing. A neural network-based ML (machine learning) model was developed for rapid alloying screening. This tool allows for thousands of material compositions to be screened to determine which alloys are likely to meet the threshold performance requirements. Using this method 50 materials were selected for testing. Due to limited experimental data, computational simulation was used to produce training data. Calphad (calculated phase diagram) modeling was used to determine material properties and material compatibility. A surrogate model developed from DFT (density functional theory) was used to predict ductility and mechanical performance. This data was validated using available experimental data and then used to train the ML model. Powder-fed laser DED (directed energy deposition) is an additive manufacturing technique where powder is directly deposited into the melt pool to build the part layer by layer. DED can utilize multiple powder hoppers where material composition can be varied throughout the part and build. This has been used to produce 10's of compositions in a single build. These coupons are comparatively very small, which allows for the reduction in both production time and production cost. Samples are physically connected through the build plate, which allows the samples to be prepared for testing simultaneously. An example of this is seen in **figure 1**. This process increases the efficiency of material testing.

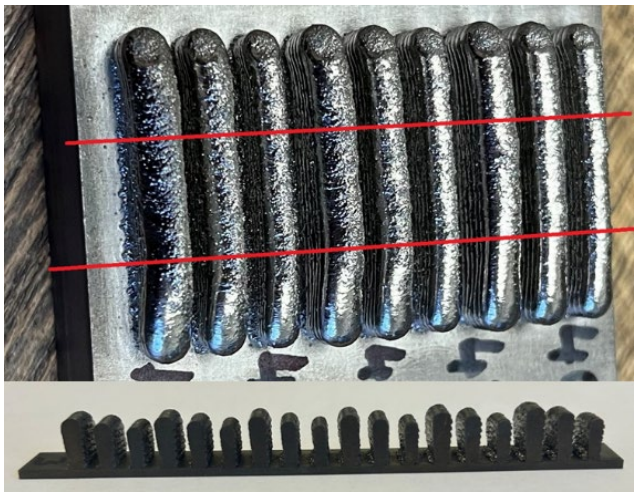

Figure 1. Sample configuration that allows for high-throughput metallographic preparation and testing.

Accomplishments and results

- Neural network was built and used to select 50 alloys. These alloys had a designed ductility above the ductility of tungsten, a minimum melting temperature of 2000°C, and predicted hardness greater than tantalum.
- 50 alloys were printed and tested. Component microstructure was analyzed, hardness was tested, and relative ductility was determined experimentally.
- Oxidation study was completed in collaboration with the Ohio State University. Samples were produced using 36 different parameter sets using three different print setups, with different methods of oxygen control. Samples were tested for hardness, defect content, and oxide formation to evaluate the effect of oxygen on the builds.

Peer-reviewed Publications

- Hilla, C.; Dinda, G. P.; Ayers, T.; Mcclane, D. Effect of directed energy deposition process parameter on build quality of tantalum. *Progress in Additive Manufacturing** (accepted, awaiting publication)
- Hilla, C.; Deschaine, L. Machine Learning Assisted Modeling for Tantalum Alloy Development. *Journal of Materials Science** (submitted)

Team Members

Guru Dinda, Cameron Gygi[a]

[a]*The Ohio State University*

Critical Infrastructure and Grid Resilience

Synthesis and characterization of critical material free permanent magnets (CM-FPM)

Binod Rai

The investigation of an actinide-based catalyst for chlorine production was accomplished by simulating different reaction mechanisms using density functional theory with the SRNL's high-performance computer. Based on this study, a deeper understanding of how actinide-based catalysts can be engineered for other key industrial processes was elucidated.

Introduction

The continual and increasing need for strong magnets in the United States to enable new technologies like quantum computing and fusion energy is currently met by the world's strongest permanent magnet family, derived from the $Nd_2Fe_{14}B$ (Neodynium magnet) intermetallic compound. Although these magnets contain only a small amount of the rare earth element Neodymium, they are predominantly made of iron. Neodymium magnets are renowned for their exceptional field strength, which has led to their widespread use in industries such as automotive, biomedical, defense, aerospace, and consumer electronics. However, the heavy reliance on Neodymium has resulted in global shortages and significant price increases. This dependence on a critical material, predominantly mined in China, poses a serious risk to the US economy, competitiveness, and technological advancement. China controls 61% of global rare earth element production, including Neodymium (see **Figure 1**).

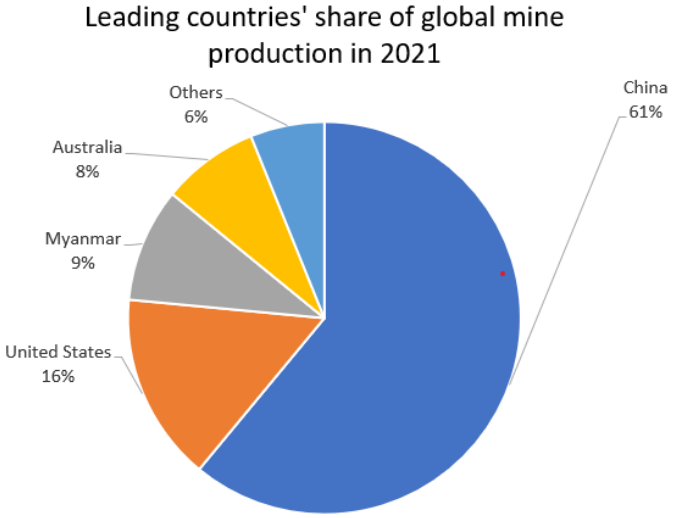

Figure 1. China dominates the rare earth mining industry, controlling nearly 61% of global mine production.

Although a rare earth itself, Cerium (Ce) is seen as an acceptable substitute to Nd as it is more commonly found in the mined bastnasite and monazite ore that hosts the other rare earth elements. Our work seeks to develop unique $Ce_2Fe_{14}B$ magnets with the increased magnetic anisotropy, a critical property for multiple technological purposes.

Approach

The demand for the rare earth element Nd and necessary dopants like Dysprosium and Terbium currently outstrip the United States' domestic supply chain's ability to produce en masse. To this end, our approach is to develop the $Ce_2Fe_{14}B$ compound via physical processing and chemical doping with focuses on improving Curie temperature (T_c) and magnetic anisotropy. The high abundant rare-earth yttrium and lutetium, and bismuth were substituted for the low cost and abundant rare earth Ce in $Ce_2Fe_{14}B$ in an attempt to improve the magnetic and thermodynamic properties similar to doping in $Nd_2Fe_{14}B$ based permanent magnets.

We utilized powder X-ray diffractometry for phase identification, SEM-EDS for microstructure analysis, DSC-TGA for Curie temperature and Quantum Design Dynacool PPMS to characterize magnetic property of synthesized samples.

Accomplishments

- We synthesized Bi doped $Ce_2Fe_{14}B$ via an arc-melting process, and incremental substitutions of Bi were included into the parent structures with nominal stoichiometries of $Ce_{2(1-x)}Bi_xFe_{14}B$, where x = 0.05, 0.1, and 0.15.

- DSC-TGA data on Bi doped $Ce_2Fe_{14}B$ shows an enhancement of Tc from 150 °C to 155 °C in between 5 to 15% Bi doping. A representative figure is presented for 10% Bi doped $Ce_2Fe_{14}B$ (see **Figure 2**).
- SEM Mapping of Bi doped $Ce_2Fe_{14}B$ shows a presence of Bi. A representative figure is presented for 5% Bi doped $Ce_2Fe_{14}B$ (see **Figure 3).**
- Manuscript in preparation on Bi doped $Ce_{2(1-x)}Bi_xFe_{14}B$.
- Manuscript currently in review at the Journal of Allows and Compounds - on Lutetium and Yttrium – ”Enhanced thermal stability and magnetic properties in Y substituted $Ce_2Fe_{14}B$”
- Alex Bretaña presented at the Up and Atom Event (presented by the CNTA)
- Alex Bretaña presented a poster at the 69th Annual American Vacuum Society Meeting
- Alex Bretaña attended and presented a poster at the 2024 6th US School on Total Scattering Analysis at Oak Ridge National Laboratory
- Alex Bretaña presented a poster at the 2024 SRNL Day at Georgia Tech
- Alex Bretaña presented a presentation at the L3330 Group Meeting – September 4th, 2024

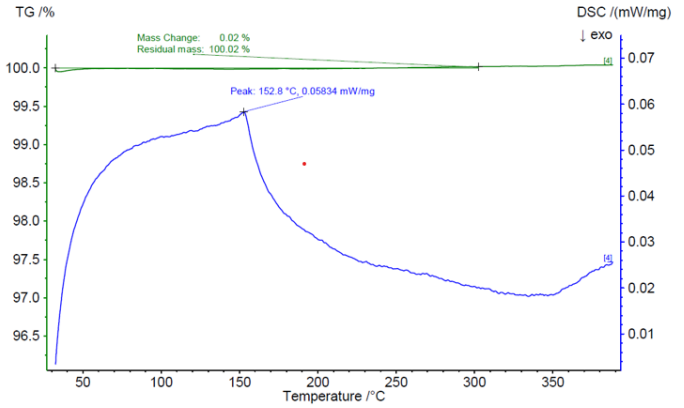

Figure 2. Curie temperatures as determined by TGA for annealed 10% Bi doped $Ce_2Fe_{14}B$.

Team Members

Alex Bretaña*, Catherine Housley, Henry Ajo, Tucker Koenig, Damien Dobson, Zach Tenner, Greg Morrison[a*], Hans-Conrad zur Loye[a]

[a] University of South Carolina – Columbia
*Laboratory Director’s Postdoctoral Fellow

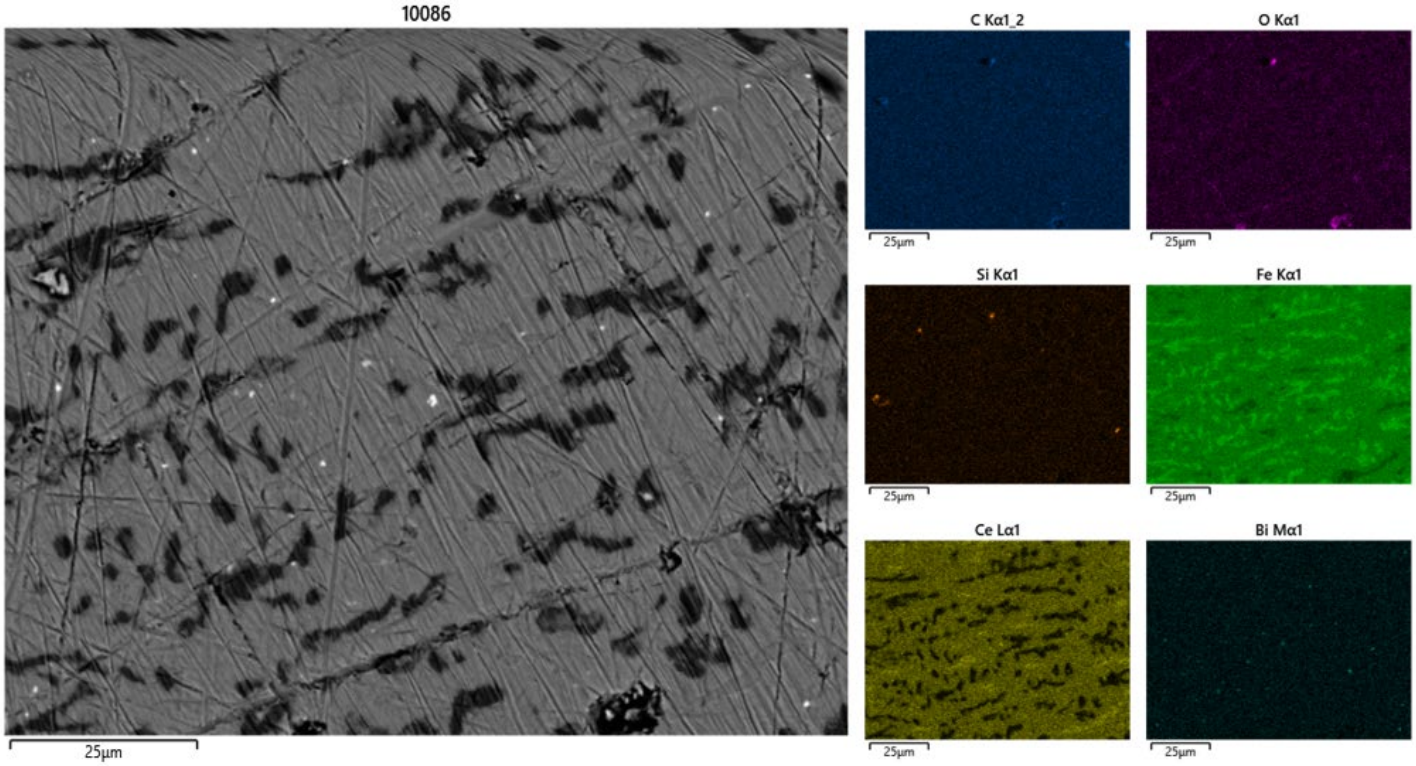

Figure 3. SEM-Mapping of 5% Bi doped $Ce_2Fe_{14}B$

Characterization of Material Properties for Blended Hydrogen-Natural Gas Pipelines

Xiankui Zhu

Repurposing natural gas pipelines to transport hydrogen blended natural gas is an effective and economic option to accelerate the hydrogen economy. Hydrogen can embrittle pipeline steels, and thus characterization of degraded material properties and recalibration of existing assessment models are critical to ensuring the structural integrity, safety and reliability of aging pipelines that are repurposed to transport gaseous hydrogen.

Introduction

Hydrogen has been extensively used in various industries. Recently, hydrogen has been getting great attention worldwide because it is likely utilized for future energy generation. While hydrogen storage technology has matured after several decades of study, research into large-scale, safe, and economical transportation of gaseous hydrogen remains unsophisticated. It is commonly accepted that repurposing the existing natural gas infrastructure to transport hydrogen is a feasible and efficient solution. This approach may minimize costly pipeline infrastructure modifications or new construction. However, hydrogen embrittlement (HE), which occurs due to absorption of atomic hydrogen into the material, weakens the atomic bonds of the metal and degrades its properties, posing a substantial threat to pipeline integrity. Therefore, understanding and quantifying effects of HE on pipeline steels is essential to ensure the safety, reliability, and integrity of aging pipelines used for hydrogen gas transport.

A literature review revealed that extensive experimental investigations have been performed to study the microscopic mechanisms of the material degradation, degraded mechanical properties, and material compatibility due to hydrogen effects. HE can significantly reduce material ductility, fracture toughness, and fatigue crack growth resistance for pipeline steels but has a relatively small effect on tensile properties of the material. As such, all existing models for assessing natural gas pipeline integrity need to be recalibrated to ensure their accuracy when used for hydrogen pipelines. One approach is to use advanced finite element analysis (FEA) to simulate full-scale burst tests and predict numerical burst strength that accounts for the effect of HE. The objective of this project is to develop numerical and theoretical burst models to ensure the integrity of hydrogen pipelines with and without corrosion defects. Achieving this will position SRNL as a technical leader in the hydrogen pipeline industry.

Approach

To assess the effect of hydrogen on burst strength, a combined technical approach of theoretical and numerical analyses was adopted to achieve the project objectives. Experimental data on the material properties of hydrogen-embrittled pipeline steels were collected for different pipeline grades. Based on the literature review and collected test data, the hydrogen concentration on the inside wall of a steel pipeline is quantified as a function of hydrogen partial pressure (**Figure 1**(a)), and the degraded material properties are characterized as a function of hydrogen blending ratio (**Figure 1** (b)). A new average equivalent stress (AES) theory of plasticity and its associated flow solution of burst pressure were developed to predict more accurate burst strengths of thin and thick-walled line pipes in ductility reduced steels due to hydrogen exposure. This new theoretical solution was validated by extensive burst test data, including a large full-scale burst dataset for a wide range of pipeline steels for natural gas service, as well as a small burst dataset of different pipes for hydrogen service (**Figure 2**). To supplement the test database, numerical results of burst pressure were determined using the commercial software ABAQUS to perform 2D and 3D elastic-plastic FEA simulations (**Figure 3**) for hydrogen pipelines with and without corrosion defects. These FEA simulations have been proven to be a quality tool and an accurate simulation of experimental burst tests (Figures 4 and 5). In summary, this study provides a sound theoretical foundation to develop the novel AES theory and the necessary data to develop new numerical models to accurately predict burst strength and ensure the reliability of hydrogen blended natural gas pipelines.

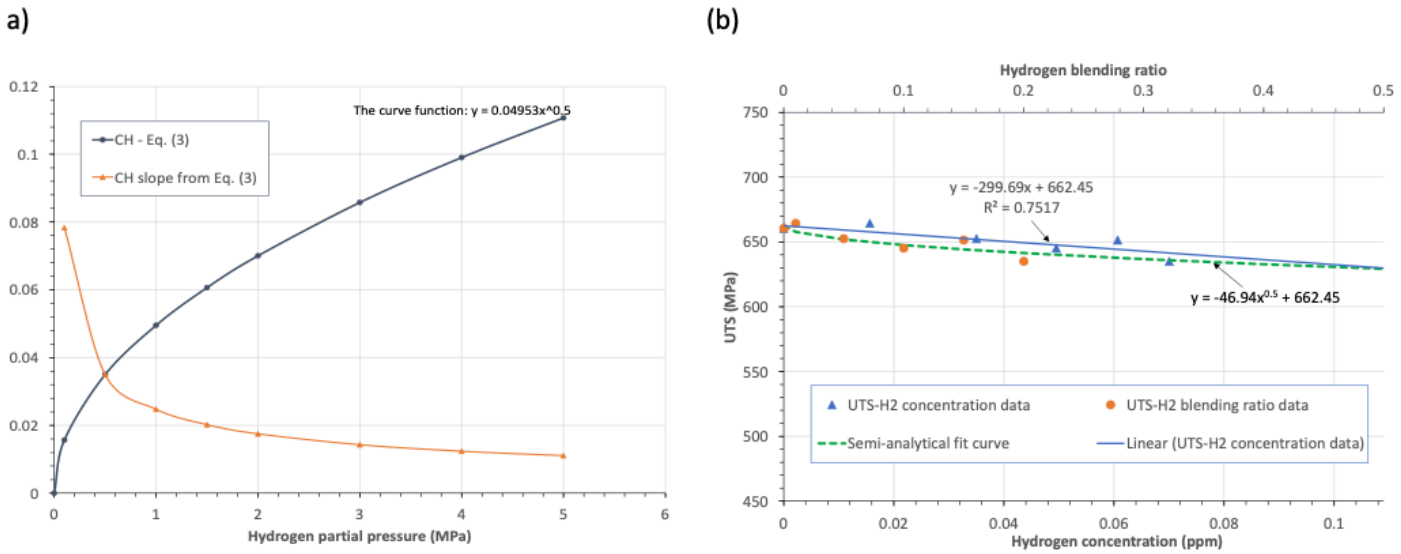

Figure 1. (a) Hydrogen concentration on the inside wall of a pipeline steel, and (b) the ultimate tensile strength (UTS) as a function of hydrogen concentration or hydrogen blending ratio for an X80 pipeline steel.

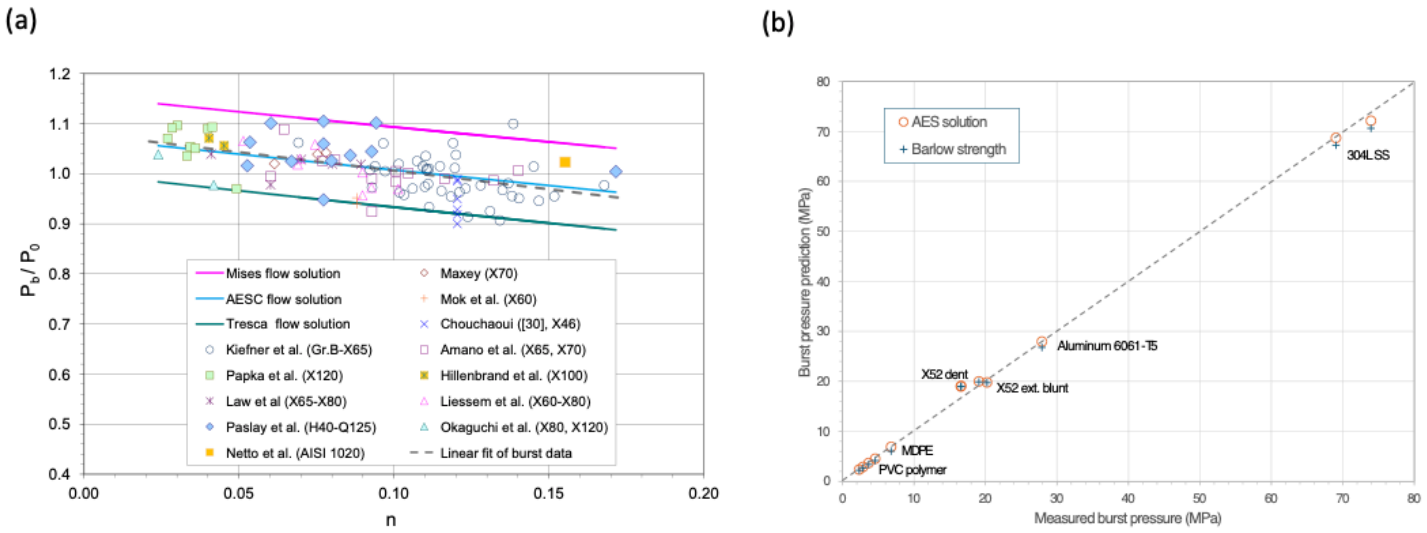

Figure 2. Validations of AES flow solutions of burst pressure with burst test data from full-scale burst tests for (a) natural gas service and (b) hydrogen service.

Accomplishments and results

From the efforts of Year-1 work, major accomplishments and results are summarized as follows.

- Performed a comprehensive literature review on hydrogen embrittlement effect on mechanical properties of pipeline steels and on material compatibility of pipeline steels used for transporting hydrogen. The review results were presented and published in the Proceedings of 2025 ASME Pressure Vessels and Pipeline Conference.
- Collected a large experimental database on the influence of hydrogen embrittlement on the material properties of pipeline steel to include the effects on tensile strengths, ductility, fracture toughness and fatigue crack growth rates for various pipeline steels when electrochemically charged or tested in hydrogen gas.
- Quantified the hydrogen concentration as a function of the hydrogen partial pressure and characterized the degraded material tensile strength as a function of the hydrogen concentration or hydrogen blending ratio for an X80 pipeline steel, as shown in **Figure 1** and will be published in Reliability Engineering and System Safety.

- Developed a new advanced AES plasticity theory and its associated flow solutions to determine the burst strength for hydrogen pipelines, as shown in **Figure 2** and published in the International Journal of Pressure Vessels and Piping. The AES flow solutions provide accurate predictions of burst pressure for several materials intended for hydrogen service with an average absolute relative error of 1.41%.
- Developed a Python script-based framework to generate, run and postprocess FEA burst pressure simulations for pipes with and without corrosion defects to enable efficient generation of FEA results for the parametric studies, as shown in **Figure 3**.
- Obtained FEA burst pressure results for defect-free pipeline in hydrogen service and found that there is only a minimal reduction in the burst strength as the partial pressure of hydrogen increases, as shown in **Figure 4**.
- Developed two novel corrosion models for burst strength predictions of pipelines with corrosion defects in hydrogen service based on the industry standard PCORRC and LPC models, as shown in **Figure 5** and will be published in Reliability Engineering and System Safety.
- Published two conference papers and 4 journal papers with one other journal paper in revision.

Peer-reviewed Publications

- Zhu, X.-K.; Herrington, J. Average equivalent stress theory and its application to determine burst strength for hydrogen pipelines. *International Journal of Pressure Vessels and Piping* **2025**, *218*, 105617. DOI: 10.1016/j.ijpvp.2025.105617. *
- Zhu, X.-K.; Herrington, J. Comments on "Failure analysis of corroded hydrogen-blended natural gas pipelines based on finite element analysis and genetic algorithm-back propagation neural network" [262 (2025) 111174]. *Reliability Engineering & System Safety* **2025**, JRESS-D-25-02769, Accepted.*
- Zhu, X.-K., Burst pressure models and validations for thick-walled pipelines containing corrosion defects. *Journal of Pipeline Science and Engineering*, Available online 23 May 2025, 100301.*
- Herrington, J.; Zhu, X.-K.; Wiersma, B. Recent Advances in Pipeline Integrity for Transporting Blended Hydrogen-Natural Gas. *Proceedings of the ASME 2025 Pressure Vessels and Piping Conference,* Montreal, Quebec, Canada, July 20-25, 2025; PVP-2025-154678.*
- Zhu, X.-K. Evaluation of maximum allowable working pressure and Svensson burst pressure recommended in API 57901 2021 Edition. *Proceedings of the Pressure Vessels and Piping Conference,* Montreal, Canada, July 20-25, 2025; PVP-2025-153989.*
- Zhu, X.-K. Experimental Validation of Exact Burst Pressure Solutions for Thick-Walled Cylindrical Pressure Vessels. *Applied Mechanics* **2025,** *6,* 20. DOI: 10.3390/applmech6010020*
- Zhu, X.-K. Determination of Constraint-Independent Crack Tip Opening Angle for Stable Crack Growth in High-Strength Ductile Steels. *Materials* **2025**, *18,* 1051. DOI: 10.3390/ma18051051*

Team Members

This Laboratory Director's Postdoc LDRD project has two research members and two supporting members.

Xian-Kui Zhu, Joshua Herrington*, Morgan Whiteside, Bruce Wiersma

**Laboratory Director's Postdoctoral Researcher*

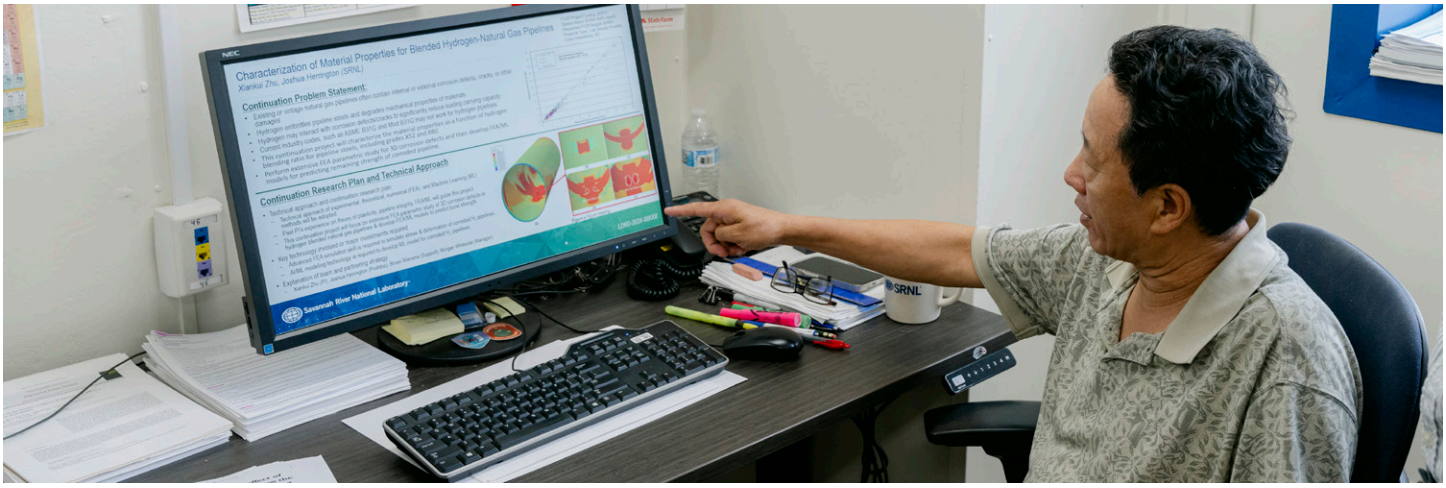

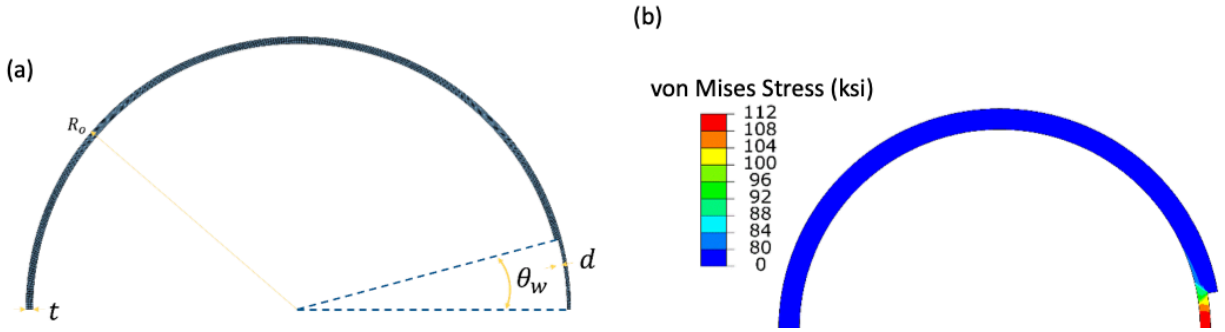

Figure 3. (a) Example parametrization of a 2D FEA model of a pipeline with a corrosion defect. (b) Distribution of the von Mises stress at the burst failure.

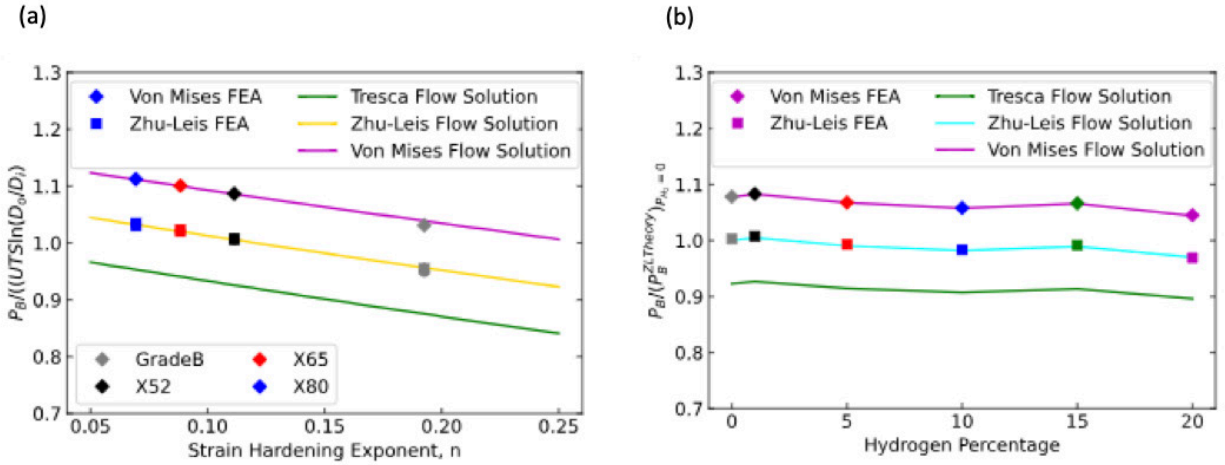

Figure 4. Two-dimensional FEA defect free pipe simulations. (a) Normalized burst pressures for different pipeline grades and geometries. (b) Effect of hydrogen on burst pressure of defect free pipes.

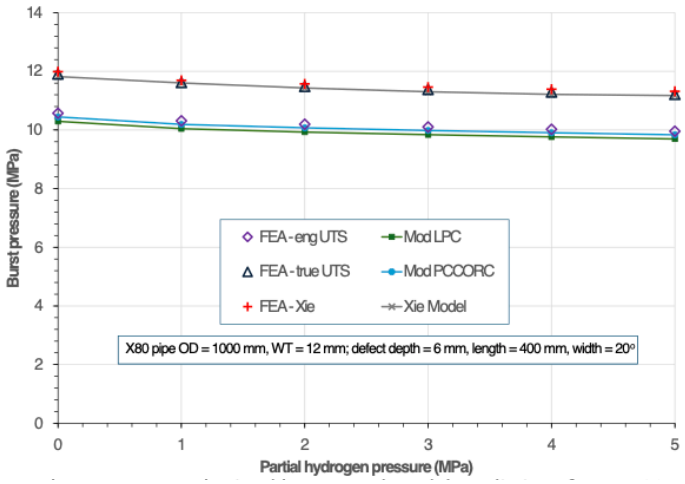

Figure 5. Hydrogen effect on burst pressure obtained by FEA and model predictions for an X80 corroded pipeline with a blunt defect of d=6 mm, L=400 mm, and w= .

Decision Science and Artificial Intelligence

Improving Radon Risk Mapping Using Advanced Data Analytics and AI/ML

Thomas Danielson

Chronic exposure to radon is the leading cause of lung cancer in non-smokers. Radon risk maps are often provided at county-wide scales, lacking resolution for higher risk areas in otherwise low risk counties. This effort applies data analytics to increase the resolution of radon risk maps to the neighborhood/property scale.

Introduction

Chronic exposure to radon is the leading cause of lung cancer among non-smokers and more than one third of the United States is estimated to have high geologic radon potential[1]. In Aiken County, SC, radon potential is generally low. However, approximately 10% of homes have measured concentrations above the recommended action level. Elevated radon concentrations found in Aiken County are attributed to sparse and naturally occurring uranium-containing mineral deposits (e.g., gorceixite)[2]. However, limited data is available to describe the precise locations of these deposits, presenting a unique opportunity to overcome challenges associated with using limited data to make predictions for a sparse target output.

Data science approaches have been increasingly applied to radon risk modeling, especially in European countries[3]. However, most studies have explored applications across large regions or have access to large sampling datasets. Here, ArcGIS has been used to merge datasets containing the geologic formations and topography in Aiken County, limited at-home radon sampling, and flyover spectral gamma readings from the NURE[4] program (**Figure 1**). Notably, all data is coarse resolution when considering localized subsurface mineral formations, hence limited soil gas sampling around the county has been performed to supplement these datasets. By applying machine learning, the correlated features within the data are used to guide sampling efforts, and the data/models are updated as new information is gained until sufficient resolution, and predictive capability is achieved. In this way, we can better inform policymakers of where to sample and the required data for adequate resolution while minimizing cost.

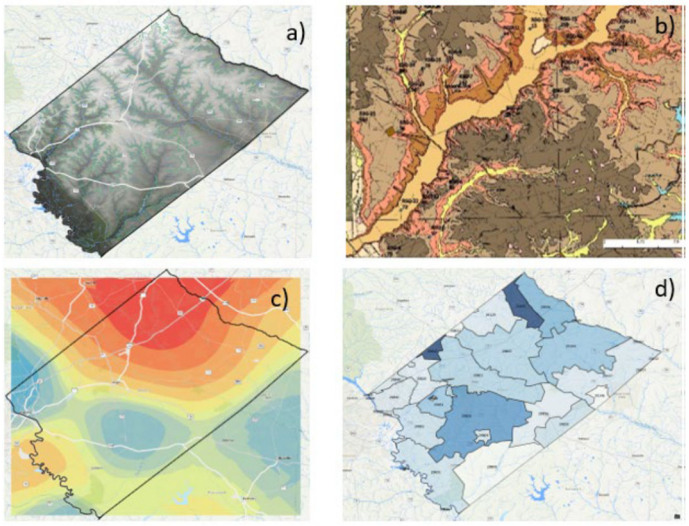

Figure 1. ArcGIS mapping of a) digital elevation, b) zoomed in geologic formations, c) spectral gamma flyover (NURE), and d) mean at-home sampling value across zip code regions in Aiken County.

Approach

The team applied data science approaches to the data in **Figure 1** with measurements of radon in soil gas around Aiken County. Correlations between the NURE spectral gamma readings (quan_ppm in the NURE dataset) and the local geology were explored. Subsequently, a random forest was trained to demonstrate that the NURE map can be reproduced using the geologic formations as predictors (**Figure 2** and **Figure 3**) and provide valuable information regarding the feature importances. Additionally, limited soil gas measurements of radon were collected in the high, medium, and low uranium resource potential regions of the county to evaluate the ability to use the NURE map as a proxy for radon potential that guides sampling.

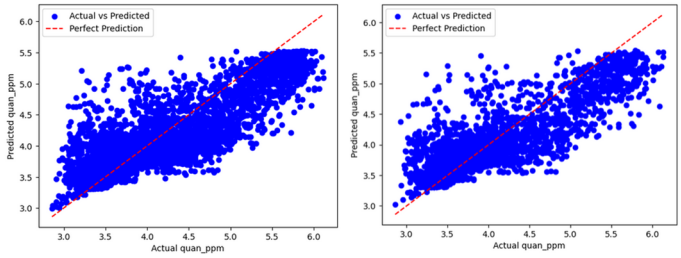

Figure 2. Performance of random forest trained to predict the uranium resource potential (NURE) given the geologic formations for the northern-most region of Aiken County (left: Train R^2 = 0.78, right: Test R^2 = 0.75).

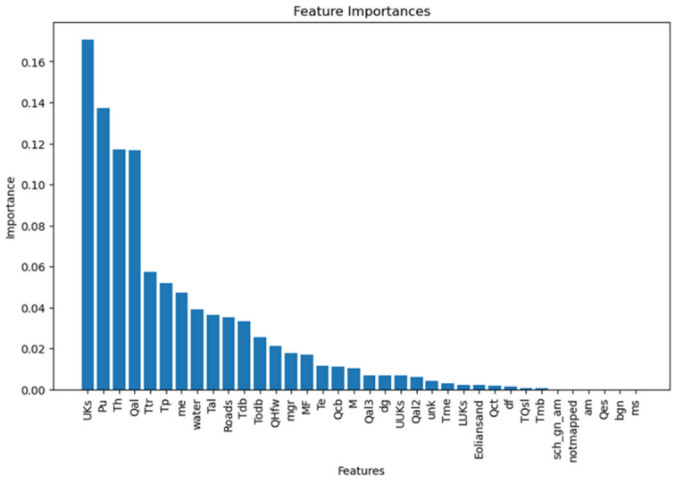

Figure 3. Feature importance of geologic formations from the trained random forest predictor.

FY24 restricted sampling to areas within the SRS site boundary that are in Aiken County (**Figure 4**). However, predominantly "low" radon soil gas concentrations were identified. In FY25, additional sampling was performed within the SRS boundary and across Aiken County using public lands including: the Aiken Gopher Tortoise Heritage Preserve, the Janet Harrison High Top Heritage Preserve, the Crackerneck Wildlife Management Area, and the Henderson Heritage Preserve (**Figure 6** and **Figure 5**). Importantly, these locations allowed broader exploration of the correlation between the measured radon concentration in soil gas and the uranium resource potential as mapped during the NURE program by providing data coverage in the northern, southern, eastern, and western regions of Aiken County. Finally, the team explored the correlation between the geologic formations with the collected samples to isolate which geologic features predominantly correlate with elevated radon concentrations (**Figure 7**).

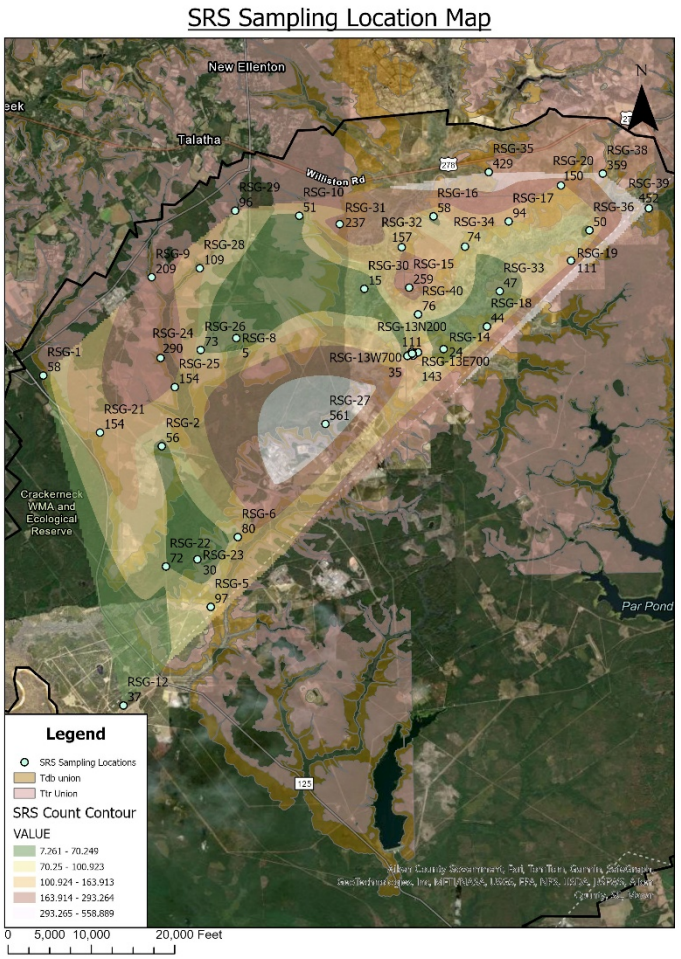

Figure 4. FY24 and FY25 Aiken County sampling locations within the SRS boundary showing the contours of radon concentrations in soil gas, as well as selected geologic formations that are present.

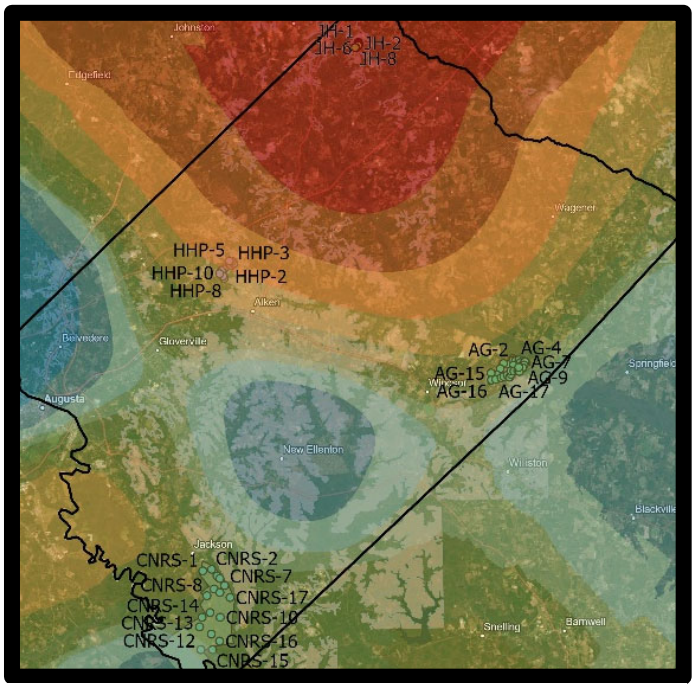

Figure 5. FY25 sampling locations at Aiken County public lands overlain by the NURE mapping contours, where red contours indicate the highest uranium resource potential and blue contours indicates the lowest uranium resource potential.

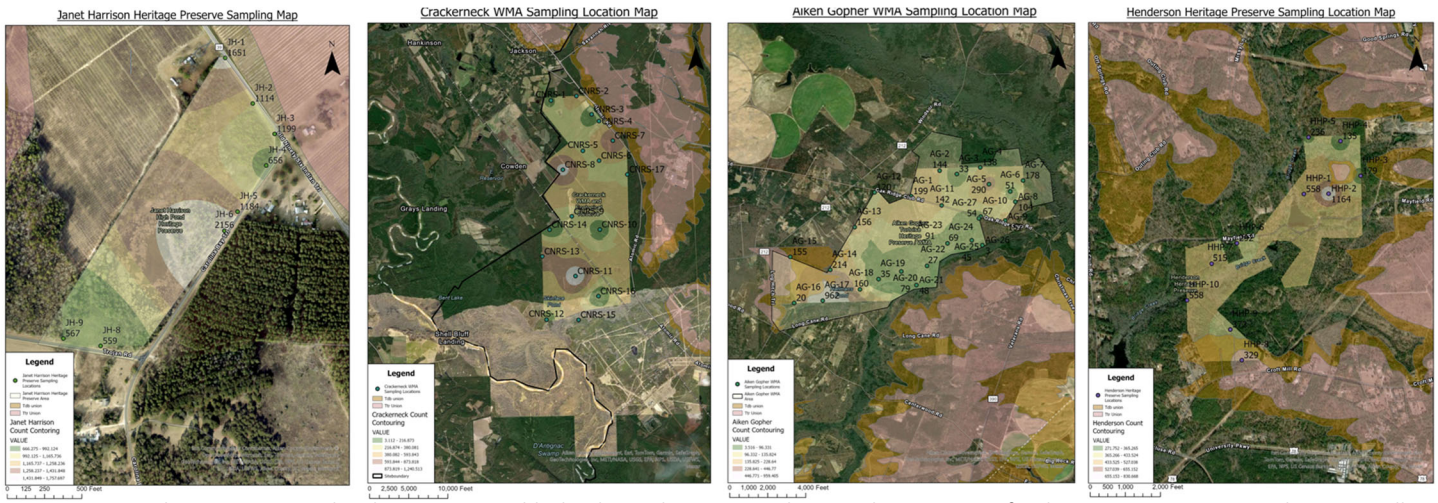

Figure 6. FY25 Aiken County sampling locations on public lands in Aiken County showing the contours of radon concentrations in soil gas, as well as selected geologic formations that are present.

Accomplishments and Results

- 105 soil gas samples were collected around Aiken County, and the concentration of radon was measured.
- Statistical analysis was performed, and machine learning approaches were evaluated for guiding sampling efforts.
- The sampling efforts showed that radon concentration follows a similar trend to the NURE mapping (e.g., higher concentrations found in the northern portion of Aiken County).
- The correlation analysis and random forest showed that geologic formations that are strong predictors of uranium resource potential have good agreement with prediction of radon potential.
- In general, quaternary alluvium sediments of different ages and Carolina bays tend to correlate with elevated radon in soil gas, indicating depositional uranium containing minerals.
- The presence of the Huber, Dry Branch, Altamaha, and Tobacco Road formations tend to correlate with elevated radon in soil gas, indicating potential residence of sparse uranium containing mineral formations.
- A broader sampling effort of up to 1,000 samples across Aiken County would strengthen findings.

Team Members

Jordan Floyd, Austin Coleman, Elizabeth LaBone, Christopher Sobecki, Fabiola Rivera-Noriega[a], Brian Looney

[a]*Florida International University*
[*]*Summer Intern*

References

1. Gundersen, L.C.S., Schumann, R. R,, Otton, J. K., Dubiel, R. F., Owen, D. E,, and Dickinson, K. A. *Geology of radon in the United States*, Geological Society of America Special Paper 271, 1992.
2. Michel, J., Cole, K. H., and Moor, W. S. *Uraniferous gorceixite in the South Carolina coastal plain (USA),* Chem. Geol., 35: 227-245, 1982.
3. Bena, E., Ciotoli, G., Petermann, E., Bossew, P., Ruggiero, L., Verdi, L., Huber, P., Mori, F., Mazzoli, C., Sassi, R. *A New Perspective in Radon Risk Assessment: Mapping the Geological Hazard as a First Step to Define the Collective Radon Risk Exposure*, Science of the Total Environment 912, 2024.
4. Duval, J. S., Carson, J. M., Holman, P. B., and Darnley, A. G. *Terrestrial Radioactivity and Gamma-Ray Exposure in the United States and Canada: US Geological Survey Open-File Report* 2005-1413, 2005.

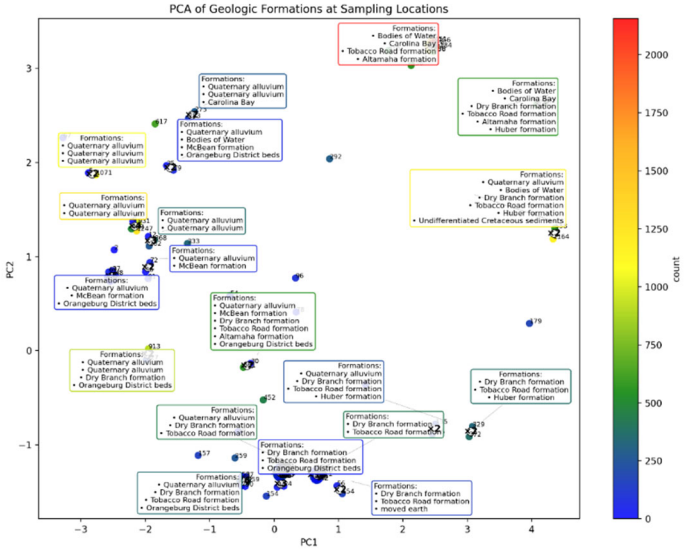

Figure 7. Principal component analysis (PCA) of geologic formations associated with sampling locations. Annotations indicate the geologic formations present at the locations and marker color indicates the radon concentrations measured at the different locations.

Rad-Hard Beyond-CMOS Reservoir Computing with Continual Learning

William Wells

Beyond-CMOS (memristors) reservoir computing systems can mitigate current intelligent systems' high computational and power requirements. Memristors' radiation hardness and low-power characteristics enable their systems to perform on-the-edge in harsh environments. The aim is to develop memristive intelligent systems and study their radiation response to enhance research in strategic areas at SRNL.

Introduction

Current intelligent systems although can achieve high classification accuracies are hampered by several factors such as high computational and learning complexity, and high-power consumption. With Moore's Law nearing its end, achieving more computing power using CMOS devices only is put into question, making CMOS chips less suitable for intelligent systems. Beyond-CMOS devices, like memristors [1, 2], offer promising alternatives for next-generation intelligent computing systems due to their low-power consumption and ability to combine storage and computation. Moreover, memristors are intrinsically rad-hard; they can withstand 1000x more neutron fluxes and ~10-100x kilograys than CMOS devices [1].

Testing memristive behavior under radiation is not novel in itself; however, previous works often assumed ideal conditions or relied on models based on ideal memristor behavior, which does not necessarily translate to real-world scenarios. This work created a SPICE model, based on a physical memristor, that emulates the memristive behavior under different types of radiation. Afterwards, this model was used to build different memristive architectures such as crossbars and reservoir computers, see **Figure 1**, to assess their behavior under different radiation types. Understanding the behavior of such architectures under radiation will open the door for designing and building efficient and low-power computing systems that can operate independently on-the-edge in harsh environments.

From the learning aspect, Continual Learning (CL) is an approach for the system to continually learn as new data becomes available. We conducted preliminary investigations into CL algorithms for varying length time-series data, preparing for the implementation of these methods on the designed intelligent systems.

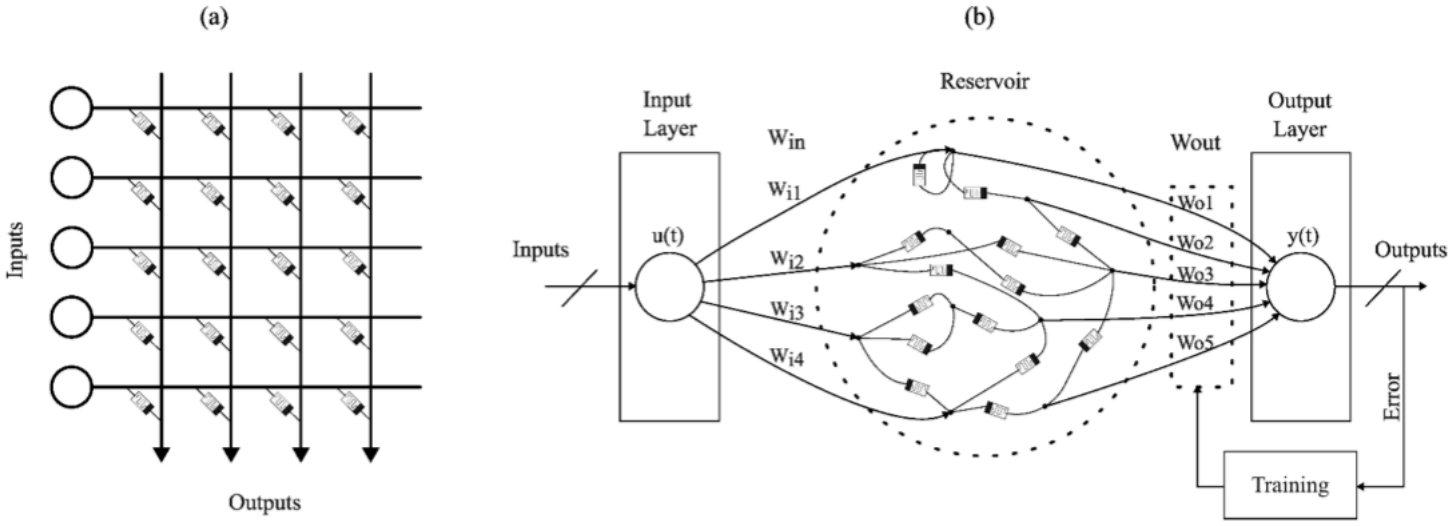

Figure 1. Examples of memristive architectures (a) Crossbar (memristors are located on the wires of the crossbar) and (b) Reservoir Computing system (memristors are located inside the reservoir).

Approach

To create the model that emulates the memristive behavior under radiation, we started with a SPICE memristor model based on a physical fabricated device [4]. We modeled the vacancy creation rate per ion of protons and alpha particles with kinetic energies ranging from 100 keV – 100 MeV in the Monte-Carlo software package Stopping Range of Ions in Matter (SRIM) for a Pt/TiO2/TiO2-x/Pt memristor. The change in vacancy concentration versus ion dose was then applied as a perturbation to the off-state Pt/TiO2 tunneling coefficient and incorporated as a rescaling of rate parameters in the memristor state model.

Using this model, we simulated three different memristive architectures (1) Hamming Distance (HD) memristive computing system [5], (2) Dot Product memristive computing system, and (3) memristive Reservoir Computing (RC) system to test their behavior and radiation hardness. These simulations were performed using, Xyce, an open-source SPICE-compatible, high-performance analog circuit simulator from Sandia National Laboratory. We used multiple (open-source and randomly generated) binary and analog data to test these systems.

For the CL methods we investigated several padding methods to homogenize variable length time-series. We also obtained, cleaned, and labelled a dataset from the mini TCAP system in HRTL. We plan to test this dataset with the investigated CL algorithms during the second year of this project.

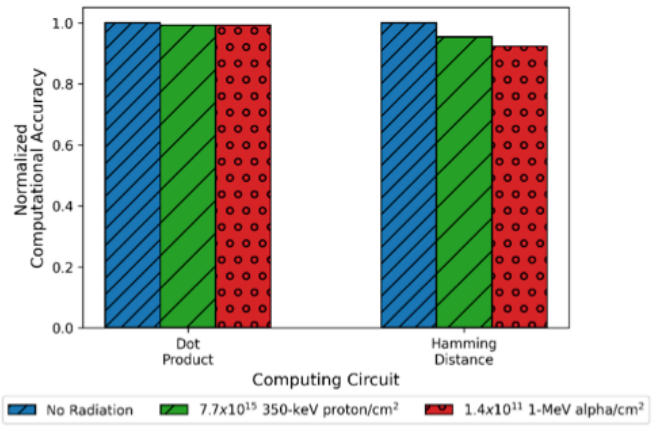

Figure 2. DP and HD memristive crossbars under different radiation conditions.

Accomplishments

- Proved that different memristive crossbar-based computing systems, namely the HD and DP, which are widely used in machine learning and error correction and detection can withstand high alpha and proton radiation doses, achieving ~94% computing accuracy, see **Figure 2**.
- Showed that the behavior of a memristive RC doesn't change under alpha and proton radiation, see **Figure 3**. This is because the RC relies on the dynamic behavior of the memristors, which is negligibly affected by radiation, to perform the computation. These results open the door for designing and building memristive sensors, monitoring systems, and computing modules suitable for on-the-edge high radiation environments.
- Preliminary results showed that padding methods substantially affect class incremental CL algorithms when dealing with varying-length time-series data. The choice of padding method and its location—prefix, suffix, or both—depends on the dataset type. For example, datasets using spectrogram data, like the InsectWingBeat [6], where the data represents the light perturbations of an insect flying through, benefited from padding methods that accentuate the upper (maximum) or lower (minimum) limits of each individual time series, see **Figure 4**. Further research on this topic will be conducted in the second year of this project.

Team Members

William Wells, Mohammad Taha*, Joshua Kleppinger, Victor Philippe†

** SRNL Postdoctoral Researcher*

† Graduate Intern from the University of Georgia

References

1. Chua, L., *Memristor-The missing circuit element,* in IEEE Transactions on Circuit Theory, vol. 18, no. 5, pp. 507-519, September 1971, DOI: 10.1109/TCT.1971.1083337
2. Strukov, D., *et al. The missing memristor found*. *Nature* 453, 80–83, 2008. https://doi.org/10.1038/nature06932
3. Prinzie, J., *et al. Low-power electronic technologies for harsh radiation environments,* Nature Electronics 4, 243–253, 2021.
4. Yang, Y., & Lu, W., *Nanoscale resistive switching devices: mechanisms and modeling, Nanoscale*, *5*(21), 10076-10092, 2013.
5. Taha, M., & Teuscher, C., *Approximate Memristive in-memory Hamming Distance Circuit*, ACM Journal on Emerging Technologies in Computing Systems (JETC), *16*(2), 1-14, 2020.
6. Chen, Y., *et al., Flying Insect classification with inexpensive sensors*, Journal of Insect Behavior, vol. 27, no. 5, pp. 657-677, 2014.

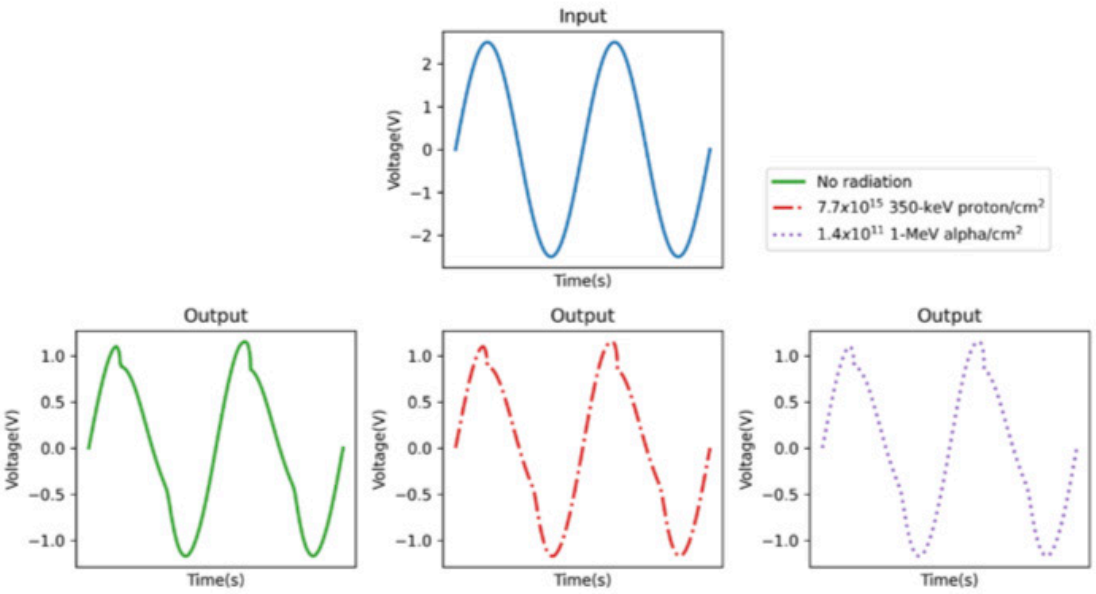

Figure 3. The input and output of a 100-node reservoir computer under varying radiation conditions, including no radiation.

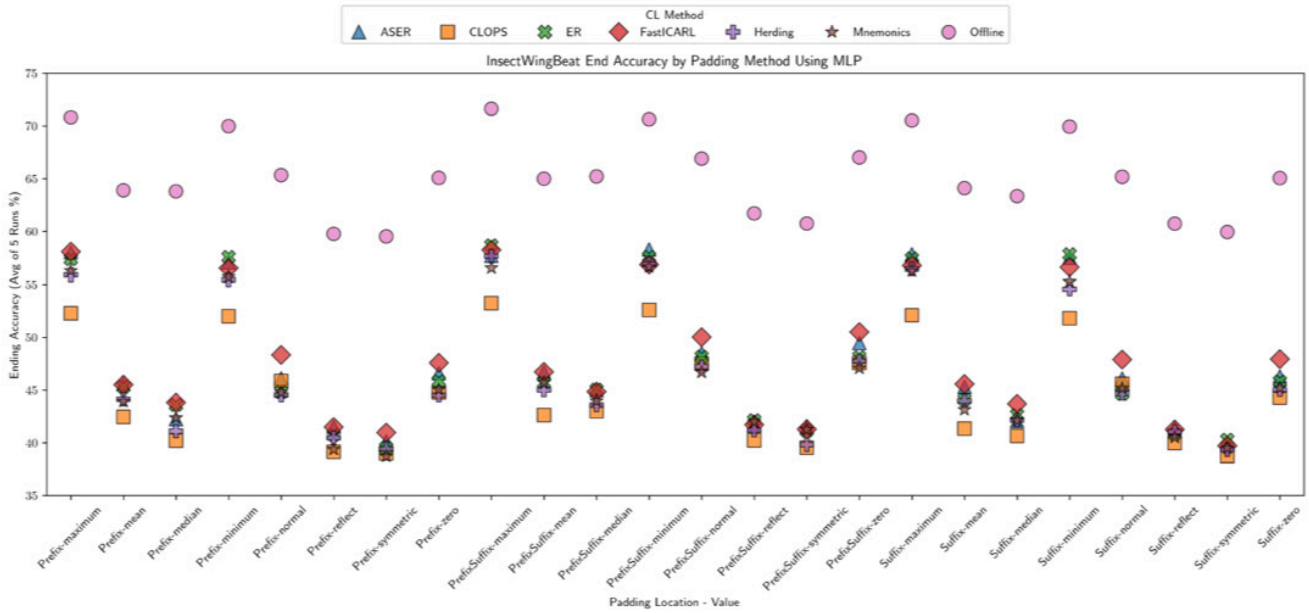

Figure 4. Classification accuracy versus a variety of combinations of time-series padding location and values for the InsectWingBeat dataset for different CL methods using a Multi-Layered Perceptron (MLP) model.

Threat Hunting Representations for Embedded-system Anomaly Tracking (THREAT)

Glenn A. Fink

This Strategic Cyber LDRD has laid a strong foundation for innovation in cybersecurity and artificial intelligence at SRNL. Through investments in computing infrastructure, targeted technical research, and a broad network of collaborators, the program has strengthened the lab's ability to lead in the development of secure, AI-enabled cyber-physical systems.

Introduction

The Threat Hunting Representations for Embedded-system Anomaly Tracking (THREAT) LDRD initiative focuses on advancing cybersecurity and artificial intelligence in cyber-physical systems, particularly those relevant to energy and nuclear infrastructure. The program's achievements this year include the acquisition and deployment of a state-of-the-art GPU-based computing cluster named Raptor, the creation of a Science DMZ boundary to facilitate secure, high-speed data access, significant collaborations including partnerships with Sandia National Laboratories and the Idaho National Lab, and participating in relevant workshops and guided tours like the one at Plant Vogtle. These activities helped attract external funding and bolster SRNL's visibility. Publications resulting from this project include a paper released on arXiv and an upcoming book chapter. Although engineering accomplishments were stunted by site-mandated cybersecurity constraints, the project contributed substantially to SRNL's capabilities and institutional competencies, demonstrating that large language models can produce vectorizations of cybersecurity data that present informative features of the data to cybersecurity defenders (**Figure 1**, **Figure 2**, **Figure 3**). The progress achieved this year positions SRNL not only to address emerging threats but also to shape the national research agenda in cyber-informed engineering for critical infrastructure.

Approach

The Threat Hunting Representations for Embedded-system Anomaly Tracking (THREAT) LDRD initiative was launched as a strategic investment to significantly advance Savannah River National Laboratory's capabilities in cybersecurity and data science. Recognizing the central importance of these domains to national security, the LDRD was structured around a central research agenda, supported by targeted organizational investments in high-performance computing infrastructure, workforce development, and partnerships with key external stakeholders. This integrated approach aimed to elevate SRNL's scientific capabilities, broaden its institutional competencies, and catalyze new collaborations aligned with its mission to support secure and resilient critical infrastructure.

This year's efforts focused on building foundational capabilities to leverage artificial intelligence for cybersecurity within cyber-physical systems, particularly for energy and nuclear contexts. By aligning technical research with infrastructure development and strategic outreach, the program not only achieved significant internal milestones but also attracted external funding and fostered institutional visibility.

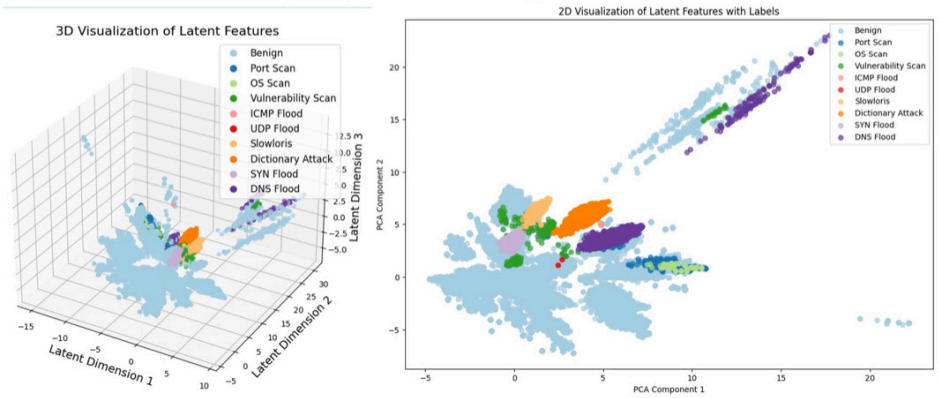

Figure 1. Embedding model done on cyber packet capture data from the Army Cyber Security Internet of Things dataset,2024, shows that traffic types and connection types create distinct clusters of embeddings.

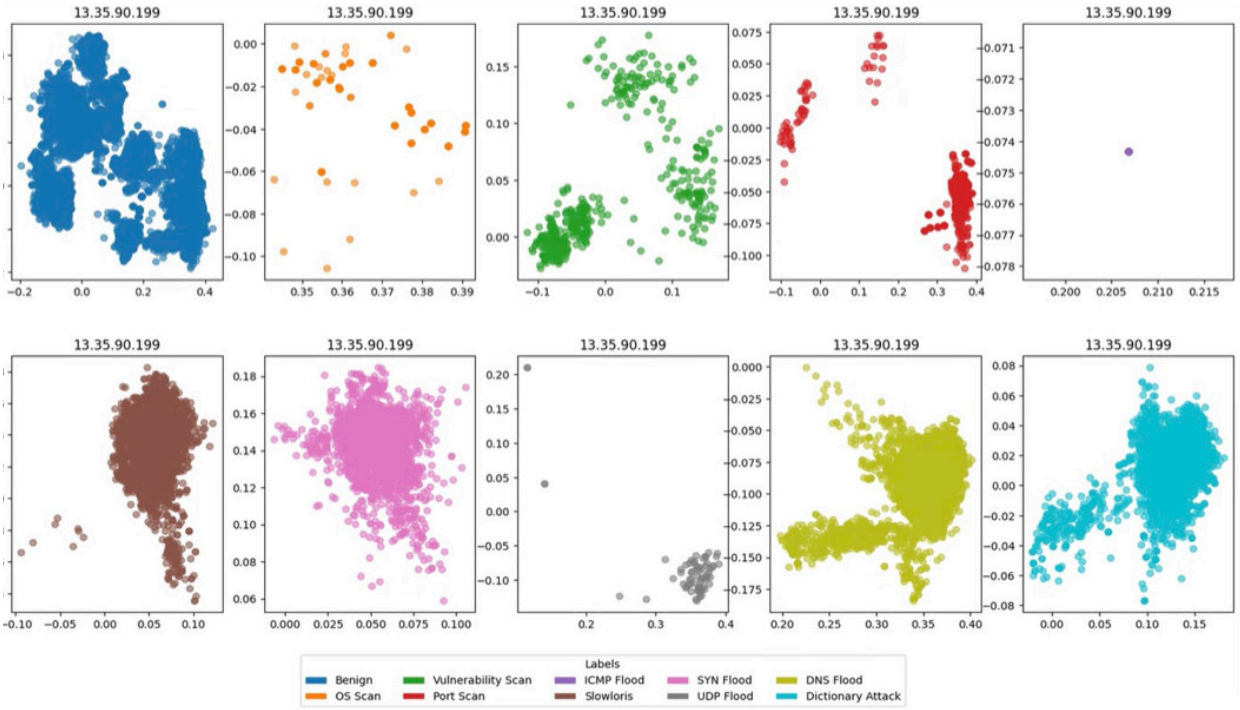

Figure 2. Embeddings of individual traffic types often show multi-modal clusterings of connections.

Accomplishments

Infrastructure and Organizational Development

- Purchased and deployed SRNL's first truly modern GPU-based computing cluster, codenamed **Raptor**. The system—a high-performance HPE Apollo 8-node platform equipped with NVIDIA H100 GPUs—was installed in November 2024. Raptor will ultimately be relocated to the Applied Manufacturing Collaborative (AMC) under the terms of a strategic agreement between SRNL and DOE. Raptor is intended to support AI model development, open science initiatives, and staff training in deep learning. It plays a foundational role in enabling language model research tailored for cyber-physical systems.
- Initiated the creation of a new **Science DMZ** boundary (planned for deployment in the AMC) in partnership with SRNL's CIO to facilitate high-speed, secure data access for research computing.
- Founding member of SRNL's **Data Review and Release Board** to manage release of scientific data responsibly.
- Established a data-sharing agreement between DOE-SR and BSRA to use operational cyber data in research. Effort is currently in final negotiation stages, and discussions are underway with DOE program offices (e.g., CESER, EM, ASCR) to formalize a broader cyber data sharing framework.

Engineering and Research Progress

- Initial exploratory prototypes to develop embeddings of cyber-physical behavior using large language models demonstrated that cyber network data naturally clusters by functional behavior. However, transitioning this research to the Raptor cluster required complete reengineering due to cybersecurity controls and environment isolation constraints.
- Despite these challenges, core codebases for model development were completed, laying the groundwork for future deployment once Raptor is moved to the Science DMZ.

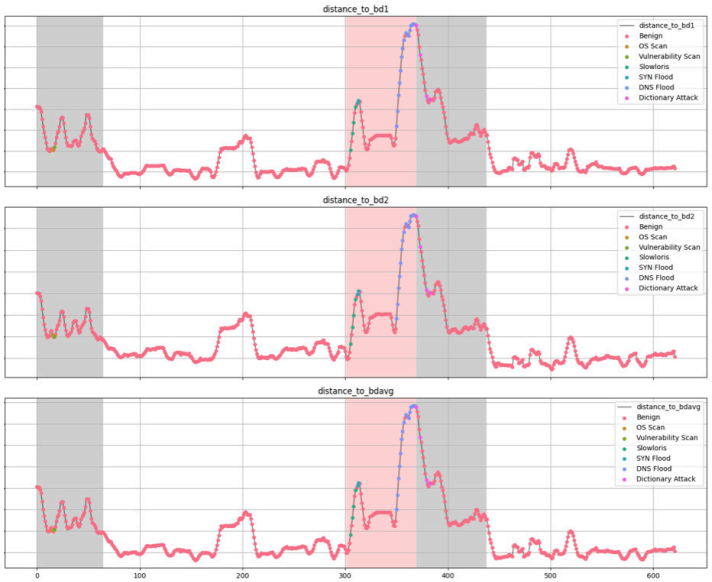

Figure 3. Anomaly metric on sliding window of cyber data over a five day period clearly shows that attack days (shaded periods near the center) appear significantly anomalous compared to normal days (white background). Initial shaded background is the experiment initialization, which is not taken into account when calculating normality.

Collaborations and Outreach. THREAT LDRD significantly expanded SRNL's visibility and collaborative footprint:

- Established recurring CIO/user-research meetings for discussing Science DMZ requirements and progress. This work is ongoing and has been transitioned to the **AI Advisory Board**.
- Partnering with SRNL's Mobile Melt-Consolidate (MMC) program under NA-23, the LDRD has played a key role in producing a MMC 2.0 recommendations paper and conducted an "Elegant Factory" demonstration showing cyber-physical event cross correlation.
- Deepened cyber partnerships with **Sandia National Laboratories** and **INL**, including on nuclear cyber design patterns.
- Participated in the **Cyber for Nuclear Systems Workshop** with Georgia Tech.
- Led a guided tour of Plant Vogtle involving 15 professionals from four organizations.
- Hosted the **FY24 Workforce Development Workshop**, attracting 160 participants from 42 organizations across nine states and two countries.
- Contributed to planning for the FY25 iteration of the workshop in collaboration with Dr. Luke Gosink.

Other engagements included:

- Mentoring at SC Competes Spring Summit in Charleston.
- Judging and participating in poster sessions with BSRA and USC-Columbia.
- Proposal reviews and mentorship for cybersecurity-focused LDRDs.
- Faculty and proposal collaboration with Clemson, Augusta University, Georgia Tech, FIU, and USC-Aiken.
- Sponsor engagement with NRC, DOE-NE, DOE CESER, DOE EM, NextEra, Southern Co., and DoD elements.
- Participated in DOE's **AI Jam for 1,000 Scientists**, which led to helping shape recommendations for establishing an AI analytics core competency at the lab.

Follow-on Funding and Proposals. The LDRD has catalyzed externally-funded projects:

- **SMR-THREAT**, a DOE-NE project focused on threat modeling for small modular reactors (SMRs), entered its second year with $300K in funding.
- **Cyber Design Patterns for SMRs**, funded by NA-211, launched its first year with $200K.

Proposals related to this work were also submitted to:

- DOE Office of Nuclear Energy's Advanced Reactor Safeguards and Security (ARSS) program (two proposals).
- DOE International Nuclear Security Agency Emerging Technologies in Security (one proposal).
- DOE-Office of Electricity and industry partners such as NextEra (proposal on grid resilience).

Joint proposals were developed with major universities (Clemson, GT, UGA, VT, UCF, FIU) demonstrating ongoing momentum in building institutional partnerships.

Team Members

Steven Weldon, Luke Gosink, Rachel Jones, Connor Coughlin, Waylon Brunette[a], Sejun Song[a] , Hala Strohmier[b] *Kristen Booth*[c]

[a] *Augusta University*

[b] *University of South Carolina, Aiken*

[c] *University of South Carolina, Columbia*

AI Informed Microfluidic Control for Additive Manufacturing

Christopher Sobecki

Our research applies artificial intelligence to identify and characterize microfluidic droplet production for additive manufacturing and inertial confinement fusion, where analyzing droplet quality at different flow rates could improve economics and manufacturing speed. The project has effectively gain notable interest, and a full proposal was submitted to NA-114.

Introduction

Additive manufacturing plays a critical role in designing and producing novel materials that support a variety of useful properties (e.g., electrical conductivity, tensile strength, etc.). Droplet formations to manufacture 3D printing feedstock in microfluidics, for example, can scale-up production from 1 kg/month to 1 ton/month.[1] However, the key to designing these materials is understanding the relationship between microfluidic pores and the corresponding properties of droplet structure (e.g., size and sphericality), production frequency, and droplet manipulation.[2] Furthermore, droplet control is challenging due to gravitational forces and the surface tension between two immiscible fluids. Using SRNL's experience in polymer feedstock production, artificial intelligence (AI), microfluidics, and image analysis, this task developed an approach to characterize and design high-precision controllers that are required to create the next generation of additive manufacturing materials. **Figure 1** shows a schematic on how particles are produced under ultra-violet photo-curation, with our main focus on the upstream of the device.

AI algorithms were implemented in the TensorFlow framework and applied to multiple images that contained droplets. Training, testing, and validation setups were applied within the approach for droplet recognition, as seen in **Figure 2**, where we applied bounding boxes on microfluidic droplets. Afterwards, a scoring system was applied on the droplets' characteristics (e.g., aspect ratio, circularity, etc.) to identify production quality conditions, e.g., aspect ratio is almost one. Having this labeled data, convolutional neural networks (CNN), random forests, and logistic regression identified high-quality and defective droplets. Finally, we simulated droplets by changing flow rates for optimal design.

Approach

The research approach integrated AI techniques with microfluidic controls to advance additive manufacturing particle production. Initially, microfluidic droplets were observed and analyzed using high-speed cameras and synthetic device simulations (**Figure 2**) to gather preliminary data.

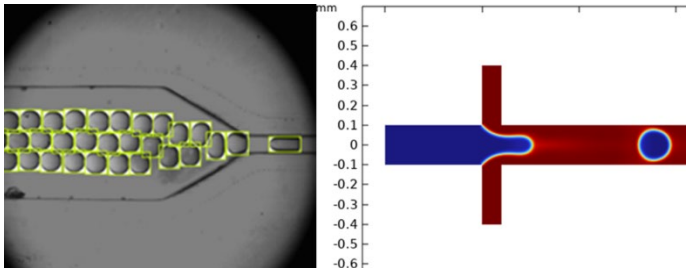

Figure 1. Schematic quality assurance and quality control for an automated particle generator.

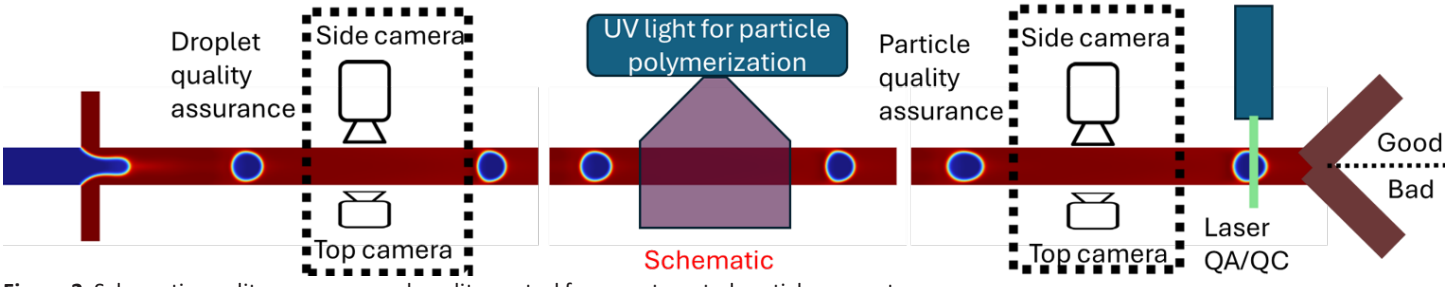

Figure 2. Schematic quality assurance and quality control for an automated particle generator.

The AI system recognized and characterized these droplets (**Figures 3 and 4**) through a scoring system that assessed key parameters such as aspect ratio and circularity to ensure production quality and quality control in real-time.

The core approach employed CNNs, support vector machines, random forests, and logistic regression, to distinguish between high-quality and defective droplets (**Figure 4**). These models were trained, tested, and validated, and they exactly agreed that 90% of 10,000 droplets were of high-quality. This process allowed the system to identify high-quality droplets reliably, ensuring consistency and efficiency in production.

Finally, the research included simulative components where different flow rates were tested to derive an optimal droplet production design. This step involved adjusting conditions to mimic real-world scenarios and predict outcomes under various operational settings, e.g., flow regimes and droplet sizes. Overall, the AI-informed microfluidic control method enhanced the precision and scalability of droplet formulations for additive manufacturing, optimizing production throughput and quality assurance while mitigating costs and time. The results from this LDRD led to full NA-114 proposal submission: **AI-Informed Microfluidic Control for Additive Manufacturing Feedstock and Inertial Confinement Fusion Target Production**. All software is stored on SRNL's HPC resources, and the workflow could be extended to AI analysis on different images, video framerates, and conduct evolutionary design on the microfluidic geometry.

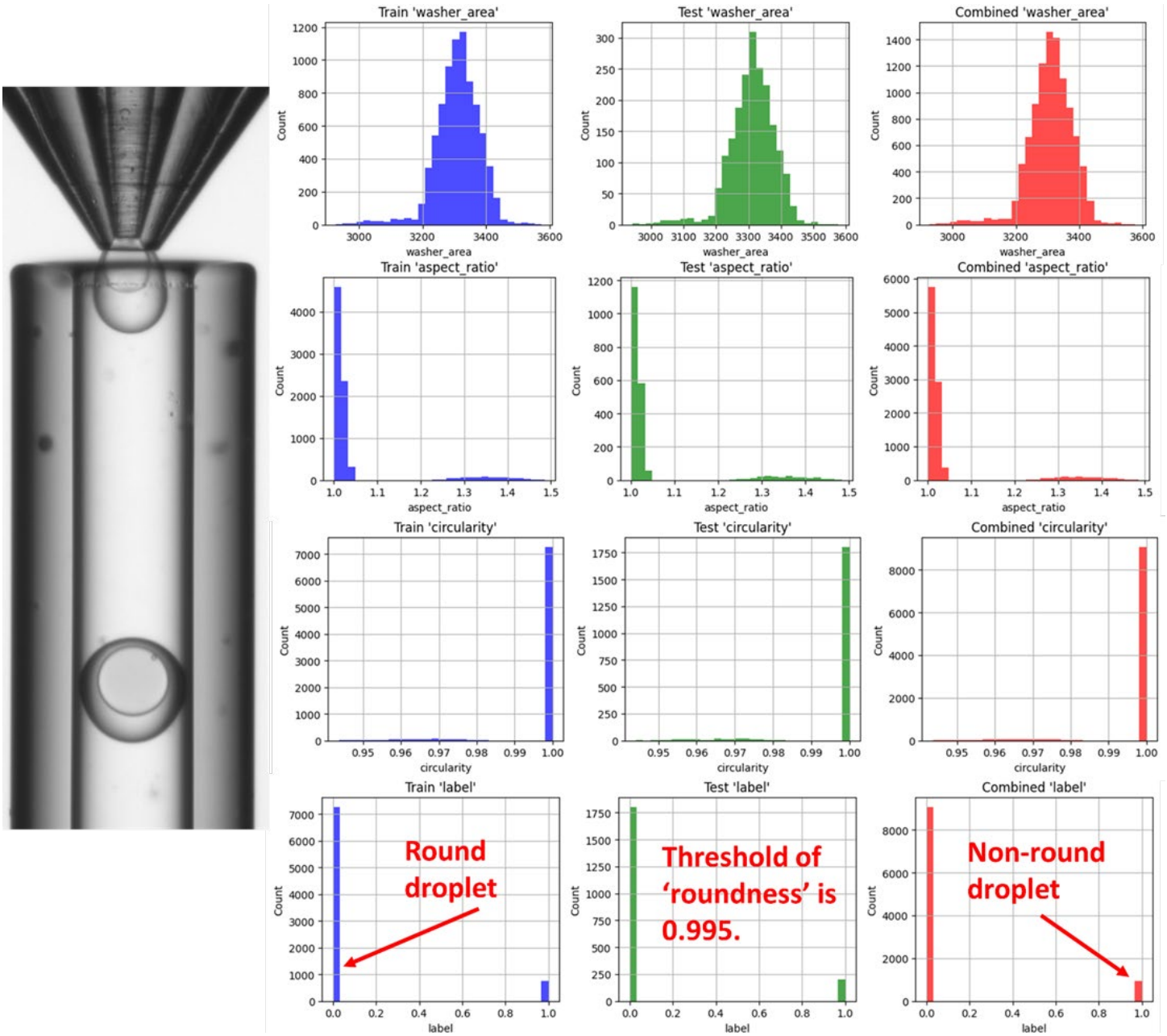

Figure 3. Example of a double-emulsion (i.e., washer) microfluidic droplet that could be used for inertial confinement fusion feed production. Synthetic washers were used for production scoring and for production quality assurance and quality control analysis. Future work includes calculating the concentricity of the area inside the washer and analyzing droplets in videos with different frame rates.

Layer (type)	Output Shape	Param #
conv2d (Conv2D)	(None, 126, 126, 32)	896
max_pooling2d (MaxPooling2D)	(None, 63, 63, 32)	0
conv2d_1 (Conv2D)	(None, 61, 61, 64)	18,496
max_pooling2d_1 (MaxPooling2D)	(None, 30, 30, 64)	0
conv2d_2 (Conv2D)	(None, 28, 28, 64)	36,928
flatten (Flatten)	(None, 50176)	0
dense (Dense)	(None, 64)	3,211,328
dense_1 (Dense)	(None, 1)	65

Total params: 3,267,713 (12.47 MB)
Trainable params: 3,267,713 (12.47 MB)
Non-trainable params: 0 (0.00 B)

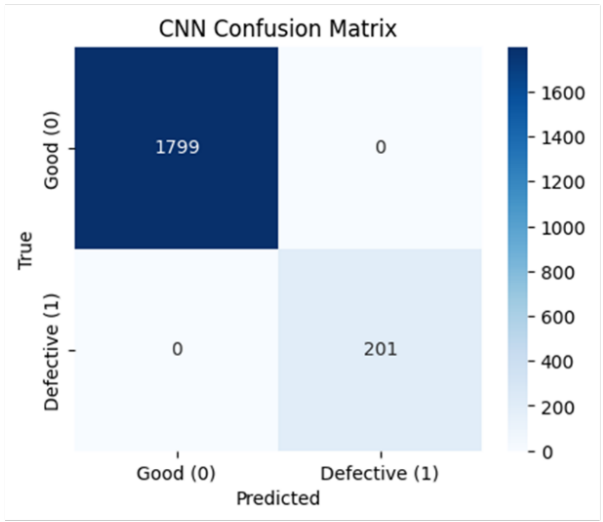

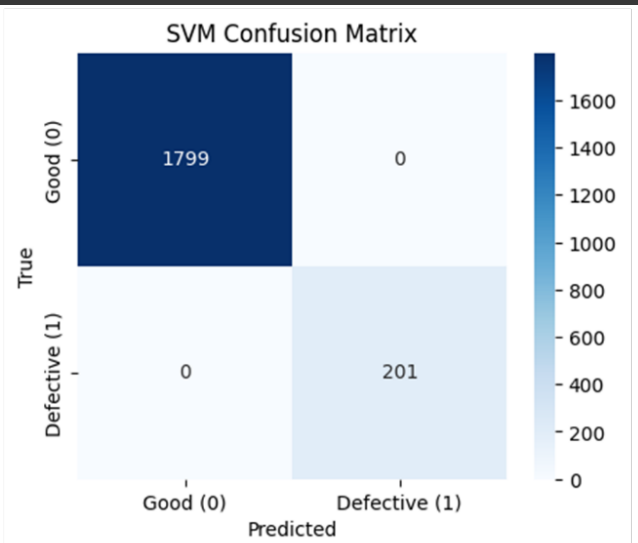

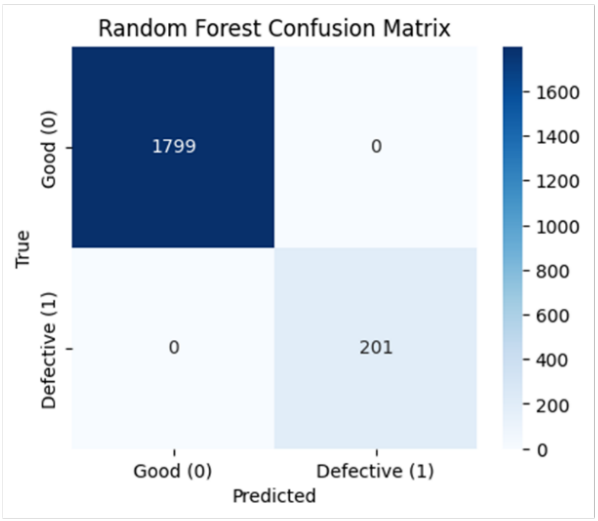

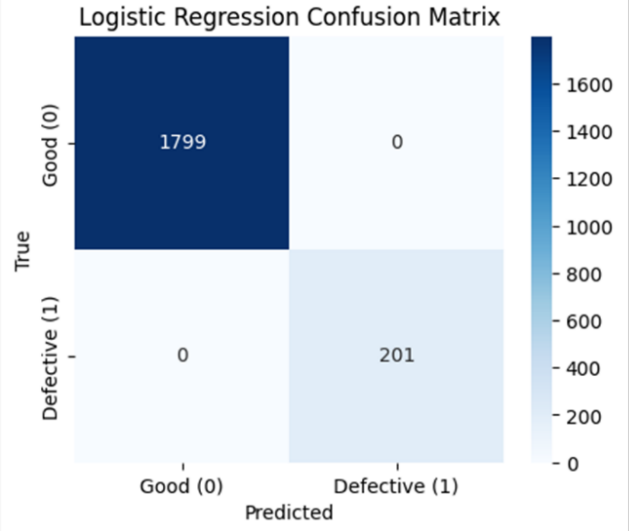

Figure 4. CNN architecture and four artificial intelligence algorithms evaluating defective and good droplets.

Accomplishments and results

- AI techniques successfully recognized and characterized droplets.
- Results showed that by describing a desired characteristic trait, we were able to decipher that almost 90% of the produced droplets were acceptable.
- Four AI algorithms evaluating high-quality and defective droplets showed strong agreement with each other
- This enables robust methodologies for on-line quality assurance and quality control of droplet production.
- The workflow is extensible to high-quality microfluidic droplet production through optimal system control to create more useable and reliable droplets with desired characteristics, meeting production objectives while reducing cost and time.
- A software integration loop was developed to optimize channel geometries and flow rates between Python, COMSOL on SRNL's HPC resources (**Figure 5**). This helped to produce synthetic videos for real-time online monitoring scenarios and automation for flow control. This method not only showed different phase flows (e.g., stream, droplet, and dripping), but it also produced droplets of different sizes for a single microchannel geometry.

The results from this LDRD led to full proposal submission for NA-114's Artificial Intelligence for Nuclear Security (AI4NS): **AI-Informed Microfluidic Control for Additive Manufacturing Feedstock and Inertial Confinement Fusion Target Production**. All software is stored on SRNL's HPC resources, and the workflow could be extended to AI analysis on different images, video framerates, and conduct evolutionary design on the microfluidic geometry.

Team Members

Larry M. Deschaine

References

1) *Telos High-Throughput Systems*; Unchained Labs. www.unchainedlabs.com/telos-high-throughput-systems/#volume (accessed 2024-11-05)
2) Baah, D.; Floyd-Smith, T. Microfluidics for particle synthesis from photocrosslinkable materials. *Microfluidics and Nanofluidics* 2014, *17* (3), 431-455. DOI: https://doi.org/10.1007/s10404-014-1333-y

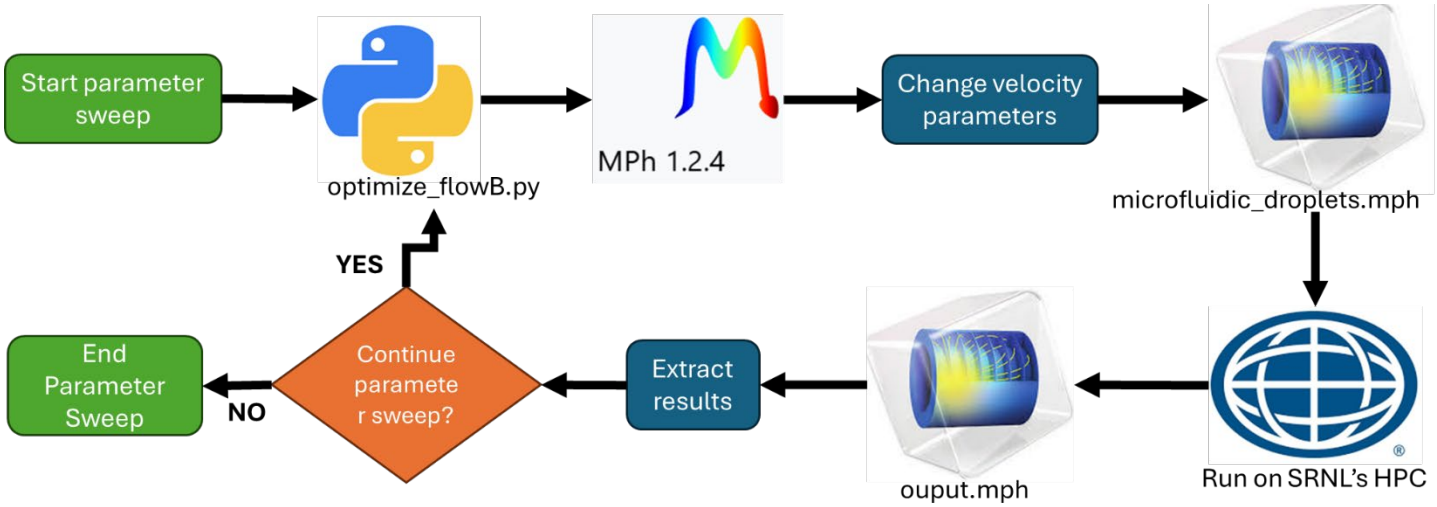

Figure 5. Prototype flowsheet adapted for the feedstock application, referencing Figure 1 (b). This figure was implemented to produce synthetic videos by using the grid search optimization method on the flow rates for the oil and water phases.

Environmental Remediation

Thiol-Functionalized Metal-Organic Frameworks (MOFs) for Inorganic Mercury Removal from Waste Tanks

Ingrid Lehman-Andino

This project provides a fundamental understanding of the chemical properties of metal-organic frameworks and how they interact with mercury species in high-level nuclear waste to accomplish our overall goal of accelerating waste remediation and mitigate environmental risks.

Introduction

Decades ago, the processing of special nuclear materials (SNM) at the Savannah River Site (SRS) and Hanford site facilities generated more than 90 million gallons of radioactive waste that is housed in waste tanks. (**scheme 1**)[1]. $Hg(NO_3)_2$ was utilized as a catalyst for dissolving the aluminum cladding on spent fuel rods to recover fission products[2] during SRS Canyon facility processing. The waste generated from these activities contains a mix of Hg^0, Hg_2^{2+}, Hg^{2+}, and various organomercury compounds currently present at SRS facilities[1-3] and the liquid waste system (LWS). The elevated levels of mercury in the tanks remain a significant concern and has become an urgent problem due to its high toxicity and regulatory compliance concerns.

It is crucial to accelerate remediation efforts by finding new avenues to solve this issue. Monitoring tank mercury levels has shown that recovery methods such as sumps, mercury striping, or mercury cells are ineffective. Traditional adsorbents like activated carbons, ion exchange resins, and zeolites usually demonstrate low capacity, weak binding affinity, and poor selectivity for mercury[5-9].

Thiol-functionalized metal-organic frameworks (MOFs) have shown promise for selectively removing Hg^{2+} in the presence of other metals such as Cu^{2+}, Ni^{2+}, Fe^{3+}, Ca^{2+}, Mg^{2+}, Cd^{2+}, Cr^{6+}, Mn^{2+}, Pb^{2+}, and Zn^{2+} across a broad pH range (1–10)[10-14]. These MOFs feature multiple thiols per organic ligand and maintain ultrahigh porosity, allowing them to remove more mercury per molecule than many industry-standard adsorbents[10-15]. The versatility and capability to selectively bind Hg^{2+} made these MOFs highly effective candidates for mercury waste removal. MOFs continue to evolve and could feature alternative materials for the highly alkaline high-level waste (HLW) that would support rapid response actions for future mercury accumulation in waste tanks.

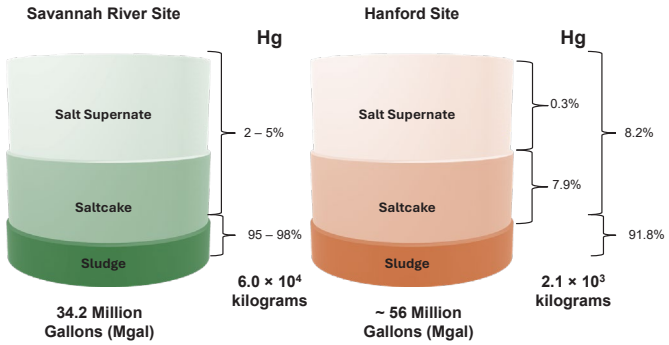

Scheme 1. Representation of Savannah River Site and Hanford Site radioactive waste amounts and mercury inventories[1-2].

Approach

The complexity of SRS waste tanks has an impact in the chemical behavior of mercury (Hg) resulting in significant concern due to the formation of high quantities of organomercury species, such as methylmercury. In our project, we focused on the chemistry and behavior of thiol-functionalized MOFs for the adsorption and sequestration of mercuric compounds. To meet this goal, we designed and structurally characterized isoreticular MOFs featuring thiol-functionalized linkers such as UiO-66-SH and UiO-67-$(SH)_2$, using powder-X-Ray diffraction (P-XRD). These promising MOF candidates demonstrated from initial tests high Hg(II) intake capacity and were evaluated using actual tank waste samples. Experiments including kinetic studies of Hg(II) uptake under varying pH conditions, as well as assessments of alkaline pH and radiolytic stability of these MOFs helped understand the behavior of these porous materials. Direct Mercury Analysis (DMA) and Inductively Coupled Plasma-Optical Emission Spectrometry (ICP-OES) were employed to determine mercury kinetics and monitor adsorption behavior using the synthesized MOFs. During this project, the team evaluated the MOFs' capacities for selectively extracting Hg from simulated tank waste samples and real tank waste samples, conducted competitive binding experiments, and tested the recyclability of the MOFs at various pH levels.

Accomplishments and results

- Isoreticular MOFs UiO-66-SH and UiO-67-$(SH)_2$ presented in **Figure 1** were successfully synthesized and characterized by Powder X-ray Diffraction (P-XRD). This included design, materials procurement, hazard analysis, environmental evaluation planning, synthesis, and characterization.
- Stability studies under a series of alkaline conditions were completed for UiO-66-SH and UiO-67-$(SH)_2$. Their stability was evaluated under similar pH waste tank conditions in lapses of 24 hours (**Figure 2**), where UiO-67-$(SH)_2$ shows a higher stability to harsh pH condition such as pH 14.
- Radiolytic studies, shown in **Figure 3**, demonstrated stability of UiO-66-SH up to a 10 Mrad cumulative dose, while UiO-67-$(SH)_2$ shows stability up to $5.61x10^4$ rad of cumulative dose. P-XRD analysis was employed to confirm their crystallinity and determine their stability.
- Thiol-functionalized MOF UiO-66-SH demonstrated an optimal adsorption by the removal of 90% Hg(II) from a pH 10 solution at 24 hours, showing a higher affinity than UiO-67-$(SH)_2$ (**Figure 4A**).
- Rapid mass transfer in the solution phase, the intraparticle diffusion, and adsorption of metal cations on the surface of the adsorbent binding sites is demonstrated in **Figure 4**, showing the best performance for UiO-66-SH.
- The kinetic data, in **Figure 4**, shows that the metal ion adsorption on UiO-66-SH increases sharply during the first 10 min and later plateaus showing these MOFs have a sufficient number of adsorption sites and high metal ion affinity for the −SH groups.

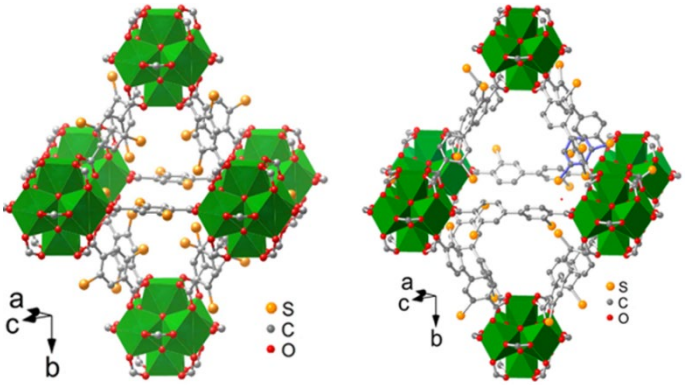

Figure 1. Octahedral cage from the single crystal structure of the UiO-67-SH[15] (left) UiO-67-$(SH)_2$ (right) framework[11].

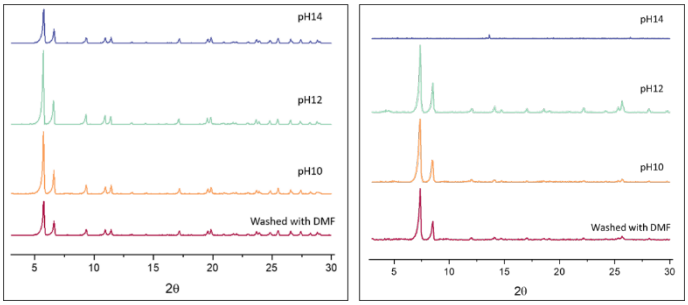

Figure 2. P-XRD spectra of UiO-67-$(SH)_2$ (left) and UiO-67-SH (right) demonstrating pH stability of MOFs under alkaline conditions for a period of 24 hrs.

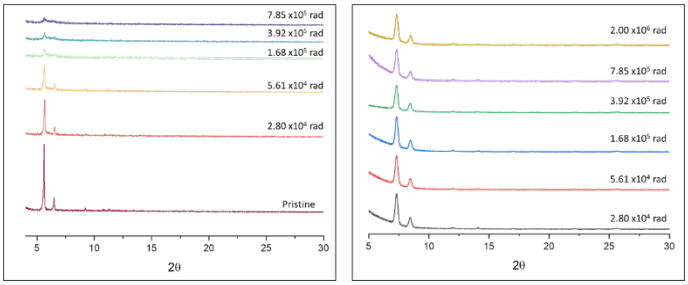

Figure 3. P-XRD spectra of UiO-67-$(SH)_2$ (left) and UiO-67-SH (right) MOFs irradiated with a Co-60 with a dose rate of $5.14x10^5$ rad/hr. The MOF was irradiated with cumulative dose up to 7.85 $x10^5$ rad.

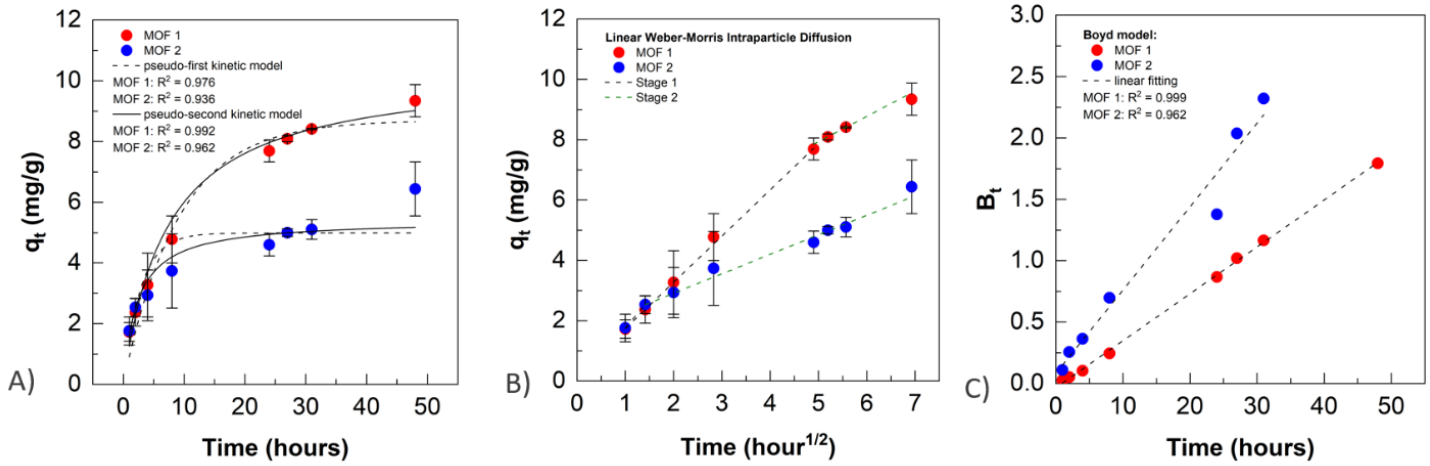

Figure 4. Kinetic data models base of adsorption experiments in pH 10: A) Pseudo-first/second models, B) Weber Morris intraparticle diffusion, and C) Boyd diffusion model. MOF 1 =UiO-66-SH, MOF 2= UiO-67-(SH)2.

- Initial computational studies modeling for these MOFs using structural optimization with Vienna AB initio Simulation Package (VASP) calculation shows Hg(II) binding preference of the thiol groups.
- Thermal Gravimetric Analyzer (TGA) instrument by Perkin Elmer is in process of being installed for future thermal stability of low level RAD samples that will potentially support LDRD projects.
- The ICP-OES data suggest that under alkaline conditions, the MOFs may decompose in the real tank waste sample, even with pH adjustment. Data shows detectable amounts of sulfur in both MOF 1 and MOF 2 samples after tank waste sample exposure. However, a significant amount of sulfur was detected specifically in the MOF 2 samples. Additionally, a higher amount of zirconium (Zr) was found in the MOF 1 samples, while zirconium was not detectable in the MOF 2 samples. The thiol ligand in MOF 2 may decompose, leading to a significant increase in sulfur detection and negatively impacting its mercury (Hg) adsorption capacity. In contrast, the zirconium-oxygen (Zr-O) bond of MOF 1 may decompose, resulting in the leaching of zirconium into aqueous solution.
- Posters were presented at SRNL Day at Georgia Tech (Phuong Pham), University of South Carolina Aiken (Ingrid Lehman-Andino), also two posters were presented at Fall American Chemical Society (ACS) Conferences in the Nuclear division during years of 2024 by Ingrid Lehman-Andino and 2025 by Morgan Cram. (SRNL-MS-2024-00453).

Team Members

Morgan Cram, Sonia Dyer, Corey Martin, Phuong Pham*, Thomas L. White, Dan Lambert, John Dekarske

**Postdoctoral Researcher- transitioned to full staff scientist 2025*

References

1. Marcial, J., Riley, B.J., Kruger, A.A., Lonergan, C.E., Vienna, J.D., Hanford low-activity waste vitrification: A review. *Journal of Hazardous Materials.* **2024**, 461, 132437.
2. Anderson, P.A., Christian, J.D., Alternative reagent to mercuric nitrate catalyst for dissolution of aluminum-clad nuclear fuels in nitric acid. *Journal of Materials Research.* **1998**, 13, 68-76.
3. Nguyen, V.Q. Literature Review Investigating Adsorbents for Mercury Removal from Salt Batch Feed Material. SRNL-STI-2024-00068, **2024**.
4. Bannochie, C. J.; Fellinger, T. L.; Garcia-Strickland, P.; Shah, H. B.; Jain, V.; Wilmarth, W. R. *Sep. Sci. Technol.* **2018**, *53*, 1935.
5. Stone, M. E., McCabe, D.J. Review of Mercury in the SRS Tank Waste Storage and Treatment Processes for Applicability to Hanford Waste Processing, SRNL, **2020**.
6. Ritter, J. A.; Bibler, J. P. Water *Sci. Technol*. **1992**, 25, 165.
7. Wilmarth, W.R.; DuoliteTM GT-73 Resin Testing in Support of the Salt Disposition Alternatives; WSRC-TR-98-00361, October, **1998**.
8. Sun, D. T.; Peng, L.; Reeder, W. S.; Moosavi, S. M.; Tiana, D.; Britt, D. K.; Oveisi, E.; Queen, W. L. *ACS Cent. Sci*. **2018**, 4, 349.
9. Inglezakis, V. J.; Kudarova, A.; Guney, A.; Kinayat, N.; Tauanov, Z. *Sustainable Chem. Pharm*. **2023**, 32, 101017.
10. Liang, L.; Chen, Q.; Jiang, F.; Yuan, D.; Qian, J.; Lv, G.; Xue, H.; Liu, L.; Jiang, H.-L.; Hong, M. *J. Mater. Chem. A* **2016**, 4, 15370.
11. Yan-Lung Wong, Yingxue Diao, Jun He, Matthias Zeller, and Zhengtao Xu. *Inorg. Chem*. **2019** 58 (2), 1462-1468.
12. Gao, J.; Li, Z.; Deng, Z.; Liu, M.; Wei, W.; Zheng, C.; Zhang, Y.; Chen, S.; Deng, P. *Nanomaterials* **2021**, *11*, 2488.
13. Ding, L., Luo, X., Shao, P., Yang, Y., Sun, D. *ACS Sustainable Chem. Eng*. **2018**, 6, 7, 8494–8502.
14. Yee, K., Reimer, N., Liu, J., Cheng, S., Yiu, S., Weber, J., Stock, N., Xu, Z. *J. Am. Chem. Soc*. **2013**, 135, 7795−7798.
15. Guo, B.; Cheng, X.; Tang, Y.; Guo, W.; Deng, S.; Wu, L.; Fu, X. *Angewandte Chemie International Edition.* **2022**, 61 (13), e202117244.

Management and Use through Novel Sulfides and Alloys

Jake Amoroso

This project explores chalcogenide and metallic alloy materials as a means to control the chemical behavior of technetium, which is mobile in the environment. The research will enable development of novel material systems to immobilize waste constituents that are difficult to immobilize in conventional waste forms due to their physicochemical properties.

Introduction

Controlling behavior of technetium (Tc) and other RedOx-sensitive compounds is important for commercial applications as well as long-term disposal of radioactive waste. Tc in radioactive waste mostly exists as pertechnetate ($Tc^{(VII)}O_4^-$) which is highly soluble and mobile in the environment. Once reduced, Tc oxide ($Tc^{(IV)}O_2$) is sparingly soluble. Tc sulfide ($Tc^{(IV)}S_2$) is insoluble, making it an attractive material for Tc immobilization. However, the reoxidation mechanism(s) remain largely unknown. Greater understanding of the reoxidation mechanisms in technetium sulfide is critical to its long-term stability and application as a waste form and storage media.[1] To prepare Tc sulfides for study, limited reported synthetic routes warrant new ways to prepare these materials which has been explored in this project using the Boron-Chalcogen Mixture (BCM) method.[2, 3]

The exploration of extended structure Tc materials gives critical knowledge about the coordination environments of Tc especially due to the amorphous nature of the binary compounds which makes characterization difficult. New crystalline Tc compounds can be synthesized from Tc oxides using the BCM method. Preparing single crystalline products will allow for facile characterization by single crystal X-ray diffraction (SXRD). The synthesis of extended structure Tc materials will give insight to stable Tc materials that could be used to sequester Tc from solution.

Alloys and intermetallic compounds can be formed by the interatomic mixing of the monometallic components. These present a class of materials with tunable composition and properties.[4,5] Exploring the synthesis of Re and Tc alloy synthesis will generate materials that can be exploited for Tc waste management applications.

Approach

A new synthetic approach to binary rhenium (Re) chalcogenides was developed to aid in the preparation of analogous technetium compounds for Tc waste management efforts. The BCM method was utilized for the first time to prepare polycrystalline powders of ReS_2, $ReSe_2$, and Re_2Te_5 using the perrhenate, NaReO4, as a rhenium source (**Figure 1**).

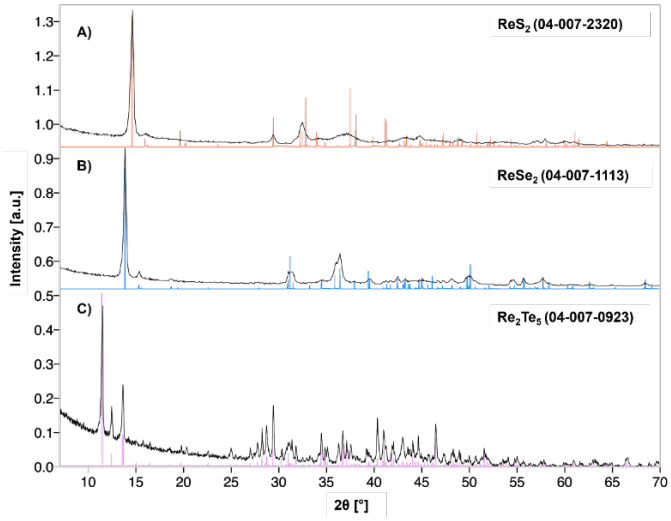

Figure 1. PXRD patterns for A) ReS2, B) ReSe2, and C) Re2Te5 overlaid with their calculated patterns.

Single crystals of ReS_2 were also synthesized using the combined BCM and molten flux methods by adding a K_2CO_3 flux to the reagent mixture (**Figure 2**). Thermal analysis using TGA/DSC revealed negligible changes from ambient temperature up to ~300 ◦C followed by the oxidation of the Re chalcogenides (**Figure 3 and 4**). High Temperature PXRD was used to investigate the crystallinity of ReS_2 at various temperatures revealing an increase in crystallinity up to 275 ◦C followed by a decrease in crystallinity due to oxidation (**Figure 5**).

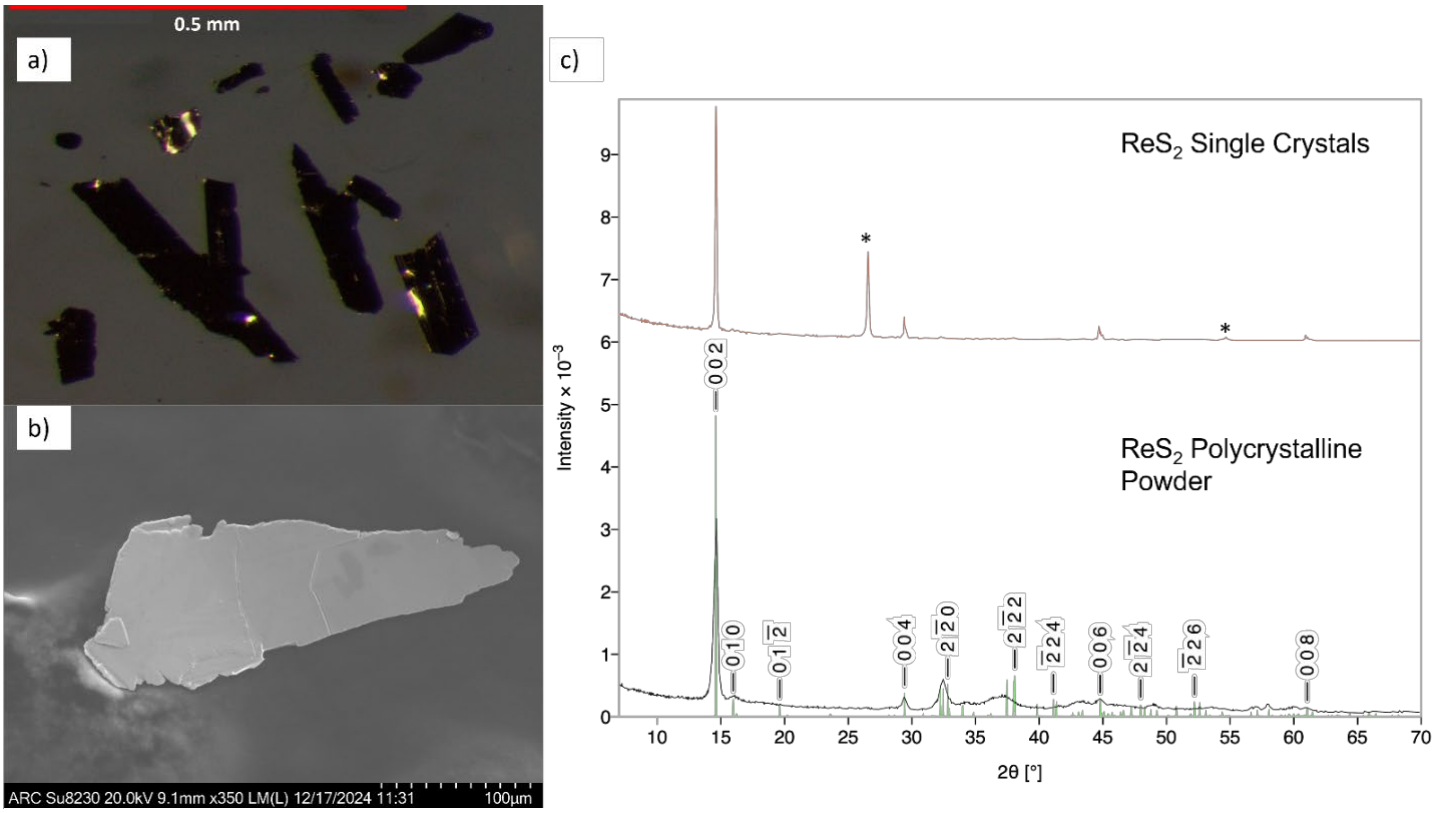

Figure 2. (a) Optical image and (b) SEM image of ReS2 crystals along with PXRDs of the (c) single crystal product (red pattern) and polycrystalline powder (black pattern) overlayed with the ReS2 calculated pattern. Graphite inclusion, denoted by *, in the PXRD is from the graphite crucible used for synthesis.

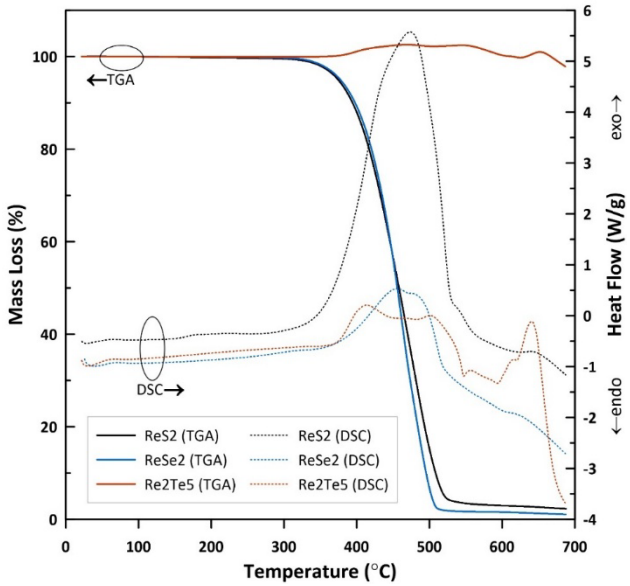

Figure 3. TGA/DSC curves of ReS2, ReSe2, and Re2Te5.

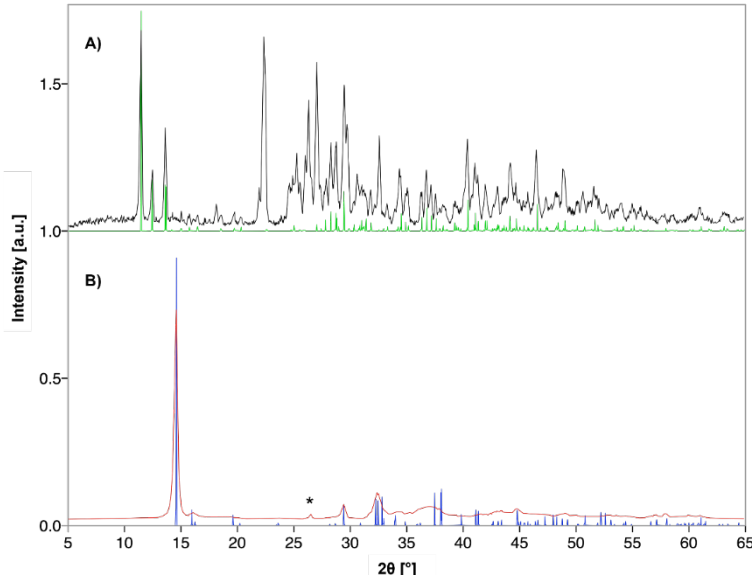

Figure 4. PXRD patterns of the products obtained from (A) Re2Te5 heated in the TGA/DSC to 525 °C and from (B) ReS2 heated in the TGA/DSC to 425 °C overlaid with their calculated patterns. Graphite inclusion, denoted by *, in the PXRD is from the graphite crucible used for synthesis.

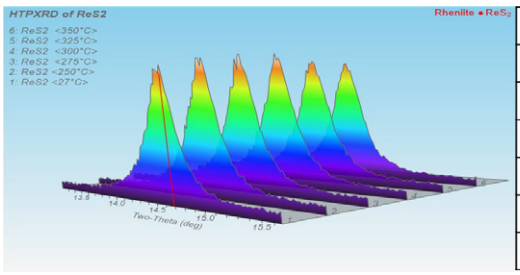

Temperature (°C)	FWHM (°)	Height (counts)	Peak Area
27	0.37	1318.5	573.7
250	0.366	1375.7	592.2
275	0.355	1397.5	584
300	0.356	1385.9	579.7
325	0.369	1283.4	556.6
350	0.338	1239	492.5

Figure 5. (left) High temperature PXRD patterns of ReS2 measured in air and (right) values for the Full-Width-Half-Max (FWHM) of the peaks, peak areas, and peak height for various temperatures obtained using the MDI JADE software.

This research on the combination of the BCM and molten flux methods resulted in a publication demonstrating a significant step towards technetium waste treatment efforts. The BCM method was further used to synthesize and structurally characterize single crystalline ternary rhenium chalcogenides, $Na_2Re_3S_6$ and $Na_2Re_3Se_6$ (**Figure 6**). This refined the crystal structure of $Na_2Re_3S_6$ and allowed for the first-time crystal structure determination of $Na_2Re_3Se_6$. We have also synthesized a series of mixed anion compounds with the formula $Na_2Re_3S_ySe_x$. The structure solution of this series is ongoing. Investigation into intermetallic compounds containing Tc can result in new materials with desired properties for waste management. Single crystals of new Re containing intermetallic were synthesized using the metallic flux technique (**Figure 7**).

This work, and future work, has been greatly accelerated due to the approval and use of a dedicated fused silica tube sealing system that was installed as part of this project in SRNL (**Figure 8**).

Accomplishments and results

- Flame sealing of fused silica tubes now active at 999-1W
- Investigated the thermal properties of ReS_2 and Re_2Te_5 using combined TGA/DSC
- Investigated oxidation mechanism of ReS_2 and Re_2Te_5 by probing intermediate products in the TGA/DSC measurements

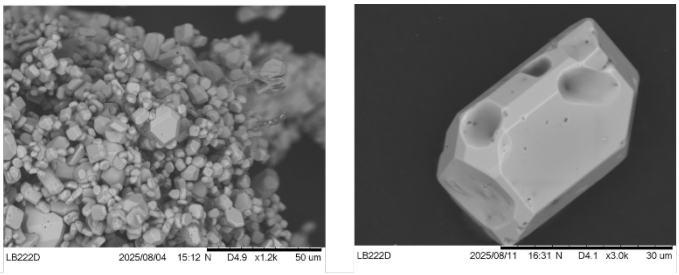

Figure 7. SEM images of a novel Re containing intermetallic compound grown using the metallic flux method.

Figure 8. Image of the fused silica tube sealing station.

- Synthesized single crystals of ReS_2 using the combined BCM method and molten flux growth methods
- Performed high temperature PXRD on ReS_2 sample to investigate increase in crystallinity with temperature

$Na_2Re_3S_6$ Structure

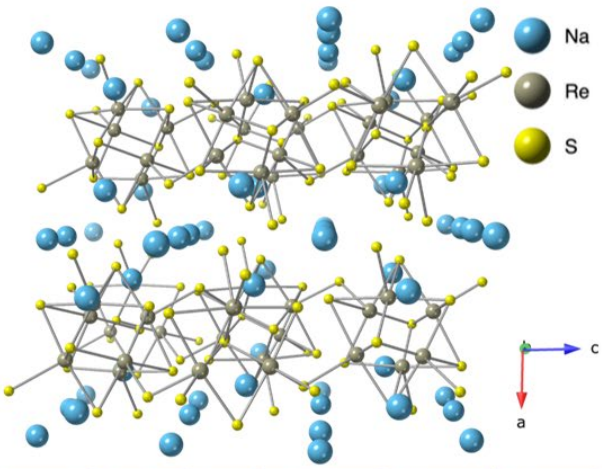

Compound	Crystal System	Space group	a,b,c (Å)	β (°)	Cell volume (Å³)	R-value
$Na_2Re_3S_6$	Monoclinic	C2/c	15.8529(2), 9.60530(10), 11.49700(10)	92.5930(10)	1748.88(3)	2.41%
$Na_2Re_3Se_6$			16.5316(4), 9.9699(3), 11.9560(3)	92.344(2)	1968.92(9)	2.25%

$Na_2Re_3S_6$ Clusters **$Na_2Re_3Se_6$ Clusters**

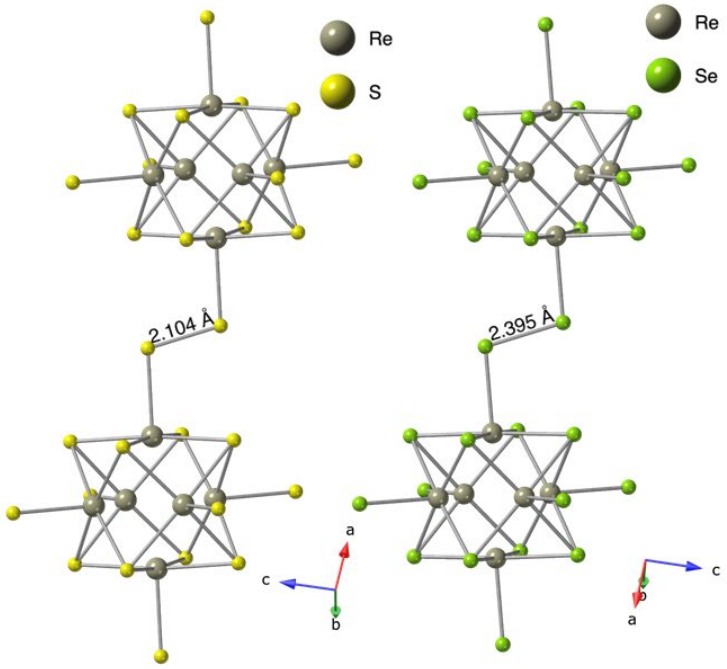

Figure 6. The crystal structures and crystallographic parameters of $Na_2Re_3S_6$ and $Na_2Re_3Se_6$.

- Published findings in Solid State Sciences
- Synthesized single crystalline $Na_2Re_3Se_6$ using the BCM method
- Solved the single crystal structure of $Na_2Re_3Se_6$ for the first time
- Synthesized series of novel mixed anion $Na_2Re_3S_ySe_x$ single crystals using the BCM method
- Synthesized novel Re containing intermetallic compound using the metallic flux technique

Peer-reviewed Publications

- Logan S. Breton; Jake Amoroso, Synthesis and characterization of rhenium chalcogenides for nuclear waste management, *Solid State Sciences*, 167, **2025**, p. 107988.*
- Won the American Chemical Society recognition of excellence award for leadership in research safety.
- Logan S. Breton; Jake Amoroso, Synthesis and characterization of rhenium chalcogenides for nuclear waste management, ACS Fall 2025, Oral Presentation.

Team Members

Logan S. Breton*
Jake Amoroso

**Laboratory Director's Postdoctoral Research Fellow*

References

1. Pearce, C. I.; Icenhower, J. P.; Asmussen, R. M.; Tratnyek, P. G.; Rosso, K. M.; Lukens, W. W.; Qafoku, N. P. Technetium Stabilization in Low-Solubility Sulfide Phases: A review. *ACS Earth and Space Chemistry* **2018**, *2* (6), 532–547. https://doi.org/10.1021/acsearthspacechem.8b00015.
2. Breton, L. S.; Klepov, V. V.; Loye, H.-C. Z. Facile oxide to chalcogenide conversion for actinides using the Boron–Chalcogen mixture method. *Journal of the American Chemical Society* **2020**, *142* (33), 14365–14373. https://doi.org/10.1021/jacs.0c06483.
3. Ferrier, M.; Kerlin, W. M.; Poineau, F.; Sattelberger, A. P.; Czerwinski, K. R. Recent developments in the synthetic chemistry of technetium disulfide. *Dalton Transactions* **2013**, *42* (44), 15540. https://doi.org/10.1039/c3dt52079j.
4. Pandey, S.; Koch, R. J.; Li, G.; Misture, S. T.; Wang, H.; Phillpot, S. R. Thermodynamics and kinetics of ordered and disordered Cu/Au alloys from first principles calculations. *Journal of Alloys and Compounds* **2019**, *809*, 151615. https://doi.org/10.1016/j.jallcom.2019.07.327.
5. zur Loye, H.-C.; Besmann, T.; Amoroso, J.; Brinkman, K.; Grandjean, A.; Henager, C. H.; Hu, S.; Misture, S. T.; Phillpot, S. R.; Shustova, N. B.; Wang, H.; Koch, R. J., Morrison, G.; Dolgopolova, E. Hierarchical Materials as Tailored Nuclear Waste Forms: A Perspective. *Chemistry of Materials* **2018**, 30, 4475-4488. https://doi.org/10.1021/acs.chemmater.8b00766.

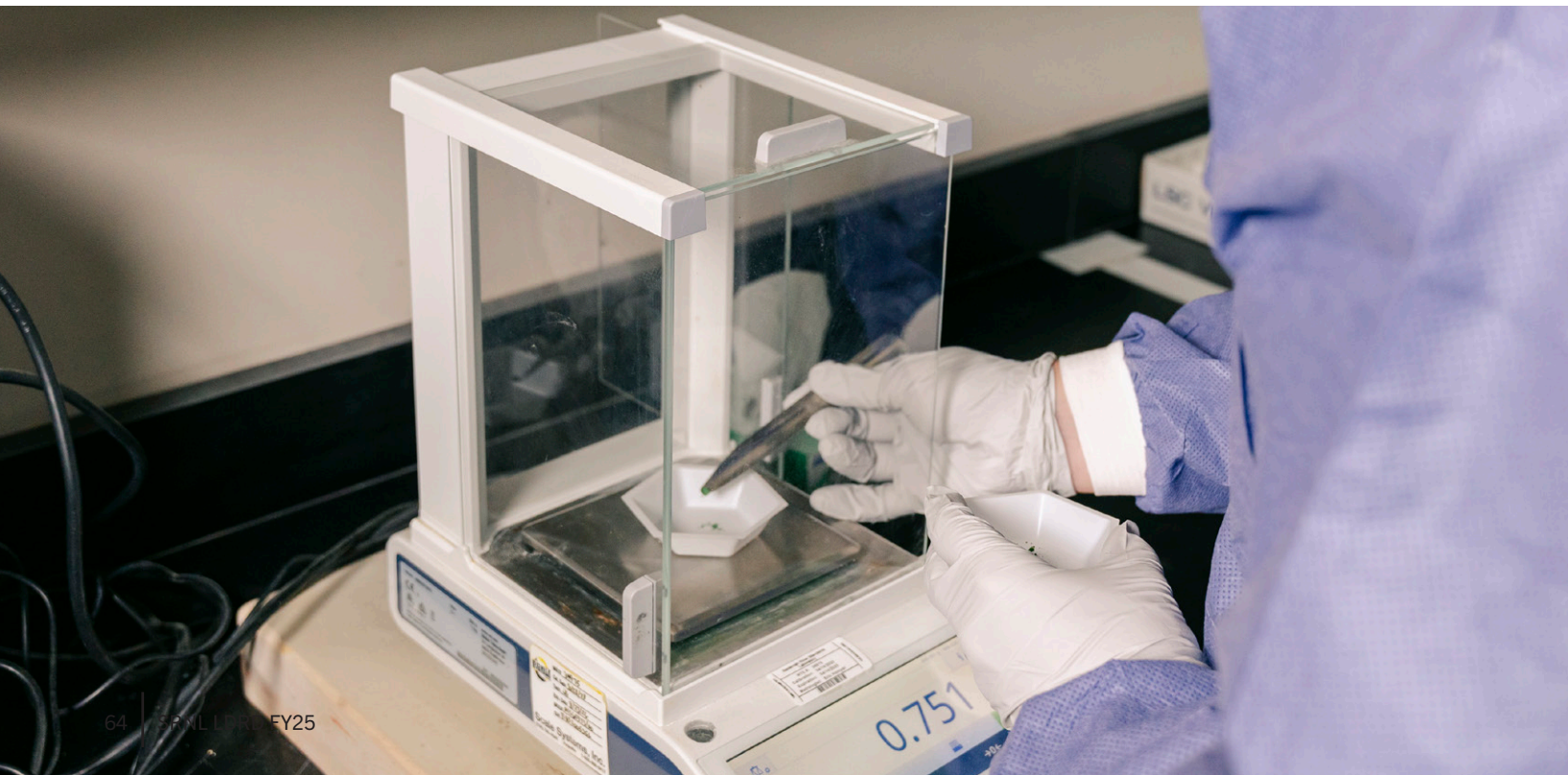

High Entropy Alloy Nanoparticles for Catalysis

Matt Craps

High entropy alloys are an exciting class of new catalysts composed of five or more elements in roughly equal amounts. These alloys often outperform even the best monometallic catalysts. We are using a microwave route to synthesize high entropy alloy nanoparticles directly onto a carbon support suitable for catalysis.

Introduction

Advanced research to develop novel catalysts is necessary to improve their performance and lessen the use of expensive and rare metals. High entropy alloys (HEAs) have been demonstrated to show remarkable catalytic performance with lower cost materials. HEAs are solid solutions composed of five or more elements in roughly equal amounts (**Figure 1a**). Often HEAs outperform the sum of their individual components due to synergistic effects. This is caused, in part, by the different sizes of each element. These differences lead to lattice distortion (**Figure 1b**), creating a strained and reactive catalytic surface. The co-location of different elements on the surface also leads to a wide mix of active sites with unique binding energies and electronics. The varied binding energy differences are especially key for multistep reactions where a monometallic catalyst would only have active sites designed for a specific elementary step. Despite their impressive catalytic properties, a real problem in the HEA field is the vast compositional space that HEAs occupy. While there are only 66 naturally occurring metals to choose from and test, the number of combinations quickly ballons to over a billion for systems of five metals. Therefore, rational decision making in alloy composition and high-throughput testing are key.

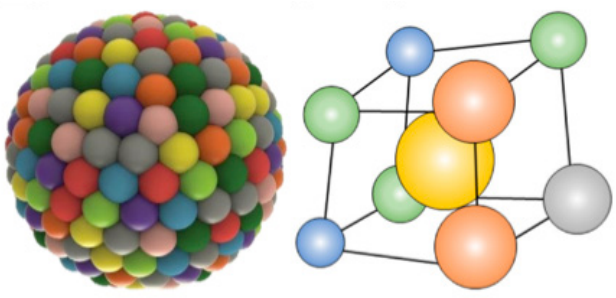

Figure 1. (a) High entropy alloy (HEA) particle with each color representing a different element. (b) HEA crystal structure displaying lattice distortion from varying atomic sizes.

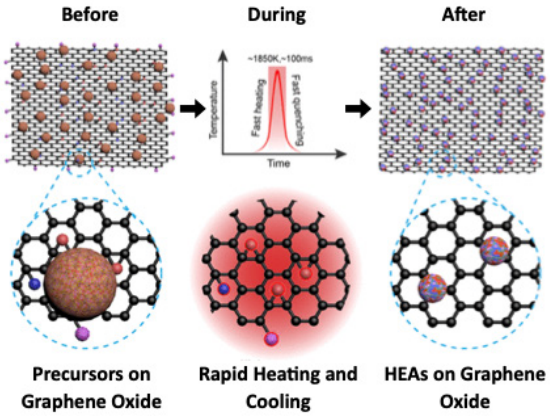

Figure 2. Synthesis scheme of high entropy alloys, showing the state before (left), during (center), and after (right) microwave heating.[1]

Approach

Due to the vast number of elemental combinations that can be made, high-throughput testing is advantageous. In our lab we use a high-throughput microwave synthesis to induce nanoparticle formation.[1] Metal salts are dried onto a graphene oxide support, which is then microwaved for a few seconds (**Figure 2**). The microwave energy causes rapid heating of the salt precursors, causing metal reduction and alloy formation. The localized heating results in hot spots where particles form. The HEA nanoparticles, synthesized directly on a carbon support can be further characterized and tested as catalysts. Electron microscopy is used to image the nanoparticles and determine size, shape, distribution, etc. (**Figure 3**). Energy dispersive X-ray spectroscopy allows for elemental composition determination and locations of each element. Powder X-ray diffraction gives crystal phase information ensuring it is a one-phase alloy system. Catalytic reactions being explored include ammonia decomposition and selective catalytic reduction of N_2O, supporting Hanford tank waste off-gas treatment system. The microwave synthesis method allows for a variety of

metals to be utilized. Current alloying elements include noble metals (e.g. gold, ruthenium, and platinum), first row transition metals (e.g. vanadium, cobalt, and nickel), main group metals (e.g. aluminum and tin) and refractory metals (e.g. tungsten and molybdenum).

Accomplishments

- Synthesized various target HEA compositions including PtRuVCoNi, CoMoGaMnAl, PtPdFeCoNi, PtPdVFeCe, AuPdCuZnGa.
- Initial unoptimized oxidative dehydrogenation of ethane catalysis results show promising data (76% ethane conversion and 71% selectivity for ethylene at 700 °C).
- Explored gas phase catalytic reactions including ethane dehydrogenation, CO_2 reduction, ammonia decomposition and selective catalytic reduction of N_2O.
- Installed flow cell reactor to allow microwaving under inert gas flow.
- Scaled synthesis up 50x to gram-scale quantities.
- Contracts with North Carolina State University and Clemson University for advanced electron microscopy characterization.
- Presented eight posters: Gordon Research Conference, Gordon Research Seminar, Southeastern Regional Meeting of the American Chemical Society, Southeastern Catalysis Society, SRNL Day at Georgia Institute of Technology, SRNL Day at the University of South Carolina, Summer intern poster session, and LDRD Poster Session.
- Matt Gordon awarded the 2025 ACS PROF Leadership Development Award.

Peer-reviewed Publications

- Mueller, M.; Chau, H.; Stofik, S.; **Gordon, M. N.**; Fushimi, R.; Lauterbach, J.; **Craps, M.**; Rodene, D. D.; Aidhy, D. S. High entropy alloys as catalysts: A focused review. *Materials Letters* **2025**, *400*, 139114.
- Chau, H.; Stofik, S.; **Gordon, M. N.**; Mueller, M.; Fushimi, R.; Aidhy, D. S.; **Craps, M.**; Lauterbach, J.; Rodene, D. D. Advancements in Abating Nitrous Oxide Emissions: A Review of Direct Catalytic Decomposition and Selective Catalytic Reduction Reactions. *Submitted**

Team Members

Matt Gordon*, Matt Craps
**Laboratory Director's Postdoctoral Research Fellow*

References

1. Qiao, H.; Saray, M. T.; Wang, X.; Xu, S.; Chen, G.; Huang, Z.; Chen, C.; Zhong, G.; Dong, Q.; Hong, M.; Xie, H.; Shahbazian-Yassar, R.; Hu, L. Scalable Synthesis of High Entropy Alloy Nanoparticles by Microwave Heating. *ACS Nano* **2021**, 15, 14928–14937.

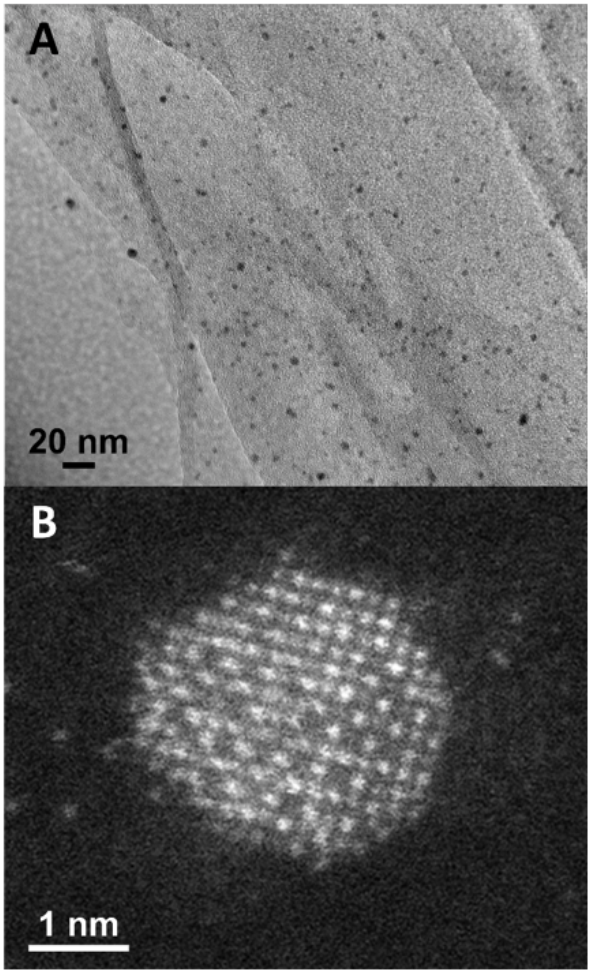

Figure 3. (a) Transmission electron micrograph of PtRuVCoNi HEA nanoparticles on graphene oxide. (b) Scanning transmission electron micrograph of an PtPdFeCoNi HEA nanoparticle.

Development of Novel Methods for the Detection of Organo-I129 Species at SRS Using Ultra-High Resolution Mass Spectrometry

Caroline Granger

Iodine-129 is a top 3 risk driver at the Savannah River Site but the exact composition of organo-I129 is an understudied topic. This work focuses on developing a method for the detection of organo-I129 species using ultra-high resolution mass spectrometry to provide a better understanding of I-129 migration and fate in the environment.

Introduction

Iodine-129 (I-129) is one of the top risk drivers at the Savannah River Site (SRS) due to its high bioaccumulation factor in the thyroid (90%), high toxicity, long half-life (15.7 million years), and high mobility in the environment.[1] Iodine exists as either iodide (I-), iodate (IO_3-), or organo-I129 and its speciation largely impacts its mobility under environmental conditions. Recent monitoring data has indicated that wetlands are not only a sink but can also act as a source, releasing I-129 into surface waters. Despite organo-I species comprising a substantial fraction of total iodine (up to 90%)[2], current methods at SRS do not directly measure organo-I129 because of the complexity associated with iodine speciation and analytical method levels of detection. In this project, ultra-high resolution mass spectrometry was used to analyze standards and simulated surface water samples extracted using XAD-7HP resin. Samples were shipped to Georgia Tech for analysis using Fourier transform - ion cyclotron resonance - mass spectrometry (FT-ICR-MS) because of its unparalleled resolving power and mass accuracy. FT-ICR-MS data enables scientists to use exact mass data to assign molecular formulas to determine structures of organo-I129 which will give insight into the mobility of the species in the environment based on their properties (e.g., molecular weight, functional groups, predicted soil adsorption coefficient, etc.). This research will provide a better understanding of I-129 migration and fate in the environment, allow for the development of improved attenuation-based strategies that would target different iodine species, and aid in the recalculation of site risk models to achieve alternative concentration levels for I-129.

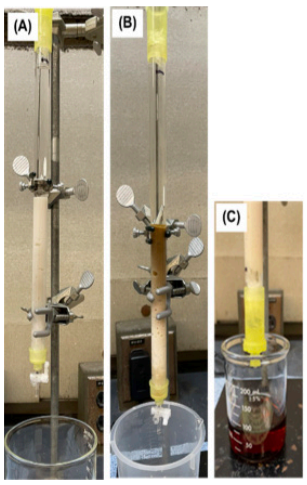

Figure 1. Glass columns packed with resins (A) before sample loading, (B) after sample loading, and (C) the eluate after a basic rinse.

Approach

Fulvic acid (FA) was extracted from aqueous samples based on a resin (XAD-7HP) adsorption method developed by the International Humic Substances Society (IHSS, **Figure 1**).[3] This method is regarded as the gold standard for this area of research and has been widely used by research institutions for decades. Research efforts in this study focused on extracting and analyzing fulvic acid because it is known to incorporate I-129 and is mobile in the environment due to it solubility across a wide pH range.[4] The exact composition of FA varies depending on source and isolation methods, but it can be broadly categorized as a mixture of relatively low molecular weight organic molecules consisting primarily of carbon (C), hydrogen (H), and oxygen (O). Due to the complexity of organo-I129 species, SRNL collaborated with Georgia Tech to utilize their FT-ICR-MS to provide exact mass data. The accurate mass data was then processed using the SmartFormula™ algorithm (Bruker Daltonik) to generate a list of elemental formulas (S/N threshold ≥ 4, only considering C (unlimited), H (unlimited), and O (< 30). The resulting data (**Figure 2**) was imported into PyKrev, a Python library designed to aid in the visualization of FT-ICR-MS data.[5] Results from the analysis of FA standards revealed that the average molecular weight was 483 m/z (**Figure 3**) and O/C and H/C ratios on the van Krevelen plot were indicative of lignin and tannin-like compounds (**Figure 4**).

Accomplishments

- Investigated and implemented a successful extraction technique for fulvic and humic acids from aqueous samples
- Performed FT-ICR-MS optimization (e.g., solvent, flow rate, scan range, resolving power, average scans, ion accumulation time, and excitation)
- Preprocessed raw data from about 18,000 peaks to 1,500 peaks using Bruker software
- Performed extensive data analysis on samples and generated van Krevelen plots and average molecular weight histograms using PyKrev.

Peer-reviewed Publications

- Publications are under development. To be submitted to *ES&T*.

Team Members

Hansell Gonzalez-Raymat[a], Holly VerMeulen[a], Stephanie Gamble[a], Joseph Mannion[a], Facundo Fernández[b], Albert Herrera[b*]

[a]*Savannah River National Laboratory*

[b] *Georgia Institute of Technology*

[*]*Postdoctoral Researcher*

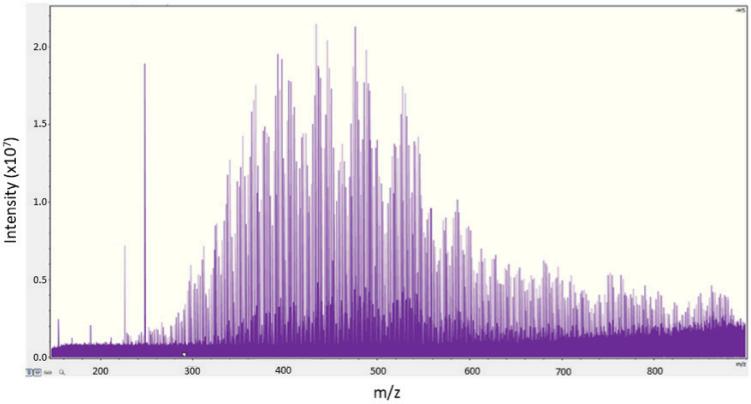

Figure 2. Mass spectrum of a fulvic acid standard analyzed using ESI(-) FT-ICR-MS.

References

1. Kaplan, D.I.; Denham, M.E.; Zhang, S.; Yeager, C.; Xu, C.; Schwehr, K.A.; Li, H.P.; Ho, Y.F.; Wellman, D.; Santschi, P.H. Radioiodine Biogeochemistry and Prevalence in Groundwater. *Crit. Rev. Environ. Sci. Technol.* **2014**, *44*, 2287-2335.
2. Otosaka, S.; Schwehr, K.A.; Kaplan, D.I.; Roberts, K.A.; Zhang, S.J.; Xu, C.; Li, H.P.; Ho, Y.F.; Brinkmayer, R.; Yeager, C.; Santschi, P.H. Factors Controlling Mobility of 127I and 129I Species in an Acidic Groundwater Plume at the Savannah River Site. *Sci. Tot. Envion.* **2011**, *19*, 3857-3865.
3. Aiken, G.R.; McKnight, D.M.; Wershaw, R.L.; MacCarthy, P. (Eds.) Isolation and Concentration Techniques for Aquatic Humic Substances. Wiley-Interscience, New York, 1985.
4. Xu, C.; Chen, H.; Sugiyama, Y.; Zhang, S.; Li, H.-P.; Ho, Y.-F.; Chuang, C.-Y.; Schwehr, K.A.; Kaplan, D.I.; Yeager, C.M.; Roberts, K.A.; Hatcher, P.G.; Santschi, P.H. Novel Molecular-Level Evidence of Iodine Binding to Natural Organic Matter from Fourier Transform Ion Cyclotron Resonance Mass Spectrometry. *Sci. Total Environ.* **2013**, *449*, 244–252.
5. Kitson, E.; Kew, W.; Ding, W.; Bell, N.G.A. PyKrev: A Python Library for the Analysis of Complex Mixture FT-MS Data. *J Am Soc Mass Spectrom.* **2021**, *32*, 1263-1267

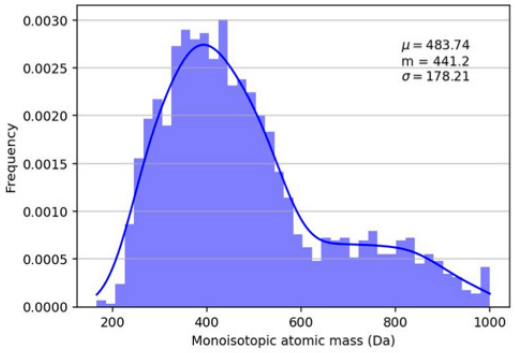

Figure 3. Histogram of monoisotopic masses with an overlaid line depicting the probability density function estimated via Gaussian kernel density.

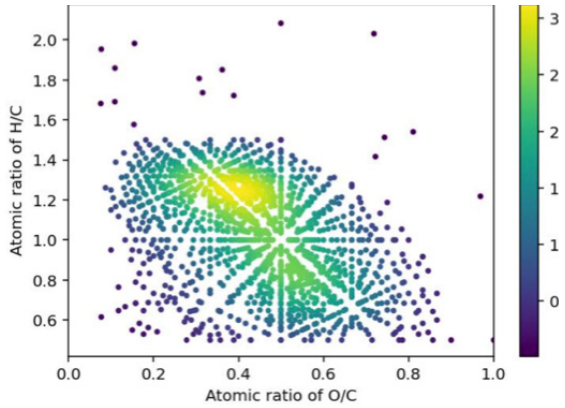

Figure 4. Van Krevelen scatter plot with formulas colored by Gaussian kernel density estimation.

PFAS and Fluoropolymer Exposure and Toxicity to Nematodes

Stephanie Jacobs

In this work we investigated the toxicity of per-and poly-fluoroalkyl substances and fluoropolymers in the nematode species *Caenorhabditis elegans* through different exposure mechanisms. Soil invertebrates, such as nematodes, may be exposed via multiple pathways and the exposure mechanism may have significant impact on toxicology.

Introduction

Currently, the body of work of PFAS studies are ad hoc and typically only considers a few PFAS overall and generally does not consider size of the molecule or the exposure route. As such, very little data has been generated for the toxicology of fluoropolymers. In this work, we consider not only the size of the non-polymer PFAS particle itself, but also the route of exposure for both PFAS and fluoropolymers. For the non-polymer PFAS, molecules of differing sizes and geometries were selected (See **Figure 1**). The mechanisms for exposure were also considered including a direct exposure on a solid surface, exposure in an aqueous environment, and exposure via a contaminated food source.

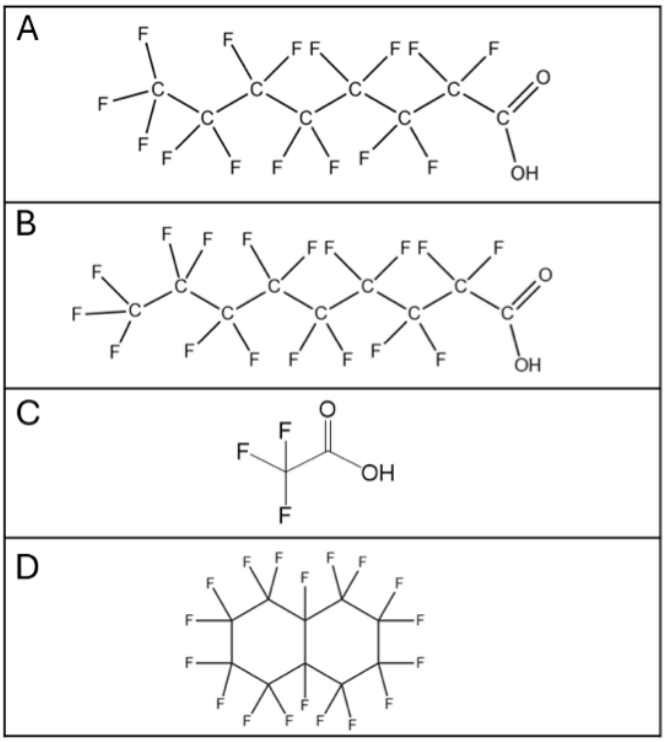

Figure 1. PFAS used in this work. A) Perfluorooctanoic acid, B) Perfluorononanoic acid, C) Trifluoroacetic acid, D) Perfluorodecalin.

A large gap in research is the lack of data regarding the toxicity of fluoropolymers on any species and with any factors considered. Here, three fluoropolymers are considered for their contributions to toxicity. These fluoropolymers are commonly utilized in commerce and have various pathways into the environment. Fluoropolymers can enter the environment directly as microplastics that can be created through use of the product including environmental degradation, abrasion, manufacturing, etc. To confirm that the animal was able to consume the fluoropolymer products, a fluorosphere was utilized to visualize the consumption of the microplastic tagged with a fluorescent probe. Additionally, easily removable fractions of the building blocks can enter the environment through contact with water or other chemicals. Here, both the microplastic itself and the easily removable fraction is investigated for its toxicity in nematodes.

Approach

Investigation of the effects of PFAS and fluoropolymers was conducted systematically. All experiments were conducted with a food source to avoid starvation effects. For each group, nematodes were counted at 24 ± 1 hours and 48 ± 1 hours.

Direct Exposure Experiments

For the direct exposure experiments, approximately 20-30 nematodes were plated into individual wells on solid nematode growth media. Approximat ely 50 µL of the liquid PFAS (0.25 mM, 0.50 mM, 1mM, 2 mM, 5mM, 10 mM, 25 mM, or 50 mM) or the fluoropolymer extracts (5 mg/ml, 10 mg/ml, 15mg/ml, 20 mg/ml) were placed into the wells (**Figure 2**A).

Exposure in Aqueous Media

Approximately 20-30 nematodes were placed into individual wells with liquid nematode growth media, and PFAS was added to the solution to the prescribed final concentrations (0.25 mM, 0.50 mM, 1mM, 2 mM, 5mM, 10 mM, 25 mM, or 50 mM) (**Figure 2**B). For the fluoropolymer solids, 1 mg, 3 mg, 5 mg, or 10 mg of size separated particles were added to the liquid nematode growth media (**Figure 2**C). For the fluoropolymer extract experiments, extracts were added to 25% and 50% of each of the prescribed concentrations.

Food Source Exposure Experiments

Bacteria were grown overnight in the presence of PFAS. The bacteria were rinsed 3x to remove free PFAS. The bacteria were then placed on peptone-free (to avoid proliferation) solid nematode growth media. Then, approximately 20-30 nematodes were placed on the media and allowed to stay throughout the duration of the experiment (**Figure 2**.D). for function. Test results improve the design iteratively.

Accomplishments

Toxicology of non-polymer PFAS

- Toxicology via the direct contact pathway had higher toxicity levels than the food source pathways indicating that the direct contact of PFAS via the cuticle of the nematode contributed more to the toxicology than the food consumption pathway (**Figure 3**).
- Perfluorononanoic acid (PFNA) was the most toxic PFAS ($LC50_{48\ hr}$ on solid matrix: 7.33 mM, $LC50_{48\ hr}$ in aqueous media: 0.18mM, and $LC50_{48\ hr}$ in food source: 2.90 mM) tested (**Figure 3**). This aligns with other data that indicates toxicity increases with increasing chain-length.
- On the solid matrix, the perfluorooctanoic acid (PFOA) and PFNA had higher LC50 values (PFOA $LC50_{48\ hr}$: 7.33 mM, PFNA: $LC50_{48\ hr}$: 0.71 mM, **Figure 3**A) than in the aqueous matrix values (PFOA $LC50_{48\ hr}$: 0.73 mM, PFNA: $LC50_{48\ hr}$: 0.18 mM, **Figure 3**B).
- Trifluoroacetic acid had the highest LC50 in the aqueous solution ($LC50_{48\ hr}$: 15.23 mM) than the other three PFAS tested indicating the lowest toxicity (**Figure 3**B). Additionally, the $LC50_{48\ hr}$ was higher than the $LC50_{48\ hr}$ for PFOA and PFNA in the food source (**Figure 3**C). This may be due to the ability of the animal to remove trifluoroacetic acid from the body using similar mechanisms to eliminate other toxic materials and wastes.
- Perfluorodecalin was the least toxic when the exposure route was a food source ($LC50_{48\ hrs}$: 112.39 mM, **Figure 3**C). This may be due to the inability of the bacteria to efficiently consume the perfluorodecalin due to its size and hydrophobicity. and the 2025 ANS Annual Conference.

Fluoropolymer Toxicology

- The fluoropolymer extracted fraction did demonstrate some toxic effects on a solid matrix, but it was significantly less than in the aqueous matrix (**Figure 4**).
- The polyvinylidene fluoride (PVDF) and polytetrafluoroethylene (PTFE) microplastics did show a mild particle-size effects in the toxicology of solid particles in a liquid matrix (**Figure 5**).
- Small differences in toxicity were observed in the weight of fluoropolymers in aqueous solutions used for the studies. This may be due to the observation that the fluoropolymer microplastics were not immersed in the liquid nematode growth media and all of the mass may not have been in contact with the nematodes (**Figure 5**).
- Energy-dispersive X-ray spectroscopy (EDS) mapping was performed on the PTFE particles. They were found to be consistent in elemental distribution (**Figure 6**).

Team Members

Courtney Burckhalter, Simona Murph

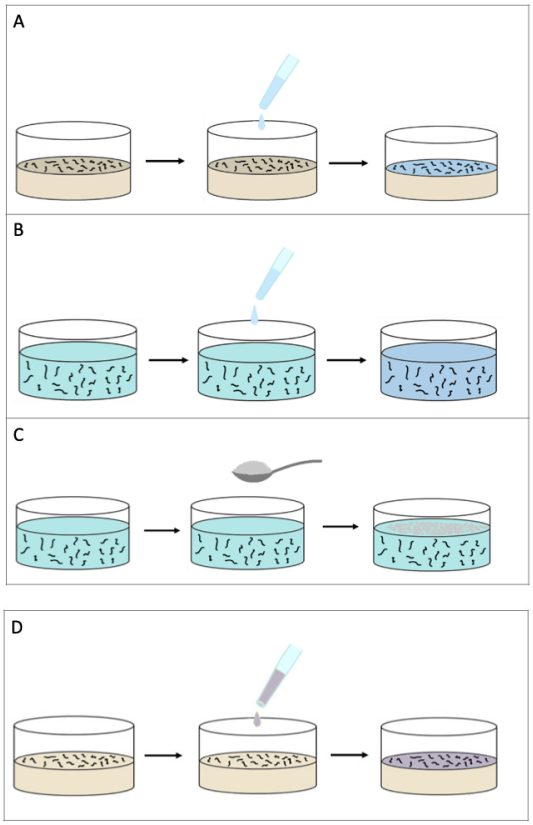

Figure 2. Schematics for the methodology of the PFAS and Fluoropolymer Exposures. A) Graphical procedure for the application of the liquid PFAS, or the liquid fluoropolymer extract to the solid nematode growth media. B) Application of the liquid PFAS to an aqueous environment. C) Graphical procedure for the addition of the size separated fluoropolymer microplastics to the liquid nematode growth media. D) Graphical procedure for the addition of a food source exposed to PFAS.

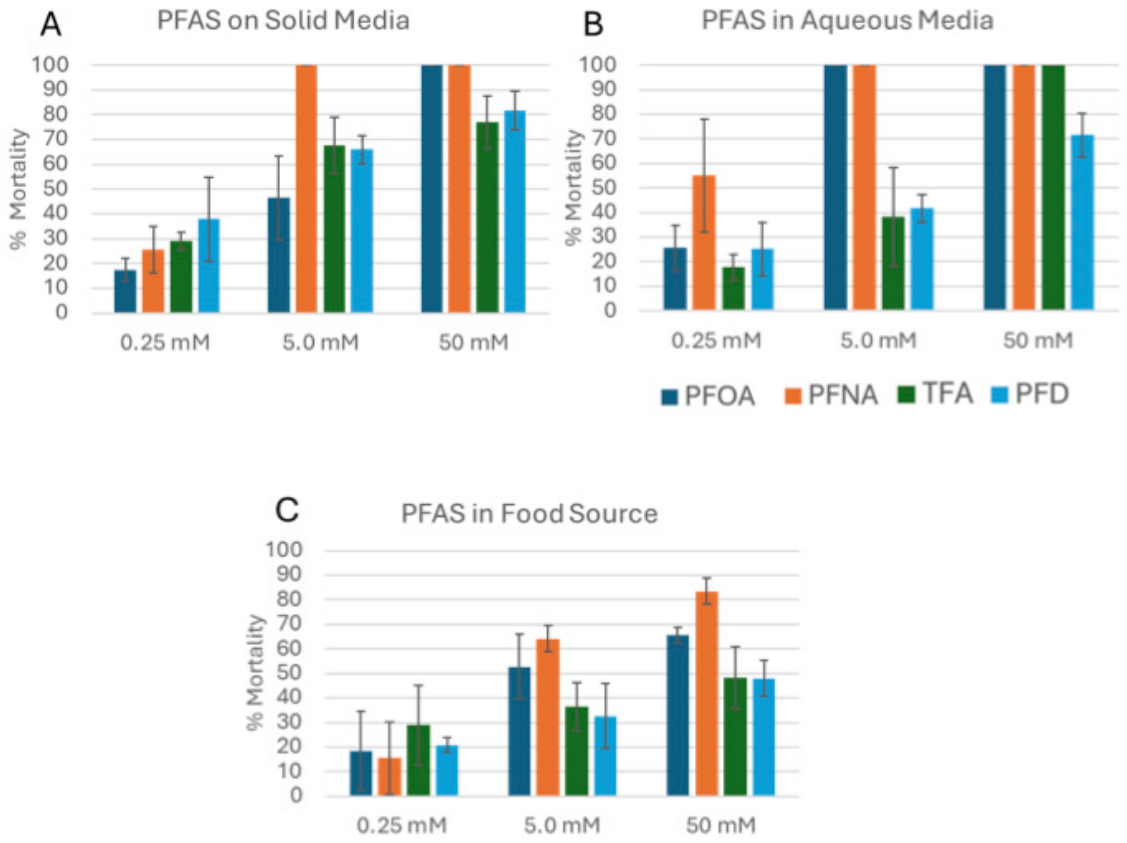

Figure 3. Toxicology of non-polymer PFAS A) On solid media, B) In aqueous media, C) In the bacteria food source.

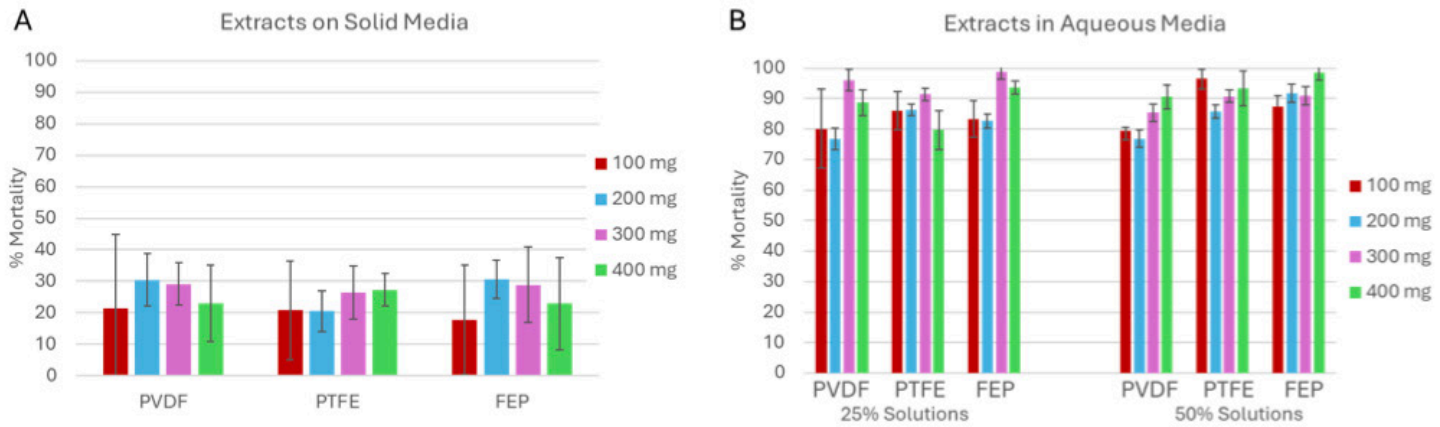

Figure 4. Toxicology of Fluoropolymer Extracts A) On solid media, and B) In aqueous media. The mortality rates of the extracts on solid media are significantly less than the mortality rates of 25% and 50% solutions in liquid media.

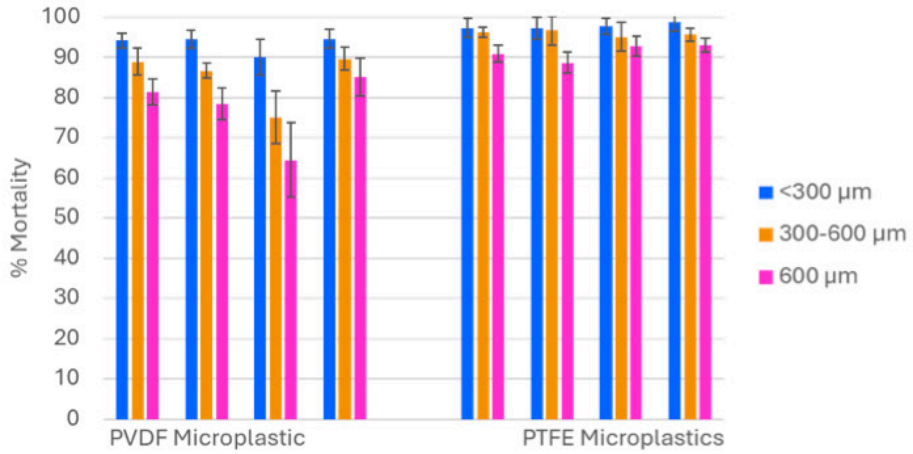

Figure 5. Toxicology of Two Fluoropolymer Microplastics Separated by Size.

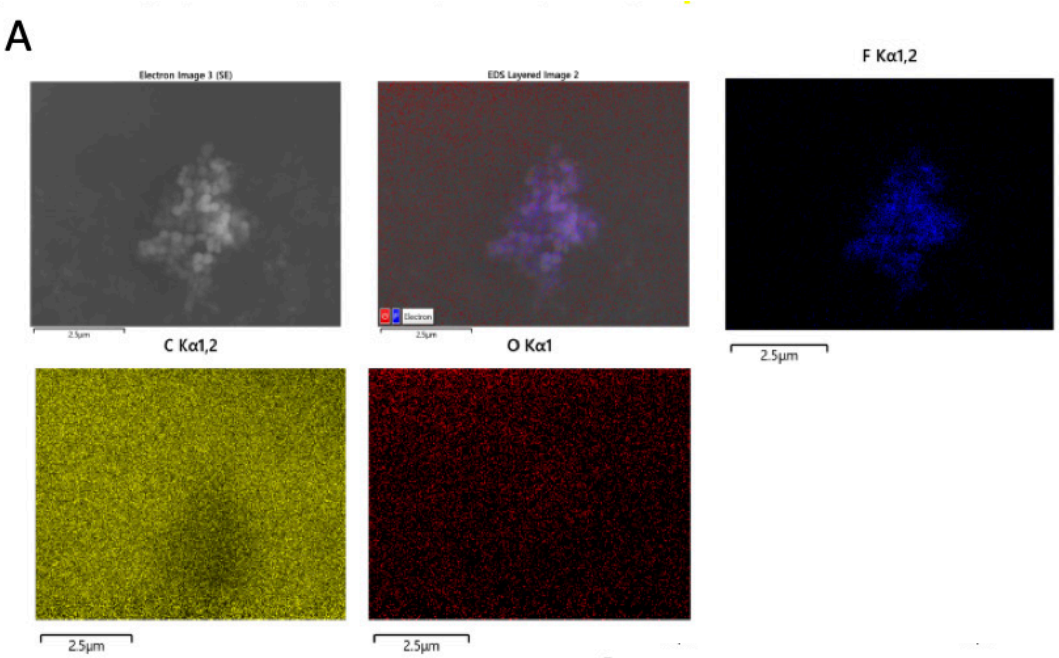

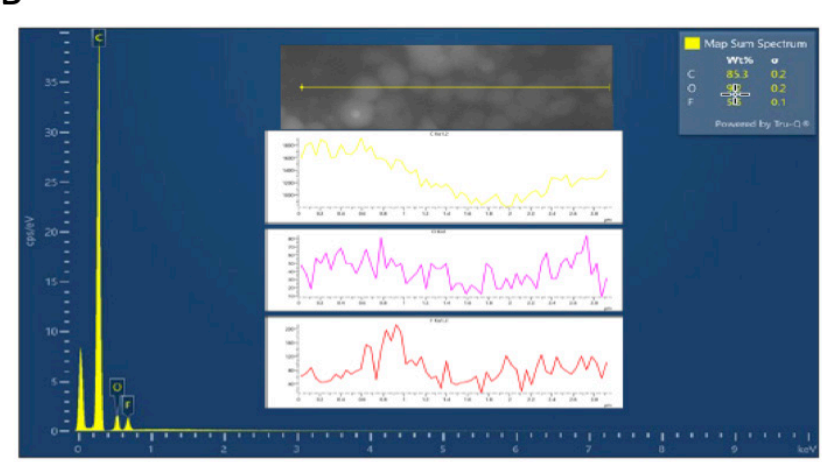

Figure 6 A) Representative EDS mapping showing the uniformity and purity of the PTFE nanoparticles confirming their consistency. B) The detailed line scan analysis detailing the nanoparticle composition.

Cementitious Remediation of Acid Mine Drainage

Cory L. Trivelpiece

Acid mine drainage (AMD), a byproduct of abandoned and active mines, poses significant environmental hazards, including water pollution, harm to aquatic life, and contamination of drinking water sources, risking human and ecosystem health. We developed passive AMD remediation technology using recycled concrete aggregate from landfills.

Introduction

Acid mine drainage is created by the interaction of water and oxygen with sulfide-bearing materials – this phenomenon is most commonly associated with mining operations that increase the exposure of these types of rock formations to the environment[1]. AMD is an acidic solution containing metals like iron, aluminum and manganese, and other toxic elements such as arsenic, cadmium, and lead[2]. The effects of AMD can be far reaching, ranging from increased turbidity all the way to the death of sensitive species[3].

There are active and passive approaches to remediating AMD. Active systems are highly efficient at decontaminating affected waters. However, these facilities require large capital investments and constant monitoring and maintenance. Additionally, most sources of AMD are located in remote areas that make building and powering active filtration facilities difficult. Passive systems rely on natural processes to remediate and filter contaminated water – these may include the use of adsorbents, natural filters, or biology. In this work, we are advancing passive remediation using recycled concrete aggregate (RCA).

At present, most passive AMD treatment systems utilize raw materials that must be mined (e.g., limestone), harvested (e.g., biological and/or organic materials), or are otherwise not geographically ubiquitous (e.g., alkaline steel slag). Our method using RCA is rooted in circular economics and takes advantage of the widespread availability of the material and the alkalinity of the constituent materials. The environmental durability of RCA in near neutral conditions means that we can recover these materials from landfills and valorize them into AMD remediation media.

Approach

Our approach in Year 1 of the proposed work focused on designing the apparatuses needed to conduct AMD remediation measurements, determining the ability to grow microbial cultures in the presence of RCA and AMD, and establishing a framework geochemical model from which we can scale our laboratory results into real-world simulations (**Figure 1**).

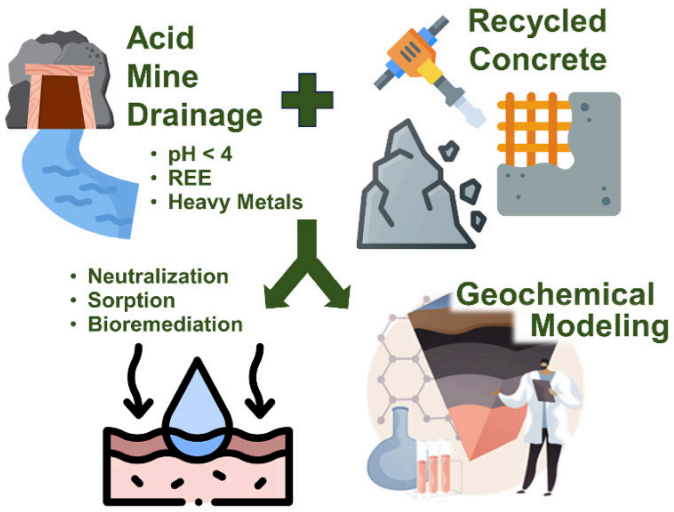

Figure 1. Our approach uses RCA to neutralize and remove harmful contaminants from AMD. We are combining lab-scale experiments with geochemical modeling to simulate real world examples.

In terms of remediation experiments, we initially determined the composition for an AMD simulant based on a literature survey of historical data as shown in **Figure 2**. We then utilized static testing to get baseline parameters for neutralization and sorption thermodynamics and kinetics. The static testing consisted of measuring the neutralization of AMD under varying conditions – we repeated these conditions in static sorption tests for lead and cadmium using "spiked" versions of the AMD simulant. We constructed a dynamic testing platform utilizing a novel approach to monitoring in which we could measure the real-time neutralization and adsorptive capacity of the RCA under varying conditions by using ion-selective electrodes (ISE) and pH meters downstream of the test column.

We used the software Geochemist's Workbench™ (GWB) to develop a "static" model that reproduced the static neutralization experiments and provided geochemical parameters for additional transport modeling. A 1-D transport model has been constructed to model the dynamic testing and will continue to be optimized throughout the second year.

We also conducted biological growth experiments to determine the ability of microorganisms to survive on the surfaces and surrounding areas of AMD given the basic conditions (pH > 9).

Accomplishments

- Established the composition of the baseline AMD simulant based on historical references and synthesized approximately 10 L of the solution.
- Conducted static experiments to determine the neutralization (**Figure 3**) and sorption properties (**Figure 4**) of the materials based on varying parameters such as mass to volume ratio and particle size.
- Designed, fabricated, and tested an apparatus to conduct first-ever dynamic, real-time measurements of the neutralization and sorption capacities of RCA under varying conditions.
- Conducted initial dynamic testing to determine the breakthrough time of Cd-spiked AMD simulants under varying conditions (**Figure 5**).
- Developed geochemical models for simulating the interactions of the AMD with RCA in both static (**Figure 3**) and dynamic conditions.
- Established and performed initial quantification of biological growth on RCA by bacteria with known remediating capabilities (**Figure 6**).

Team Members

Will Jolin, Rich Wyrwas, Margaux Lavenue, Brinley Swanson, Ethan Pham, Benjamin Pershing, Elizabeth Tsekrekas*

**Postdoctoral Researcher*

References

1. (1) Akcil, A.; Koldas, S. Acid Mine Drainage (AMD): causes, treatment and case studies. *Journal of Cleaner Production* **2006**, *14* (12), 1139-1145. DOI: https://doi.org/10.1016/j.jclepro.2004.09.006.
2. (2) Simate, G. S.; Ndlovu, S. Acid mine drainage: Challenges and opportunities. *Journal of Environmental Chemical Engineering* **2014**, *2* (3), 1785-1803. DOI: https://doi.org/10.1016/j.jece.2014.07.021.
3. (3) Ighalo, J. O.; Kurniawan, S. B.; Iwuozor, K. O.; Aniagor, C. O.; Ajala, O. J.; Oba, S. N.; Iwuchukwu, F. U.; Ahmadi, S.; Igwegbe, C. A. A review of treatment technologies for the mitigation of the toxic environmental effects of acid mine drainage (AMD). *Process Safety and Environmental Protection* **2022**, *157*, 37-58. DOI: https://doi.org/10.1016/j.psep.2021.11.008.

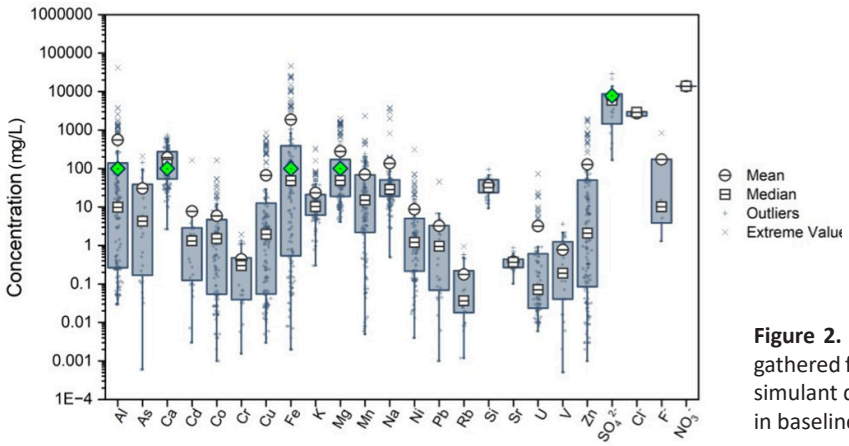

Figure 2. Box-and-whisker plot of AMD species concentrations gathered from literature review, used in laboratory AMD baseline simulant development. Primary species concentrations included in baseline simulant formulation are marked in green.

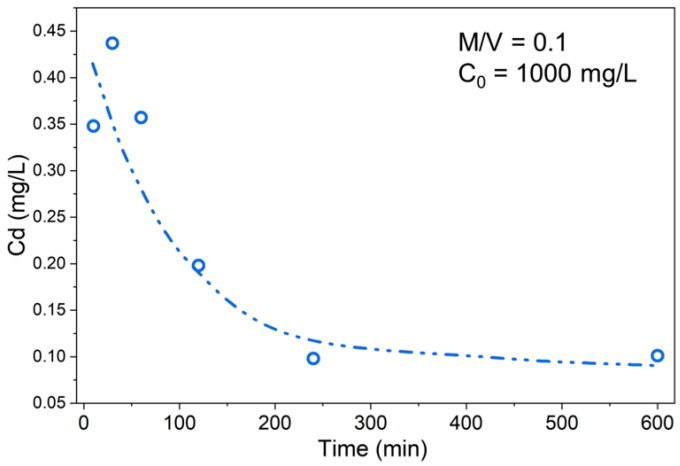

Figure 3. Results of static AMD simulant neutralization experiments, utilizing three different mass/volume ratios of RCA and AMD and two mesh sizes of RCA: Group 1 (fine) and Group 2 (coarse). The dotted line shows the results of the respective GWB simulation.

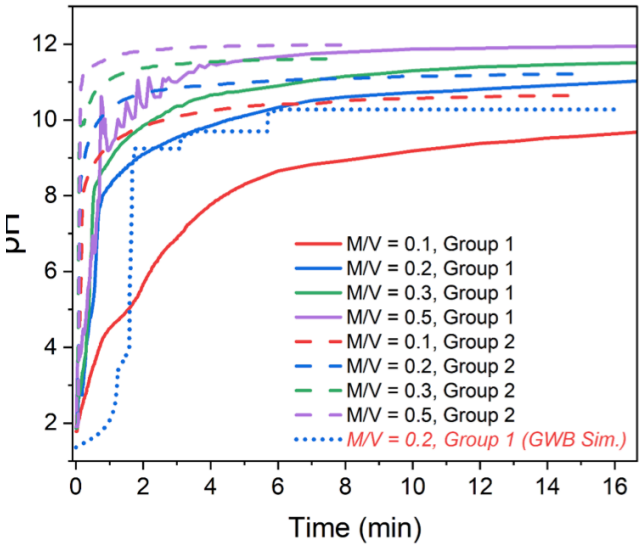

Figure 4. The results of a static sorption experiment with a starting concentration of 1000 mg/L Cd and a M/V = 0.1. It should be noted that in all other experiments, both the Cd and Pb were completely removed from the simulants prior to the first aliquot being sampled at 10 minutes, demonstrating the high efficacy of RCA at remediating these contaminants.

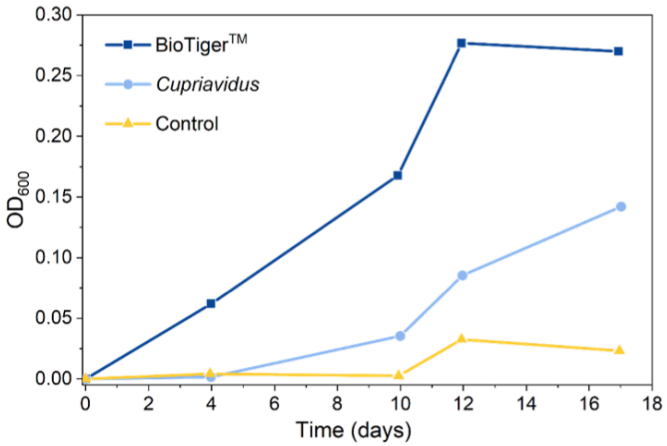

Figure 5: Results of dynamic pH neutralization and Cd sorption tests, utilizing AMD simulant doped with 100 mg/L Cd and 75 g of RCA. Column effluents were measured real-time for changes in metal concentration and pH. Tests 3 and 4 noticeably hit breakthrough more quickly, as those tests involved a faster flow rate: 5 mL/min, vs. 10 mL/min in tests 5 and 6.

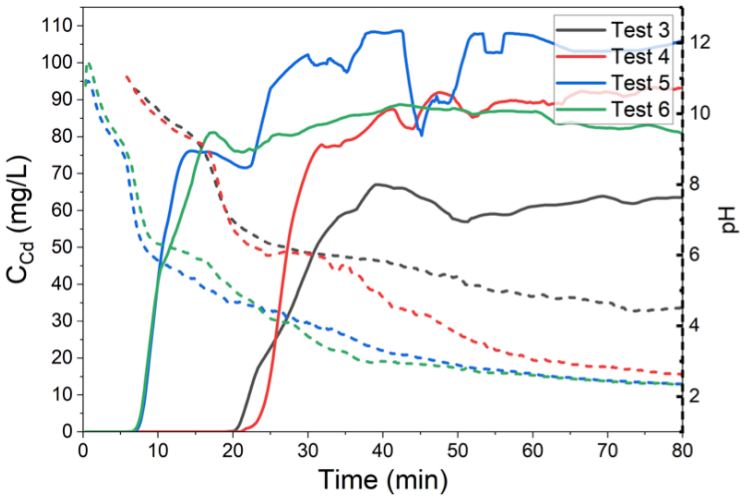

Figure 6. Biological growth experiments on ~3 cm diameter pieces of RCA demonstrated the ability of Cupriavidus and BioTigerTM to grow on the materials.

Enabling Field Deployable Ion Chromatography

Sue Clark and Joe Mannion

The monitoring of groundwaters is necessary to assess the impact of industrial processes and agricultural activities on the environment. Remote and autonomous monitoring devices present a significant opportunity to increase public safety via accelerated response to groundwater contamination problems while reducing overall environmental monitoring costs. This project aims to develop a miniaturized chromatographic analysis for nitrate, nitrite and ammonia, which are indicators of industrial processing including uranium milling, as well as explore the use of ion chromatography to isolate these species for isotopologue characterization by ultra-sensitive radiometric measurement.

Introduction

The overarching goal of this work is to develop an effective and efficient method for separating three major nitrogen-containing molecules of environmental concern (nitrate, nitrite, and ammonia) using ion chromatography. In the environment, the nitrogen cycle (see **figure 1** for a detailed illustration of the nitrogen cycle) is an integral component of ecological systems. Eutrophication is a potential consequence of excess nitrate being present in a localized area. It is common to sample fresh water for the overall nitrogen content, but this does not consider the speciation of the nitrogen present, which determines the chemistry and further impacts of the nitrogen-containing species. Additionally, in areas such as the Savannah River Site where environmental tritium is present, the nitrogen cycle may may be a pathway through which tritium is bio-incorporated through isotopologues such as NH_2T. The ecological fate of tritium introduced through the nitrogen cycle has not been well studied in the literature.

Modern analytical tools and methods are needed to support accelerating environmental remediation and to reduce risks associated with Department of Energy legacy sites. This work is building on SRNL's core competencies E1 "Accelerating remediation, minimizing waste, and reducing risks" and E5 "Sensing, characterizing, and assessing materials production and environmental impacts". SRNL leads the DOE complex in developing remote, autonomous, field-deployable sensors for monitoring groundwater (SRNL, 2024). Recent work has shown that ion chromatography systems (shown in detail in **figure 2**) can be used in a portable form for the determination of the nitrate, nitrite, and ammonia in limited environmental conditions (Mikhail, 2024); however, these conditions are not adequately varied for field deployment.

Approach

In this work, we aim to determine the efficacy of ion chromatographic separations of nitrate, nitrite, and ammonia over a variety of experimental conditions, from lab grade reagents to groundwater samples from Department of Energy legacy sites. We aim to determine a sufficiently wide band of separatory parameters to pursue the deployment of miniaturized, field-deployable ion chromatographic systems for the quantification of our target nitrogen-containing chemical species. Working from the approach described by White et al. (2022) to separate and identify the glycolate anion species from tank waste matrices employing an existing bench-top ion chromatographic system, parameters and protocols for the separation of nitrate, nitrite, and ammonia will be determined. The separation should be simpler to attain than that of White et al. (2022) as they were exploring a more complex sample matrix than groundwater.

After determining the efficacy of the separation over a variety of ionic strengths, parameters such as column flow rate, matrix ion strength, concentration of analytes, and temperature will be analyzed. Analyte separations will be affected by factors that contribute to broadening of the chromatographic bands, as such the optimization of these parameters will receive particularly close attention. Microfluidic platforms will be examined as the presence of multiple flow paths associated with a packed stationary phase becomes a limiting factor to separatory performance. From here, we aim to miniaturize the separations scheme through nano-scaled stationary, packed columns and a move toward an open tubular configuration, with the end goal of a field-deployable, small sensor.

Accomplishments

- The Metrohm 930 Compact Ion Chromatograph was selected as an instrument for preparation of environmental and ultra-low level radiometric samples. This is a cross-cutting instrument and was procured in FY25 to support other projects. The instrument will not be fully utilized by those projects, so will support this effort when available.
- This instrument was selected as it will be run with a carbonate-based elution method so that less potassium is introduced to the samples that are going for ultra-low level radiometric counting. Furthermore, Metrohm is a top vendor for ion chromatography systems, and their software is compatible with Agilent laboratory software which is currently used in the Mass Spectrometry system that may be integrated into the workflow in the future.
- Lab space in SRNL Building 735-11A, room 141 has been cleared out for the instrument to occupy.
- An environmental Evaluation Checklist (EEC) (TC-A-2025-00044-0, "Ion chromatography Operation") was completed.
- A poster ("Development of Ion chromatographic Methods for Nitrate, Nitrite, and Ammonia Quantitation in Groundwater Samples") was presented at the SRNL Internal Postdoc Poster Session.

Team Members

Joseph Mannion, Sue Clark, Rebecca Mueller*

**Postdoctoral Researcher*

References

1. LDRD-2025-00225 proposal.
2. J. K. Boehlke, R. L. Smith, and Daniel N. Miller (2006). "Ammonium transport and reaction in contaminated groundwater: Application of isotope tracers and isotope fractionation studies." *Water Resources Research* **42.**
3. Savannah River National Laboratory (2024). https://www.srnl.gov/fact-sheets/altemis/. Accessed Sep 16, 2025.
4. Mikhail, I., E. Murray, S. Bluett, S. Astrakhantseva, Brett Paull (2024); "Simultaneous separation and detection of monochloramine, nitrite, and nitrate by step-gradient mixed-mode ion chromatography: Translation from benchtop to portable ion chromatograph". *Analytica Chimica Acta*. 1304-342557.
5. White, T. L., C. J. Coleman, D. D. DiPrete, B. B. Looney, F. F. Fondeur (2022); Analysis of Glycolate in Radioactive Waste by Ion Chromatography (IC) and Proton Nuclear Magnetic Resonance (H NMR); J.Radioanalyt. Nucl. Chem; 331:4837–4849; https://doi.org/10.1007/s10967-022-08507-7.Kitson, E.; Kew, W.; Ding, W.; Bell, N.G.A. PyKrev: A Python Library for the Analysis of Complex Mixture FT-MS Data. J Am Soc Mass Spectrom. 2021, 32, 1263-1267

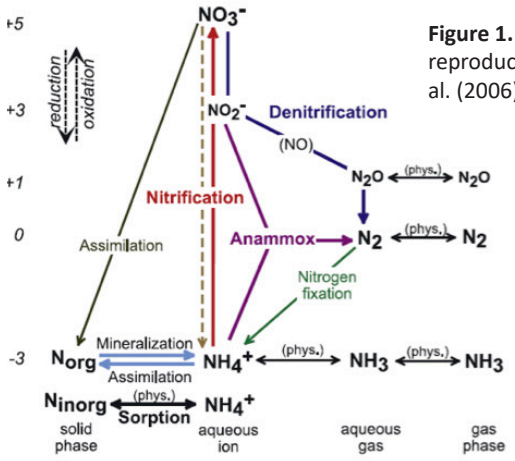

Figure 1. The Nitrogen Cycle, reproduced from Boehlke, et al. (2006) (2).

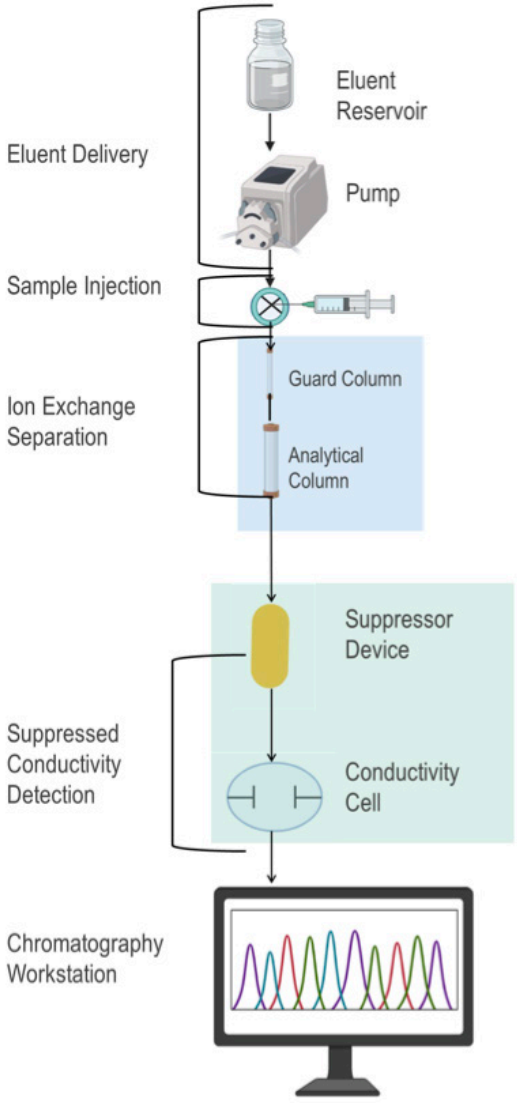

Figure 2. An illustration of an ion chromatography system, broken down by process and component.

Engineered Colloidal Hetero-nanocrystals for Photocatalytic Hydrogen Production

Krishna Acharya

This research is focused on the development of novel semiconductor hetero-structured nanocrystals which can convert solar energy into hydrogen using photocatalytic water splitting reactions. The newly developed nanomaterials could produce cost-effective chemical fuel by employing less-energy intensive technology.

Introduction

Hydrogen is a promising solar fuel source, however its contribution to the global energy is <1% because the conventional hydrogen production technologies such as steam reforming and water electrolysis are energy intensive. Photocatalytic (PC) water splitting using nanostructured semiconductors provides one of the most practical strategies for hydrogen generation because it directly converts solar energy into chemical fuel. Photocatalytic materials for hydrogen evolution from water are typically metal oxides, which are not efficient because they absorb light only in the ultraviolet range, which consists of < 5% of solar energy. The other materials such as chalcogenides and perovskite semiconductors absorb light both in ultraviolet & visible regions, however, they often contain toxic elements such as cadmium and lead. Therefore, this project is aimed at developing colloidal hetero-structured nanocrystals using less-toxic elements from group III-V and II-VI semiconductors, enabling broadband light absorption and excited-state charge separation. To achieve this, we have synthesized doped and undoped indium phosphide/zinc selenide/zinc sulfide (InP/ZnSe/ZnS) core/shell quantum dots (QDs), InP/ZnSe nanorods (NR), and ZnSe/ZnS NRs. These hetero-nanocrystals have tunable broad band absorption, favorable energy levels, and offer suitable electronic characteristics to drive photo-induced charge separation for hydrogen generation from water.

Approach

To achieve the objectives of this project, colloidal core/shell nanocrystals were synthesized using surfactant-controlled growth in a hot solution. For example, InP QDs were synthesized by heating indium oleate with organophosphine and trioctylphosphine (TOP) in a non-coordinating solvent at 280 °C. After purification of InP, ZnSe and ZnS layers were coated using TOP-selenide and sulfide, respectively. The absorbance and fluorescence spectra show there is a red shift in the absorption onset and fluorescence peak indicating the delocalization of the electrons (see **Figure 1a**). This relaxation of confinement potential of electrons indicates the formation of a quasi-type-II heterostructure. From transmission electron micrograph (TEM), average diameter of core/shell QDs is measured to be ≈10 nm (See **Figure 2a**). Magnetic elements are doped in the core/shell QDs by introducing metal e.g., (Nd, Ni) precursors during the shell growth to enhance magneto-assisted charge separation. Time-resolved photoluminescence (TRPL) measurements were performed on the core/shell QDs under different excitation power densities to assess their exciton recombination dynamics. The results show that the lifetime of the excited states is reduced at higher excitation fluence due to the multi-exciton recombination (see **Figure 1b**).

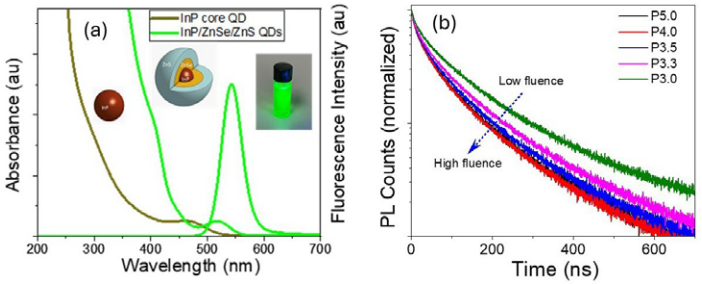

Figure 1. (a) Absorbance spectrum of InP core; absorbance and fluorescence spectra of InP/ZnSe/ZnS core/shell QDs. Inset shows the green fluorescence from the QDs when excited with a blue light (b) TRPL decay curves of Nd doped InP/ZnSe/ZnS QDs at different excitation power.

While Auger recombination shortens their lifetimes, these additional carriers may still enhance charge-transfer efficiency to surface sites or catalytic moieties if extraction occurs on faster timescales. Also, we have synthesized InP/ZnSe ZnSe/ZnS, ZnS NRs, and ZnSe/ZnS nanostructures using the seeded-growth method (**Figure 2 b-e**). These nanocrystals are suitable to enhance solar light absorption and photo-induced charge separation, which will be tested for the PC hydrogen generation properties.

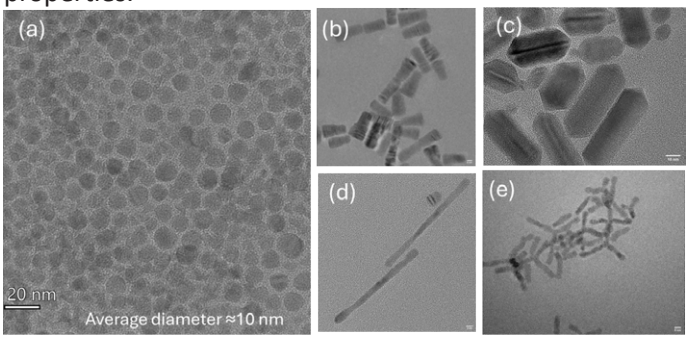

Figure 2. TEM image of (a) InP/ZnSe/ZnS QDs (b) InP/ZnSe nanorod (NR); (c)-(d) ZnS NR with low and high aspect ratio (d) multi branched ZnSe/ZnS hetero-nanostructures.

Accomplishments and results

- Developed an alternative method to synthesize large-sized InP/ZnSe/ZnS colloidal quantum dots with improved optical quality.
- Synthesized doped InP/ZnSe/ZnS QDs with dopant such as Nd with concentration up to ≈2%. These materials have been characterized for optical, morphological, structural, compositional, and excited-states carrier dynamics properties.
- Synthesized colloidal InP/ZnSe NR, ZnS NR, and ZnSe/ZnS multi-branched hetero-nanostructures using the seeded growth method.

Team Members

Mikhail Zamkova, Amelia Waltersa [‡] Binod Rai, Austin Dorris[*], Corey Martin, Matthew Page, Bryce Brechin, Gavin Kingb[†]

[a] Bowling Green State University, Ohio
[b] East Tennessee State University
[*]Postdoctoral Researcher
[‡] Graduate Student
[†]Undergraduate intern

Fusion Fuel Cycle

Light Isotope Separation using Deep Eutectic Solvents

Kori D. McDonald

Lithium- 6 and boron-10 enrichment has become an important research area within developing commercialized fusion, with the only limitation being the lack of environmentally friendly industrial scale purification methods. This project seeks to identify different Deep Eutectic Solvent's that may be used for Lithium- 6/7 or Boron- 10/11 isotope separation.

Introduction

Interest in the enrichment of light isotopes has grown in recent years as nuclear fusion continues to develop as a viable source of alternative energy. The primary light isotopes of interest for these applications are Lithium- 6 for breeding tritium and Boron-10, serving as a neutron scavenger in nuclear reactions. Historically, isotope enrichment involves the use of aggressive conditions such as the COLEX process for Lithium- 6 enrichment and boron trifluoride distillations for Boron- 11 enrichment, both of which have been phased out creating a gap in production. Deep eutectic solvents are a potential alternative due to their ease of generation in addition to the minimal environmental impact and concern.[1] In the case of both critical isotopes, DES systems have been utilized in general Li and B extractions.[2,3] Recent work within this presented study investigated such a system to separate lithium isotopes based on previous findings within the literature.[4] From that work various Lewis acid-base pairs were surveyed and key properties identified to afford efficient separation. However, it was determined that system optimization was crucial for usage and scalability. As work continues, the work presented herein explores alternative experimental designs to better enhance isotope separation.

Approach

DESs historically have been used for recycling lithium within lithium-ion batteries and recent efforts have begun to use them for the removal of boron compounds from aqueous media. Previously investigated systems continued to be explored for separation efficiency in different experimental systems. DESs were synthesized with various combinations of Lewis acid-base pairs, modifying the functional groups interacting with the lithium binding site. (**Figure 1**) Solvent systems are characterized using traditional analytical techniques prior to extraction. During the extraction process, the DES is supplied as the electrolyte in an electrochemical cell where the migration of lithium isotopes proceeds. (**Figure 2**) Following migration between the anodic and cathodic chambers, extracted lithium is analyzed via Inductively Coupled Plasma Mass Spectrometry (ICP-MS) to determine bulk and isotope concentrations.

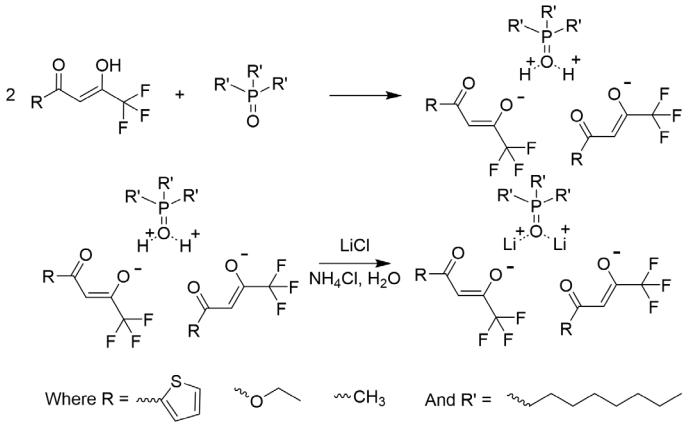

Figure 1. Synthetic scheme for DES and lithium extractions

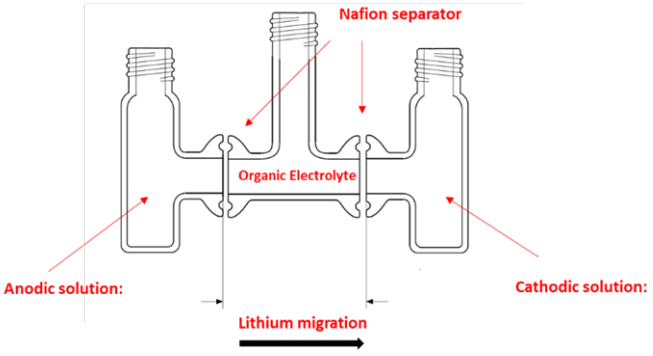

Figure 2. Experimental design for electromigration assisted enrichment

Accomplishments and Results

- Uncovered alternative systems for lithium isotope separation that utilize DESs.
- Screened different DESs in electromigration experiments for lithium- 6/7 separation.
- Began investigations into the separation of boron isotopes within DESs.
- Submitted two full proposals to The DOE Isotope Program (DOE IP) within the Office of Science
- Presented findings at an invited talk at Clemson University Department of Chemistry

Team Members

Jesse E. Smith*, Kori D. McDonald, Dale A. Hitchcock, Brenda L. Garcia Diaz, Shelby Bowden

* *Laboratory Director's Postdoctoral Research Fellow*

References

1. Hansen, B. B.; Spittle, S.; Chen, B.; Poe, D.; Zhang, Y.; Klein, J. M.; Horton, A.; Adhikari, L.; Zelovich, T.; Doherty, B. W.; Gurkan, B.; Maginn, E. J.; Ragauskas, A.; Dadmun, M.; Zawodzinski, T. A.; Baker, G. A.; Tuckerman, M. E.; Savinell, R. F.; Sangoro, J. R., Deep Eutectic Solvents: A Review of Fundamentals and Applications. *Chemical Reviews* **2021,** *121* (3), 1232-1285.
2. Hanada, T.; Goto, M., Synergistic Deep Eutectic Solvents for Lithium Extraction. *ACS Sustainable Chemistry & Engineering* **2021,** *9* (5), 2152-2160.
3. Ghazal, A.; Khalifeh, H. A.; Zuburtikudis, I.; Almustafa, G.; AlNashef, I., Enhancing boron removal efficiency through a design of experiments approach with a customized hydrophobic deep eutectic solvent. *Journal of Molecular Liquids* **2025,** *423*.
4. Smith, J. E.; McDonald, K. D.; Hitchcock, D. A.; Garcia-Diaz, B. L., Deep Eutectic Solvents as Candidates for Lithium Isotope Enrichment. *Separations* **2024,** *11* (11), 314.

Functionally Graded Plasma Facing Component for a Magnetic Fusion Energy Device

Luke Olson

Current fusion pilot plant first wall options are not expected to survive long due to extreme heat and radiation loading. We are focusing science for energy security by using additive manufacturing to fabricate easily replaceable, multifunctional liquid metal plasma facing components, that can address engineering needs in this challenging environment.

Introduction

Among the proposed fusion energy concepts, tokamak-based Magnetic Fusion Energy (MFE) concepts are generally believed to be the most developed technologies with the highest likelihood of commercialization. At the plasma edge in a tokamak, particles from the plasma that are being held at several hundred million degrees Celsius can erode material from the plasma-facing walls of the reactor through bombardment. Atoms of the removed material will subsequently be heated by the plasma and parasitically remove heat from the fusion reaction; lower Z materials will have lower parasitic losses. One conceptualized solution to address parasitic losses from solid wall particle ejections is to use a liquid wall of lithium that is not as prone to parasitic heat loss and whose surface is constantly refreshed, i.e., self-healing. Many within the fusion research community believe Liquid Metal Plasma Facing Components (LMPFCs) will be needed to realize practical fusion energy. However, this environment is still exposed to an intense neutron flux and components must now be low activation, be compatible with liquid lithium and have favorable tritium retention characteristics, as this is the region where most of the tritium in an MFE reactor will be bred.

Based off an initial concept, **Figure 1**, the SRNL team designed an additive manufactured (AM) tungsten surfaced LMPFC with a low activation vacuum permeation section directly underneath. The LMPFC was then printed using AM, **Figure 2**, for rapid manufacture and testing to prove that the combined system is lithium compatible, can handle the expected thermal stresses, and is functionalized as planned.

Approach

To make a component that could perform many functions simultaneously, a solid structure made of tungsten and vanadium is paired with liquid lithium. Liquid lithium provides a refreshed self-healing surface at the plasma interface, neutron moderation and shielding, while also breeding tritium that is needed to close the DT fusion fuel cycle. Additionally, the lithium removes fusion ash and impurities that could poison the fusion reaction. Tungsten is located just under the lithium at the plasma interface and above the vanadium regions and is within the first 2 cm of the plasma interface. Here, the tungsten keeps the lithium in place through surface tension, and lithium is constantly churned and cooled by a combination of thermoelectric magneto hydrodynamics and a mostly bypassed, lithium stream. The tungsten also provides a fallback structure to resist plasma erosion in case of localized dry-out during disturbances, while not absorbing any formed tritium. The vanadium is just under the tungsten and allow for bred tritium to be recovered close to where it is formed, though closely coupled vacuum spaces opposite lithium, thereby allowing for reduced overall tritium inventory and more efficient and cost-effective use. Because Li bonds strongly to hydrogen isotopes as LiH, the component will be closely coupled with an SRNL process referred to as direct electrolysis, that makes it energetically favorable for hydrogen to release from lithium.

Initial component designs are made using computer aided design programs, and these designs are fabricated and tested for function. Test results improve the design iteratively.

Accomplishments

- Added vanadium and grade 91 as options for additive manufacture at SRNL using laser powder bed fusion
- Brought in Clemson expertise for tungsten alloy property modeling and prediction
- Iterated a multitude of CAD component designs, using two different LMPFC interface concepts (capillary pore structure and LIMIT concepts)
- Made several test prints of regions of component using laser powder bed fusion, and one test printing of an entire component using electron beam powder bed fusion
- Installed OpenFOAM for computational fluid dynamics modeling of heat and lithium flow within the component
- Presented concept at the TMS 2025 Annual Meeting and the 2025 ANS Annual Conference.

Team Members

Colleen Hilla[*], Adam Gootgeld, Dilpuneet Aidhy[a], Paul Rowell, Guru Dinda, Dale Hitchcock, Christopher Dandeneau, Holly Flynn, Alex Somers, Collin Malone, Thomas Volta[*]

[a]*Clemson University*
[*]*Postdoctoral Researcher*

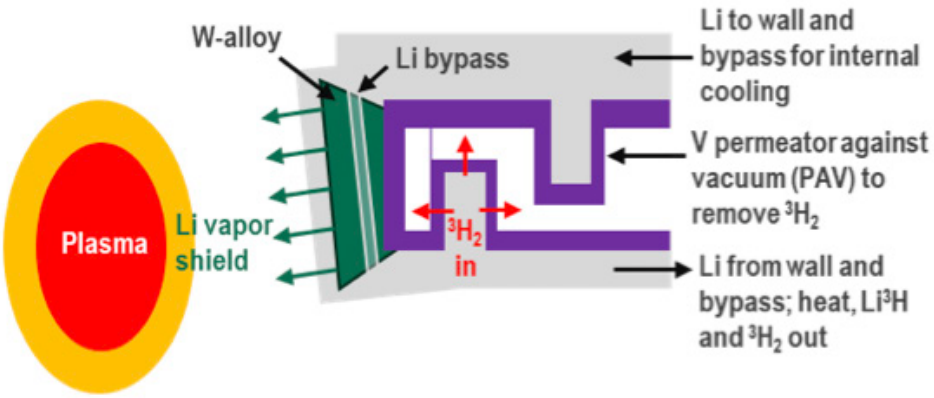

Figure 1. Functionally graded W-V liquid metal plasma facing component.

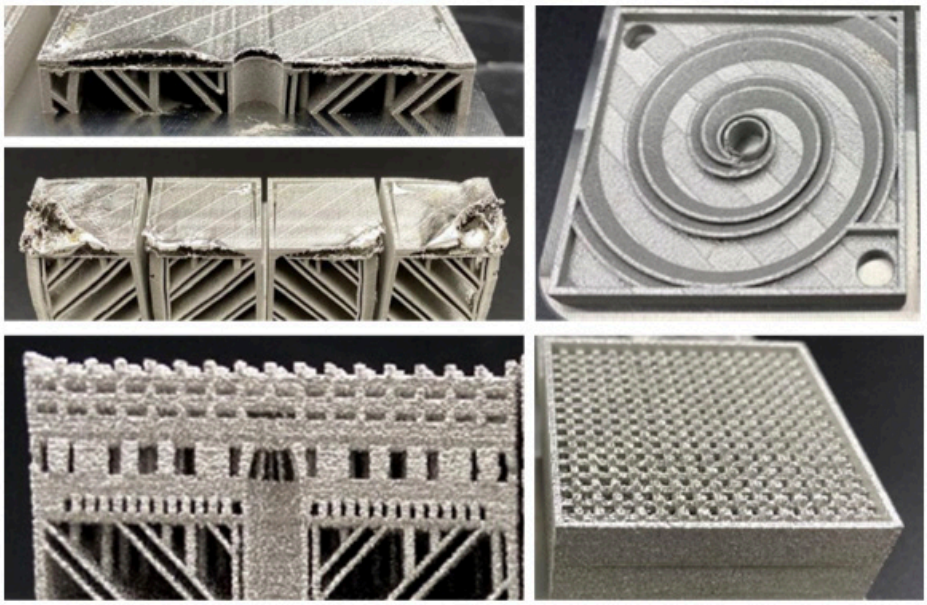

Figure 2. Test printings of specific regions of the component, some before and after fixing issues, and on two different printer types with different printing resolutions.

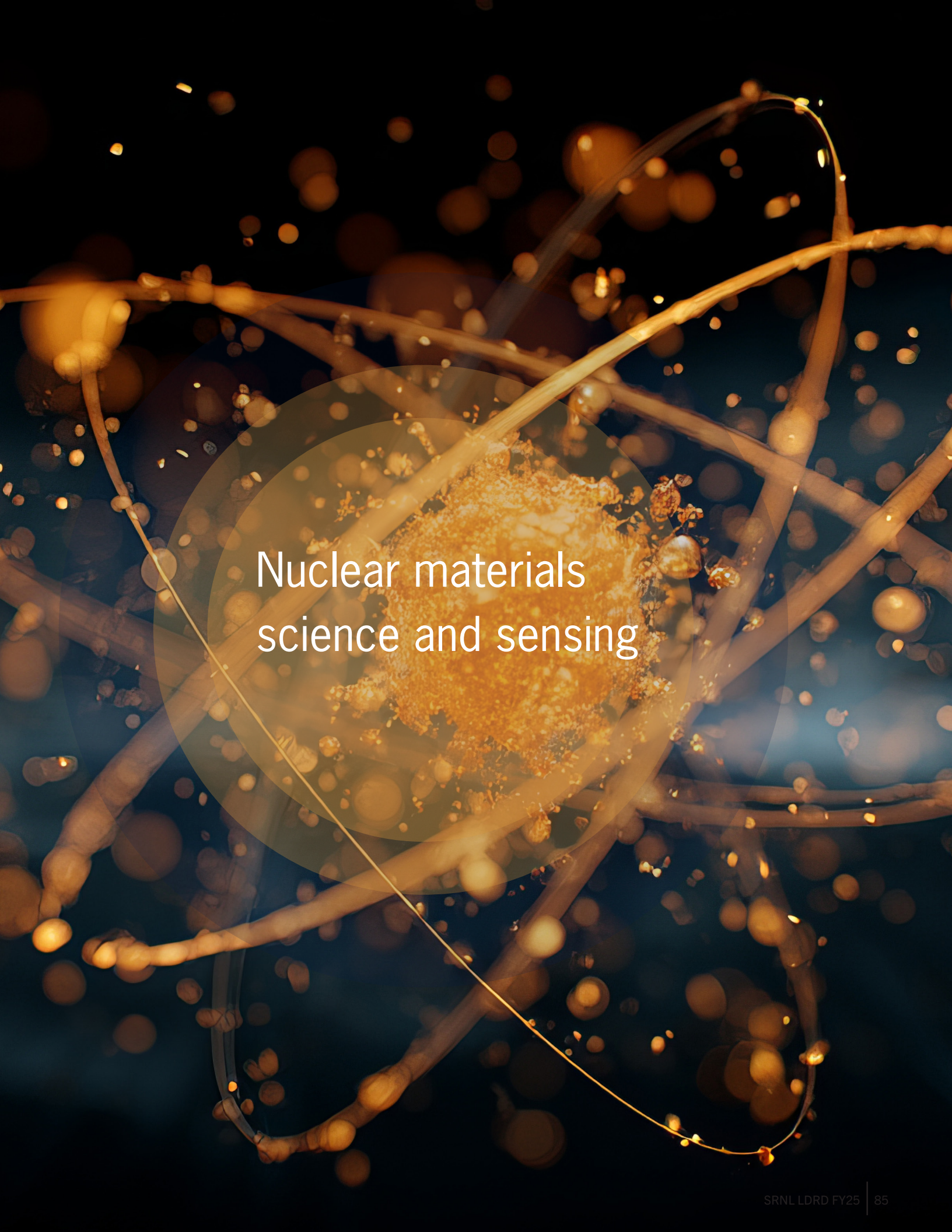

Nuclear materials science and sensing

Understanding the Chemistry and Physics of the Pu Metal-Oxide Interface with Vibrational and LIBS Spectroscopy

Don Dick

Develop spectroscopic tools to understand the corrosion of Ce and Pu metal with the goals to understand the fundamental corrosion mechanisms in actinide materials.

Introduction

The stability of a Pu metal surface is highly dependent on the ambient environment and the intrinsic alpha decay from Pu. In the presence of air, Pu metal oxidizes to PuO_2. A thin layer of Pu_2O_3 can then form at the metal – PuO_2 interface (see **Figure 1**) and Pu_2O_3-catalyzed corrosion can occur at the metal surface [1, 2].

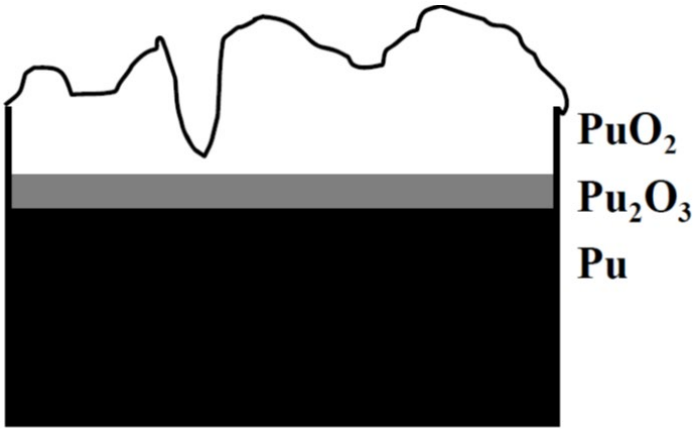

Figure 1. Depiction of surface oxide contaminants that form on the surface of Pu metal and impact metal integrity.

Under slightly elevated temperatures, Pu metal can react with moist air to form PuH_2 which is flammable and can react with O_2 and N_2 to generate Pu oxides. Ultimately, the growth of PuO_2, Pu_2O_3, and PuH_2 depends on atmospheric conditions, pressures, and temperatures.

To date, reactions at the Pu metal surface have been studied almost exclusively with X-Ray photoelectron spectroscopy (XPS) and X-ray diffraction (XRD). While XPS and XRD are useful tools for bulk analysis, their application towards interrogating very thin layers on a Pu metal surface is limited because the high penetration of highly energetic X-rays that exceed the thickness of very thin surface layers. In contrast to XPS and XRD, vibrational spectroscopic tools might enable the identification of different chemical species, layer thickness, oxide layer growth, and possibly radical reactions in very thin microscopic regions on the surface of Pu metal. The goal of this project is to use Raman spectroscopy and laser-induced breakdown spectroscopy to characterize Pu, Pu oxides and the molecular transition from bulk to surface [3-6].

Approach

Characterization of the surface of actinide compounds requires the development of unique tools to work with these difficult to handle materials. SRNL designed and developed double-walled cells for handling actinide materials. The concept revolutionized the spectroscopy research of Pu-bearing compounds. In FY25, the new cells were further modified to enable the study of Pu metal with laser-induced breakdown spectroscopy and Raman spectroscopy. As Pu metal hydride is flammable, the hydriding process was designed to be performed in a glovebag with flowing hydrogen gas that is placed inside an argon glovebox. *In situ* Raman spectroscopy is then used to monitor the Pu hydriding process.

Laser-induced breakdown spectroscopy with low peak power pulses was developed to monitor regions as small as 80 micrometers of PuO_2 (see **figure 2**). The highly efficient setup design for light capture enabled the acquisition of a spectrum with only 400 µJ/pulse. Our partners at the University of Florida evaluated these spectra using machine learning algorithms to for spectral discrimination and to determine thermodynamics. This ablation technique also enabled the ablation of surface oxides from the Pu metal.

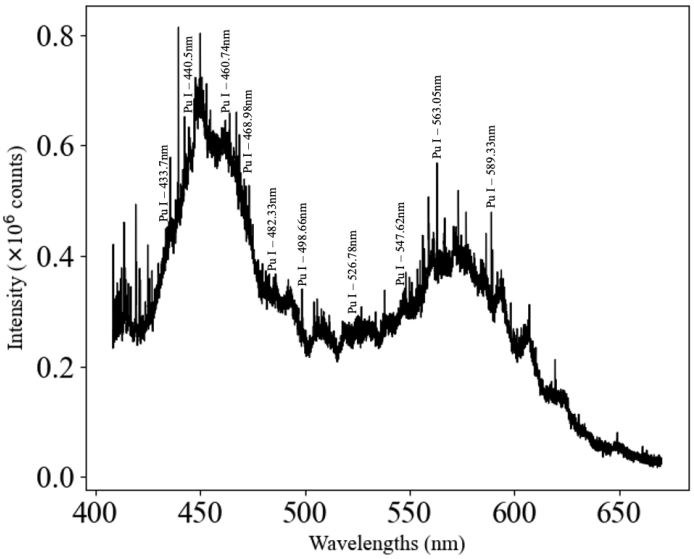

Figure 2. Identified neutral Pu lines at 350 ns gate delay time from the onset of laser ablation.

Accomplishments and results

- Method development to study Ce and Pu surfaces with Raman spectroscopy.
- Method development for hydriding actinide surfaces using a glovebag inside an argon glovebox.
- Assembled and tested a fiber Raman spectrometer for use in an Ar glovebox.
- Developed a stabilized double walled cell environment to prevent oxidation of Ce metal. The cell can hold an inert atmosphere long enough to allow hydriding studies to be conducted.
- PuO_2 surface studies with deep ultraviolet has been published. Includes new experimental work to confirm or deny the shape of bands and the presence of new bands.
- As part of the collaboration for this LDRD, two Journal articles from our partner at the University of Florida are submitted and under review.

Peer-reviewed Publications

- Villa-Aleman*, E.; Darvin, J. R. ; Dick, D. D. ; Shehee, T. C. ; Foley, B. J. Characterization of PuO_2 With Visible and UV Raman Spectroscopy: Discrimination Between the Bulk, Surface, and an Intermediate Disordered Layer. *Journal of Raman Spectroscopy* 56 (4), 324-336. DOI: 10.1002/jrs.6770
- Medici, E., Villa-Aleman, E., Darvin, J.R. et al. Machine learning for fundamental spectroscopic and thermodynamic data of actinides and lanthanides. *J Radioanal Nucl Chem* 334, 8989–8997 (2025). https://doi.org/10.1007/s10967-025-10396-5

Team Members

Jason R. Darvin, Don D. Dick, Bryan J. Foley, Thomas C. Shehee, Henry M. Ajo, Kyle C. Hartig[a], Weslee A Kersey[a*], Justin Borrero[a*], Enrique Medici [a*]

[a]*University of Florida*
*PhD Student Researcher

References

1. Dihn, L.N.; Haschke, J.M.; Saw, C.K.; Allen, P.G.; McLean II, W. *J. Nucl. Mater*. 408 (2011) 171-175.
2. Saw, C.K.; Haschke, J.M.; Allen, P.G.; McLean II, W.; Dinh, L.N. *J. Nucl. Mater*. 429 (2012) 128-135.
3. Villa-Aleman, E.; Dick, D.D.; Christian, J.H.; Foley, B.J. *Journal of Raman Spectroscopy*, 52, 1486.
4. Villa-Aleman, E.; Bridges, N.J.; Shehee, T.C.; Houk A.L. *Journal of Nuclear Materials* 2019, 515, 140.
5. Villa-Aleman, E.; Houk, A.L.; Shehee, T.C.; Bridges N.J. *Journal of Nuclear Materials* 2021, 551, 152969.
6. Villa-Aleman, E.; Houk, A.L.; Bridges, N.J.; Shehee, T.C. *Journal of Raman Spectroscopy* 2019, 50, 899.

Understanding MOF Gas Entrapment Through Modeling

Steven M. E. Demers

Understanding the trapping and retention mechanisms at the atomic level using modelling for metal organic framework materials allows for the creation of cheaper and higher purity gas production equipment and more sensitive detection of trace gases in the environment.

Introduction

In a previous gas chromatography study at SRNL, there was a large (30-65%) retention of noble gas in a calcium-center metal organic framework (Ca-MOF) material[1] that was unexplained in current literature. To address the knowledge gap, atomic modelling studies of the Ca-MOF as well as a similar cobalt-based MOF (Co-MOF)[2] were taken to understand the retention of noble gases within two similar MOF materials. **Figure 1** shows a graphical representation of the calcium and cobalt MOF crystalline structures. This retention would need to be understood if these materials are to be implemented into existing gas separation systems, either in industrial gas processing plants or in the next generation of trace gas detection equipment. At the basic science level, there is a large variety of different separation mechanisms for zeolitic and MOF material that are often hard to distinguish from one another. Topics such as if the gas-adsorbent separation interaction is at the surface of the material or within the pores, are electronic or physical interactions the main mechanisms for gas separations, and other discussion points. By studying these two materials, it is hoped that a greater understanding of these separation mechanisms can be elucidated with atomistic modelling.

Approach

The crystalline structure of the two MOF materials were first brought into DFT programs such as VASP or QE. The structures then had different noble gases (He, Ne, Ar, Kr, Xe) inserted into the MOF pores along with different contaminates (N_2, CO_2, O_2, H_2O) to determine the charge densities and electronic states of the different gas-MOF systems. **Figure 2** illustrates the formation energies of the different noble gas atoms within the pore structure as a function of position along the pore.

In parallel to the computational studies, experimental measurements were also undertaken to get a basis of comparison to the computational findings and better align them with real-world findings. Surface area measurements such as Brunauer–Emmett–Teller (BET) surface area measurements, adsorption isotherms of noble gases, and gas chromatography were taken of the materials to understanding the uptake mechanisms of the different noble gases in the two materials. The experimental findings would then feed back into the computation work to make sure the modelling assumptions for the system were correct in the calculations.

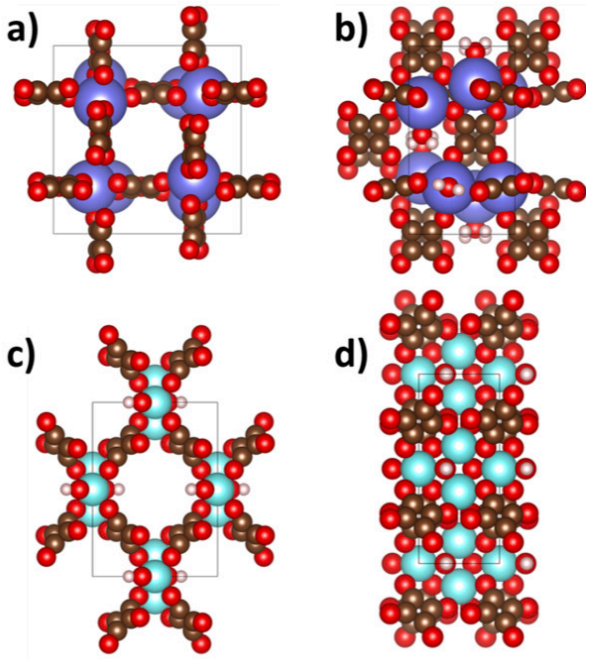

Figure 1. a) Pore-view of Ca-MOF UTSA-280, b) side-view of the Ca-MOF UTSA-280, c) pore-view of Co-MOF $[Co_3(C_4O_4)_2(OH)_2]\cdot 3H_2O$, and d) side-view of the Co-MOF $[Co_3(C_4O_4)_2(OH)_2]\cdot 3H_2O$. All structures are visualized with VESTA3 [https://doi.org/10.1107/S0021889811038970].

Accomplishments

- Fully modelled in DFT software VASP and other atomistic modelling software 2 metal organic framework materials and their interactions with 5 noble gases and 4 atmospheric gases.
- Gas chromatography and adsorption measurements were taken of the metal organic framework materials to determine correct the computational findings.
- New framework for atomistic modelling was created for different zeolites, metal organic frameworks, and other gas capture lattices for the uptake of select effluents for future materials studies.

Peer-reviewed Publications

- Demers, S. M. E, Szaro, N., Hoover, M., et. al. "Mechanisms for Noble Gas Retention in Metal Organic Framework Materials" In preparation*

Team Members

Steven M. E. Demers, Nicholas Szaro*, Megan Hoover, Douglas Hunter, Matthew Campbell, Harry Garcia Flores, Mark Morey[a], Manual Manard[a], Mark Philips[aa] *Special Technologies Laboratory*

**Postdoctoral Researcher*

References

1. Lin, RB., Li, L., Zhou, HL. et al. Nature Mater **17**, 1128–1133 (2018).
2. Liangying Li, Lidong Guo, Zhiguo Zhang, Qiwei Yang, Yiwen Yang, Zongbi Bao, Qilong Ren, and Jing Li. *Journal of the American Chemical Society* **2019** *141* (23), 9358-9364

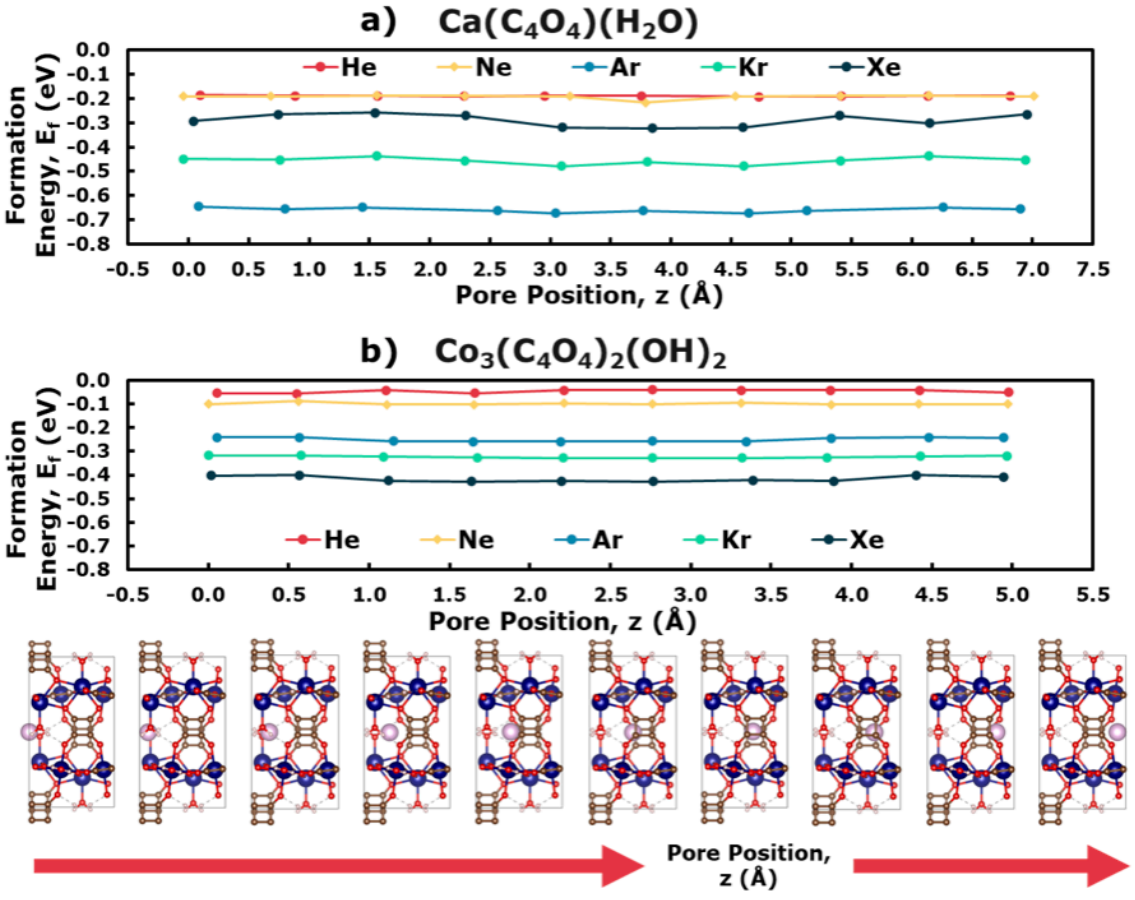

Figure 2 The formation energies for the noble gases within the a) Ca-MOF and b) Co-MOF pores as a function of noble gas species and z-position within the main pore axis. Bottom) Graphical depiction of Ar moving through the Ca-MOF pore at different z-positions and the resulting structural reconfigurations of the MOF lattice to account for the Ar.

Development of Transuranic Stimuli-Responsive Metal-Organic Frameworks

Corey Martin

On-demand tuning of materials properties by the inclusion of photochromic moieties provides a unique method to enhance the applicability of "smart" optoelectronic devices. A fundamental understanding of the cooperativity between f-elements and photochromic molecules will enable a new generation of semiconducting materials that can be applied to high resolution spatially- and temporally-resolved sensors.

Introduction

Optoelectronic devices constructed of lanthanide-based metal-organic frameworks (MOFs) is an attractive area of research due to imminent interest in a new generation of diode materials, optical and magnetic sensors, ratiometric thermometers, light-gated "smart" field-effect transistors.[1–3] Lanthanide- and actinide-based MOFs (Ln-MOFs and An-MOFs, respectively) are particularly useful for these applications due to their ultra-high porosity and accessible internal surface area, structural tunability that enables judicious design choices, and robust stability at a range of temperatures, pHs, and solvent conditions.[4,5] Although there have been extensive explorations into the fundamental properties of Ln-MOFs with promising photophysical applications, a correlation of structural and photophysical properties in An-MOFs is strongly lacking, likely due to the difficulty of preparing and handling radioactive species. Interest in this area is largely due to the possibility for metal centers possessing both luminescence and magnetic properties that enables the design of multifunctional materials and devices. Harnessing their unique electronic structure and photophysical properties, such as high spin-orbit coupling and access to forbidden *f-f* transitions that lead to hypersensitive and narrow emission profiles, enables the unique application of An-MOFs.[6–8]

An in-depth understanding of lanthanide- and actinide-based MOFs electronic structure is essential to determining their unrevealed potential (**Figure 1**). This project merges the area of *f*-element-containing MOFs with photochromic molecules to provide on-demand modularity of embedded photoswitchable moieties and, thus, tunable materials properties. An established correlation between dynamic photophysical response under light and optoelectronic properties enables the creation of the next-generation optoelectronic and magneto-optical devices.

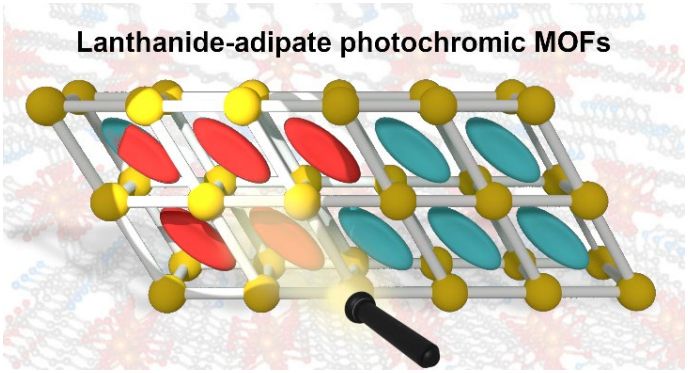

Figure 1. Lanthanide-adipate metal–organic frameworks are in the spotlight as a platform for embedding photochromic molecules in lanthanide-containing frameworks and harnessing the combinatorial power of f-electrons and stimuli-responsive molecules.

Approach

The incorporation of photochromic molecules within lanthanide- and actinide-based MOFs is a promising approach to directly probe the interactions between *f*-element metal centers and organic light-responsive components. The on-demand tuning of optical and electronic properties was realized by the inclusion of photochromic azopyridine in a series of lanthanide MOFs, allowing for high spatiotemporal control using light as a noninvasive stimulus for the bulk material.[9–11] The reversible interconversion between photoisomers leads to distinct and on-demand properties (e.g., absorption and emission profiles, magneto-optical response, polarization, and dielectric constants). The overall goal of this research is to merge the areas of *f*-element chemistry and photochromic molecules using MOFs as a platform to control and understand the unique properties of *f*-elements (e.g., spin-orbit coupling, relativistic effects, narrow emission profiles).

Photochromic azo compounds (i.e., organic molecules with diazenyl (R–N=N–R') functional groups) are an attractive class of organic molecules that impart light-

based optical and electronic response. Photoresponsive azobenzene derivatives integrated in bulk materials have previously been applied as light-sensitive actuators due to significant changes in their molecular confirmations, polarity, and light absorption upon their photoisomerization. In this study, the synthesis of photochromic lanthanide-based MOFs with various photochromic molecules were attempted, including diarylethene and spiropyran derivatives. The associated photoisomerization mechanisms and bulky sizes of these two classes of photoswitch were not suitable for MOF inclusion and subsequent photoisomerization. Azobenzene derivatives fit well within the pores of the MOFs due to their relatively small molecular size, and furthermore, photoisomerization was observed to occur without significant structural disruption. Azobenzene-based materials have been used to control liquid crystal domains or photophysical properties of nonlinear optical materials and sensors due to their long thermal lifetimes, large extinction coefficients, high photoisomerization quantum yields, and excellent fatigue resistance.[11,12]

This project combined diffuse reflectance, ^{1}H nuclear magnetic resonance, Fourier-transform infrared, and energy-dispersive spectroscopies to understand optical and materials properties (**Figure 2**). Photoisomerization kinetics were determined using time-resolved diffuse reflectance (**Figure 3**). Powder- and single-crystal X-ray diffraction were used to characterize the MOFs' structure and understand metal-ligand distances, angles, and first-principle interactions. This project was the first to report on the photoisomerization kinetics of Ce-, Pr-, and Nd-MOFs containing azobenzene molecules. Additionally, a significant number of attempts to directly synthesize An-MOFs provided information on the synthetic and characterization challenges associated with directly synthesizing actinide-based MOFs. Dozens of attempts of preparing an isostructural An-MOF with Pu, Am, and Np produced crystalline powders of a material representing an isostructural MOF by powder X-ray diffraction, but no suitable single crystals were able to be measured. It is likely that the targeted An-MOFs were produced, but self-ionizing radiation would destroy the MOF before suitable X-ray diffraction data could be collected. Due to this consideration, transmetallation attempts (i.e., a cation metathesis reaction) with actinides from Azo@Ce-MOF were explored as an alternative route to direct synthesis since powder X-ray diffraction could be employed before and after transmetallation to ensure structural retention. It was shown that small amounts of actinides (e.g., Am and Pu) could be included in the isostructural Azo@Ce-MOF and ongoing attempts are focused on enhancing the quantity of transmetallated metal in the prepared material.

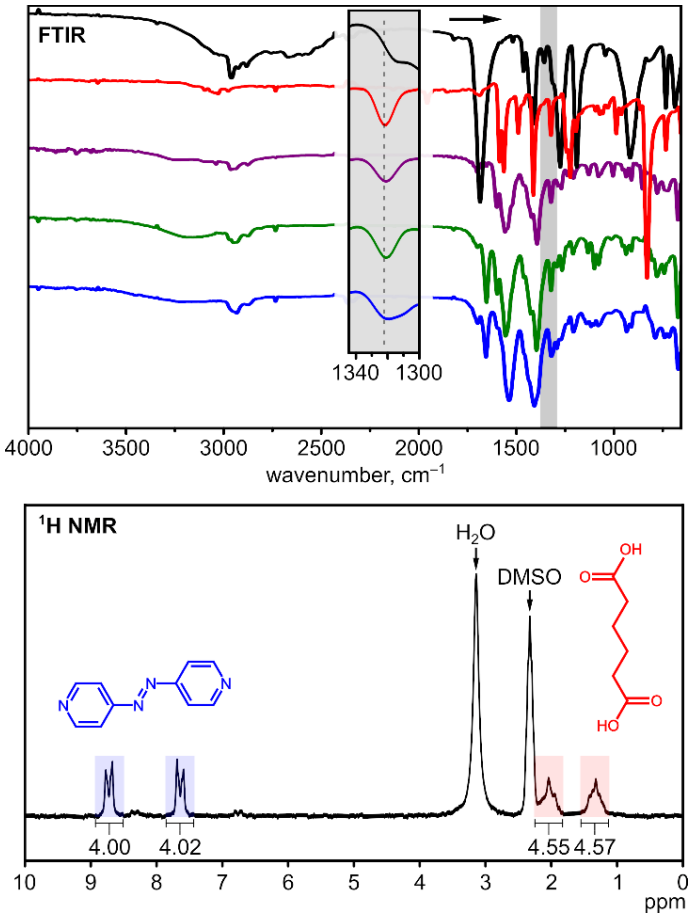

Figure 2. (Top) FTIR spectra of (blue) Azo@Ce-MOF, (green) Azo@Pr-MOF, (purple) Azo@Nd-MOF, (red) 4,4'-azopyridine, and (black) adipic acid. The inset shows δ(C–H: in-plane bend) coupled to ν(C–C: stretch) at 1322 cm^{-1} in 4,4'-azopyridine and MOFs containing 4,4'-azopyridine. (Bottom) ^{1}H NMR spectrum of digested Azo@Pr-MOF in dimethyl sulfoxide-d_6. The resonances corresponding to 4,4'-azopyridine and adipic acid are colored blue and red, respectively.

Accomplishments

- Reported the first photoisomerization studies for Ce, Pr, and Nd-MOFs containing azobenzene molecules.
- Established first-order rate kinetics for azobenzene-containing lanthanide MOFs (Azo@Pr-MOF, Azo@Ce-MOF, and Azo@Nd-MOF) that showed a more rapid photoisomerization than azobenzene in solution (e.g., 4.3-fold faster photoisomerization kinetics in Azo@Pr-MOF compared to free 4,4'-azopyridine).
- Confirmed photochromic retention of azobenzene in photoswitch-embedded lanthanide frameworks. Measured in solution and embedded in a MOF (solid-state) for photoisomerization rate comparison.
- Successfully cycled photoisomerization of azobenzene within Azo@Pr-MOF to show fatigue resistance of installed photochromic molecules as well as reversible photoisomerization.
- Prepared the first examples of transmetallated actinide-based photochromic MOFs, confirmed by ICP-MS and PXRD.

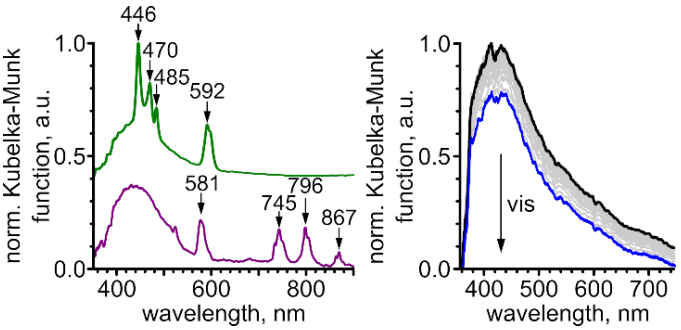

Figure 3. (Left) Normalized diffuse reflectance spectra of Azo@Pr-MOF (green) and Azo@Nd-MOF (purple). The wavelengths of the sharp absorption features in Pr- and Nd-containing samples are marked. (Right) Normalized diffuse reflectance spectra of Azo@Ce-MOF after 30 s of 300 nm irradiation (black) followed by attenuation under visible light (blue).

Peer-reviewed Publications

- *Martin, C. R.; Thaggard, G. C.; Lehman-Andino, I.; Mollinedo, E.; Rai, B. K.; Page, M. A.; Taylor-Pashow, K.; Shustova, N. B. Photochromic Ln-MOFs: A Platform for Metal-Photoswitch Cooperativity *Inorg. Chem.*, **2024**, *63*, 12810–12817.

Team Members

Corey R. Martin,[a]* Krishna Acharya,[a] Ingrid Lehman-Andino,[a] Eduardo Mollinedo,[a]* Binod K. Rai,[a] Matthew A. Page,[a] Kathryn Taylor-Pashow,[a] Grace C. Thaggard,[b†] Natalia B. Shustova[b]

[a]*Savannah River National Laboratory*
[b]*University of South Carolina*
[*]*Postdoctoral Researcher*
[†]*Graduate Student Researcher*

References

1. Islamoglu, T.; Ray, D.; Li, P.; Majewski, M. B.; Akpinar, I.; Zhang, X.; Cramer, C. J.; Gagliardi, L.; Farha, O. K. From Transition Metals to Lanthanides to Actinides: Metal-Mediated Tuning of Electronic Properties of Isostructural Metal-Organic Frameworks. *Inorg. Chem.*, **2018**, *57*, 13246–13251, DOI: 10.1021/acs.inorgchem.8b01748
2. Karmakar, A.; Li, J. Luminescent MOFs (LMOFs): recent advancement towards a greener WLED technology. *Chem. Commun.* **2022**, *58*, 10768–10788, DOI: 10.1039/d2cc03330e
3. Wang, X.; Zhang, X.; Li, P.; Otake, K. I.; Cui, Y.; Lyu, J.; Krzyaniak, M. D.; Zhang, Y.; Li, Z.; Liu, J.; Buru, C. T.; Islamoglu, T.; Wasielewski, M. R.; Li, Z.; Farha, O. K. Vanadium Catalyst on Isostructural Transition Metal, Lanthanide, and Actinide Based Metal-Organic Frameworks for Alcohol Oxidation. *J. Am. Chem. Soc.* **2019**, *141*, 8306– 8314, DOI: 10.1021/jacs.9b02603
4. Roy, S.; Chakraborty, A.; Maji, T. K. Lanthanide-organic frameworks for gas storage and as magneto-luminescent materials. *Coord. Chem. Rev.* **2014**, *273-274*, 139–164, DOI: 10.1016/j.ccr.2014.03.035
5. Black, C. A.; Costa, J. S.; Fu, W. T.; Massera, C.; Roubeau, O.; Teat, S. J.; Aromí, G.; Gamez, P.; Reedijk, J. 3-D Lanthanide Metal-Organic Frameworks: Structure, Photoluminescence, and Magnetism. *Inorg. Chem.* **2009**, *48*, 1062–1068, DOI: 10.1021/ic8017826
6. Bünzli, J.-C.; Eliseeva, S. V. Intriguing aspects of lanthanide luminescence. *Chem. Sci.* **2013**, *4*, 1939–1949, DOI: 10.1039/c3sc22126a
7. Fang, Y.; Xing, C.; Zhan, S.; Zhao, M.; Li, M.; Liu, H.; Wang, C. Multifunctional Magnetic-Fluorescent Nanoparticle: Fabrication, Bioimaging, and Potential Antibacterial Applications. *ACS Biomater. Sci. Eng.* **2019**, *5*, 6779–6793, DOI: 10.1021/acsbiomaterials.9b01332
8. Jankowski, R.; Wyczasany, M.; Chorazy, S. Multifunctionality of luminescent molecular nanomagnets based on lanthanide complexes. *Chem. Commun.* **2023**, *59*, 5961–5986,DOI: 10.1039/D3CC00342F
9. Thaggard, G. C.; Maldeni; Kankanamalage, B. K. P.; Park, K. C.; Haimerl, J.; Fischer, R. A.; Shustova, N. B. Switching in Harmony: Tailoring the Properties of Functional Materials with Orthogonal Stimuli. *Chem. Phys. Rev.* **2024**, *5*, 011305, DOI: 10.1063/5.0189069
10. Mehlana, G.; Bourne, S. A. Unravelling chromism in metal-organic frameworks. *CrystEngComm* **2017**, *19*, 4238–4259, DOI: 10.1039/C7CE00710H
11. Rice, A. M.; Martin, C. R.; Galitskiy, V. A.; Berseneva, A. A.; Leith, G. A.; Shustova, N. B. Photophysics Modulation in Photoswitchable Metal-Organic Frameworks. *Chem. Rev.* **2020**, *120*, 8790–8813, DOI: 10.1021/acs.chemrev.9b00350
12. Russew, M.-M.; Hecht, S. Photoswitches: From Molecules to Materials. *Adv. Mater.* **2010**, *22*, 3348–3360,DOI: 10.1002/adma.200904102

Computational Investigation of CdTeSe growth and doping strategies for PV applications

Jonathon Baker

To manufacture high quality thin films for use in photovoltaic cells and radiation detectors, fine tuning of the manufacturing process is required to minimize defective growth. This research outlines novel atomistic insights by directly modeling the interactions between adsorbates. With these insights, the manufacturing process can be more effectively engineered.

Introduction

Zincblende semiconductors cadmium telluride (CdTe) and zinc selenide (ZnSe) are important wide-bandgap semiconductors of the wider CdTeZnSe family and are utilized in various optoelectronic applications such as photodetectors, LEDs, diode lasers, and photovoltaic cells [1-3]. All these applications require smooth and defect-free thin films that can be difficult to manufacture. Physical vapor deposition (PVD) techniques, such as molecular beam epitaxy (MBE), have been widely used for manufacturing high-quality thin films. However, there is a lack of comprehensive first-principles studies elucidating the detailed adsorption chemistry on CdTe and ZnSe surfaces. In order to bridge this gap, a first-principles analysis was conducted to investigate the unary and binary adsorption phenomena on CdTe(111) and ZnSe(111). The adsorption formation energies were calculated as a function of adsorbate identity, adsorption site, and adsorbate-adsorbate interatomic distance. Insights from adsorption formation energies can allow for engineering conditions that better support smooth growth. Furthermore, interaction energies between adatom pairs were calculated to determine binary pairs that could lead to either clustering or island formation at high coverage conditions. These detailed DFT simulations contribute significantly to advancing the understanding of adsorption chemistry on CdTe and ZnSe surfaces; and thus, this research provides insights into the factors that influence the adsorption chemistry during epitaxial growth. The formation energy calculations of unary and binary adsorption are pivotal for identifying the most stable configurations and understanding the surface dynamics under different growth conditions.

Approach

Adsorption phenomena of CdTe and ZnSe were simulated using spin-polarized density functional theory (DFT) calculations on SRNL's high-performance computer. For both CdTe and ZnSe, all possible unary and binary adsorption configurations were evaluated. Specifically for CdTe, pairs of Cd-Cd, Cd-Te, Cd-Se, Cd-Zn, Te-Te, Te-Se, Te-Zn, Se-Se, Se-Zn, and Zn-Zn adatoms were simulated. For ZnSe, simulations included Zn-Zn, Zn-Se, and Se-Se adatom pairs. The top, fcc, and hcp sites are shown in **Figure 1**. The formation energy of adsorption, calculated for both unary and binary adsorption scenarios, includes three main components: electronic contribution, elastic contribution, and vacuum adatom binding contribution. **Figure 2** displays a schematic breakdown of this approach. The electronic contribution reflects the energy resulting from charge density variations induced by electron density differences.

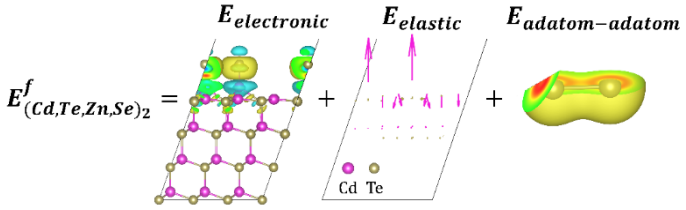

Figure 1. Left: A top view of the CdTe(111)A surface and three adsorption sites for adatoms: top, fcc, and hcp. Right: A top view of the CdTe(111)A surface and three adsorption sites for adatoms: top, fcc, and hcp.

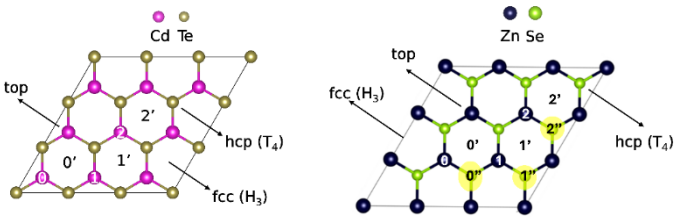

Figure 2. Pictorial representation of the binary formation energy. Overall formation energy is the sum of electronic, elastic, and vacuum adatom binding contributions.

Charge density difference plots for Cd-Cd, Cd-Te, and Te-Te pairs on CdTe(111) and for Zn-Zn, Zn-Se, and Se-Se pairs on ZnSe(111) are shown in **Figure 3** and **Figure 4**, respectively. These differences were determined by subtracting charge densities of the distorted clean slab and isolated adatom pairs from the fully relaxed system with binary adatoms. The elastic contribution accounts for the energy due to slab distortion caused by the adsorption process. The vacuum adatom binding contribution measures the energy of interaction between adatoms placed in vacuum at their respective adsorption positions. Additionally, the interaction energy between adsorbates was calculated for all binary pairs, indicating whether two adatoms attract or repel each other independently of chemical potential, assessing their interaction based on temperature and reagent partial pressure.

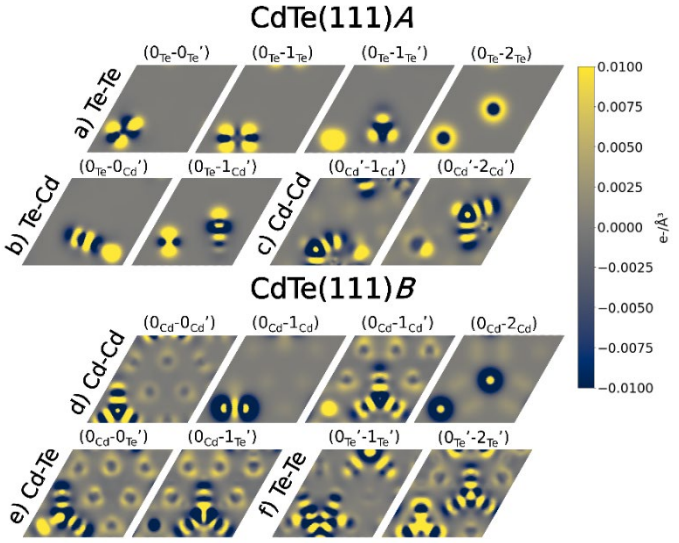

Figure 3. Two-dimensional charge density difference plots for a) Te-Te, b) Te-Cd, and c) Cd-Cd on CdTe(111)A and for d) Cd-Cd, e) Cd-Te, and f) Te-Te on CdTe(111)B. The units of charge density are e/Å^3.

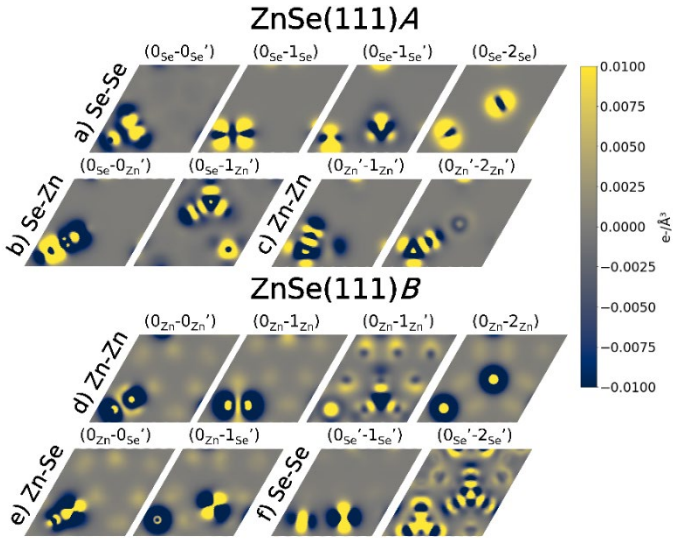

Figure 4. Two-dimensional charge density difference plots for a) Se-Se, b) Se-Zn, and c) Zn-Zn on ZnSe(111)A and for d) Zn-Zn, e) Zn-Se, and f) Se-Se on ZnSe(111)B. The units of charge density are e/Å^3.

Accomplishments and results

- Conducted a detailed computational analysis that showed adsorbate-adsorbate interactions significantly impact early growth behavior and surface smoothness, affecting the quality of the thin film
- Identified that under Cd-rich conditions, the Cd-terminated surface should yield a smoother, more stoichiometric, and defect-free thin film in agreement with previous theoretical literature
- A journal article was published in Surface Science that communicates all the insights from the unary and binary adsorption simulations to theoretical ternary adsorption.
- Presented two posters: SRNL Day at the University of South Carolina and LDRD Poster Session
- This is the first work to examine unary adsorption of Zn and Se and interactions between Zn-Zn, Zn-Se, and Se-Se binary pairs on ZnSe(111)

Peer-reviewed Publications

- Nicholas A. Szaro*, Megan Hoover, Jonathon N. Baker, A first principles study on the adsorbate-adsorbate
  interactions on the CdTe(111) surface with Cd, Te, Zn, and Se adatoms, *Surf. Sci.*, **2025**, 122941, doi: 10.1016/j.susc.2025.122841
- Nicholas A. Szaro*, Megan Hoover, Jonathon N. Baker, A first principles study of unary and binary adsorption on the ZnSe(111) surface with Zn and Se adatoms, In Preparation to submit to *Appl. Phys. Lett.*

Team Members

Nicholas Szaro*, Megan Hoover

*Laboratory Director's Postdoctoral Fellow

References

1. Peng, J., Lu, L., & Yang, H. Review on life cycle assessment of energy payback and greenhouse gas emission of solar photovoltaic systems. Renew. Sustain. Energy Rev. **2013**, *19*, 255-274. DOI: 10.1016/j.rser.2012.11.035
2. Zheng, X., Kuciauskas, D., Moseley, J., Colegrove, E., Albin, D. S., Moutinho H., Duenow J.N., Ablekim T., Harvey S.P., Ferguson A., & Metzger, W. K. Recombination and bandgap engineering in CdSeTe/CdTe solar cells. APL Mater. **2019**, *7* (7), 071112. DOI: 10.1063/1.5098459
3. Chikamura T., Fujiwara S., Shibata T., Miyata Y., Terui Y., Wada T. IEEE Trans. Electron Devices. **1982**, *29* (6), DOI: 10.1109/T-ED.1982.20821

Reverse Engineering of Medical Devices for Innovation and Advancement in Healthcare

David Baldwin

The medical field has garnered significant attention in the realm of cybersecurity. This project addresses that attention by performing big picture-oriented research on medical devices and uncovered bad practices, vulnerabilities, and usage hazards. It also built relationships with Army medical personnel, the FBI, WellStar, and strengthened ties with Augusta University.

Introduction

Medical cybersecurity research addresses the intersection of healthcare and security. As medical devices become more interconnected, the sector becomes a target for cyber warfare. This project aims to mitigate risks in a field that often underestimates cybersecurity's importance.

The research focused on personal and mobility-oriented medical devices that integrate newer technologies like smartphone connectivity, Bluetooth, and Wi-Fi Direct. These technologies expand medical device capabilities, but introduce risks to patient safety, privacy, and data integrity. They also pose threats to hospitals and supporting organizations via interconnected networks.

The objective of the project was to comprehensively identify and analyze risks associated with wireless and smartphone enabled medical technologies. This involved analyzing the security countermeasures for wireless data transmission using techniques such as data interception and wireless reconnaissance to reveal vulnerabilities. The hardware and software components of medical devices and their companion applications were meticulously reverse engineered (Figures 2, 3, and 4). This process provided a detailed understanding of the devices' inner workings, highlighting specific vulnerabilities exploitable by adversaries (**Figure 5**).

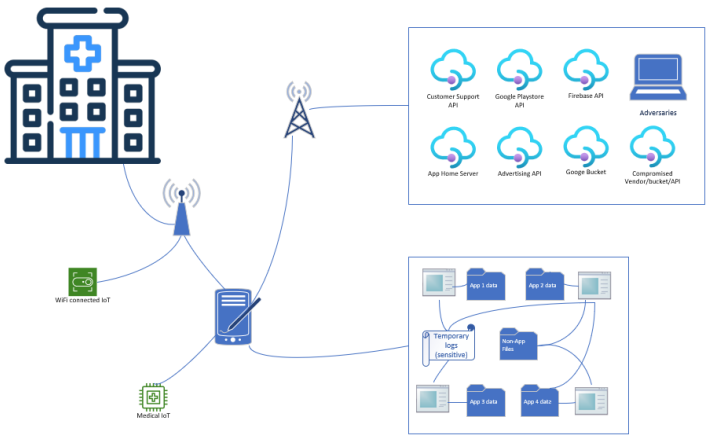

Figure 1: The diagram illustrates the interconnectivity of various applications within a cellphone, highlighting the pathways through which attackers can potentially pivot between these apps. It also demonstrates the connections to external resources, including interconnected devices, hospitals, Google buckets, APIs, and other external resources, showcasing the broad vulnerability landscape that attackers might exploit.

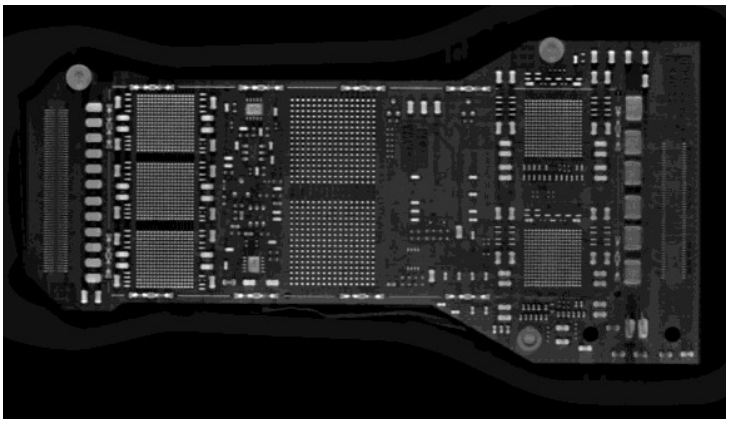

Figure 2: CT scan of VScan Air ultrasound device utilized to reverse engineer Printed Circuit board(PCB) without destructive testing

The project's insights and findings are crucial for developing stronger security frameworks for medical devices. By addressing vulnerabilities and implementing robust security measures, the healthcare sector can better protect patient data, ensure patient safety, and secure hospitals and related organizations against cyber threats.

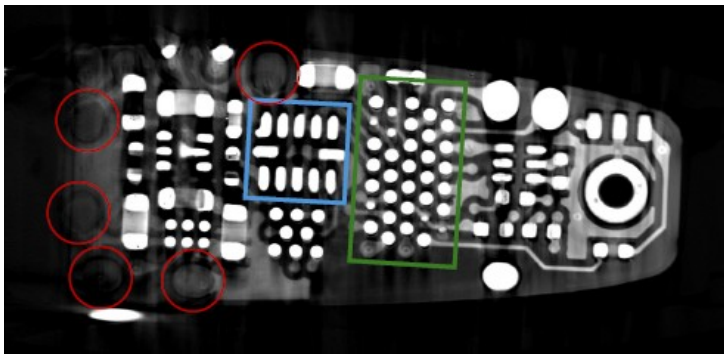

Figure 3: Hearing AId CT hardware teardown highlighting Digital Signal Processors in green, EEPROM in blue, and device testing pads in red

Approach

To make a component that could perform many functions In this research project, our objective was to identify and understand the vulnerabilities in Medical Internet of Things (MIoT) devices to enhance patient security and provide comprehensive documentation for the safety of future devices. We employed a two-pronged approach involving wireless reconnaissance and attacks performed within a Faraday cage, and robust reverse engineering of hardware and software components.

Our approach was designed to emulate the Tactics, Techniques, and Procedures (TTP) utilized by real-world adversaries. By focusing on device identifiability and signals reconnaissance techniques, coupled with application reverse engineering, we aimed to mimic the low-cost methods often exploited by attackers. This enabled us to identify not only geolocation capabilities that could be leveraged against the devices, but also potential vulnerabilities and locations of servers and application programming interfaces (API) utilized by the devices (see **Figure 6**).

Moreover, this research yielded eye-opening results regarding the general hygiene of mobile applications, particularly those used within the healthcare sector. Our findings highlighted.

Accomplishments and results

- Successfully identified two potential communication channels that could compromise the operational security of a key medical device used by the U.S. Army, enabling strategic recommendations to mitigate adversary geolocation risks and enhance device stealth (**Figure 4**).
- Discovered hardcoded secrets embedded in 7 devices (CWE-312), exposing critical and sensitive information to potential attackers and leading to immediate action plans to secure the vulnerabilities and protect organizational data integrity (**Figure 5**).
- Uncovered root capabilities (CWE-250) and credential-less remote access vulnerabilities (CWE-919) in multiple devices, exposing Medical Internet of Things (MIoT) devices and connected cellphones to potential adversary exploits, prompting urgent remediation measures to safeguard network security (**Figure 5**).
- Results provide foundation for drafting document outlining the status of mobile application development and establishing a robust framework for developers, enhancing the security and resilience of future platforms.
- Conducted in-depth analysis and documentation of findings, pending CVEs (Common Vulnerabilities and Exposures), built and documented the vulnerability reporting process for the Savannah River National Laboratory (SRNL) and laid a robust foundation for future scope in vulnerability research initiatives.

Peer-reviewed Publications

- Tauscher, D.; Nowatkowski, M.; Morris, J. D.; Baldwin, D. Medical Devices: Reverse Engineering for Innovation and Advancement in Healthcare. Proceedings of SoutheastCon 2024, Atlanta, GA, USA, 2024, pp. 860-862. DOI: 10.1109/SoutheastCon52093.2024.10500213.*
- Tannenbaum, N.; Baldwin, D.; Bergum, B.; Johnson, R.; Lyon, M. Evaluating Emissions Signatures of Handheld Ultrasound in Tactical Medicine: Operational Risk, Detection Threats, and Mitigation Strategies. J. Spec. Oper. Med. (JSOM), under review.*

Team Members

Michael Nowatkowski[a], Jeffrey Morris[a], Justin Carney[b], Mitchell Jordan, Matthew Lyona*, Nicholas Tannenbaum[a]

[a] *Augusta State University*

[b] *Augusta University doctorate student*

**WellStar Doctor*

```
public void setGpsInfo(Location location) {
    if (location == null) {
        return;
    }
    setAttribute(TAG_GPS_PROCESSING_METHOD, location.getProvider());
    setLatLong(location.getLatitude(), location.getLongitude());
```

Figure 4: Reverse engineered code excerpt from Wi-Fi direct dependency code that collections latitude and longitude data from connected phones GNSS chip to enable connection through proper application programming interface(API)

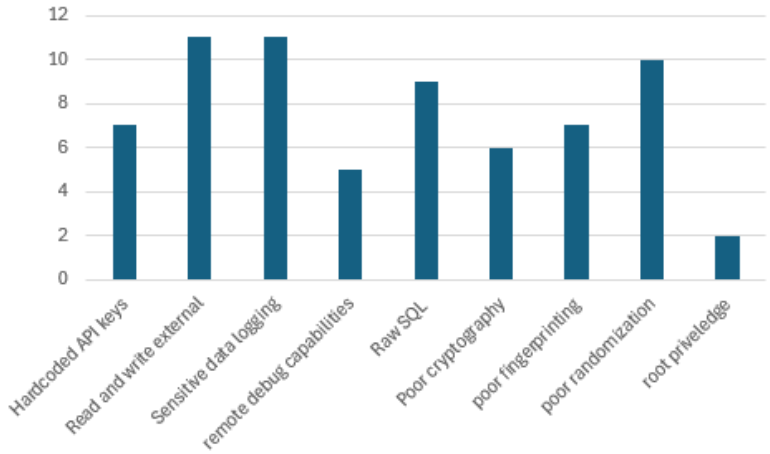

Figure 5: The bar graph illustrates poor security posturing, and the vulnerabilities found in medical device applications analyzed in this research.

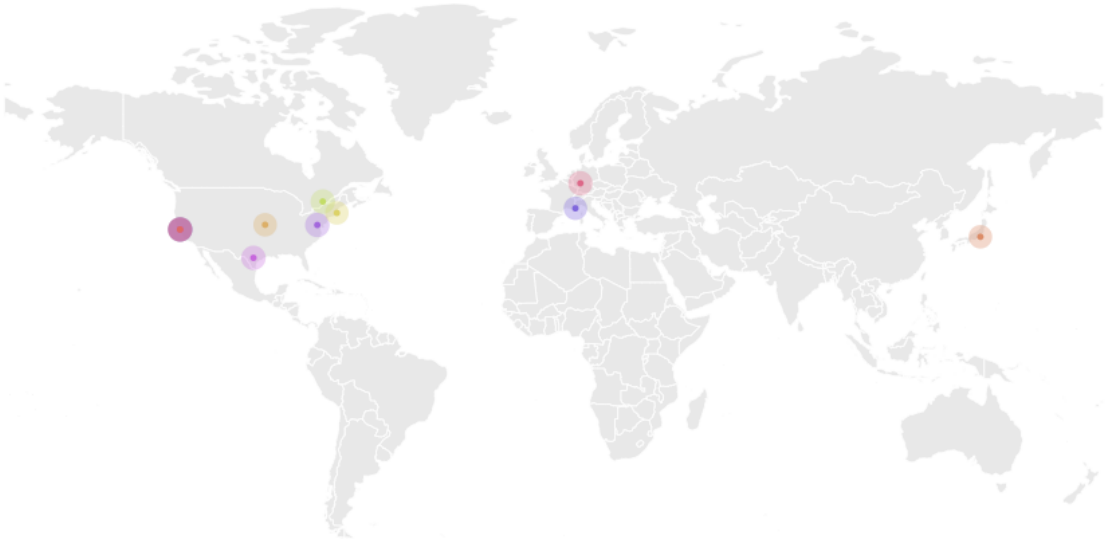

Figure 6: locations of servers hardcoded within mobile applications

Rapid, rigorous, reproducible data analysis software for high-precision mass spectrometry

Kyle Samperton and Elizabeth LaBone

Mass spectrometry is a critical capability for diverse SRNL mission areas. There is currently a lack of software for processing raw data output by multicollector mass spectrometers. The goal of this project was to develop a flexible, transparent software package for mass spectrometric data analysis based on cutting-edge statistical methods.

Introduction

High-precision mass spectrometry is a key technology in enabling all SRNL mission organizations (ELM, GSD, WPT) and advancing SRNL's Core Competency of *Sensing, Characterizing, Assessing, and Deterring Nuclear Proliferation* for domestic and international customers. Despite the centrality of precision mass spectrometry to SRNL projects and organizations, no software currently exists with either basic or advanced data analysis tools and data interactivity functions necessitated by modern high-precision methods, including thermal ionization mass spectrometry (TIMS) and multicollector–inductively coupled plasma–mass spectrometry (MC-ICP-MS). The lack of such software presents a significant limitation in being able to maximize the scientific and technical potential of these "gold standard" analytical technologies, both at SRNL and beyond. The objective of this project was to develop a comprehensive data analytics software package and Graphical User Interface (GUI) for SRNL's diverse high-precision mass spectrometric capabilities. In the first year, efforts were focused on developing statistically mature, "frequentist" data analysis tools and the main GUI framework for MC-ICP-MS data. In the second year, the focus shifted to adding TIMS data analysis and Bayesian data analysis tools. This new software is compatible with and supports diverse SRNL high-precision mass spectrometry capabilities and will help to establish SRNL as a leader in precision data analytics for such technologies.

Approach

To build a mass spectrometry data analysis software suite, this project leveraged the power of R[1], a popular, free, open-source programming language and environment for statistical computing. R functionality can be augmented by freely downloading any of the >19,000 user-contributed packages on the online Comprehensive R Archive Network (CRAN) repository. One such package is Shiny[2], which provides tools for convenient development and customization of "point-and-click" GUIs within the R environment. Integrating R-based data analytics with Shiny-enabled data interactivity offers an attractive route for analysts to take advantage of R's statistical and computational power, allowing researchers without any programming experience to harness its considerable data analysis and visualization capabilities. In addition to Shiny, this project implemented Golem[3], a framework for production-grade Shiny applications that includes software documentation, structure, and testing standardization. These elements were integrated with team subject matter expertise in mass spectrometry, data analysis, and mathematics/statistics to develop **PRISMS** (**PR**ecision **IS**otopic **M**ass **S**pectrometry), a software package for importing, processing, visualizing, and reporting high-precision mass spectrometry information that addresses shortcomings of current commercial and open-source software. The software codifies best practices in the data analysis and technical literature[4], yielding a flexible, Monte Carlo method-based statistical package and GUI framework. In addition, PRISMS incorporates pertinent quality assurance and control components, including establishing metrological traceability of analytical results to specified reference materials and applying rigorous uncertainty propagation and analysis techniques. Example screenshots of the PRISMS interface and outputs are given below in **Figures 1 and 2**.

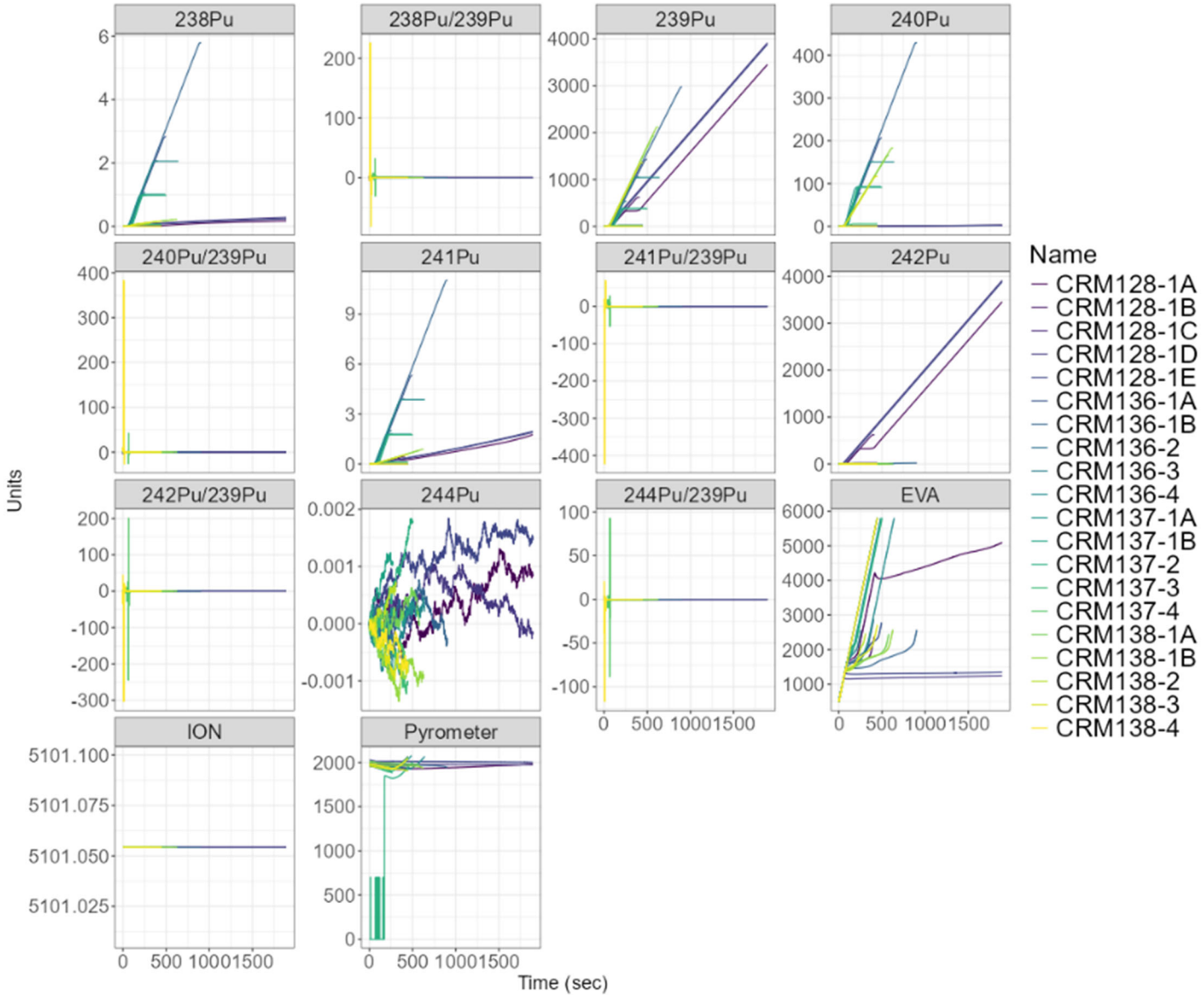

Figure 1. PRISMS software showing data screening module for TIMS plutonium isotopic analysis traces.

Accomplishments and results

- Developed "base R" code for MC-ICP-MS and TIMS data reduction.
- Constructed a flexible, "point-and-click" Graphical User Interface for processing, visualizing, and reporting mass spectrometry results (**Figures 1, 2**).
- Presented software at multiple technical conferences, including Goldschmidt, MARC, and DATAWorks.
- Multiple papers describing the development and use of PRISMS software currently in peer review.
- Project graduate student intern, Ellis McLarty (Clemson University), awarded student travel grant and won Best Conference Poster Award at DATAWorks 2025.

Peer-reviewed Publications

- *Bowden, S.; Samperton, K. Modeling of theoretical precision for ICP-MS measurements. *Journal of Radioanalytical and Nuclear Chemistry*, under review.
- *McLarty, E.; Riche, A.; Samperton, K.; LaBone, E.; Bowden, S. Bayesian statistical analysis for mass spectrometric data processing. *Journal of Radioanalytical and Nuclear Chemistry*, under review.
- *Bowden, S.; Shultz-Johnson, L.; Harrell, M.; Bronikowski, M.; Fitzgerald, C.; Barrett, C.; Wellons, M.; Samperton, K.; Koh, K.; Green, G. Precision and accuracy of highly-enriched double-spike Fe taggant measurements using Quadrupole- and Multicollector-ICP-MS. *Journal of Analytical Atomic Spectrometry*, under review.
- *Bowden, S.; Furman, T.; Alhumimidi, M.; Stolinas, E. Lithospheric stability and recycling linked to ancient metasomatic processes. *Communications Earth and Environment*, under review.

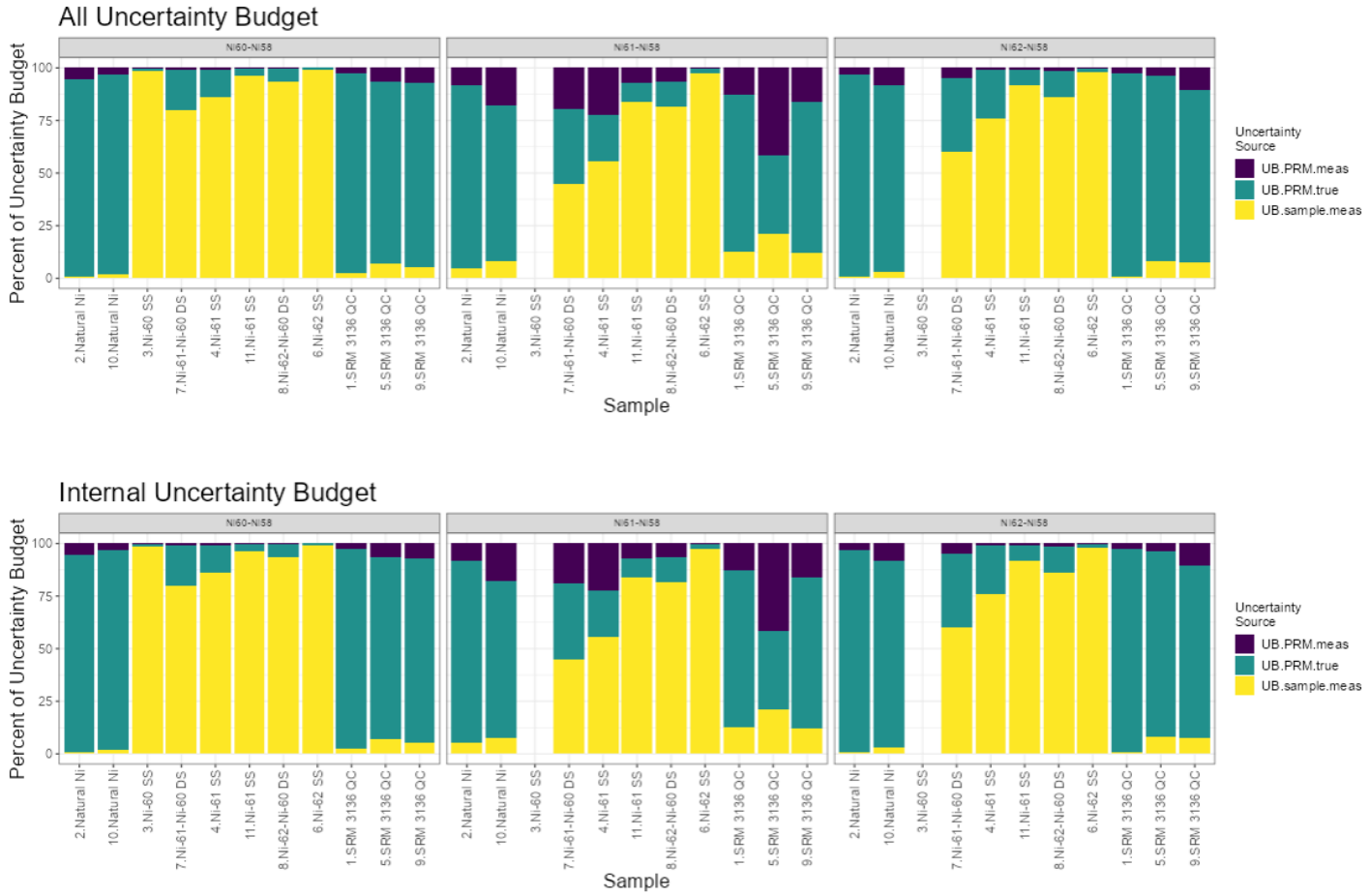

Figure 2. PRISMS software showing uncertainty budget module for MC-ICP-MS nickel isotopic analyses.

Intellectual Property

Copyright Disclosures

- PRecision ISotopic Mass Spectrometry (PRISMS) computer software
- PRecision ISotopic Mass Spectrometry Graphical User Interface (PRISMS.GUI) computer software

Team Members

Shelby Bowden[*], Alexis Riche[*], Ellis McLarty[a#]
[*] *Postdoctoral Researcher*
[a] *Clemson University*
[#] *Student Researcher*

References

1. R Core Team. *R: A Language and Environment for Statistical Computing*. R Foundation for Statistical Computing, Vienna, Austria, 2025. https://www.R-project.org/
2. Chang, W.; Cheng, J.; Allaire, J.; Sievert, C.; Schloerke, B.; Xie, Y.; Allen, J.; McPherson, J.; Dipert, A.; Borges, B. *shiny: Web Application Framework for R.* R package version 1.8.1.1. 2024. https://CRAN.R-project.org/package=shiny
3. Fay, C; Guyader, V.; Rochette, S.; Girard, C. *golem: A Framework for Robust Shiny Applications*; R package version 0.4.1. 2023. https://CRAN.R-project.org/package=golem
4. BIPM, IEC, IFCC, ILAC, ISO, IUPAC, IUPAP, and OIML. Evaluation of measurement data — Guide to the expression of uncertainty in measurement. Joint Committee for Guides in Metrology, JCGM 100:2008. doi:10.59161/JCGM100-2008E.

Determining Mercury Loading and Source Trends from Isotopic Records of SRS Environmental Matrices

Heather Brant

Mercury is a toxic element that is found both naturally and as an introduced contaminant in most Savannah River Site environments. This work focused on determining mercury isotope composition of Site environmental media as a utility to trace mercury contamination sources over space and time.

Introduction

Mercury (Hg) is a toxic element that occurs both naturally and as an introduced contaminant in many Savannah River Site (SRS) environments and across the DOE complex. Extensive research has documented Hg within environmental matrices of the SRS[1]. There are numerous possible sources of mercury contamination to the SRS environment, including legacy operations of the SRS, offsite point sources, and atmospheric deposition. The contributions and roles of these sources to legacy Hg observations within the SRS environment remain uncertain. Recent advances in multicollector–inductively coupled plasma–mass spectrometry (MC-ICP-MS) have enabled the ability to conduct highly precise measurements required to detect subtle differences in the isotopic composition of heavy elements, including Hg. Determination of stable Hg isotope ratios in various environmental media proves useful to trace Hg source(s) and processes involved in the transfer of Hg into the environment.[2] This study aimed to (1) optimize SRNL's existing MC-ICP-MS capabilities to include Hg isotopes (2) develop a novel, rapid method for simultaneous total Hg concentration determination and sample preparation for Hg isotopic analysis (**Figure 1**), (3) determine the concentration and stable isotopic composition of Hg in various SRS environmental matrices (**Figure 2**, 3), and (4) investigate the relationship of possible sources and trends of Hg loading in the SRS environment over past decades (**Figure 3**).

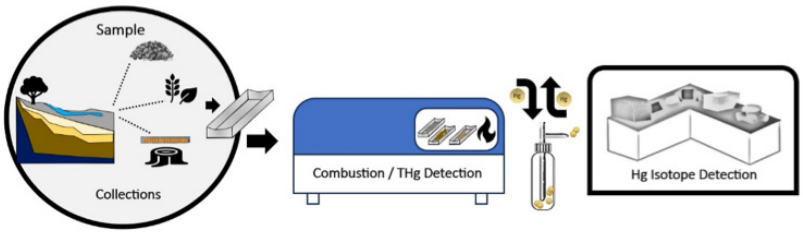

Figure 1. Simplified illustration of rapid detection method. Environmental media loaded directly into autosampler, combusted, total mercury (THg) detection by atomic absorbance, while off gas collected into trapping solution.

Approach

In this work, we aim to determine the efficacy of ion The goal of this study is to determine if Hg isotopic compositions within SRS environmental matrices preserve signatures of local and regional sources. Support of this goal coincides with strategic sampling and analytical method development. Hg contamination of the SRS environment is well documented.[1,3] Data from these documents were reviewed to provide insight on selection of regional sampling sites that received legacy Hg discharges from different sources, including background. Environmental matrices considered for sampling included tree bore wood cores, sediment, and soil. Literature suggests dendrochronology and stratigraphy coupled with Hg isotope ratios provide a natural archive of Hg source exposure.[4,5] Recent and archived sediment and tree core samples were utilized to develop and validate parameters associated with the novel, rapid method of simultaneous total Hg concentration analysis and preparation for Hg isotopic measurements. Analytical parameters determined during this study included optimal sample weights, concentration ranges, detection limits, trapping solutions, and instrument criterion for Hg concentration and isotope analysis. Several field trips allowed for the collection of 34 tree cores from three locations (**Figure 4**). Age dating and sectioning methods were developed for the cores. Determinations indicate Hg concentrations fluctuate with temporal growth of the sampled trees (**Figure 3**). Sediment total Hg concentrations were determined from 27 locations both on and off SRS. Concentration and isotope ratios of the sediments indicate spatial differences between and within sampling locations (**Figure 2**).

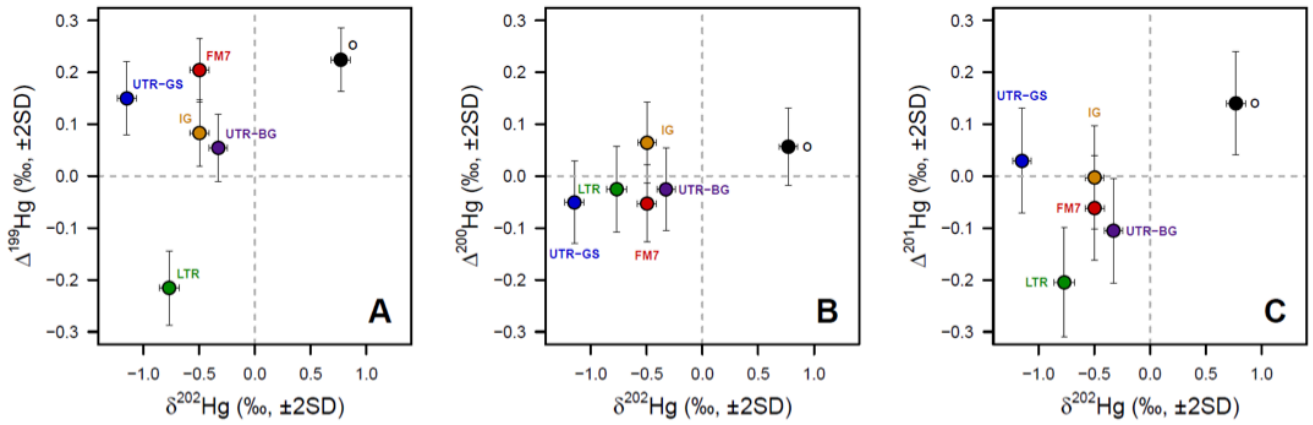

Figure 2. Cross plots demonstrating a range of mass dependent fractionation (MDF; even isotopes) and mass independent fractionation (MIF; odd isotopes) of stream sediment from on and off the Savannah River Site (SRS). Uncertainties are 2 standard deviations (SD). Dotted lines indicate natural values as related to NIST standard 3133. Colored circles represent deviations from the natural values for each listed location. Locations: Upper Three Runs (UTR); two locations; Four Mile Branch (FM7), Indian Grave Branch (IG), offsite industry upstream of SRS collected within the Savannah River (O), Lower Three Runs (LTR).

Accomplishments

- Determined SRS environmental media exhibit spatiotemporal trends of Hg concentration and isotopic composition.
- Determined Hg isotopic composition of SRS environmental media differs from offsite locations.
- First determination of mercury isotopic ratios within environmental media of the Savannah River Site (SRS).

Team Members

Shelby Bowden*, Haley Cole, Wendy Kuhne, Alexis Riche*, Kyle Samperton, and Ashlee Swindle

**Postdoctoral Researcher*

References

1. Halverson, N. (2008). Final Report on the Aquatic Mercury Assessment Study. doi:10.2172/939852.
2. Blum, J. D., L. S. Sherman, and M. W. Johnson (2014), Mercury isotopes in Earth and environmental sciences, Annu. Rev. Earth Planrt. Sci., 42, 249– 269.
3. Pickett, C.E, T.G. Campbell, and W.E. Harris. 1989. Mercury Requirement for Separation Processes, OPS-STH-890145, Westinghouse Savannah River Company, Aiken , SC.
4. Scanlon, T. M., Riscassi, A. L., Demers, J. D., Camper, T. D., Lee, T. R., & Druckenbrod, D. L. (2020). Mercury accumulation in tree rings: Observed trends in quantity and isotopic composition in Shenandoah National Park, Virginia. Journal of Geophysical Research: Biogeosciences, 125. https://doi.org/10.1029/2019JG005445.
5. Meixnerová J, Blum JD, Johnson MW, Stüeken EE, Kipp MA, Anbar AD, Buick R. Mercury abundance and isotopic composition indicate subaerial volcanism prior to the end-Archean "whiff" of oxygen. Proc Natl Acad Sci U S A. 2021 Aug 17;118(33). doi: 10.1073/pnas.2107511118.

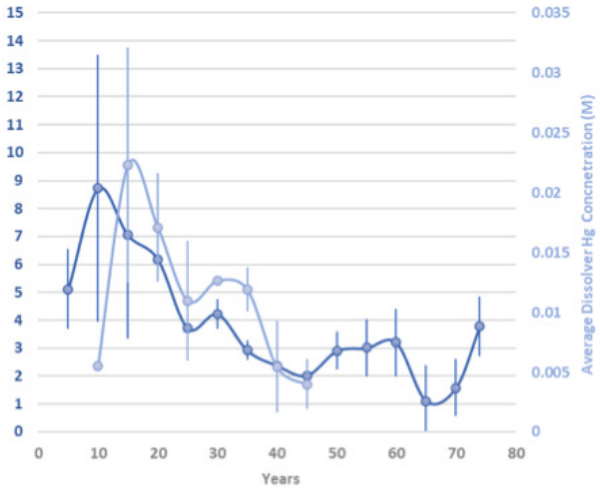

Figure 3. Radial pattern of Hg concentration in bore wood of a pine tree near F- and H-Area at SRS (dark blue). Each blue circle represents a five-year average Hg concentration (ng/g ± 1σ). Bore wood core growth dates from 1950 (year 0) to 2024 (year 74). Each light blue circle on the secondary axis represents a five-year average Hg concentration (M ± 1σ) as reported for the SRS Separation Areas dissolvers (F- and H-areas)[3]. Secondary

Figure 4. Bore wood core collection from a pine tree. Radial pattern (light/dark) within the core indicates annual increment growth. Hg concentration can be determined on each year (one ring), averaged though years, or as several years analyzed together (several rings). Analysis of Hg isotopes may require combining rings (spanning several years) to meet quality control requirements of the MC-ICP-MS instrument.

Controlled Reaction Dynamics of Binary Hexafluorides to Explore New Chemical Signatures

Louis McNamara

This project's goal is to better understand uranium hexafluoride reactivity for an improved quantitative understanding of fate, transport, and propagation of signatures related to highly enriched uranium production.

Introduction

Uranium hexafluoride (UF_6) plays a critical role in the nuclear fuel cycle since it is the primary form of uranium used in enrichment processes. UF_6 is very reactive and reacts vigorously with moisture in the air to form uranium particulates which are often cited as important nonproliferation signatures. Despite its use since the 1940s, this reactivity is poorly understood. In this project, we have used cryogenic trapping to slow down UF_6 reactions and monitor the formation of intermediate species, **Figure 1**. We have investigated reactions of both UF_6 and MoF_6 with H_2O, alcohols, and ammonia to better understand the general reaction space of binary hexafluoride. There is little literature about these types of reactions, and our work has yielded interesting results which challenge some long-standing assumptions about UF_6 reactivity.

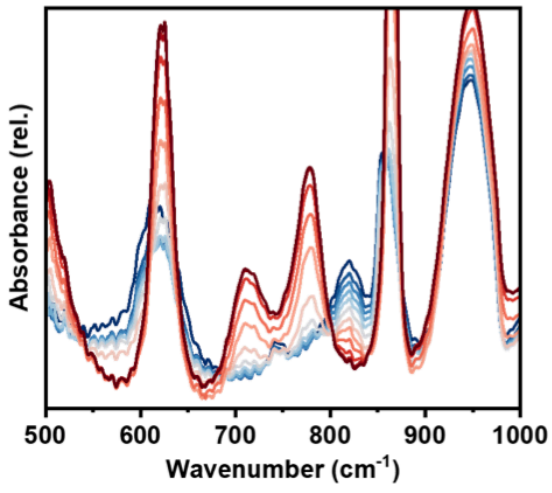

Figure 1. Comparison of experimental spectra of the UF_6 hydrolysis reaction obtained by SRNL (left) with computational modeling performed by SNL (right). The spectra on the left are a time series while monitoring the reaction, with Blue being earlier in time and red being later in time. The bottom plane of the right figure is SRNL experimental data pulled at different times during the reaction. This is the first observation of these intermediate compounds and the first combined experimental and computational effort in understanding this reaction.

Approach

To quantify the amount of protium ingress and tritium UF_6 reacts with water too rapidly at room temperature and pressure for monitoring by traditional methods. The only ways to monitor the reaction are to utilize ultrafast lasers or to slow the reaction down. In this project we have chosen the latter and used liquid nitrogen and liquid helium cryostats to capture and slow the reactions down to measurable time scales. We have also looked at surrogate compounds, such as MoF_6, which react less rapidly. Additionally, we have explored reactions outside the hydrolysis reaction. Alcohol and ammonia react similarly to water, but the introduction of steric hindrances changes the reaction kinetics and thermodynamics. We are monitoring the reaction using infrared (IR) spectroscopy. IR spectroscopy provides information on the chemical structure of a sample and can be used to identify the formation of new chemical species. Other spectroscopic techniques, such as Raman and UV-vis spectroscopy, are also being employed to improve characterization of intermediate compounds.

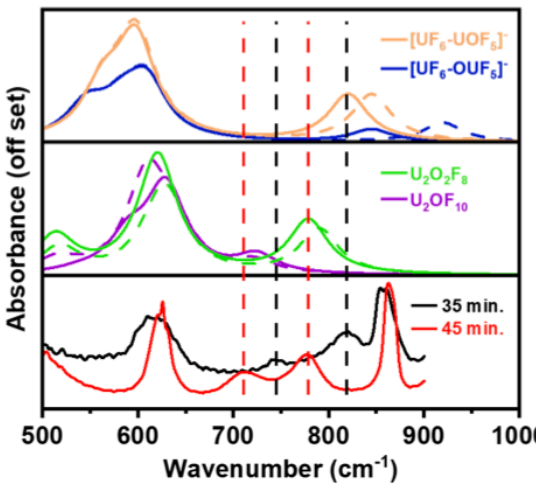

Accomplishments and results

- Demonstrated multiple competing reaction mechanisms at the molecular level for the UF_6 hydrolysis reaction for the first time.
- Demonstrated effects of sterics on the reaction of UF_6 with alcohols and observed counterintuitive tends on the reactions activation energy with alcohols reacting at significantly lower temperatures than water.
- Observed some changes in final product formation from controlling the reaction through temperature.

Peer-reviewed Publications

- Austin L. Dorris, Abigail M. Waldron, Louis E. McNamara, "Controlled Reaction Dynamics of UF6 and MoF6 with Methanol to Elucidate New Chemical Signatures," JRNC, 2025, *SUBMITTED**
- Louis E. McNamara, Austin L. Dorris, Abigail M. Waldron, John T. Kelly, Jesse J. Lutz, K. Alicia Strange Fessler, "Uranium Hexafluoride Hydrolysis Reaction Dynamics from Cryogenic Layering, FTIR Spectroscopy, and Isotopic Substitution", JPCA, 2025, *SUBMITTED (invited publication)**
- Austin L. Dorris, Abigail Waldron, Joy McNamara, Louis McNamara, "In Situ Measurement Vibrational Spectra of Ammonia and Water Ice Mixtures During Mixing," Vibrational Spectroscopy, 2025, *SUBMITTED**

Team Members

Louis McNamara, Austin Dorris[*], Abigial Waldron, Kyle Hartig[a], Mike Duncan[b], Jesse Lutz[c], K. Alicia Fessler[d]

[a]*University of Florida*
[b]*University of Georgia*
[c]*Sandia National Laboratory*
[d]*Oak Ridge National Laboratory*
[*]*Postdoctoral Researcher*

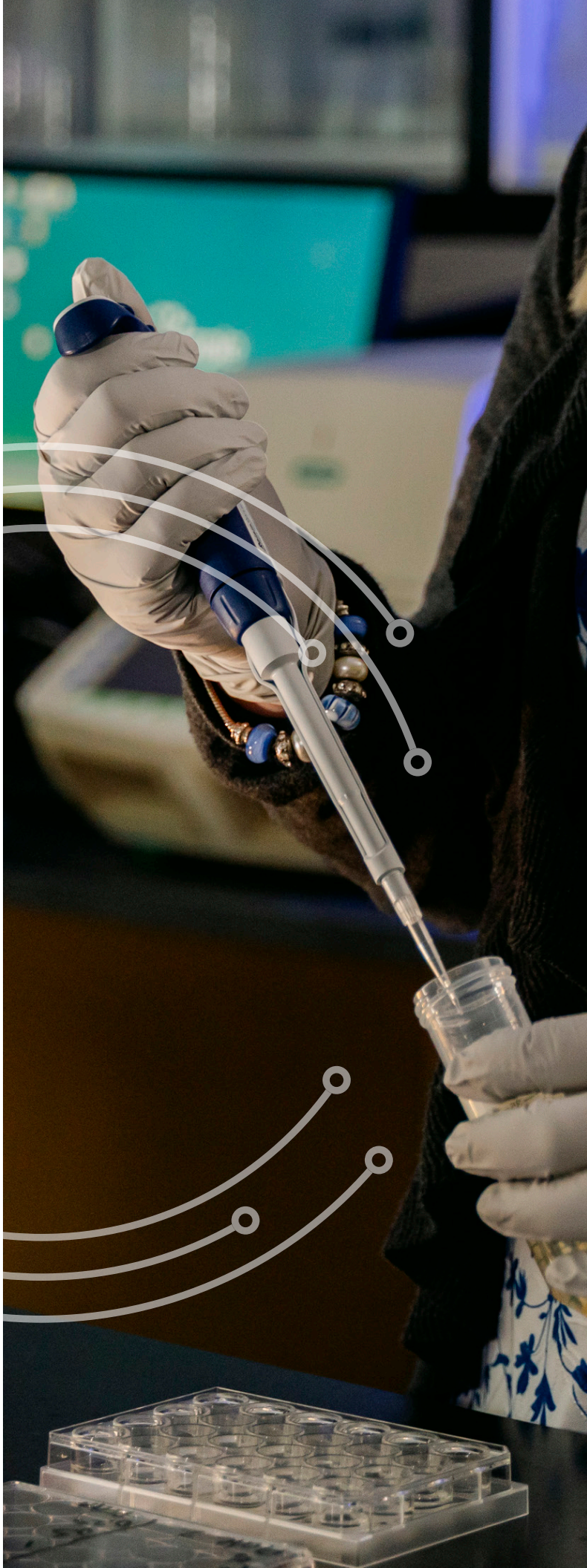

Ultra-Sensitive Liquid Scintillation Counting

Henning O. Back

The future environmental radiation detection challenges are associated with smaller samples, faster reporting, expansion of sample suite, and low concentrations of target radionuclides. Leveraging the East Coast's only cosmic ray reduced underground laboratory (1), we aim to develop the World's most sensitive liquid scintillation counter at Savannah River National Laboratory.

Introduction

To meet these challenges, the development of ultra-low-background (ULB) radiation detection equipment beyond the state-of-the-art and operation in underground laboratories is required. Increasingly, the sensitivity of low-background radiation detection is limited by the radiopurity of the materials that are central to the instruments and the chemistry methods used to prepare the samples for radioisotope analysis. Underground laboratories offer environments where the backgrounds associated with cosmic rays are highly reduced, making the radioactivity of the detector materials the greatest contributor to the background. The sensitivity of some commercial off-the-shelf instruments benefits from operating in the cosmic ray reduced environment of underground locations (e.g., high-purity germanium detectors), but not in the case of commercial off-the-shelf liquid scintillation counters. The aim of this work is to take advantage of recent advances to develop the World's most sensitive liquid scintillation counter operating in the low-background environment of Savannah River National Laboratory's underground counting facility. For this to come to fruition a thorough understanding of the radioactive environment in the underground counting facility and thereby how to mitigate those radioactive backgrounds is required. Likely the greatest challenge is minimizing the impact of the radioactive impurities in the light detectors, which will need to be moved away from the scintillator and necessitates the development of a light collection modality that maximizes light collection while minimizing radioactive impurities. The most successful ultra-low-background liquid scintillation counter operating in an underground laboratory had very low backgrounds but suffered significantly from poor light collection (2).

Approach

To tackle these challenges requires first modeling the cosmic rays throughout the underground count facility environment and how they will interact with facility and detector materials to produce secondary particles as well as the radioactive activation products in the materials that will cause backgrounds when they decay sometime after the cosmic ray (or secondary) has passed. To benchmark the models there are historical data available from operating detectors in the underground counting facility and from previous publications, however they are not sufficient to be the predictor of detector backgrounds, because those backgrounds may be from detector materials. The planned outcome is to both accurately predict the background of the future ultra-sensitive liquid scintillation counter, and to create a model flexible enough to be used by other underground laboratories and for engineering future underground laboratories. The second challenge to be tackled is that low-background commercial off-the-shelf liquid scintillation counters use photomultipliers (PMT) that are placed very close to the scintillator vial, which means that the radioactivity in the glass of the PMT is not mitigated and contributes significantly to the instrument's background. The project aims to explore the use of low-radioactivity silicon photo multipliers (SiPM) being developed by rare-event physics experiments (neutrino physics and direct dark matter searches) (3,4,5) coupled with a new novel light guide design that will be developed. Through commercial optical modeling software and particle physics models of radioactivity from SiPMs, the backgrounds can be minimized while the light collection is maximized. Optical model benchmark experiments are expected.

Team Members

Henning Back, Sue Clark, Joe Mannion, Chris Sobecki, Ashlee Swindle, John Armstrong*, Rebecca Mueller*, Caitlyn English*, Samuel Hartness*, Sean Dziubinski*

**Postdoctoral Researcher*

References

1. Winn, G. W.; Bowman, W. W.; Boni, A. L., Ultra-Clean Underground Counting Facility for Low-Level Environment Samples. *The Science of the Total Environment,* **1988,** 69, 107-144
2. Erchinger, J. L.; Orrell, J. L.; Aalseth, C. E.; Bernacki, B. E.; Douglas, M.; Fuller, E. S.; Keillor, M. E.; Marianno, C. M.; Morley, S. M.; Mullen, C. A.; Panisko, M. E.; Warren, G. A., Background characterization of an ultra-low background liquid scintillation counter. *Applied Radiation and Isotopes* **2017**, 126, 168-170
3. Aalseth, C. E.; et al., Cryogenic Characterization of FBK RGB-HD SiPMs. *JINST* **2017**, 12, P09030
4. Kochanek, I.; for DarkSide Collaboration, Packaging strategies for large SiPM-based cryogenic photo-detectors. *NIM* **2020**, A980, 164487
5. Acerbi, F.; et al., NUV and VUV sensitive Silicone Photomultiplier technologies optimized for operation at cryogenic temperatures, *NIM* **2023,** A1046, 167683

Tritium and Hydrogen Isotope Science

Tritium Inventory Loss from Diffusion into Process Piping

Holly Flynn

Stainless-steel process piping will be a major component in transporting tritium throughout a fusion power plant. This material will be a source of tritium loss due to diffusion. Tritium inventory is finite and a goal of SRNL's fusion modeling group is to determine the loss from process piping.

Introduction

Within a fusion power plant (FPP) there will exist a fuel cycle that is made of several components. These components all aid in removing impurities and delivering deuterium-tritium fuel to the fusion chamber. Prior to steady-state operation, the plant must undergo a commissioning phase to ensure reliable and efficient use of the tritium startup inventory. The tritium startup inventory is the amount of tritium necessary to fill all processing components and make up for losses including decay, burnup, and diffusion. Many of the fuel cycle components such as process piping will be made of stainless-steel. Tritium can easily diffuse into this material and protium ingress is likely due to a thin water layer that is known to be adsorbed onto the surface.

Tritium diffusivity and solubility is not well understood at and this is approximated by extrapolating from high temperature data. With this approximation we found that tritium uptake in stainless-steel piping is greater than protium ingress. This uptake does not affect startup inventories. However, from a tritium accountancy point of view the approximated tritium diffusivity if wrong could have serious implications.

In this work, we address this by calculating the diffusivity and solubility of tritium exposed stainless steel at room temperature from legacy Savannah River National Laboratory digital autoradiograph images. This information will then be combined with a diffusion model, where we will compare the approximated (extrapolated) to the calculated tritium diffusivity to gauge how different tritium uptake is in stainless steel. industry.

Approach

To quantify the amount of protium ingress and tritium uptake from stainless-steel process piping, we employed the Quantitative Tritium Migration Model (QTRIMM) which was developed by Matthew Sharpe at the University of Rochester.1 This model is based on Fickian Diffusion, where water layers can be incorporated onto a stainless-steel surface and tritium can isotopically exchange with protium and diffuse further into the metal.

Our next objective was to determine if tritium uptake into stainless-steel affected startup inventories. Tritium inventories throughout a fuel cycle can be estimated by utilizing SRNL's Reduced Hydrogen INventory Optimization Model (RHINO).2 This model can calculate time-dependent tritium inventories of fuel cycle components given a flow rate. From this model we were able to determine the total amount of steady-state tritium inventory for all the components. That inventory is then used to calculate the total length of piping required if all the tritium in a failure case scenario had to be off loaded into piping. This length is what a fuel cycle would require during normal operations. The QTRIM Model can take this length as a surface area and calculate the total amount of protium ingress and tritium diffusion.

Our previous finding still holds, but we realized that we have an opportunity to determine tritium diffusion at and not rely on extrapolated data. Currently a python model is being developed to analyze autoradiograph images of stainless-steel that have been exposed to tritium for long periods of time.

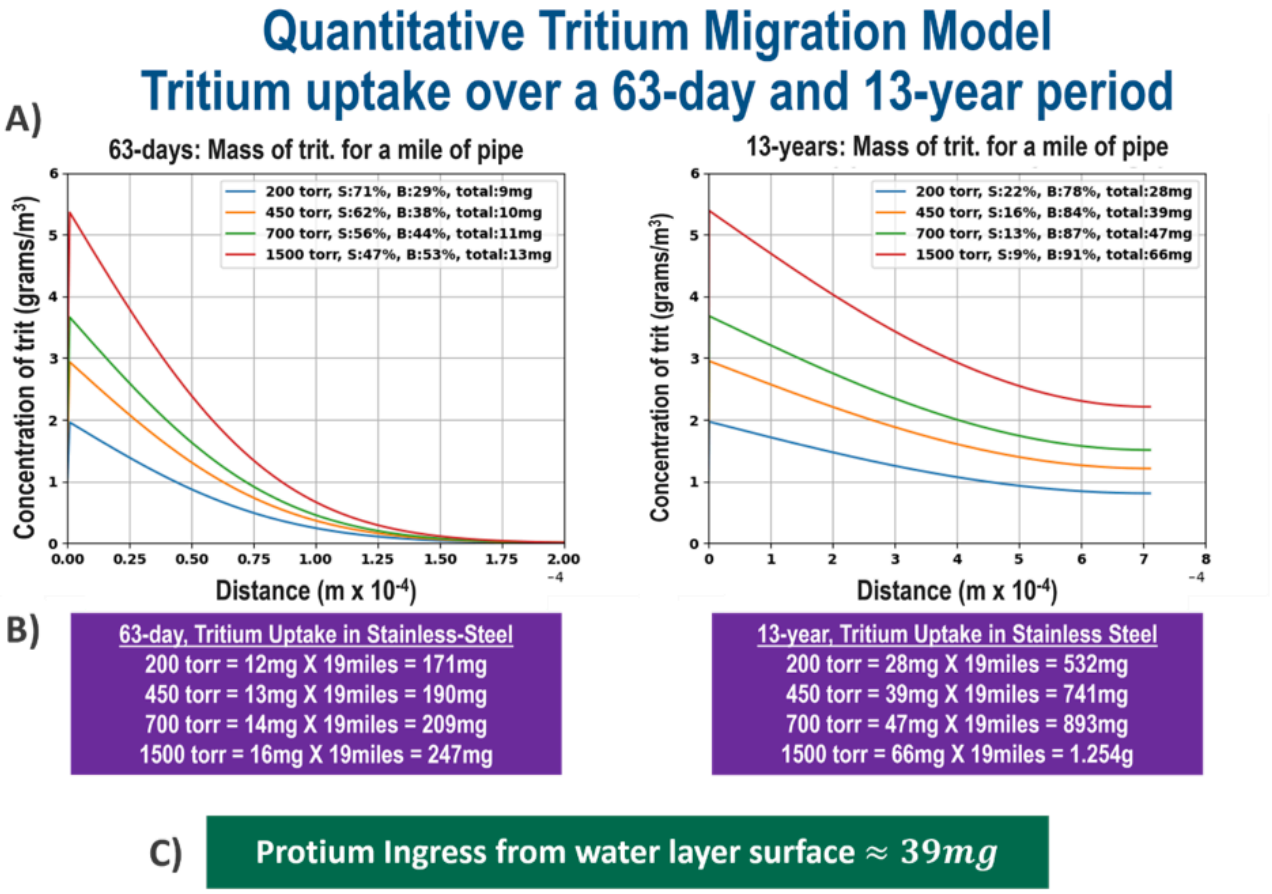

Figure 1. A) 63-days and 13-year tritium diffusion into stainless steel for different pressure. The stainless-steel thickness is 712 microns, where S and B stand for surface and bulk percent tritium mass for a mile of pipe, respectively. B) 63-days and 13-year total mass of tritium for 19-miles of pipe. C) Total amount of protium ingress regardless of pressure.

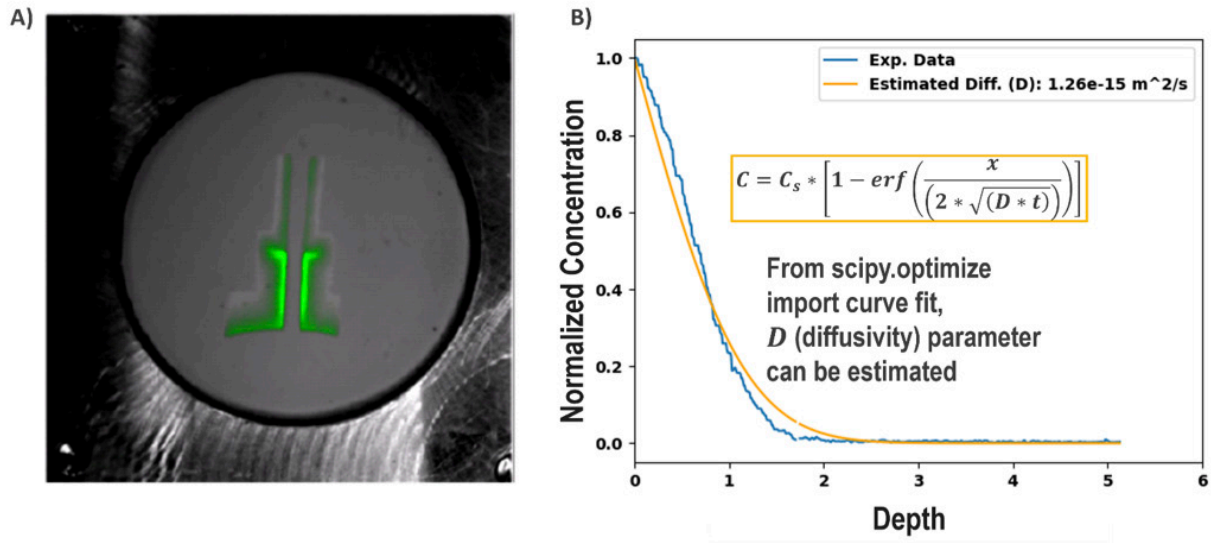

Figure 2. A) Digital autoradiograph of tritium (neon green) in stainless steel. B) Fitting raw data from digital autoradiograph in blue to the analytical diffusivity equation, in orange, from a python optimizer.

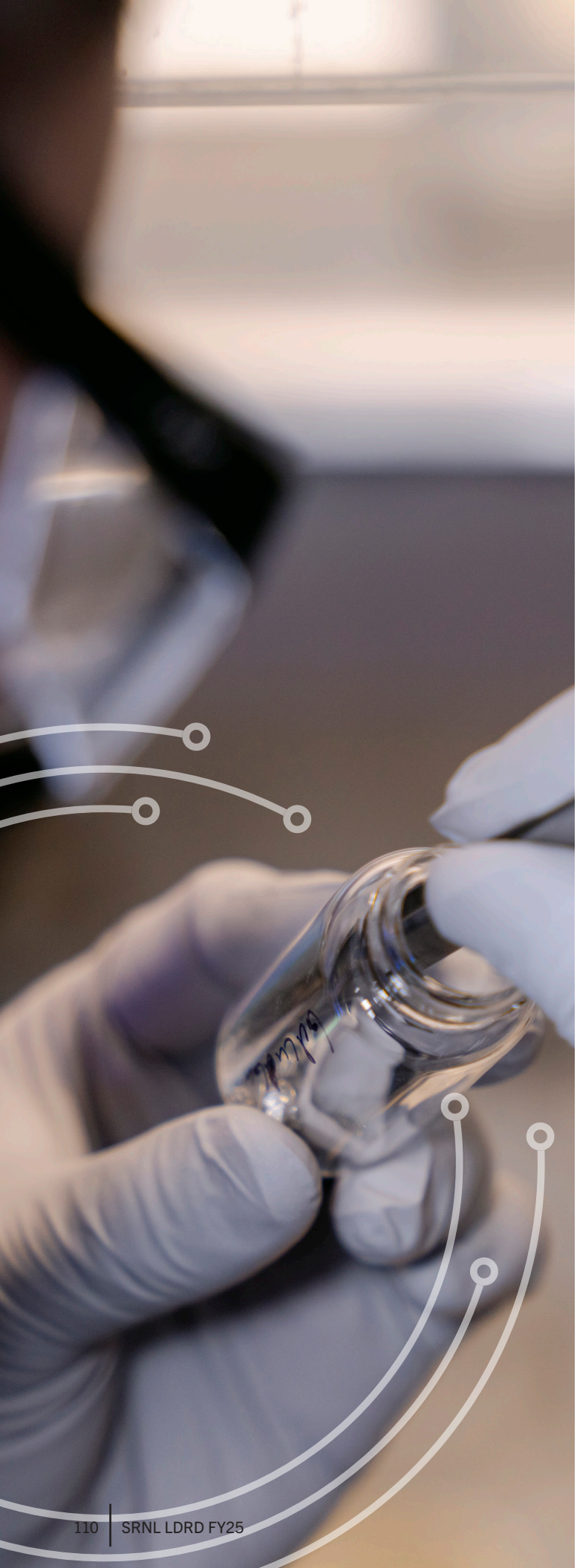

Accomplishments and results

- From the RHINO calculations we determined that the total tritium inventory of fuel cycle components is on the order of ~219 grams which translates to ~19 miles of ¼ inch piping required of a fuel cycle where all tritium and deuterium needs to be off loaded into piping.
- The surface area of ~19 miles of ¼ inch piping was combined with QTRIMM to determine that tritium uptake is on the order of ~100's of mg's, while protium ingress is ~40mg's regardless of pressure studied.
- **Figure 2** A) represents digital autoradiograph SRNL data of tritium in stainless-steel at room temperature. A python script was written to analyze images like that to back calculate room temperature tritium diffusion. Preliminary data suggest, **Figure 2** B), that the diffusivity is $\sim D = 1.26 \, X \, 10^{-15} \frac{m^2}{s}$ instead of the extrapolated data1: $D = 3.83 \, X \, 10^{-16} \frac{m^2}{s}$.

Team Members

Holly Flynn, Alex Somers, Collin Malone, and Paul Rowell

**Laboratory Director's Postdoctoral Research Fellow*

References

1. Sharpe, M. On the Interaction of Tritium with the Surfaces of Aluminum, Copper, Stainless Steel (Type 316), and Gold. Ph.D. Thesis, University of Rochester, 2016.
2. Malone, C. R.; Flynn, H. B.; Somers, A. D.; Rowell, P. A.; Larsen, G. K. Approach to Startup Inventory for Viable Commercial Fusion Power Plant. *Fusion Eng. Des.* 2024, *206*, 114563..

Enhancing Tritium Recovery in Nuclear Fusion Reactors through Catalyst-Infused Membrane Technology

Jennifer Naglic

The progress of the development of the SRNL catalyst-infused membrane technology for ammonia decomposition has been encouraging, supported by the successful infusion of metal onto the membrane. These infused membrane materials have been tested for NH3 decomposition activity, and they perform similarly to unpromoted NH3 decomposition catalysts while no powdered or pelletized catalyst is required.

Introduction

The recent demonstration of net-positive confined fusion and the energetic development of fusion pilot plants show that fusion increasingly becoming a viable energy source in the future. However, significant technological advances are required to address gaps that exist in the fusion blanket and fuel cycle. One approach is to extract the hydrogen isotopes at the plasma chamber exhaust for direct reinjection. It is anticipated that large amounts of ammonia will form from contact between the divertor nitrogen seeding coolant and the fusion plasma, as well as the well-known formation of ammonia catalyzed by tritium decay in the presence of nitrogen[1-3]. For these ammonia-bound hydrogen isotopes to be utilized and maximize the direct reinjection of hydrogen isotopes, the ammonia must be decomposed as close to the plasma exhaust as possible.

Membrane reactors, seen in **Fig. 1**, and metal foil pumps are the leading options for the hydrogen isotope extraction from the plasma exhaust[4]. Both routes rely on the hydrogen isotopes permeating through the membranes. Traditional catalytic decomposition of ammonia relies on catalyst particles being present in the gas phase, which can lead to significant pressure drops. A new method to decompose the ammonia at the surface of the membrane

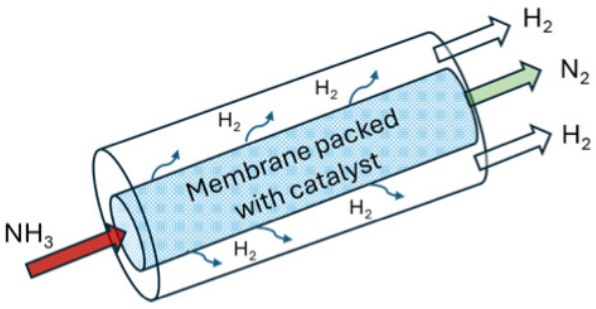

Figure 1. Traditional membrane packed with ammonia decomposition catalyst.

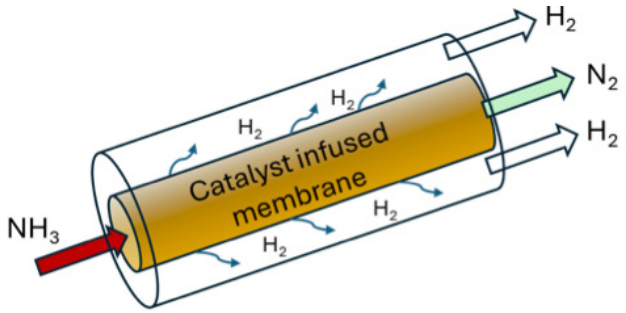

Figure 2. Catalyst infused membrane for NH_3 decomposition and simultaneous H_2 separation.

would help promote the hydrogen isotope permeation, eliminate detrimental pressure drop, and would be applicable to either the membrane reactor or metal foil pumps. This involves infusing the catalyst directly onto the membrane as seen in **Fig. 2**.

Approach

In order to infuse the membrane material with the catalyst, a deposition method was employed. First a design of experiments was conducted to determine the best method for preparing the surface of the membrane. This involved physical polishing and chemical etching of the surface. Nitrate and chloride metal salt precursors were evaluated to determine the optimal source of the metal. A design of experiments was also conducted surrounding the deposition solution with variables of chemicals and process parameters resulting in a total of 28 materials to be synthesized and tested for ammonia decomposition activity. The optimal stock solution was prepared, and the catalyst was deposited on the surface of the membrane material, **Fig 3**.

A dedicated reactor system for this project was built for ammonia decomposition experiments. The prepared membrane materials were evaluated for ammonia decomposition activity between 300°C and 550°C in 25° increments. A MKS Cirrus 3 atmospheric mass spectrometer was used to analyze the final gas mixture.

All membrane materials were evaluated by SEM-EDX. This includes pre- and post- preparation, pre- and post-catalyst deposition, pre- and post- reaction membrane materials.

Accomplishments and results

- A dedicated plug flow reactor was plumbed out for this project with effluent monitoring using a MKS Cirrus 3 mass spectrometer.
- In the first design of experiments surrounding the preparation of the membrane, it was discovered it was unnecessary to use physical polishing or chemical etching for the preparation of the membrane material before catalyst deposition. There was no noticeable difference in the NH_3 conversion. However, there was noticeable changes in the surface of the membrane when looked at under SEM which may change the membrane efficacy.
- The active catalyst source was investigated, and it was determined that nitrate containing metal salts showed better NH_3 decomposition activity compared to the materials with chloride containing salts. SEM-EDX imaging also showed minimal catalyst uptake on the samples prepared with the chloride containing salts which is in line with literature.
- A design of experiments surrounding the stock solution yielded an optimal combination of materials and parameters. This combination allowed for a 60% NH_3 conversion at 450°C in 100% NH_3, Fig. 4. This aligns with literature values for unpromoted NH_3 decomposition catalysts under these conditions.
- Time on stream study conducted at 450°C for 4 weeks showed little change in activity.

Team Members

Lucas Angelette

References

1. Angelette, L. M.; Belliveau, R. G.; Coopersmith, K. J.; Cooper, J. J.; Steedley, J. A.; Morrell, B. B. Evaluation of catalysts for decomposition of ammonia in hydrogen isotope purification systems. *Fusion Engineering and Design* **2021**, *173*. DOI: 10.1016/j.fusengdes.2021.112895.
2. Lukacs, M.; Williams, L. G. Nuclear safety issues for fusion power plants. *Fusion Engineering and Design* **2020**, *150*. DOI: 10.1016/j.fusengdes.2019.111377.
3. Linke, J. D., Juan; Loewenhoff, Thorsten; Pintsuk, Gerald; Spillker, Benjamin; Steudel, Isabel; Wirtz, Marius. Challenges for plasma-facing components in nuclear fusion. *Matter and Radiation at Extremes* **2019**, *4* (5). DOI: 10.1063/1.5090100.
4. Tosti, S., Pozio, A. Membrane Processes for the Nuclear Fusion Fuel Cycle. *Membranes (Basel)* **2018**, *8* (4). DOI: 10.3390/membranes8040096 From NLM PubMed-not-MEDLINE.

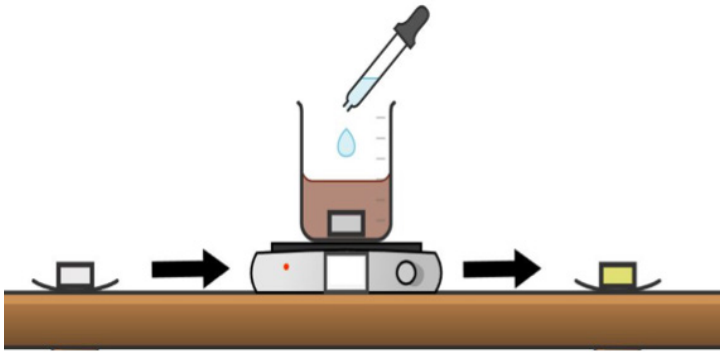

Figure 3. Flow diagram of deposition method.

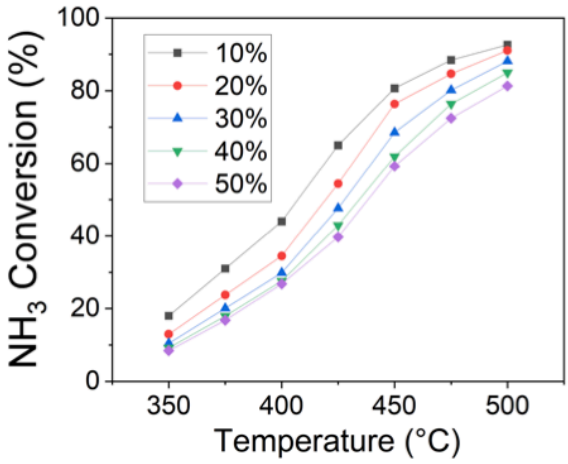

Figure 4. Ammonia decomposition activity of optimized catalyst infused membrane in varying concentrations of NH_3.

LDRD FY25 ANNUAL REPORT CONTRIBUTORS

Jacqueline Ramos

LJ Gay, photography

Susanna King, Anthony Castellano, design and layout

published April 2026

Savannah River National Laboratory®